

https://dspace.org/

Virtual reconstruction and description of the lower face definition of STW498- a Sterkfontein: australopithecus

Reddy, Shani

2019

https://hdl.handle.net/10539/28811

Reddy, Shani (2019) Virtual reconstruction and description of the lower face and dentition of STW 498 - a Sterkfontein Australopithecus, University of the Witwatersrand, Johannesburg, <http://hdl.handle.net/10539/28811>

Downloaded from a DSpace repository. https://dspace.org/

VIRTUAL RECONSTRUCTION AND DESCRIPTION OF THE LOWER FACE AND DENTITION OF STW 498 – A STERKFONTEIN *AUSTRALOPITHECUS*

Shani Reddy

574876

A dissertation submitted to the Faculty of Science, University of the Witwatersrand, Johannesburg, in fulfilment of the requirements for the degree of Master of Science.

Johannesburg, May 2019.

DECLARATION

I declare that this thesis is my own, unaided work. I have followed the necessary conventions in referencing the thoughts and ideas of others. It is being submitted for the Degree of Master of Science at the University of the Witwatersrand, Johannesburg. It has not been submitted before for any degree or examination at any other University.

Signature: 

13th day of May 20 19 at Johannesburg

ABSTRACT

On the 30th of September 1988, a team directed by Alun Hughes and Phillip Tobias excavated portions of a skull of an *Australopithecus* (StW 498) from square P/41 at Sterkfontein Member 4. The fossil was found at a depth of 17'9" to 19'9" ft below datum. StW 498 consists of cranial vault fragments, relatively complete left and right maxillae, and relatively complete left and right mandibles. While the mandibular and maxillary dentition is complete, the right mandible and right maxilla are fragmentary and anatomically displaced. Because of its fragile condition, a physical reconstruction was not advisable. The primary purpose of this research was to virtually reconstruct StW 498 using high resolution image data acquired from microCT scanning and to describe the morphology of the specimen. The reconstruction of StW 498 provided a valuable opportunity to conduct quantitative analyses and qualitative observations in order to place it within a framework of hominid cranio-dental variation, focusing in particular on *Australopithecus africanus*, *Australopithecus prometheus* and *Paranthropus robustus*. Based on the internal morphology and size of the dental arcade, StW 498 is a young adolescent male. The specimen exhibits dental pathology, specifically crowding of the maxillary dentition which resulted in the atypical eruption and position of the left maxillary canine. However, contra to the suggestion by Schwartz and Tattersall (2005), the right lower canine reflects taphonomic disruption of the intact anatomy rather than an eruptive anomaly. The results of this research indicate that StW 498 is morphologically more similar to specimens attributed to *A. prometheus*, such as MLD 9, StW 252, and StW 573, than *A. africanus* and *P. robustus*.

Keywords: *Australopithecus*, Sterkfontein, Virtual reconstruction

ACKNOWLEDGEMENTS

First and foremost I would like to thank Prof Ronald J. Clarke for his encouragement, patience, and mentorship not only during my MSc, but throughout my academic career. I am forever grateful for what you have taught me. I would like to thank Prof. Kathleen Kuman, without whom I would have never found my passion for archaeology and palaeoanthropology. To my incredible team of supervisors, Prof R.J. Clarke, Dr. Dominic J. Stratford, Prof Kristian J. Carlson, and Prof José Braga, thank you for dedicating your time to this project and especially for your patience while I was sick.

Thank you to Clément Zanolli and Amélie Beaudet for offering their assistance and expertise.

Thank you to the Evolutionary Studies Institute and the Ditsong National Museum of Natural History, South Africa, for allowing access to their fossil collections. For access to tomographic scans and associated digital data, I thank Ditsong National Museum of Natural History, South Africa.

I gratefully acknowledge the funding provided for my research by the DST-NRF Centre of Excellence in Palaeosciences (CoE-Pal) and by the Palaeontological Scientific Trust (PAST), Johannesburg, South Africa, without which this project would not have been possible.

I would like to thank my team of doctors and surgeons, without whom I would not have been able to complete this project. Thank you to Nadia and Stavros Michas for their hospitality and generosity while I was in Johannesburg to complete my research.

To my partner, Luke Michas, thank you for your unconditional love and support throughout this project, I would not have been able to do this without you.

Finally, I would like to thank my parents, Sanjiva and Laura Reddy. I cannot put into words how grateful I am to have your continued support and encouragement. Dad and Laura, you got me through my first degree and you taught me the value and power of knowledge. I dedicate this thesis to you.

CONTENTS

Declaration i

Abstract ii

Acknowledgments iii

Contents v

List of Figures viii

List of Tables xvi

Glossary xviii

CHAPTER 1 - INTRODUCTION 1

1.1. Aims…….…….....2

1.2. Hypothesis and questions……....……3

1.3. Rationale……..……..…...……..….……4

1.4. Structure of the dissertation……...….….……..…….…….....5

CHAPTER 2 - LITERATURE REVIEW AND BACKGROUND 6

2.1. Sterkfontein and the importance of Member 4….……...6

2.2. Hominid taxonomy: a complicated history……...……..……11

2.2.1. The Second Species Hypothesis……..……13

2.3. *Australopithecus africanus*, *Paranthropus robustus*, and *Australopithecus prometheus*: cranio-dental traits……..…...……20

2.4. Virtual, three-dimensional reconstruction and analysis….....……..24

2.4.1. Defining and correcting plastic deformation…….……25

CHAPTER 3: MATERIALS AND METHODS 28

3.1. Materials.....28

3.1.1. StW 498.....31

3.1.2. Comparative specimens.....38

3.2. Methods……46

3.2.1. Digitisation of StW 498 and comparative material …….…….46
3.2.2. Quantitative measurements and qualitative observations….....48
3.2.3. Virtual restoration and reconstruction of the lower face and dentition of StW 498…….……...53
3.2.4. Digital partitioning of the dentition for the analysis of dental form……...…….56

CHAPTER 4: RESULTS 60

4.1 Reconstruction and description of StW 498…….60
4.1.1. Reconstruction of the maxilla…….....61
4.1.2. Anatomical descriptions: the maxilla and associated dentition……..…….……65
4.1.3. Reconstruction of the mandible.……...……..83
4.1.4. Anatomical descriptions: the mandible and associated dentition…….……..…..…….…...88
4.1.5. The complete reconstruction of StW 498……..……...104
4.2. Quantitative measurements and qualitative observations.....…..…..109
4.2.1. Comparative metric analysis……..……..……..……..109
4.2.2. Virtual, three-dimensional analysis and dental Form…...……126
4.2.3. Anatomical observations…….……...…….....……..132

CHAPTER 5: DISCUSSION AND CONCLUSIONS 144

5.1. Discussion…….144
5.1.1. Material and methods……..…….…....……144
5.1.2. StW 498: reconstruction and anatomical observations.....146
5.1.3. The taxonomic attribution of StW 498……...…….....148
5.1.4. Limitations and future directions……..…...…….…155
5.2. Summary and conclusions……. ……..156

Appendix A: Parameters needed for image acquisition of StW 498…….…..161

Appendix B: Parameters needed for image acquisition of comparative material....162

Appendix C: Image processing.....163

Appendix D: Scores and loadings for the PCA of the maxillary canines…….164

Appendix E: Scores and loadings for the PCA of the maxillary and mandibular canines……...165

Appendix F: Scores and loadings for the PCA of the maxillary third premolars....167

Appendix G: Scores and loadings for the PCA of the maxillary fourth premolars.168

Appendix H: Scores and loadings for the PCA of the maxillary second molars.....169

Appendix I: Scores and loadings for the PCA of the maxillary third molars.....170

Appendix J: Scores and loadings for the PCA of the maxillary second and third molars.....171

Appendix K: Morphological features which distinguish the two groups of Sterkfontein and Makapansgat australopithecines according to Clarke (1988, *et seq*.).....173

References.....……...174

LIST OF FIGURES

Figure A. Occlusal view of the dental arcade illustrating the directional terminology utilised throughout this study.....xix

Figure B. Occlusal view of a maxillary molar illustrating the different cusps.....xx

Figure C. Occlusal view of a mandibular molar illustrating the different cusps.....xx

Figure 1.1. Plan view of the concentration of 'StW' prefixed hominids excavated between 1971 and 1993……..2

Figure 2.1. The vertical relationship of Sterkfontein Members 1 to 5…….9

Figure 2.2. Schematic view of the north-south section of Sterkfontein to show the general relationship of Members 1 through Members 6……...10

Figure 2.3. Virtual 3D rendering of the Taung skull……..26

Figure 2.4. The virtual reconstruction of the OH 7 mandible…….27

Figure 3.1. Illustrations of the StW 498a left maxilla.....32

Figure 3.2. Illustrations of the StW 498b right maxilla.....33

Figure 3.3. Illustrations of the StW 498c right mandible.....34

Figure 3.4. Illustrations of the StW 498d left mandible.....35

Figure 3.5. Illustrations of the petrosal (StW 498e) and fragments of the cranial vault (StW 498f).....36

Figure 3.6. Illustrations of cranial fragments, StW 498g-q and StW 499.....37

Figure 3.7. Illustrations of the Sts 36 mandible, a Sterkfontein *A. prometheus*.....38

Figure 3.8. Illustrations of the Sts 52a (maxilla) and Sts 52b (mandible), a Sterkfontein *A. africanus*....……..…….....39

Figure 3.9. Illustrations of the Sts 71 partial cranium belonging to Sterkfontein *A. prometheus*…….....40

Figure 3.10. Illustrations of the StW 73 maxilla, a Sterkfontein *A. africanus*….....41

Figure 3.11. Illustrations of StW 183, the right and left maxillary canines belonging to Sterkfontein *A. prometheus*…….....41

Figure 3.12. Illustrations of the Sterkfontein StW 252 maxilla belonging to Sterkfontein *A. prometheus*…….....42

Figure 3.13. Illustrations of the StW 287 left maxillary canine belonging to a Sterkfontein *A. africanus*….....43

Figure 3.14. MLD 11/30 right maxillary canine and third premolar of a Sterkfontein *A. africanus*…….....43

Figure 3.15. SK 843 right partial mandibular corpus belonging to a *P. robustus* from Swartkrans…….....44

Figure 3.16. *P. robustus* type specimen from Kromdraai, TM 1517, right partial mandibular corpus and right partial maxilla….....45

Figure 3.17. An example of the surface renderings resulting from the segmentation of the StW 498a left maxillary central incisor to the left maxillary canine prior to final reconstruction….....54

Figure 3.18. Reconstructed left mandibular molar crown and the EDJ (StW 498d)….....58

Figure 3.19. Enamel thickness distribution on the maxillary molars of *Homo neanderthalensis* and extant humans…….....59

Figure 4.1. 3D renderings of the left maxilla (StW 498a) prior to reconstruction.....61

Figure 4.2. The complete reconstruction of the left maxilla (StW 498a).....62

Figure 4.3. 3D renderings of the crushed right maxilla (StW 498b).....63

Figure 4.4. The complete reconstruction of the StW 498 maxilla.....64

Figure 4.5. The complete reconstruction of the StW 498 maxillary dental arcade....66

Figure 4.6. 3D renderings of the left maxillary central incisor (StW 498a) before and after reconstruction 67

Figure 4.7. Illustrations of the isolated right maxillary central incisor (StW 498b).....68

Figure 4.8. 3D renderings of the left maxillary lateral incisor (StW 498a) before and after reconstruction.....69

Figure 4.9. 3D renderings of the left maxillary canine (StW 498a) before and after reconstruction.....70

Figure 4.10. 3D renderings of the right maxillary canine (StW 498b) before and after reconstruction.....71

Figure 4.11. 3D renderings of the left maxillary third premolar (StW 498a) before and after reconstruction.....72

Figure 4.12. 3D renderings of the right maxillary third premolar (StW 498b) after segmentation.....73

Figure 4.13. 3D renderings of the left maxillary fourth premolar (StW 498a) before and after reconstruction.....74

Figure 4.14. 3D renderings of the right maxillary fourth premolar (StW 498b) after segmentation.....75

Figure 4.15. 3D renderings of the left maxillary first molar (StW 498a) before and after reconstruction.....76

Figure 4.16. 3D renderings of the right maxillary first molar (StW 498b) before and after reconstruction.....77

Figure 4.17. 3D renderings of the left maxillary second molar (StW 498a) before and after reconstruction.....78

Figure 4.18. 3D renderings of the right maxillary second molar (StW 498b) before and after reconstruction.....79

Figure 4.19. 3D renderings of the left maxillary third molar (StW 498a) before and after reconstruction.....81

Figure 4.20. 3D renderings of the right maxillary third molar (StW 498b) before and after reconstruction.....82

Figure 4.21. 3D renderings of the left mandible (StW 498d).....83

Figure 4.22. 3D renderings of the crushed right mandible (StW 498c).....84

Figure 4.23. MicroCT sagittal view and 3D rendering of the labial view of the mandibular canines 85

Figure 4.24. The complete reconstruction of the left mandible (StW 498d).....86

Figure 4.25. The complete reconstruction of the StW 498 mandible.....87

Figure 4.26. 3D rendering of the left mandibular central (StW 498d) incisor.....89

Figure 4.27. 3D renderings of the right mandibular central incisor (StW 498c) before and after reconstruction.....90

Figure 4.28. Illustration of the left mandibular lateral incisor (StW 498d).....91

Figure 4.29. 3D renderings of the right mandibular lateral incisor (StW 498c) before and after reconstruction.....92

Figure 4.30. 3D renderings of the left mandibular canine (StW 498d) before and after reconstruction.....93

Figure 4.31. 3D renderings of the right mandibular canine (StW 498c) before and after reconstruction.....94

Figure 4.32. 3D renderings of the left mandibular third (StW 498d) premolar after segmentation.....95

Figure 4.33. 3D renderings of the right mandibular third premolar (StW 498c) after segmentation.....96

Figure 4.34. 3D renderings of the left mandibular fourth premolar (StW 498d) before and after reconstruction.....97

Figure 4.35. 3D renderings of the right mandibular fourth premolar (StW 498c) before and after reconstruction.....98

Figure 4.36. 3D renderings of the left mandibular first molar (StW 498d) before and after reconstruction.....99

Figure 4.37. 3D renderings of the right mandibular first molar (StW 498c) before and after reconstruction.....100

Figure 4.38. 3D renderings of the left mandibular second molar (StW 498d) after segmentation.....101

Figure 4.39. 3D renderings of the right mandibular second molar (StW 498c) before and after reconstruction.....102

Figure 4.40. 3D renderings of the left mandibular third molar (StW 498d) after segmentation.....103

Figure 4.41. 3D renderings of the right mandibular third molar (StW 498c) after segmentation.....104

Figure 4.42. The complete reconstructed lower face of StW 498.....105

Figure 4.43. Lateral views of the reconstructed lower face of StW 498.....106

Figure 4.44. Reconstructed cranial vault fragments belonging to StW 498f, StW 498q, and StW 499.....107

Figure 4.45. The reconstructed lower face of StW 498 with frontal and parietal cranial vault fragments.....108

Figure 4.46. Principle Component Analysis of the maxillary canines of StW 498 and selected comparative specimens.....119

Figure 4.47. Principle Component Analysis of the maxillary and mandibular canines of StW 498 and selected comparative specimens.....120

Figure 4.48. Principle Component Analysis of the maxillary third premolars of StW 498 and selected comparative specimens.....121

Figure 4.49. Principle Component Analysis of the maxillary fourth premolars of StW 498 and selected comparative specimens.....122

Figure 4.50. Principle Component Analysis of the maxillary second molars of StW 498 and selected comparative specimens.....123

Figure 4.51. Principle Component Analysis of the maxillary third molars of StW 498 and selected comparative specimens.....124

Figure 4.52. Principle Component Analysis of the maxillary second and third molars of StW 498 and selected comparative specimens.....125

Figure 4.53. The virtually separated enamel-dentine junction and enamel surfaces of selected teeth from StW 498.....126

Figure 4.54. The virtually separated enamel-dentine junction and enamel surfaces of selected teeth from TM 1517.....127

Figure 4.55. The virtually separated enamel-dentine junction and enamel surfaces of selected teeth from StW 252.....127

Figure 4.56. Topographic surface renderings representing enamel distribution on the molars and premolars of StW 498, Sts 52 (*A. africanus*), TM 1517 (*P. robustus*), and StW 252 (*A. prometheus*).....130

Figure 4.57. Incisor root morphology of specimens attributed to *A. africanus*, *A. prometheus*, and StW 498.....133

Figure 4.58. Canine root morphology of specimens attributed to *A. africanus*, *A. prometheus*, and StW 498.....134

Figure 4.59. Comparison of the palates of StW 498, SK 48 (*P. robustus*), StW 252 (*A. prometheus*), StW 73 (*A. africanus*), Sts 53 (*A. africanus*), and StW 576 (*A. africanus*).....136

Figure 4.60. Comparison of the anterior maxilla of StW 573 (*A. prometheus*), Sts 52 (*A. africanus*), and SK 12 (*P. robustus*)….....136

Figure 4.61. Comparison of the maxillary roots and dental arcade of StW 573 (*A. prometheus*) and StW 498.....138

Figure 4.62. Comparison of the incisor procumbence between Sts 52 (*A. africanus*) and StW 252 (*A. prometheus*).....139

Figure 4.63. StW 498a left maxilla joined with the MLD 9 right maxilla.....140

Figure 4.64. Comparison of mandibular shape and size of StW 498, SK 843 (*P. robustus*), StW 573 (*A. prometheus*), Sts 36 (*A. prometheus*), Sts 52 (*A. africanus*), and MLD 18 (*A. africanus*).....142

Figure 4.65. Casts comparing the mandibles of Sts 36 (*A. prometheus*), StW 498, and MLD 40 (*A. africanus*) in basal views.....143

Figure 4.66. Comparisons of the mandibular second and third molars of StW 498, StW 109 (*A. prometheus*), and MLD 2 (*A. prometheus*).....143

LIST OF TABLES

Table 2.1. Specimens attributed to *Australopithecus prometheus* according to Clarke (1988, *et seq*.)..…..19

Table 2.2. A summary of the cranio-dental traits that distinguish *Australopithecus africanus*, *Paranthropus robustus*, and *Australopithecus prometheus*.....23

Table 2.3. Cranio-dental diagnostic features which differentiate *Australopithecus africanus* and *Australopithecus prometheus*……..24

Table 3.1. A list of comparative hominid fossils included in this study…….....30

Table 3.2. Parameters needed for the image acquisition of StW 498.....47

Table 3.3. Parameters needed for the image acquisition of selected comparative material (Sts 36, Sts 52, Sts 71, SK 843, StW 252, and TM 1517).....48

Table 4.1. Maxillary dental dimensions of StW 498 and comparative specimens...110

Table 4.2. The crown area and crown shape index of the maxillary premolars and molars of StW 498 and comparative specimens.....112

Table 4.3. Palatal dimensions of StW 498 and selected comparative material.....113

Table 4.4. Mandibular dental dimensions of StW 498 and comparative specimens.....114

Table 4.5. The crown area and crown shape index of the mandibular premolars and molars of StW 498 and comparative specimens.....116

Table 4.6. Mandibular dimensions for StW 498 and selected comparative material.....117

Table 4.7. The average enamel thickness of the maxillary and mandibular second and third molars of StW 498 and selected comparative specimens.....128

Table 4.8. The three-dimensional average enamel thickness of the maxillary and mandibular molars of StW 498 and selected comparative specimens of *A. africanus*, *A. prometheus*, and *P. robustus*.....129

Table 4.9. The maximum enamel thickness distribution for the maxillary premolars, and the maxillary and mandibular second and third molars of StW 498 and selected comparative specimens.....131

Glossary

Directional Terms

Mesial: axis running toward the front of the dental arcade.

Distal: axis running away from the front of the dental arcade.

Labial: axis running toward the lips. This term is reserved for anterior teeth (incisors and canines).

Buccal: axis running toward the cheeks. This term is reserved for posterior teeth (premolars and molars).

Lingual: axis running toward the tongue.

Occlusal: refers to the chewing surface of a tooth.

Incisal: the chewing surface (occlusal edge) of the incisors.

Labiolingual: refers to the axis running from the lips (labial) to the tongue (lingual). Interchangeable with buccolingual, but reserved for anterior teeth. The maximum labiolingual diameter was taken on the surface of a tooth.

Buccolingual (BL): the axis running from the cheek (buccal) to the tongue (lingual). Reserved for posterior teeth. The maximum buccolingual diameter was taken on the surface of a tooth.

Mesiodistal (MD): axis running from the front of the dental arcade (mesial) toward the distal surface of a tooth. The maximum mesiodistal diameter was taken from the midline point on the surface of a tooth.

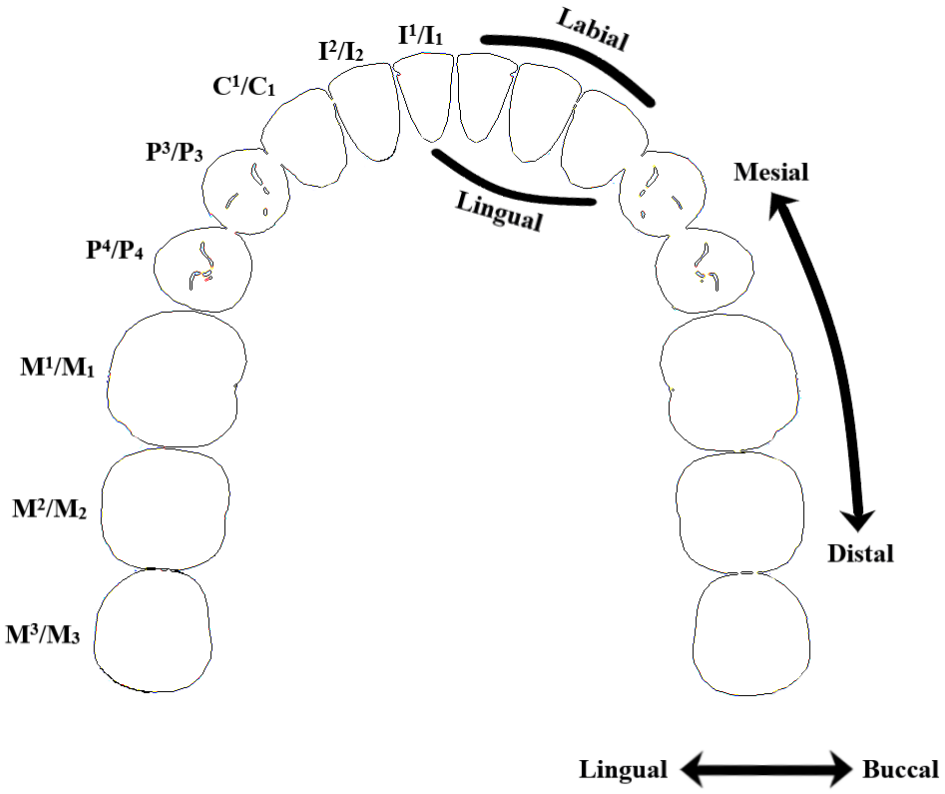

Figure A. Occlusal view of the dental arcade illustrating the directional terms utilised throughout this study.

Dental Morphological Features

The following terms are employed throughout Chapter 4 Results and closely follow the descriptive terminology of Robinson (1956), as modified by Tobias (1967), Johanson, White & Coppens (1982), and Moggi-Cecchi *et al*. (2006):

Paracone: a cusp situated on the buccal surface of maxillary premolars and on the mesiobuccal surface of maxillary molars.

Metacone: a cusp situated on the distobuccal surface of a maxillary molar.

Protocone: a cusp situated on the lingual surface of maxillary premolars and on the mesiolingual surface of maxillary molars.

Hypocone: a cusp situated on the distolingual surface of a maxillary molar.

Carabelli's cusp: an additional cusp occasionally present on the maxillary molars; situated on the mesiolingual surface.

Protoconid: a cusp situated on the mesiobuccal surface of mandibular premolars and molars.

Hypoconid: a cusp situated on the distobuccal surface of mandibular molars.

Metaconid: a cusp situated on the mesiolingual surface of mandibular premolars and molars.

Entoconid: a cusp situated on the distolingual surface of mandibular molars.

Hypoconulid: a fifth cusp situated on the distal-most surface of mandibular molars.

C6: an additional cusp occasionally present on mandibular molars; often situated between the hypoconulid and entoconid.

C7: an additional cusp rarely present on mandibular molars; often situated on the distolingual surface, beneath the C6.

Cervix: the junction between the root and the neck of the crown.

Cingulum: a protuberance of enamel that forms just above the cervix on the lingual surface of the incisors and canines.

Anterior fovea: presents as either a depression or an elongated groove on the mesial occlusal surface of premolars and molars.

***Crista obliqua*:** an obliquely-directed crest on the metaconid and protoconid cusps that results in the hypoconid being isolated from the remaining cusps.

Distal lingual fossa: a shallow fossa found on the distolingual surface of the anterior teeth. The distal marginal ridge borders the distolingual fossa.

Distal marginal ridge (DMR): a rounded border of enamel that forms on the occlusal edge on the distal surface of premolars and molars, and on the distolingual surface of incisors and canines.

Enamel hypoplasia: irregularities on the outer enamel surface of a tooth; often appear as lines or pits.

Fissure: appears as a cleft on the occlusal surface and divides the cusps.

Fossa: a depressed area, often broad and shallow.

Fovea: a pit-like depression, smaller than a fossa.

Groove: a wide or long fissure between the cusps.

Interproximal contact facets (IPCFs): facets that develop on the mesial and distal surfaces of a tooth as a result from contact with the other teeth.

Lingual median ridge: a ridge of enamel that runs from the cingulum to the apical half of a tooth crown; this ridge is found on the lingual surface of the incisors and canines.

Mesial lingual fossa: a depressed area found on the mesiolingual surface of the anterior teeth. The mesial marginal ridge borders the mesial lingual fossa.

Mesial marginal ridge (MMR): a rounded border of enamel that forms on the occlusal edge on the mesial surface of premolars and molars, and on the mesiolingual surface of incisors and canines.

Posterior fovea: presents as either a depression or an elongated groove on the distal occlusal surface of premolars and molars.

Maxillary and Mandibular Incisors and Canines

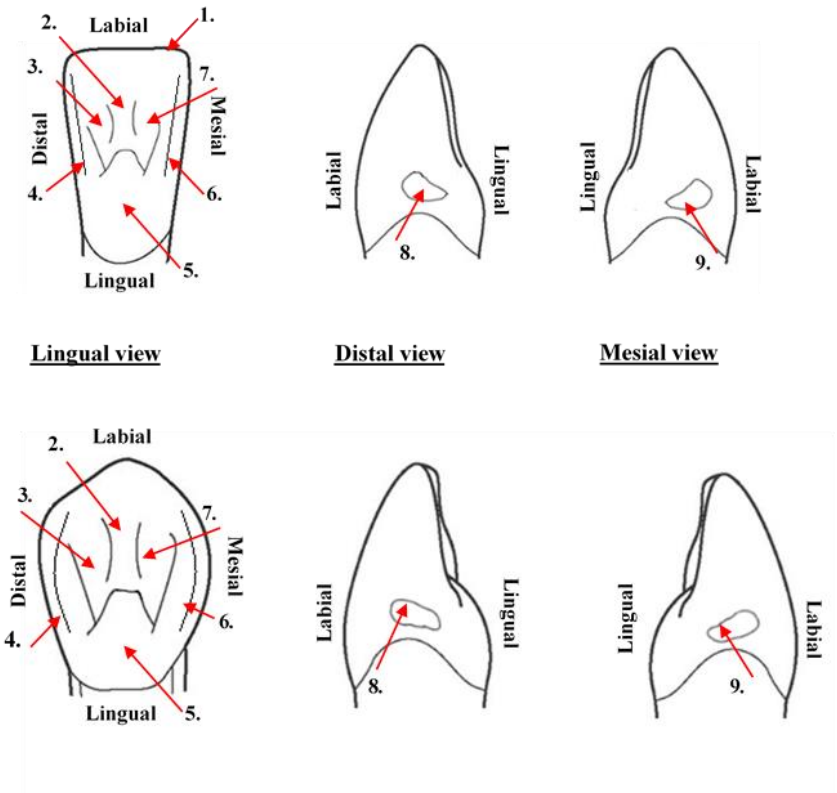

1. Incisal edge
2. Lingual median ridge
3. Distal lingual fossa
4. Distal marginal ridge (DMR)
5. Cingulum
6. Mesial marginal ridge (MMR)
7. Mesial lingual fossa
8. Interproximal contact facet (IPCF)
9. Interproximal contact facet (IPCF)

Maxillary and Mandibular Premolars

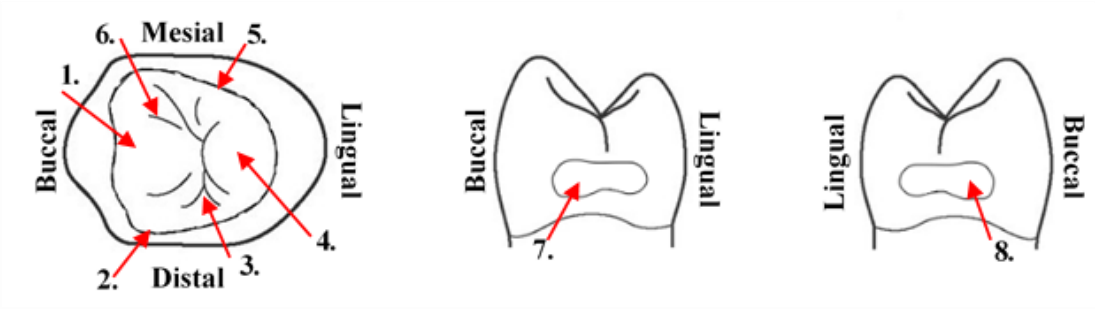

Occlusal view **Distal view** **Mesial view**

1. Paracone (metaconid in the mandibular premolars)
2. Distal marginal ridge (DMR)
3. Grooves
4. Protocone (protoconid in the mandibular premolars)
5. Mesial marginal ridge (MMR)
6. Fissures
7. Interproximal contact facet (IPCF)
8. Interproximal contact facet (IPCF)

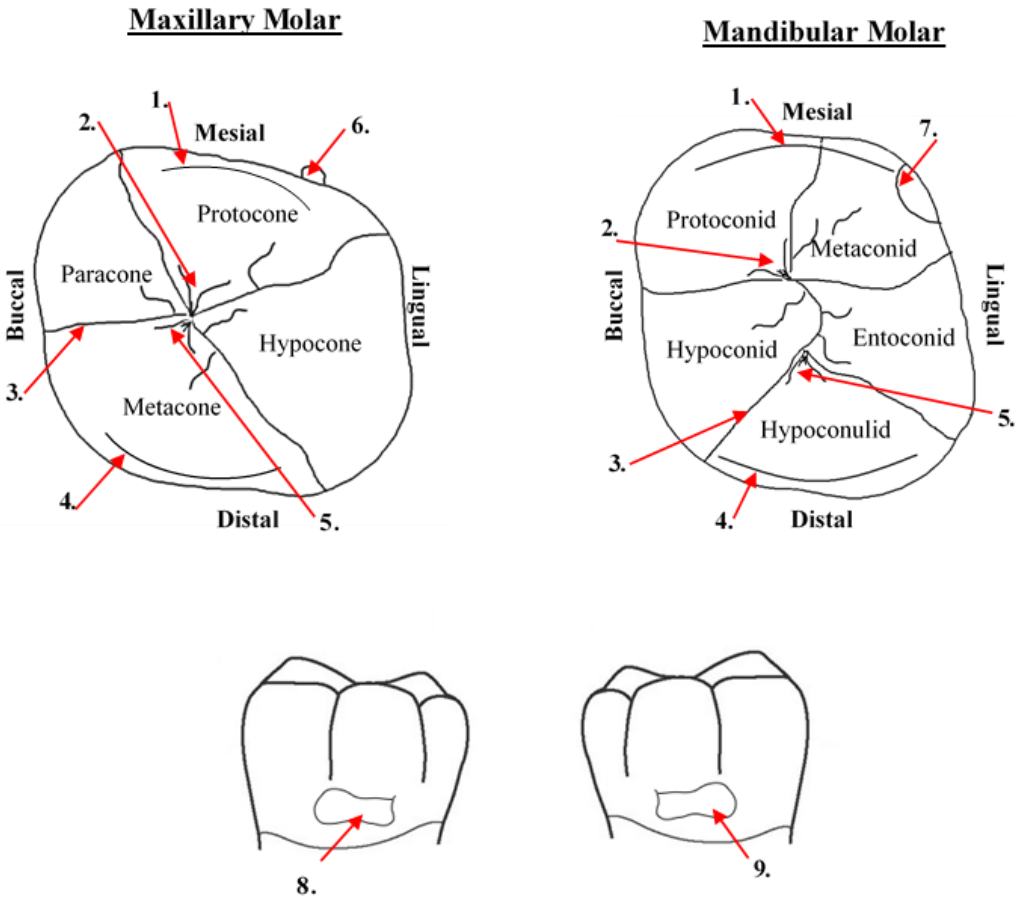

1. Mesial marginal ridge (MMR)
2. Mesial groove
3. Fissures
4. Distal marginal ridge (DMR)
5. Distal groove
6. Carabelli cusp
7. C6/C7
8. Interproximal contact facet (IPCF)
9. Interproximal contact facet (IPCF)

Chapter 1

Introduction

On the 30th of September, 1988, a team directed by Alun Hughes and Phillip Tobias excavated portions of an *Australopithecus* skull (StW 498) from square P/41 at Sterkfontein, Member 4. The fossil was found at a depth of 17'9" to 19'9" (feet and inches) below datum (Figure 1.1). StW 498 consists of cranial vault fragments, relatively complete left and right maxillae, and relatively complete left and right mandibles. While the mandibular and maxillary dentition is complete, the right mandible and right maxilla are fragmentary and anatomically displaced. Due to the extreme crushing, fragmentation, and plastic deformation of the bones, a physical reconstruction would be difficult and is not advisable.

The primary goal of this project is to virtually reconstruct and anatomically describe the reconstructed, accurate form of StW 498. Reconstructing and describing StW 498 offers the opportunity to reinforce taxonomic interpretations and to improve our understanding of australopithecine cranio-dental morphology and variation. This research will provide valuable data and therefore important resolution to current models of fossil hominid variation and, by extension, taxonomy and phylogeny.

This study utilised microfocus X-ray Computed Tomography (microCT) scanning of StW 498 in order to reveal and clarify both internal and external aspects of the morphology. This information permitted comparisons with the maxillae, mandibles, and dentition of various hominid species in order to determine the probable taxonomic attribution of StW 498.

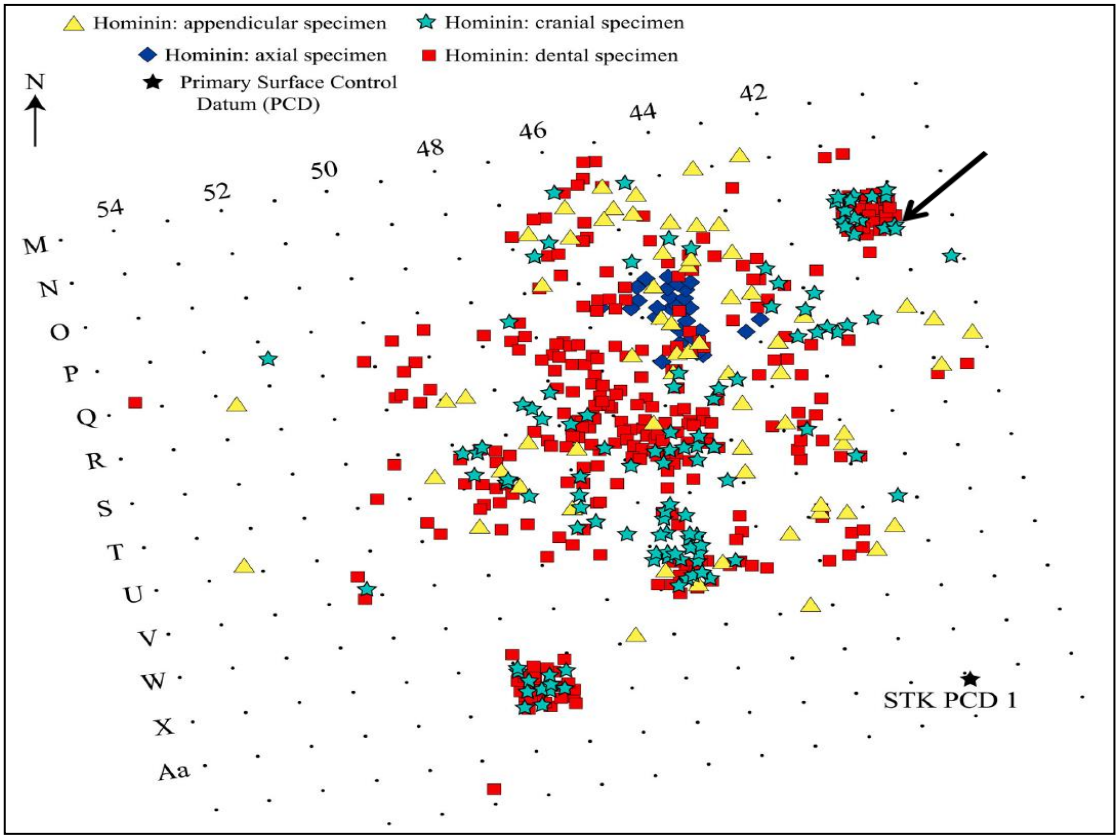

Figure 1.1. Plan view of the concentration of 'StW' prefixed hominids excavated between 1971 and 1993. The black arrow indicates the position of StW 498 (adapted from Stratford *et al*. 2016, Figure 8, p. 8).

1.1. Aims

The primary aim of this project was to virtually reconstruct and describe the lower face and dentition of StW 498. Such a reconstruction permitted comparison and contrast of the StW 498 morphology to selected specimens that have been classified as *Australopithecus prometheus*, *Australopithecus africanus*, and *Paranthropus robustus*. These comparisons enabled designation of the taxonomic affinity of StW 498, and utilised traditional morphological and quantitative-based methods. Moreover, the high resolution CT scans permitted examination of the internal morphology of StW 498 in order to determine whether this individual exhibits

pathological traits, as suggested by Schwartz and Tattersall (2005: 311), who state that eruption of the right lower canine is anomalous.

1.2. Hypothesis and questions

A complete, virtual reconstruction of StW 498 may help document the range of variation that exists in the *Australopithecus* assemblages from Sterkfontein, Makapansgat, Kromdraai, and Swartkrans. In other words, the virtual reconstruction of StW 498 may allow me to help better define the range of morphological variability that exists in the dental and lower face features of South African australopiths.

For the purpose of this project, the following questions were addressed:

1. Based on the virtual (*in silico*) reconstruction, what is the accurate morphological form of StW 498?

2. What are the morphological differences and/or similarities between the maxillae, mandibles, and dentition of StW 498, and those which have been classed as *A. africanus* (e.g., Sts 52), *A. prometheus* (e.g., StW 252, Sts 71, and Sts 36), and *P. robustus* (e.g., TM 1517 and SK 843)?

3. Is the problematic position of the right lower canine a pathological trait of this individual, as suggested by Schwartz and Tattersall (2005: 311), or rather due to taphonomic distortion, as proposed by Clarke (pers. comm.)?

1.3. Rationale

Although StW 498 has been briefly discussed by Schwartz and Tattersall (2005), and its broken dentition briefly described by Moggi-Cecchi *et al*. (2006), a detailed anatomical description of StW 498 has not be completed as no attempt has yet been made to reconstruct the fragmentary maxilla, mandible, and dentition. Associated mandibles and maxillae are extremely rare in the fossil record. The only other such South African australopithecines that preserve portions of an associated maxilla and mandible include: the Taung child (the type specimen of *A. africanus*) (Dart 1925), the Sts 52 partial maxilla and mandible attributed to *A. africanus* (Clarke 1990), the StW 573 skull with complete upper and lower dentition attributed to *A. prometheus* (Clarke 1998; 2018), and the Swartkrans SK 12 partial maxilla and mandible attributed *P. robustus* (Broom & Robinson 1952). StW 498 is more complete than either SK 12 or East African hominids such as KGA10-525 (*Australopithecus boisei*) from Konso, Ethiopia (Suwa *et al*. 1997) and AL 444-2 (*Australopithecus afarensis*) from Hadar, Ethiopia (Kimbel *et al*. 1994).

Given the debate surrounding Clarke's suggestion of a second *Australopithecus* species at Sterkfontein (1988; 1994; 1998; 1999; 2002; 2008), further investigation of the understudied StW 498 cranial specimen offers a critical opportunity to produce relevant new information. The existence of a second australopith species has significant implications to palaeoanthropology. If we were to accept Clarke's (1988, *et seq.*) claim, then the variability that exists within the various hominid taxa needs to be critically re-assessed and re-defined. Although StW 498 is attributed to *A. africanus* in many publications (e.g., Lockwood & Tobias 2002; Guatelli-Steinberg 2003; Schwartz & Tattersall 2005; Moggi-Cecchi *et al*. 2006), it has been suggested by Clarke (2013) that it should be attributed to *A. prometheus*. Reconstruction of the lower face and dentition would enable more accurate comparisons to be made with other representatives of *A. prometheus* (e.g., StW 252, Sts 71, and Sts 36) that retain the same anatomies, and to compare these anatomies to representatives of *A. africanus* (e.g., Sts 52), and of *P. robustus* (e.g., TM 1517 and SK 843).

Since 1936, *Australopithecus* at Sterkfontein has been a topic of very high international interest. Now, with high resolution CT scanning and the possibility of virtual reconstruction, we are able to correct for plastic deformation and restore broken specimens that may be too fragile for undergoing a physical reconstruction. Reconstructing StW 498 offers the opportunity to reinforce taxonomic interpretations and to improve our understanding of australopithecine cranio-dental evolution. Specifically, this research may help document and help better define the range of morphological variability that exists in the dental and lower face features of *A. prometheus* and to compare these features with the range of variability that exists in *A. africanus* and *P. robustus*.

1.4. Structure of the dissertation

Chapter 2 presents a detailed background to the study of cranio-dental analysis and fossil reconstruction. Here, the Sterkfontein Cave system, hominid taxonomy, and distinguishable cranio-dental traits of *A. africanus*, *A. prometheus*, and *P. robustus* are discussed. Virtual methods and approaches to reconstructing and analysing hominid cranio-dental morphologies are also discussed.

Chapter 3 discusses the materials and methods that were utilised throughout this research. This section presents (and briefly describes) the comparative specimens included in this study, and also provides a comprehensive list of the morphological traits that were compared on specimens. Moreover, this chapter describes, in detail, the digitisation and reconstruction protocol of StW 498 and the software programs utilised in this study.

Chapter 4 presents the complete reconstruction and detailed anatomical descriptions of the StW 498 maxilla, mandible, and the associated dentition. This chapter presents the quantitative results and qualitative observations of this study. Lastly, Chapter 5 is a discussion of the results presented in Chapter 4. Additionally, this chapter provides a summary and conclusions of the research presented in the preceding chapters.

Chapter 2

Literature Review and Background

The aim of this chapter is to provide a comprehensive background on research that is pertinent to this dissertation. Given the extensive amount of literature available on the cranio-dental analysis of hominids and fossil reconstruction, and the abundance of fossil discoveries in South Africa, it is beyond the scope of this thesis to give a complete and thorough review. For the purpose of this dissertation, the author accepts the definition of *Australopithecus prometheus* as put forth by Clarke (1988, *et seq.*).

This chapter is divided into four sections. The first provides an outline of the Sterkfontein Cave system, focussing on Member 4. The second section examines the complicated history of hominid taxonomy at South African fossil sites and discusses the second species hypothesis. The third section focuses on traits that distinguish *Australopithecus africanus*, *Australopithecus prometheus*, and *Paranthropus robustus*. The last section discusses virtual, three-dimensional reconstruction approaches that are used to understand hominid cranio-dental morphologies.

2.1. Sterkfontein and the importance of Member 4

The Sterkfontein Caves site, located roughly 50km north-west of Johannesburg, is among the world's most important paleoanthropological sites. Although stratigraphically complex in nature (Figure 2.1), the cave system has yielded an abundance of Plio-Pleistocene faunal specimens, archaeological material, and hominid fossils dating from over 3.6 to 1.5 million years ago (Granger *et al*. 2015). The youngest hominid material originates from the Member 5 Early Acheulean deposits and is dated to 1.4 Ma (Kuman & Clarke 2000). However, Herries and Shaw (2011) argue that some material may be as young as 800,000 years. In 1936, Robert Broom discovered the first adult *Australopithecus* cranium (TM 1511) from breccia blasted out by lime miners. Broom (1936) attributed this fossil to a new species,

Australopithecus transvaalensis (now considered *A. africanus*). Two years after the discovery of TM 1511, Broom (1938b) recovered a child mandibular symphysis (TM 1516) containing large canines (Sts 50). Broom (1938b) considered this symphysis so different from the Taung skull that he created a new genus, *Plesianthropus*, to accommodate the Sterkfontein fossils. The discovery of Mrs. Ples (Sts 5) by Broom (1947) and the partial skeleton of Sts 14 by Broom and Robinson (1947) further secured the site's paleoanthropological importance. Since then hundreds of *Australopithecus* fragments have been uncovered from excavations of surface-exposed deposits. Although these have generally been considered to belong to one species, *A. africanus*, Clarke (1988) suggested that two different morphologies were represented in dentition and cranial structure, and eventually recognised the second species as being attributed to Dart's (1948) previously named *A. prometheus,* which Dart created for fossils from Makapansgat (Clarke 1988; 1994; 1998; 1999; 2002; 2008). Other hominid species documented at Sterkfontein include *P. robustus* (Kuman & Clarke 2000), *Homo ergaster (*Kuman & Clarke 2000), and *Homo habilis* (Reddy 2015), all of which are found in Member 5 (Clarke 1994; Kuman & Clarke 2000; Reddy 2015).

The Sterkfontein deposits (named the Sterkfontein Formation) are divided into six stratigraphic members (Members 1 to 6) in chronological order of deposition (Partridge 1978; Partridge & Watt 1991); a schematic view of the Members can be seen in Figure 2.2. Member 4 (M4) has yielded the majority of the *Australopithecus* fossils, including TM 1511, Mrs. Ples (Sts 5) (Broom 1936; Broom & Robinson 1952; Clarke 2013) and two partial *Australopithecus* skeletons, Sts 14 (Broom, Robinson & Schepers. 1950) and StW 431 (Toussaint *et al*. 2003). In addition to the hominid fossil discoveries, M4 is the only deposit to have yielded fossil wood, which provides a useful indication of the peri-depositional environmental conditions for some of the deposit (Bamford 1999). The discovery of StW 573 in the Member 2 deposit in the Silberberg Grotto (Figure 2.1) attributed to *A. prometheus* and colloquially known as 'Little Foot' (Clarke 1998), is of great importance for

paleoanthropological research. Not only does the virtually complete skeleton of StW 573 represent the oldest, dating to 3.67 Ma (Granger *et al*. 2015), and most complete hominid skeleton in southern Africa, it provides us with a template to which current and future cranial and post-cranial fossils can be compared.

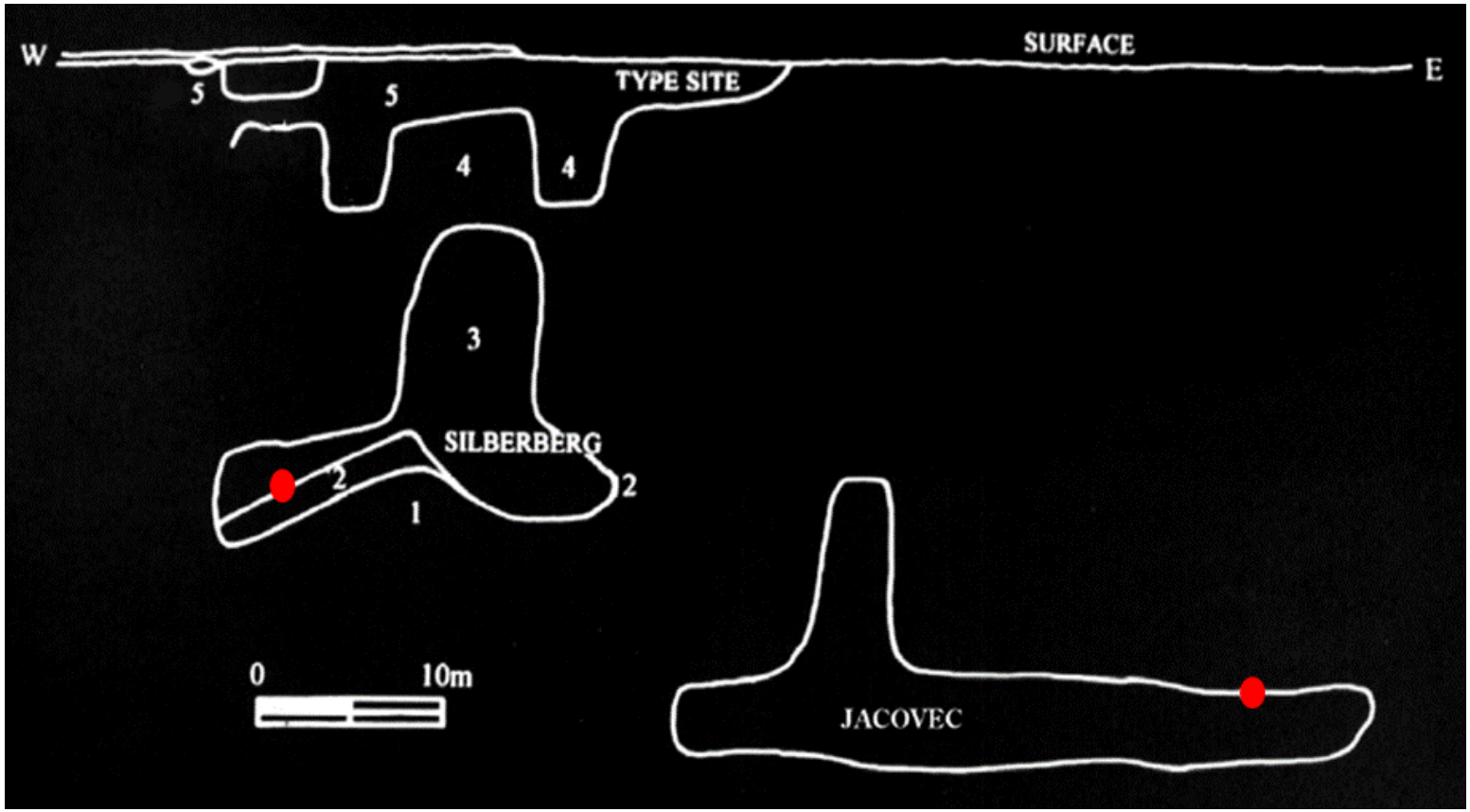

Figure 2.1. The vertical relationship of Sterkfontein Members 1 to 5. Red dots in the Silberberg and Jacovec caverns indicate positions of *Australopithecus* fossils (adapted from Clarke 2006, Figure 6, p. 115).

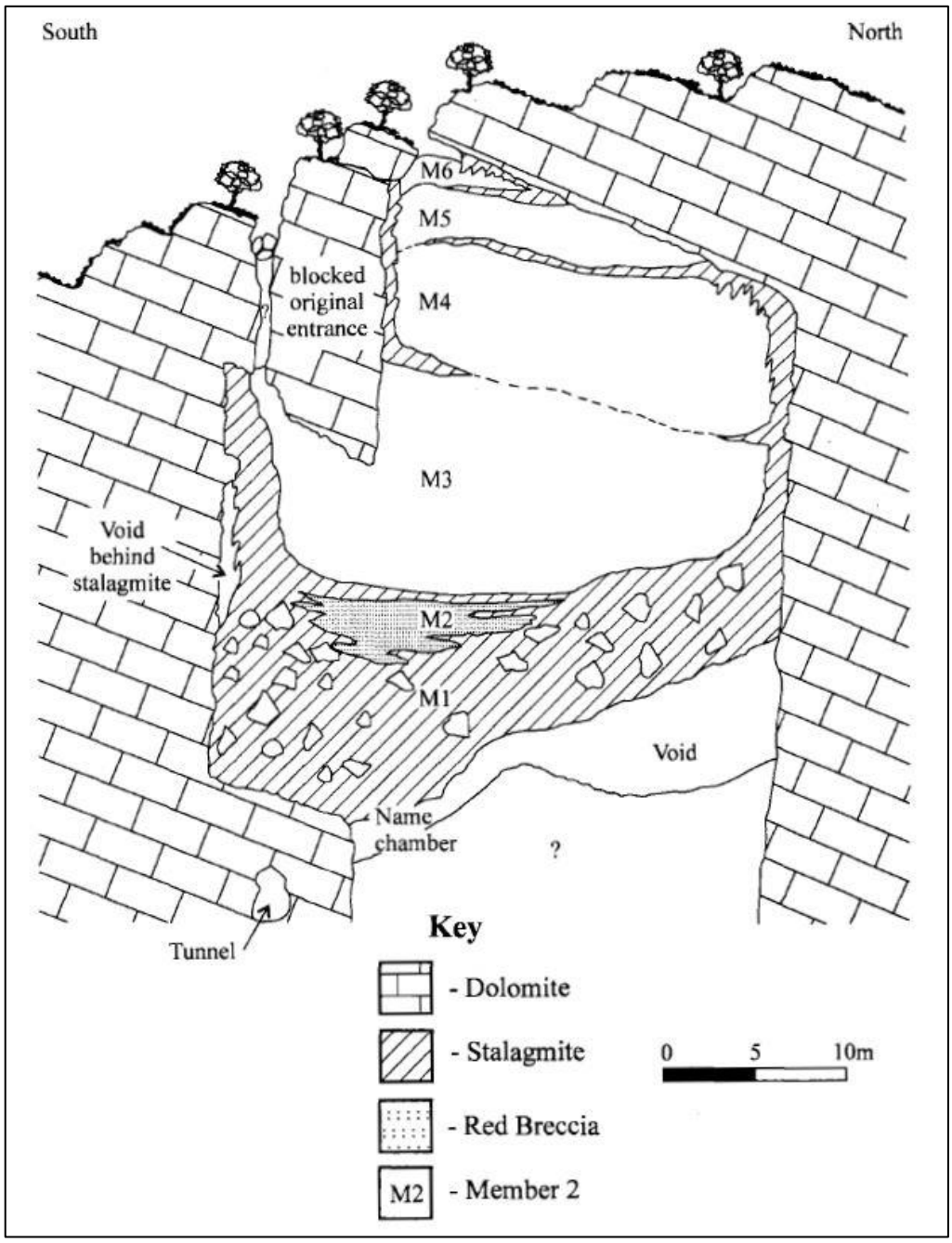

Figure 2.2. Schematic view of the north-south section of Sterkfontein to show the general relationship of Members 1 through Members 6 (from Clarke 2006, Figure 13, p. 119).

2.2. Hominid taxonomy: a complicated history

Discovered by Raymond Dart in 1924, the type specimen of *A. africanus* is represented by an adolescent partial cranium, mandible, and natural endocast from the site of Buxton Limeworks near Taung, South Africa (Dart 1925). Eleven years later, Robert Broom (1936) discovered the first adult cranium of what is now considered to be *A. africanus* (TM 1511) at the Sterkfontein Caves. Based on his initial observations, Broom attributed the TM 1511 cranium to a new species, *A. transvaalensis*. Just two years later, Broom (1938a, b) re-assigned the specimen to an entirely new genus, *Plesianthropus*.

In 1938, Broom discovered a partial cranium, a robust right mandibular corpus, and some isolated teeth at the site of Kromdraai, South Africa (Broom 1938a). In addition to its large cheek teeth, it was clear to Broom that the facial structure was markedly different from that of *A. africanus*. Broom named the fossils (TM 1517) as a new genus and species, *Paranthropus robustus* (Broom 1938a; Broom & Schepers 1946). Work on the fossil sites ceased during the Second World War, but resumed in 1947. With the assistance of J.T. Robinson, Broom recovered several significant cranial specimens, including Sts 5, Sts 17, Sts 19, Sts 52, and Sts 71. Robinson (1954) later classified all the Sterkfontein and Makapansgat australopithecines into one species, *A. africanus*. Robinson (1972) later re-assessed his taxonomic attributions and re-classified the material as *Homo africanus*.

In 1947, Dart procured funds to systematically excavate and survey the Makapansgat Caves. Excavations began the same year and were overseen by A.R. Hughes, G. Gardiner, and J.W. Kitching, who discovered an occiput (MLD 1) belonging to an adult *Australopithecus* (Dart 1948a, c). Upon examination, Dart (1948a, c) noticed the inferior position of the inion and further observed that the cranial vault showed a significant increase in thickness compared to those of living anthropoids and known primitive hominids. However, the differences between MLD 1 and the Taung cranium were not the only reasons behind the naming of a second *Australopithecus*

species. Dart (1948a) argued that "even if there were none of these differences, the locality and novel evidence it affords would justify reference of the specimen to a new species: *Australopithecus prometheus*" (Dart 1948a: 278-279). Although Dart (1948a) was correct to attribute MLD 1 to a second *Australopithecus* species, his reasoning was not. A new species cannot be created on the basis of locality, but should rather be based on the morphology of the specimen. In a recent paper, Berger and Hawks (2019) agree that Dart's (1948a) attribution of MLD 1 to a new species was not based on valid criteria. However, Berger and Hawks (2019) question the validity of the species *A. prometheus*, and have gone as far as to suggest that the species be considered as a *nomen dubium*.

In July 1948, while sorting through the excavation dumps at Makapansgat, Hughes discovered a mandible of an adolescent *Australopithecus* (MLD 2). Based on the broad and square-like molars retained in the mandible, and the considerable massiveness of the jaw and teeth, Dart (1948b) attributed the Makapansgat mandible to *A. prometheus*. In 1988, Clarke observed that this second *Australopithecus* species was also present at Sterkfontein Caves.

Dart (1948c) expressed his doubts regarding Broom's generic level separation of *Plesianthropus* and *Australopithecus* at Sterkfontein. Instead, Dart (1948c) believed that the Sterkfontein and Makapansgat assemblages represent distinct species of the same genus. Broom (1950) continued to propose that these species could be separated at the sub-familial level. In 1949, Broom and Robinson discovered an adult mandible (SK 15) at Swartkrans, South Africa. In order to accommodate the species, which they argued was more "man-like" than the *Pleisianthropus* specimens, Broom and Robinson (1949) created a new genus and species, *Telanthropus capensis*. Two other specimens, a mandibular fragment (SK 45) and a maxillary fragment (SK 80), were later added to this species (Robinson 1953).

Following the death of Broom in 1951, Robinson (1954) re-assessed the taxonomic status of all the South African australopithecine fossils. Robinson (1954) lumped *P.*

transvaalensis and *A. prometheus* (as well as the Tanzanian Garusi maxilla) with the species of the Taung child, *A. africanus*. Robinson (1954) further divided the *Australopithecus* specimens into two sub-species: the Taung cranium was classified as *A. africanus africanus*, whereas specimens from Sterkfontein and Makapansgat were classified as *A. africanus transvaalensis*. Robinson's classification of *Australopithecus* at these three sites gained increased support following his detailed analysis of the dentition (Robinson 1956). Robinson (1954) re-affirmed his reasons for separating the Kromdraai and Swartkrans fossils at a generic level and attributed the Swartkrans and Kromdraai specimens to *Paranthropus*, again with two sub-species included: Swartkrans specimens were assigned to *P. robustus crassidens*, and Kromdraai specimens were assigned to *P. robustus robustus*.

The idea that there was only a single *Australopithecus* species present at Sterkfontein became the general consensus. From the time Dart (1925) discovered the Taung child, lumping specimens according to locality and not morphology has been an error that has been made throughout palaeoanthropology. This can also be extended to East Africa, where Louise Leakey lumped all the specimens into *H. habilis* simply because they came from Olduvai Gorge, Tanzania (Leakey, Tobias & Napier 1964). The lumping of specimens set the stage for the consensus that there was a single species present at Sterkfontein.

2.2.1. The second species hypothesis

Clarke (1985a, b; 1988) questioned the concept of a single species and proposed that the Sterkfontein M4 assemblage represents two morphologically distinct hominids: the first characterised by relatively small dentition and a convex mid-face skeleton, and the second characterised by large dentition and a concave mid-face skeleton.

Four hypotheses have been put forward in order to explain the observed range of variation within the M4 assemblage. For the purpose of this chapter, individual

variation and the change-through-time hypotheses are discussed first, followed by theories of sexual dimorphism, and lastly, attribution to different species.

Following Robinson (1954), *Australopithecus* fossils from the sites of Makapansgat and Sterkfontein are considered by most researchers to belong to one species, *A. africanus*. If all *Australopithecus* fossils from these sites represent *A. africanus*, the implication is that there is a wide range of variation within this species. Consequently, three scenarios have been put forward in an attempt to explain the phylogenetic status of *A. africanus*. Some researchers (e.g., Robinson 1967; Olson 1985) believe that individuals with relatively smaller dentitions were ancestors of *Homo* and should thus be classified as *Homo*, while others (e.g., Johanson & White 1979; White, Johanson & Kimbel 1981; Rak 1983) consider individuals with relatively larger dentitions to be ancestors of *Paranthropus*. Other researchers (e.g., Tobias 1980; Skelton *et al*. 1986) argue that this variability is the result of the species being ancestral to both *Homo* and *Paranthropus*.

With M4 potentially sampling up to 600,000 years of accumulation (Pickering *et al*. 2010) and fossils being recovered from the entire depth of the Member, it has been proposed that intraspecific variation through time is responsible for the morphological variation observed in the M4 assemblage (e.g., Kimbel & White 1988; Moggi-Cecchi, Tobias & Beynon 1998). Although the M4 sample is undoubtedly time-averaged, the *A. prometheus* specimens are found close to *A. africanus* throughout the deposit, suggesting that they were coeval. One could argue that the stratigraphy of a talus cone is complex and that theoretically older and younger fossils could be found at a single horizontal level. However, in the case of Member 4, this argument is not supported by the stratigraphic reality, which shows the distribution of both *Australopithecus* forms horizontally and vertically. Moreover, the anatomies of *A. prometheus* and *A. africanus* specimens found within the M4 talus cone argue against one being ancestral to the other (Clarke 1988).

Among the aforementioned phylogenetic interpretations, it has been proposed that variation within the *Australopithecus* samples can be attributed to sexual dimorphism in a single species. Broom (1950), for example, rather than recognizing taxonomic distinctions, believed that sexual dimorphism accounted for some, if not most, of the observed variation in the Sterkfontein and Makapansgat assemblages (Broom & Robinson 1950; Grine 2013). The issue of sexing cranio-dental remains from these assemblages is instrumental to the second species hypothesis, as it directly relates to the use of sexual dimorphism to explain variation. Most researchers (e.g., Rak 1983; 1985; Loth, Henneberg & Thackeray 1995; Thackeray 1997) have followed Broom and Robinson's (1950) criteria of using absolute size of the specimen, especially that of the canines, to determine sex. Researchers have employed various quantitative and qualitative techniques to address questions surrounding sexual dimorphism, hominid taxonomy, cranio-dental variation, and species diversity (e.g., see Wolpoff 1974; Kimbel & White 1988; Kimbel & Rak 1993; Ahern 1998; Lockwood & Tobias 2002; Moggi-Cecchi, Grine, & Tobias 2006; Thackeray 2007; Harmon 2009; Fornai *et* al. 2010; Williams, Schroeder, & Ackerman 2012; Grine *et al*. 2013; Fornai, Bookstein & Weber 2015). Additionally, researchers have also relied on other criteria, such as stages of dental development, to assign sex, and numerous disputes have occurred as a result. For example, the Sts 52 maxilla and mandible exhibits classic *A. africanus* traits, and is considered by most (e.g., Wallace 1972; Wolpoff 1975; Clarke 2008; Grine *et al*. 2012) to be male. However, Rak (1985) argues that specimens (such as Sts 52) exhibiting fewer derived features should be regarded as female. Rak's (1985) argument is not plausible. If we were to accept that females have fewer derived features, it would mean that female *Homo sapiens* retain primitive features, while males have derived features.

Determining sex of a specimen has taxonomic implications. This is best exemplified by the well-preserved facial skeleton, Mrs. Ples (Sts 5), which is most relevant to this dissertation. On the basis of the anterior pillars, Rak (1983; 1985) proposed that Sts 5 was male. The proposition of Sts 5 being male was taken up by Thackeray and

colleagues (see Loth, Henneberg & Thackeray 1995; Thackeray 1997; 2000; Thackeray *et al*. 2002; Potze & Thackeray 2010) who went further and suggested that Sts 5 was a juvenile male. Thackeray (1997; 2000) and colleagues (Thackeray *et al*. 2002) suggested that Sts 5 was an adolescent male on the basis of the zygomatic morphology and the presence of a sagittal crest. Grine *et al*. (2012) refuted these claims and provided favourable evidence that supported Broom and Robinson's (1950) initial assessment of the specimen being an adult female. This identification has taxonomic implications. Kimbel and White (1988: 186) contested that if Sts 5 is a female, "it is unlikely that the total variation in the facial morphology in the Sterkfontein Type Site collection is attributed to sexual dimorphism".

The question of whether sexual dimorphism can account for the observed morphological variation within *Australopithecus* assemblages, especially those at Sterkfontein, has been discussed, or at the least suggested, by numerous researchers (see Grine 2013 for review). However, Kimbel and White (1988), for example, suggest that *A. africanus* samples from the Sterkfontein M4 assemblage exhibit a wide range of variation that cannot be attributed to sexual dimorphism alone. They noted that in sexually dimorphic hominids, "robust" features and greater facial prognathism are to be expected, but the extremely prognathic face of Sts 5 (considered to be a female) cannot be explained only by sexual dimorphism; since Kimbel and White (1988) regarded the orthognathic cranium of Sts 71 as male (based on the size of the post-canine dentition and the facial robusticity), they concluded that variability within the M4 assemblage cannot be explained by sexual dimorphism or individual variation.

Based on their observations, Kimbel and White (1988: 189) proposed two alternative hypotheses. First, the samples taken from the M4 assemblage represent "temporally mixed populations of an evolving lineage". Or second, that there is more than one hominid species present in the Sterkfontein M4 hominid assemblage. This second hypothesis corroborates Clarke's (1985a, b) proposal of a second australopith species at Sterkfontein.

Over the last twenty years, different interpretations of the evidence have resulted in ongoing debates surrounding the existence of a second *Australopithecus* species. While some (e.g., Fornai *et al*. 2010) support this hypothesis, others merely allude to its possibility (e.g. Calcagno *et al*. 1997; Kimbel & Rak 1993; Lockwood & Moggi-Cecchi 1998; Lockwood & Tobias 2002; Schwartz & Tattersall 2005; Moggi-Cecchi, Grine & Tobias 2006). This debate is further exemplified by the numerous studies that have been conducted on the variation of dental morphology within the australopithecine assemblages (e.g., Wood *et al*. 1983; Hills *et al*. 1983; Suwa *et al*. 1994; Grine *et al*. 2003; Strait & Grine 2004; Grine *et al*. 2013).

According to Clarke (1988, *et seq.*), specimens such as Sts 71, StW 252, and StW 505 are distinguishable from known *A. africanus* specimens such as Sts 5, Sts 17, Sts 52, and MLD 6. The diagnostic differences exhibited by these two groups of crania assigned to *A. africanus* and *A. prometheus* are detailed in the next section. Clarke (1994) made favourable comparisons between the *A. prometheus* holotype, MLD 1, and the occipitals of Sts 71 and StW 252, which was the main justification for placing them together, followed by dental comparisons with MLD 2. A list of specimens attributed to *A. prometheus* according to Clarke (1988, *et seq.*) is provided in Table 2.1.

Fornai (2009; Fornai *et al*. 2010) conducted a geometric morphometric study on maxillary molars of Sterkfontein australopithecines, the results of which offer further support to the second species hypothesis. However, Fornai *et al*. (2015: 190) later argued that although Sts 52 closely resembles the "supposed *A. prometheus*", a larger australopith dental sample is needed in order to determine whether molar teeth offer insight into taxonomic differentiation, specifically that of *A. prometheus* and *A. africanus*.

Increasing evidence provided by Clarke (1988, *et seq*.) supports the existence of a second species among the fossil assemblages from Makapansgat and Sterkfontein. In 1948, because there was such a limited sample, Dart's claim of a second

Australopithecus species could be justifiably dismissed by arguing in favour of morphological variation or sexual dimorphism. However, with the larger collection that exists today, it becomes increasingly evident that Dart's hypothesis (1948a, c) was correct. Whether through predation or through scavenging, hominids were most likely competing with several species of carnivore. The abundance of faunal evidence demonstrates the co-existence of multiple carnivore and monkey species at sites like Sterkfontein and Makapansgat. For example, multiple species of carnivores (*Panthera leo* and *Panthera pardus*) co-occurred at Sterkfontein at the same time as *A. africanus* (O'Regan & Reynolds 2009). At Makapansgat, there were two co-existing species of monkey, *Parapapio broomi* (Broom 1940) and *Parapapio jonesi* (Jones 1937; Freedman, 1976; El-Zaatari *et al*. 2005). We readily accept the co-existence of multiple carnivore and monkey species at these sites. However, many reject the possibility of co-occurring australopithecine species. The diverse fauna and co-occurrence of multiple species should be enough for us to seriously consider the possibility of two contemporary species of *Australopithecus*.

Table 2.1. Specimens attributed to *A. prometheus* by Clarke (1988, *et seq*.), unless referenced otherwise. "MLD" represents specimens found at Makapansgat, "Sts" and "StW" specimens originate from Sterkfontein, and "TM" specimens are found at Kromdraai.

Specimen	**Part**	**Reference**
MLD 1	Occiput	Dart 1948a-c
MLD 2	Mandible	Dart 1948a-c
MLD 9	Maxillary portion	Clarke 1994, *et seq.*
Sts 1	Maxilla	Clarke 1994, *et seq.*
Sts 7	Post-cranial fragments and a partial mandible	Clarke 1994, *et seq.*
Sts 8	Left M^1 and M^2	Clarke 2008, *et seq.*
Sts 28	Right M^2	Fornai 2009
Sts 36	Mandible	Clarke 1998, *et seq.*
Sts 71	Cranium	Clarke 1988, *et seq.*
StW 14	Crushed partial mandible	Fornai 2009
StW 183	Maxillary portion	Clarke 2008, *et seq.*, Fornai 2009
StW 188	Right M^2	Clarke 2008, *et seq.*, Fornai 2009
StW 189	Left M^3	Clarke 2008, *et seq.*, Fornai 2009
StW 252	Cranium	Clarke 1988, *et seq.*
StW 280	Isolated maxillary and mandibular teeth	Clarke 2008, *et seq.*, Fornai 2009
StW 384	Partial right mandibular corpus	Clarke & Kuman (2018)
StW 450	Right M^1	Fornai 2009
StW 505	Cranium	Clarke 1994, *et seq.*
StW 573	Complete skeleton	Clarke 1994, *et seq.*
StW 578	Partial cranium	Partridge *et al*. 2003
StW 648	Partial cranium	Clarke & Kuman (2018)
StW 667	Isolated L^C	Clarke & Kuman (2018)
TM 1516	Mandibular symphysis with canines	Clarke & Kuman (2018)

2.3. *Australopithecus africanus, Paranthropus robustus,* and *Australopithecus prometheus*: cranio-dental traits

For the purpose of this chapter, cranio-dental traits of *A. africanus* are discussed first, followed by *P. robustus*, and finally *A. prometheus*. A summary of the cranio-dental traits that distinguish these species is provided in Table 2.2. Note that when referring to specific cranio-dental features, the term "relatively" is used to qualitatively refer to the observed size of features within the *A. africanus*, *A. prometheus,* and *P. robustus* samples used in this study unless stated otherwise.

A. africanus had relatively large canines and large post-canine teeth (Robinson 1956). According to Clarke (1988; 2008), within the fossil assemblages from Makapansgat and Sterkfontein, morphological features distinguish males and females: males exhibit large canines (as seen in TM 1511 and StW 53) and females exhibit smaller canines (as seen in Sts 5 and TM 1512). However, Kimbel and White (1988) noted that sexual dimorphism in the mandibular canines of *A. africanus* is less marked. The palate of *A. africanus* is short, relatively deep, and square, while the maxilla is narrow and rounded anteriorly. The nasal aperture is relatively small (as seen in Sts 5 and StW 53). The nasoalveolar clivus is also relatively small. The glabella is prominent, with a narrow interorbital region (as seen in the Taung Child and Sts 5) (Dart 1925; Rak 1983). Overall, the facial structure of *A. africanus* is gracile, especially when compared to *P. robustus*.

In contrast to *A. africanus*, the glabella of *P. robustus* is positioned at a lower level than the supraorbital margin (as seen in the Swartkrans specimen SK 48) (Broom & Robinson 1952; Clarke 1996). This taxon is characterised by flattened nasals and hyper-developed zygomatic processes, creating a dished-shaped appearance of the mid-face region (Broom & Schepers 1946; Clarke 1996). The nasoalveolar clivus is thick and slopes into the floor of the nasal cavity (McCollum *et al*. 1993). The palate of *P. robustus* is shallow anteriorly and deep posteriorly (Broom 1938a; Grine 1989; Clarke 1994; Grine & Strait 1994). The mandibular corpus is extremely robust and

thick, and the premolars and molars are large with bulbous cusps. The anterior teeth and canines of this taxon are small in comparison to its post-canine teeth (Broom 1938a; Broom & Schepers 1946; Clarke 1996) The unique cranial architecture, specialised dentition, and robust mandible of *P. robustus* are reflective of dietary specialisations that reflect niche separation of this species and *Australopithecus* (Broom 1938a; Robinson 1963; Tobias 1967; Grine 1987; Grine *et al*. 2010; Grine *et al*. 2012). Peterson *et al*. (2018) studied micro-wear dispersion patterns on the lower molars of *A. africanus* and *P. robustus* and found that the molars of *A. africanus* exhibited smaller features and smoother micro-wear surfaces, which indicate that *A. africanus* had a softer, tougher diet. In contrast, the molars of *P. robustus* exhibited more surface complexity and larger features, implying that the diet of this species consisted primarily of hard, brittle foods (Peterson *et al*. 2018). The results of the study were consistent with those of Scott *et al*. (2005). However, some (e.g., Chamberlain & Wood 1985; Turner & Wood 1993; Sponheimer *et al*. 2006) argue that differences in mandibular corpus dimensions within *Paranthropus* may reflect patterns of sexual dimorphism rather than dietary adaptations.

The mandibular corpus of *P. robustus* is exceptionally deep (especially when compared to that of *A. africanus*) and transversely thick. In contrast, *A. prometheus*, has large post-canine teeth similar to those of *Paranthropus* and has a relatively thin and shallow mandibular corpus (as seen in MLD 2 and Sts 36) (Clarke 2013). Although these may be idiosyncratic features, it is more likely that this is a diagnostic morphological trait of the species. Differences in mandibular shape and size are primarily reflective of increased biomechanical stresses, such as parasagittal bending, transverse bending, and torsion, and not necessarily reflective of post-canine megadontia (Daegling & Grine 1991).

As demonstrated by the virtually complete skeleton of StW 573, the fragmentary cranium of StW 252, and the partial cranium of Sts 71, *A. prometheus* had large canines and incisors like *Australopithecus* and large premolars and molars with bulbous cusps similar to *Paranthropus* (Clarke 1988; 1994; 2007; Fornai 2009).

According to Clarke (2008), this combination of features can be attributed to species-level morphological differences rather than to sexually dimorphic differences within *A. africanus* samples from both Sterkfontein and Makapansgat. In addition, other features that differentiate *A. prometheus* from *A. africanus* include a wider interorbital region of the former (as seen in StW 252 and Sts 71), and cheek bones that are deeper and relatively more prominent anteriorly (as seen in StW 252 and the StW 505 cranium) (Clarke 1994). Moreover, the face of *A. prometheus* is much taller (in terms of facial height) in comparison to *A. africanus* (Clarke 2008). The primary cranio-dental diagnostic features, as defined by Clarke (1988, *et seq.*), that differentiate *A. africanus* and *A. prometheus* are detailed in Table 2.3.

Table 2.2. Summary of the cranio-dental traits that distinguish *A. africanus*, *P. robustus*, and *A. prometheus*. References appear in the text.

	Australopithecus africanus	***Paranthropus robustus***	***Australopithecus prometheus***
Incisors	Relatively large	Relatively small	Large, especially the maxillary central incisors
Canines	Relatively large	Relatively small	Extremely large
Posterior teeth	Large with pointed cusps	Large with flat bulbous cusps	Large with bulbous cusps
Palate	Short, square and relatively deep anteriorly	Shallow anteriorly and deep posteriorly; broad and extremely thick	Long, rectangular, shallow anteriorly, and deep posteriorly
Anterior maxilla	Narrow and rounded with minimal sloping into the nasal gutter	Moderately sloped into the nasal gutter	Steeply sloped into the nasal gutter
Mandible	Small and deep, but extremely thick corpus	Large, robust, and thick corpus	Large and relatively shallow (except in Sts 7 and Sts 36) and an extremely thin inferodistal corpus
Zygomatic bones	Gracile arch	Hyper-developed	Robust and anteriorly prominent
Interorbital region	Narrow, prominent glabella	Wide	Wide, weak glabellar prominence

Table 2.3. Clarke's (1988, *et seq.)* cranio-dental diagnostic features that differentiate *A. africanus* and *A. prometheus*.

	Australopithecus africanus	***Australopithecus prometheus***
Anterior teeth	Vertical incisors and canines	Procumbent incisors and canines
Anterior teeth roots	Small, straight and thin	Large, curve distally and thick
Posterior teeth	Small	Large
Molar cusp shape	Higher and pointed	Lower and bulbous
Molar cusp position	Tips point vertically	Tips point towards the centre of the crown
Tooth wear	Generalised	Excessive wear on anterior teeth
Clivus	No corrugations over clivus	Prominent corrugations over clivus
Incisor-canine diastema	No	Yes
Supraorbital margin	Thick	Thin
Glabellar prominence	Strong	Weak
Mid-face skeleton	Convex	Flat, concave
Position of nasion	Below fronto-maxillary suture	Above fronto-maxillary suture
Position of malar root	Posterior	Anterior
Zygomatic arch	Gracile	Robust
Occipital profile	Low, convex	High, gently curved

2.4. Virtual, three-dimensional reconstruction and analysis

Two of the most challenging limitations paleoanthropologists must overcome are the incomplete state and relatively poor preservation of fossils. Fragmentary and distorted fossils are the norm. Although researchers are able to extract anatomical information from distorted specimens, such fossils are often omitted from innovative morphological and morphometric analyses (Benazzi *et al*. 2014). Consequently,

fossils sample sizes are reduced, and in turn, further limit our understanding and knowledge of hominid evolution and variation.

Micro-computed tomography (microCT) scanning offers several advantages to both the reconstruction and analysis of a fossil. Firstly, with microCT scans, we are able to more easily discern boundaries between bone and sediment-filled cavities. Secondly, microCT scans allow us to a) view the internal structure of a fossil on every image slice in a non-destructive manner, and b) digitally visualise a fossil using a reconstructed, three-dimension volume. Thirdly, because multiple directions are employed when measuring a fossil, microCT scans are not affected by parallel distortion (Schwartz *et al*. 2005). With regards to the quantitative analysis of specimens, microCT scans can, for example, provide us with angles, surface areas, and landmark co-ordinates in ways that physical specimens cannot. Moreover, microCT scans permit digital correction for plastic deformation and restoration of damaged specimens.

2.4.1. Defining and correcting deformation

If parts of a fossil are either missing or deformed, then every reconstruction, whether physical or virtual, will be based on prior assumptions. Assumptions about taxonomic affinity, taphonomy, biological and functional constraints, and symmetry, are inherent to the reconstruction process. Formalising these assumptions and developing a rigorous reconstruction protocol allows the process to be both transparent and reproducible.

MicroCT scanning and virtual reconstruction allows for both the correction of plastic deformation and for the restoration of fragile, broken specimens. This permits extraction of more abundant morphological information on a particular specimen, and thus a species. The best approach when it comes to restoring such distorted specimens is to re-establish bilateral symmetry (Gunz *et al*. 2009). This can be accomplished by

using mirror imaging if the fossil in question has undistorted, well-preserved parts from at least one side of the specimen (as is the case with the left side of StW 498). Using data sets acquired from microCT scanning, the better-preserved sides of a fossil can be replicated, mirrored, and aligned to overlapping anatomical structures, thus restoring bilateral symmetry and estimating missing areas. In a situation like this, biological constraints can be advantageous. For example, biomechanical function between bones and dental wear patterns on occluding upper and lower dentition of the left mandible and left maxilla can serve as a guide to identifying deformations, and thus as a criterion for correcting them.

An example of this technique was performed on the cranium and endocast of the Taung skull (Gunz *et al*. 2009). Although most of the Taung skull is complete, the left side is missing. Using microCT scans and reconstruction software, such as Amira (Thermo Fisher Scientific Group, https://www.thermofisher.com), Gunz *et al*. (2009) were able to manually segment the embedded frontal portion of the endocast. Manually segmenting anatomical structures from each slice of a microCT scan allows researchers to manipulate them in 3D morphospace. Once the segmentation process was complete, mirror imaging was used to complete the left side of the Taung cranium and endocast (Figure 2.3).

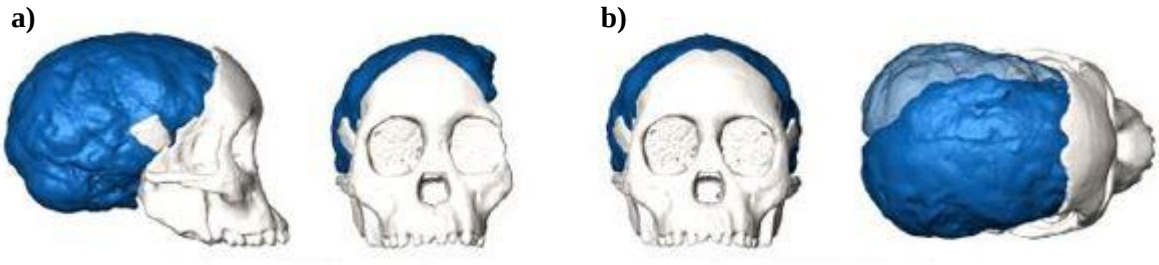

Figure 2.3. Virtual 3D rendering of the Taung skull: a) rendering of the original Taung skull, lateral and anterior views; b) rendering of the complete Taung skull using mirror imaging, anterior and cranial views. The white represents the preserved bone, the blue the preserved endocast, and the transparent blue represents the mirrored endocast (adapted from Gunz *et al*. 2009, Figure 7, p. 55).

Moreover, the continued advancement and flexibility of virtual techniques in multiple disciplines allows researchers to cater for the unique reconstruction requirements of each specimen. An exceptional example of such a reconstruction was done on the *H. habilis* OH 7 mandible (see Spoor *et al*. 2015). By using high quality microCT image scans, Spoor *et al*. (2015) were able to graphically visualise the morphology of the OH 7 mandible. Through virtual extraction techniques, researchers were able to reconstruct the partial mandible and correct plastic deformation. This, in turn, allowed researchers to mirror image the specimen in order to create a complete, accurate virtual rendering of the OH 7 mandible (Figure 2.4). Virtual reconstruction offers the opportunity for additional taxonomic interpretations and improving our understanding of hominid evolution.

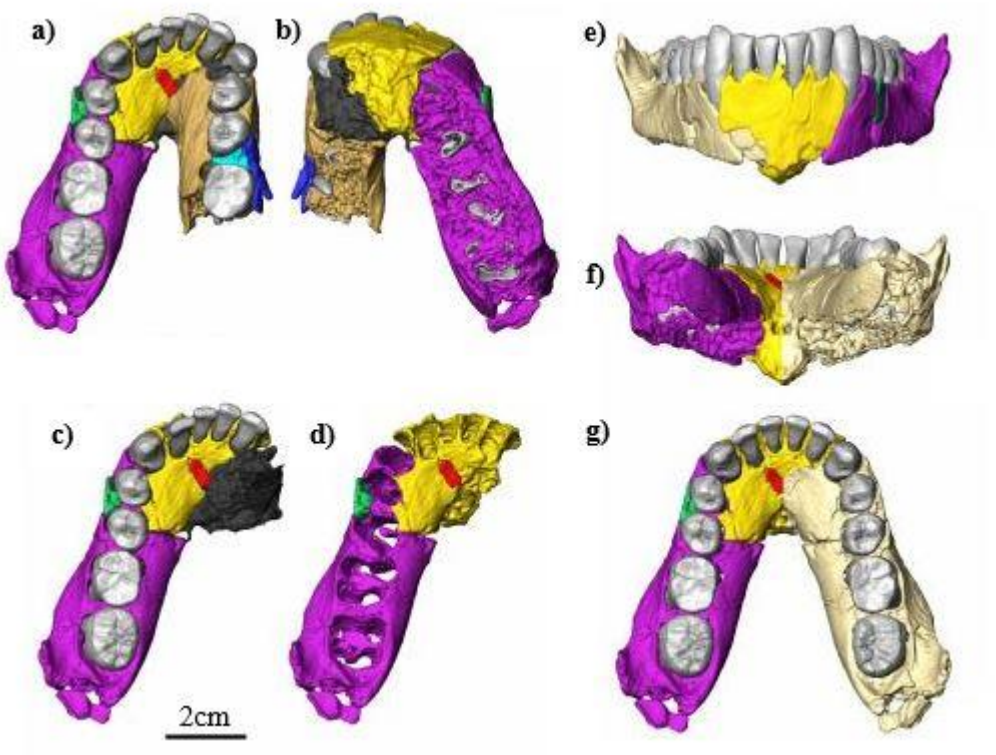

Figure 2.4. The reconstructed OH 7 mandible: a) As preserved in occlusal view; b) As preserved in inferior view; c) Occlusal view without the right corpus and showing matrix fill; d) Without the right corpus, dentition, and matrix; e) Reconstruction of OH 7 using mirror imaging in anterior view; f) Reconstruction of OH 7 in posterior view; g) Reconstruction of OH 7 in occlusal view; a-d) The black represents matrix and the grey represents the teeth, while the remaining colours represent the preserved parts of bone; e-g) the faded yellow represents the mirrored right half of the mandible (adapted from Spoor *et al*. 2015, extended data, Figure 1, p. 90).

Chapter 3

Materials and Methods

This study utilised microfocus X-ray Computed Tomography (microCT) in order to develop a virtual (*in silico*) reconstruction of StW 498. The acquired high resolution image data were imported into the visualisation software Avizo 9.0.1 (Thermo Fisher Scientific Group, https://www.thermofisher.com), enabling the use of segmentation tools in order to produce a reconstructed rendering of the specimen. The reconstructed rendering of StW 498 was used to describe its maxillary, mandibular, and dental morphology, and to make qualitative and quantitative comparisons with the maxillae and mandibles of other fossil hominids in order to test assess the taxonomic attribution of StW 498. These comparisons relied on qualitative morphological observations and quantitative linear measurements.

This chapter is divided into two sections. The first section discusses the preservation state of StW 498, and provides an overview of the comparative sample. Section 3.2. Methods consists of several sub-sections that detail information pertaining to the digitisation of the specimens that provide a list of the chosen quantitative linear measurements, that describe the virtual restoration and reconstruction process of StW 498, and that detail the steps involved in the digital partitioning of the dentition for the qualitative analysis of dental form.

3.1. Materials

StW 498 was compared with a total of 51 hominid specimens (see Table 3.1). Specimens were selected that have at least one of the relevant comparative features preserved in good condition (e.g., minimal occlusal wear). The hominid specimens are housed at the Evolutionary Studies Institute, University of the Witwatersrand, Johannesburg, South Africa, and the Ditsong National Museum of Natural History, Pretoria, South Africa. These specimens, with the exception of Sts 52, are undistorted and do not require any reconstruction. Palatal and mandibular dimensions of StW 573

('Little Foot') were incorporated from a recent preprint by Clarke and Kuman (2018). East African hominids such as KGA10-525 and AL 444-2 were not available for use in this study, although future comparisons would be informative.

Table 3.1. Comparative hominid fossils included in this study. These comparative fossils are here divided utilising the morphological features and classification of *A. prometheus* according to Clarke (1988, *et seq.*). Only palatal and/or mandibular measurements were taken for specimens indicated with a *.

Specimen	Taxon	Maxillary dentition	Mandibular dentition	Specimen	Taxon	Maxillary dentition	Mandibular dentition
Sts 7 *	*A. prometheus*			**StW 287**	*A. africanus*	C	
Sts 36	*A. prometheus*		C - M_3	**StW 412**	*A. africanus*		M_2
Sts 71	*A. prometheus*	P^3 - M^3		**StW 421**	*A. africanus*		M_1 - M_3
StW 14	*A. prometheus*		M_3	**StW 446**	*A. africanus*		C
StW 183	*A. prometheus*	I^1 - M^3		**StW 491**	*A. africanus*		C - M_3
StW 189	*A. prometheus*	M^3		**StW 524**	*A. africanus*	M^3	
StW 252	*A. prometheus*	I^1 - M^3		**StW 529**	*A. africanus*		M_2, M_3
StW 280	*A. prometheus*	P^3 - M^3	M_3	**StW 537**	*A. africanus*		I_2, C, P_4, M_1 - M_3
StW 384	*A. prometheus*		M_1 - M_3	**StW 560**	*A. africanus*		M_3
StW 573*	*A. prometheus*			**MLD 11/30**	*A. africanus*	C, P^3	
StW 450	*A. prometheus*	M^1		**MLD 18***	*A. africanus*		
StW 578	*A. prometheus*	M^1 - M^3		**MLD 34***	*A. africanus*		
Sts 5*	*A. africanus*			**MLD 40***	*A. africanus*		
Sts 52	*A. africanus*	I^1 - M^3	I_1 - M_3	**SK 12***	*P. robustus*		
Sts 53*	*A. africanus*			**SK 13/14**	*P. robustus*	P^3 - M^3	
StW 13*	*A. africanus*			**SK 23***	*P. robustus*		
StW 3	*A. africanus*		M_2	**SK 34**	*P. robustus*		
StW 73	*A. africanus*	P^3 - M^2		**SK 31**	*P. robustus*	M^3	
StW 109	*A. africanus*		M_3	**SK 41**	*P. robustus*	M^3	
StW 116	*A. africanus*		I_1 - C	**SK 46**	*P. robustus*	P^3 - M^3	
StW 123	*A. africanus*		M_1	**SK 47***	*P. robustus*		
StW 131	*A. africanus*		P_4, M_1	**SK 48**	*P. robustus*	C - M^3	
StW 133	*A. africanus*		M_3	**SK 843**	*P. robustus*		M_1, M_2
StW 179	*A. africanus*		M^3	**SK 847***	*P. robustus*		
StW 193	*A. africanus*		P_4	**TM 1517**	*P. robustus*	C - M^3	
StW 213	*A. africanus*		C - M_2				

3.1.1. StW 498

On the 30th of September, 1988, a team directed by Alun Hughes and Phillip Tobias excavated portions of an *Australopithecus* skull (StW 498) from square P/41 at Sterkfontein, Member 4. The fossil was found at a depth of 17.9 to 19.9 feet (ft) below datum. StW 498 consists of a variably crushed right maxilla and mandible, a more intact left maxilla and mandible with broken permanent dentition, fragments of the cranial vault along with various splanchnocranium and basicranium fragments, and a well-preserved, fairly large, right petrosal.

These fragments, when united, constitute a fairly well-preserved maxilla and mandible with near complete dentition (the only missing tooth is the right maxillary lateral incisor) and a partial cranial vault of a single young adult individual, which is corroborated by the dental specimens that display occlusion between the left upper and lower jaws and complementary degrees of wear. Furthermore, there is close spatial association of all the fossils in the site and a compatible state of preservation and colour for all the parts of this skull.

Several observations of Schwartz and Tattersall (2005) on StW 498 are evaluated below, along with details on its state of preservation. Brief descriptions for preserved elements are also provided. Formal, detailed anatomical descriptions of the reconstructed dentition and lower face of StW 498 are provided in Chapter 4. The various cranial vault fragments were not included in the present study, although reconstruction and analysis will be conducted for future publication.

StW 498a

The left maxilla (StW 498a) is mostly intact and exhibits minimal brittle deformation (fragmentation while maintaining original shape and anatomical association). It consists of a partial palate that extends to the M^1, which is in situ, but fragmented, and retains the I^1 to M^1, and an isolated M^2 and M^3 (Figure 3.1). There is extensive manganese and soil staining over most of the lateral surface, and some on the palate and enamel surfaces of the dentition. All the teeth have varying degrees of occlusal wear and the canine exhibits atypical eruption. The posterior portion of the palate situated alongside the M^1 has been displaced by crushing within the deposit. Both the intermaxillary suture and incisive canal are well-preserved, though not clearly visible in its current form.

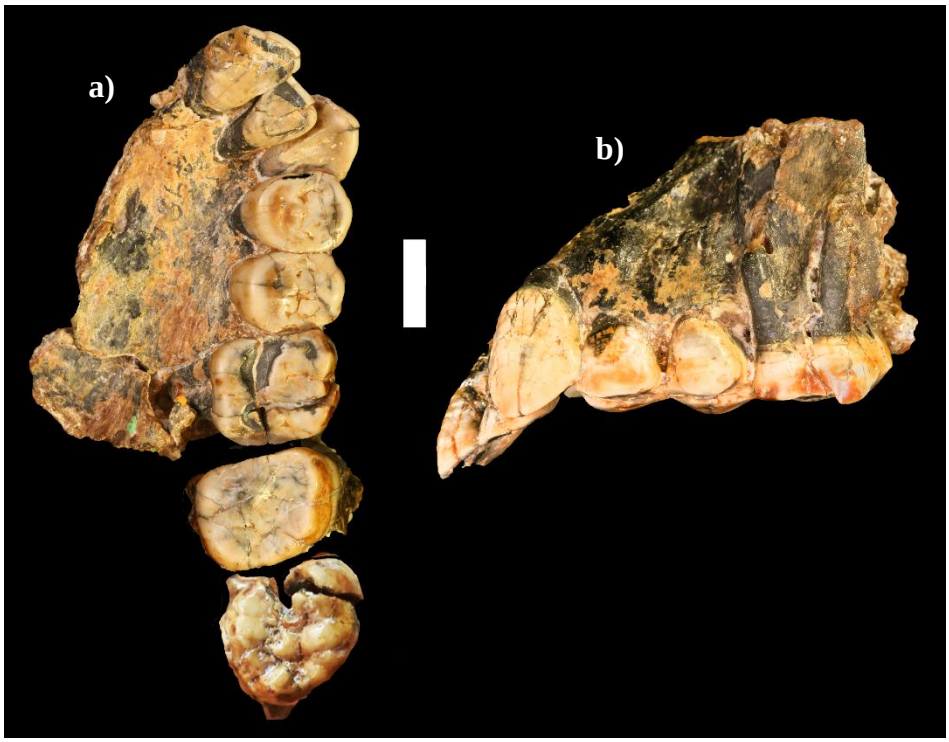

Figure 3.1. StW 498a left maxilla: a) Occlusal view with the isolated LM^2 and LM^3 included; b) Lateral view. Scale bar = 10 mm

StW 498b

The right maxilla (StW 498b) exhibits extensive fragmentation (caused by crushing within the deposit) which resulted in the displacement of the right maxillary dentition (Figure 3.2). All of the bone has been displaced, with some showing signs of plastic deformation. There is extensive manganese and soil staining over the surfaces of the fragmented and displaced bone. The teeth have some soil staining on the enamel surface while exposed dentine is stained by manganese. There is little cortical bone preserved, with most of it encased by matrix. All of the permanent dentition is present, although variably cracked, with the exception of the lateral incisor which was not recovered. The central incisor is isolated and broken, while the remaining dentition is lodged in the deformed bone. All the teeth exhibit varying degrees of occlusal wear.

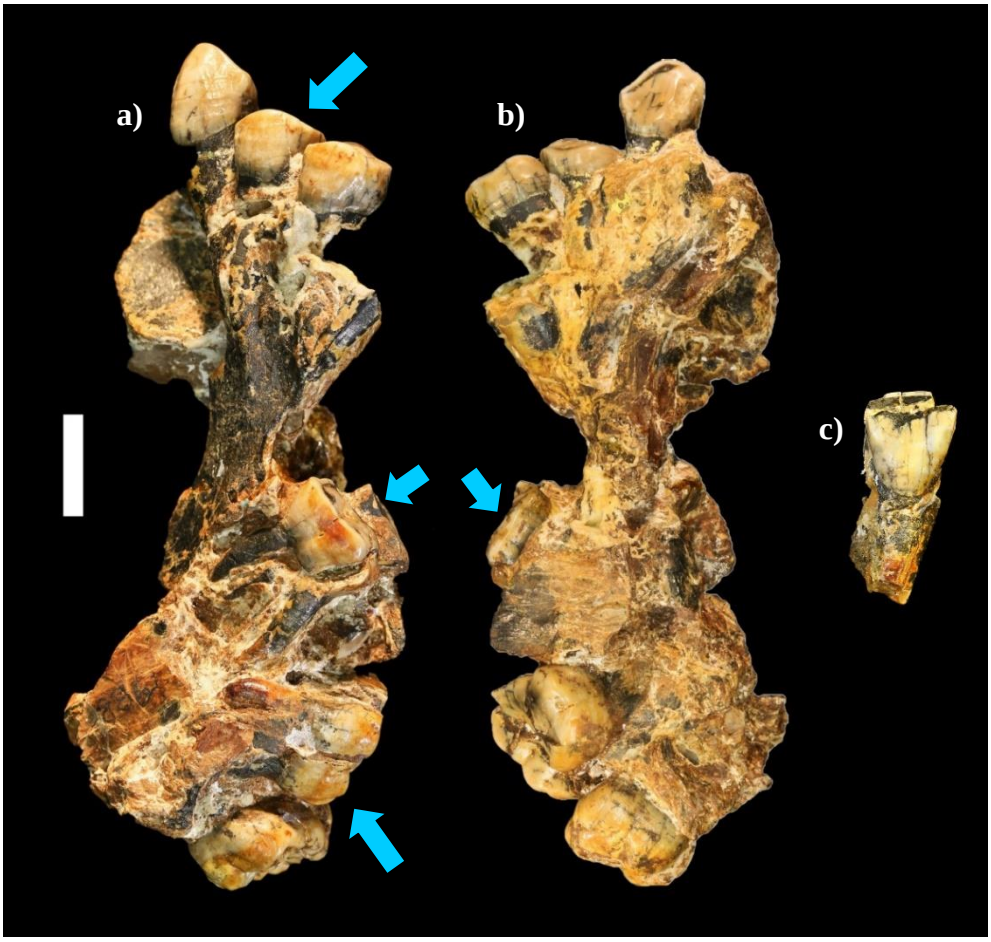

Figure 3.2. StW 498b right maxilla: a) Basal view; b) Occlusal view; c) Labial view of the RI[1]. The blue arrows indicate the position of the teeth. Scale bar = 10 mm.

StW 498c

The right mandible (StW 498c) exhibits severe fragmentation and displacement of the bone, including, but not limited to, the right ascending ramus (Figure 3.3). Schwartz and Tattersall (2005: 311) mislabel this specimen as StW 498d.The well-preserved mandibular symphysis exhibits an intact, undistorted genial fossa. The right mandibular dentition is preserved (I_1 to M_3), along with the left central incisor and canine which appear to have been crushed and pushed under the right canine. The presence of the symphysis enabled a horizontal mandibular length measurement upon reconstruction. All the teeth are variably cracked on the occlusal aspect, with the M_1 and M_2 being fragmented into several pieces and displaced. All the teeth have varying degrees of occlusal wear.

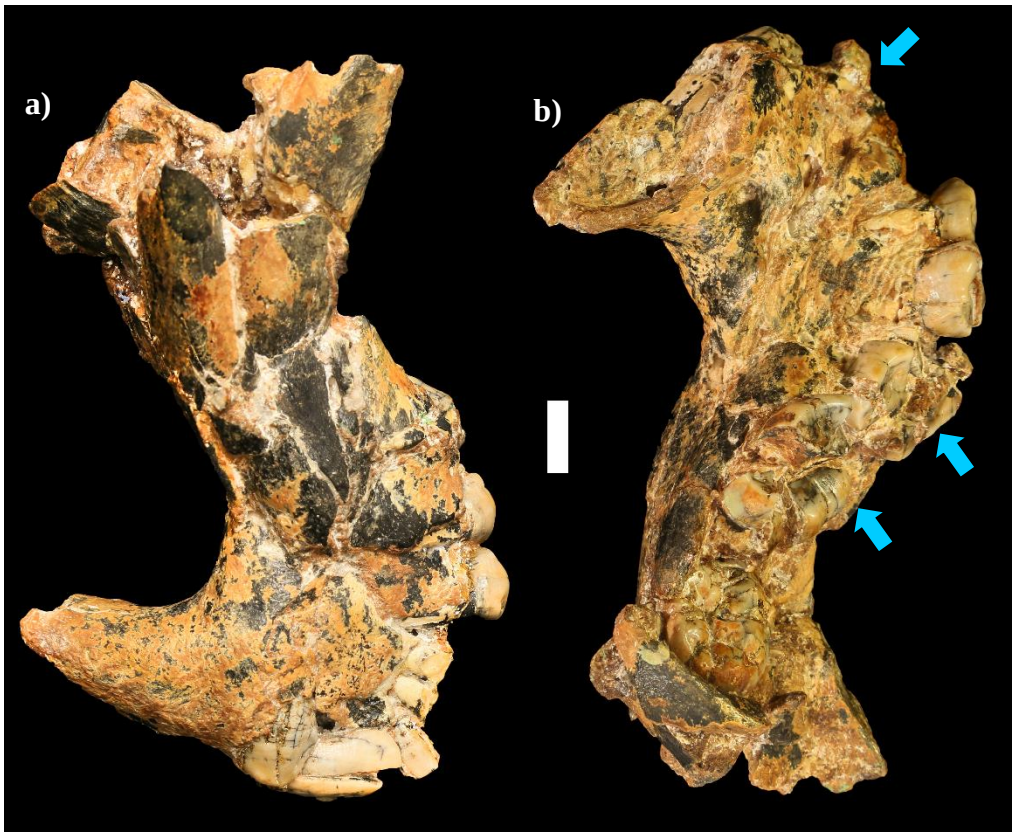

Figure 3.3. StW 498c right mandible: a) Basal view; b) Occlusal view. The blue arrows indicate the position of hard-to-see teeth. Scale bar = 10 mm.

StW 498d

The left mandible (StW 498d) is well-preserved with little brittle deformation. It consists of a mandibular corpus with in situ M_1 to M_3 and an associated P_3 and P_4 (Figure 3.4). Schwartz and Tattersall (2005: 310) mislabel this specimen as StW 498c. There is soil staining across the entire bone surface and the corpus and ramus have extensive manganese staining on the lateral and medial surfaces. There is some manganese staining on the occlusal surfaces of the dentition and soil staining on the buccal and lingual surfaces. There is an inferiorly-directed crack along the corpus between the M_1 and M_2. There are scratch marks on the medial and lateral surfaces of the ascending ramus, which appear to have been made by sharp rocks within the talus that crushed other parts of the skull (Pickering 1999). The distal end of the ascending ramus, including the mandibular condyle, is missing, which makes dimensions for the ascending ramus and for the condyles difficult to estimate. The P_4 and M_1 are missing enamel on their mesiobuccal surfaces and all the teeth exhibit varying degrees of occlusal wear.



Figure 3.4. StW 498d left mandible: a) Medial view; b) Occlusal view; c) Lateral view. Scale bar = 10 mm.

StW 498e

StW 498e consists of a well-preserved, relatively large right petrosal portion of the temporal bone (Figure 3.5). Schwartz and Tattersall (2005: 307) mislabel this petrosal as StW 498p, and again as StW 498r (2005: 327). Schwartz and Tattersall (2005: 326) identify StW 498e as a "fragment of ramus", and there is no StW 498r. StW 498f consists of five re-joined frontal and parietal cranial vault fragments (Figure 3.5).

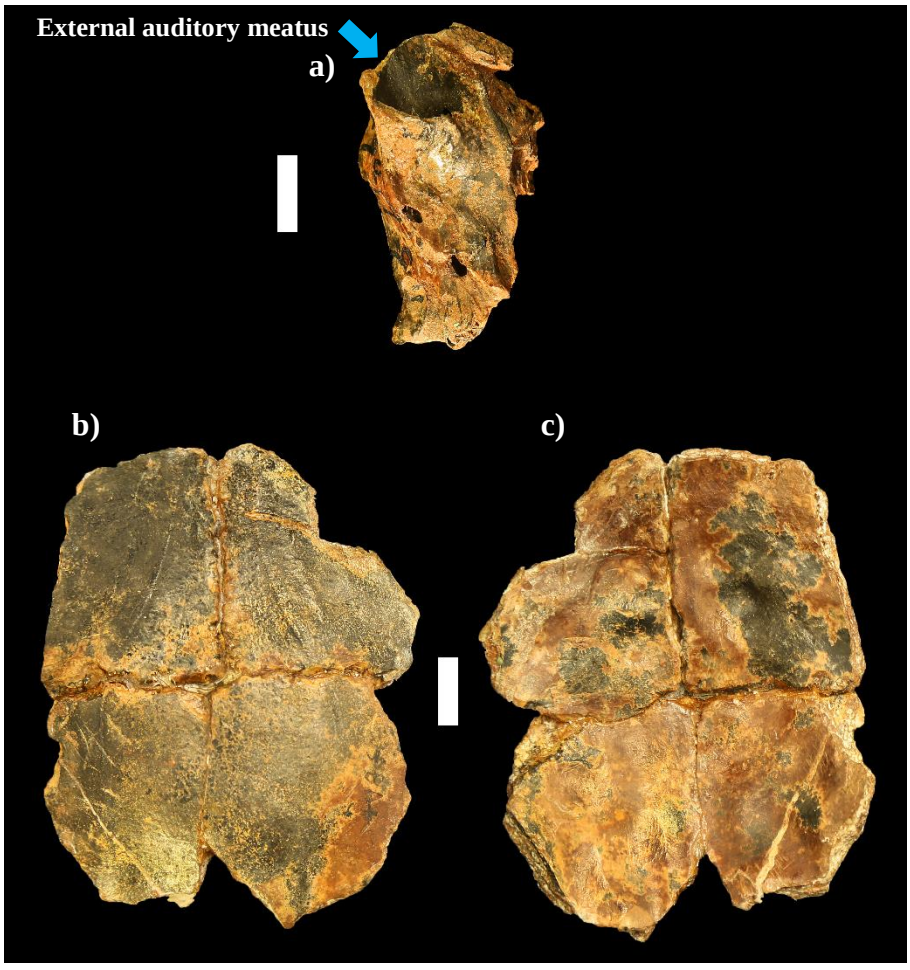

Figure 3.5. Illustrations of the cranial vault fragments: a) StW 498e, the right petrosal, anteromedial view. The blue arrow indicates the external auditory meatus; b) Ectocranial view of StW 498f, anterior towards the top; c) Endocranial view of StW 498f, anterior towards the top. Note that for "b" and "c" the parietals are towards the top in the illustration and the frontal bones are towards the bottom. Scale bars = 10 mm.

StW 498g-q

StW 498g-q and StW 499 consists of various, additional splanchnocranium and basicranium fragments. All of the fragments have manganese staining on the surface and vary in size, with the smallest being approximately 10 mm and the largest 30 mm. These fragments have not yet been identified, but appear to have mostly "clean" breaks, which may facilitate reconstruction and analysis in the future (Figure 3.6).

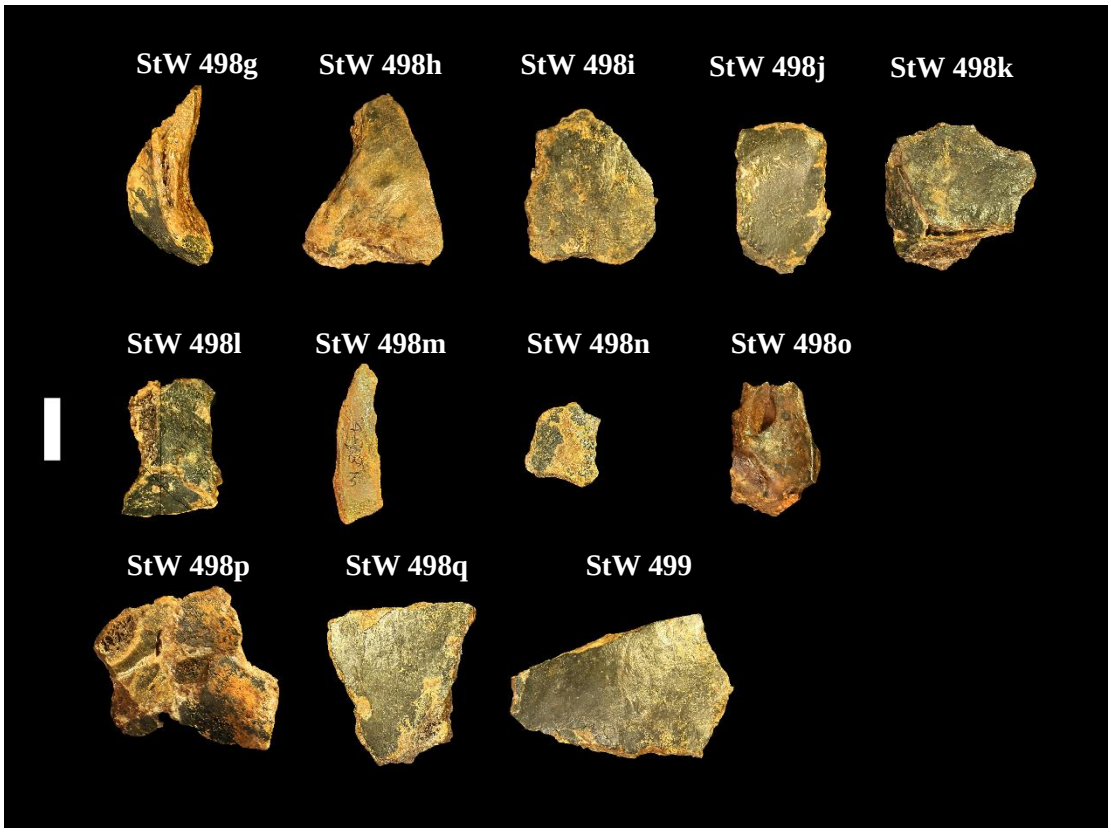

Figure 3.6. Illustrations of cranial fragments, StW 498g-q and StW 499. Scale bar = 10 mm.

3.1.2. Comparative specimens

Below are brief descriptions of selected comparative specimens used in this study. For the purpose of this dissertation, these descriptions are limited to specimens that I personally analysed. References to specimens (and their descriptions) which were included in this study, but which were not personally analysed, can be found in Tables 4.1 and 4.3. Specimens attributed to *A. prometheus* are classified as such according to and following Clarke (1988, *et seq*.) Taxonomic classification of specimens attributed to either *A. africanus* or *P*. *robustus* are generally accepted; references can be found in text.

Sts 36 (Figure 3.7). An adult *A. prometheus* mandible (Clarke 1990) with heavily worn left C_1 to LM_3 and RP_3 to RM_3. Note the moderately deep and relatively thin mandibular corpus. A complete description of this specimen is provided by Clarke (1990).

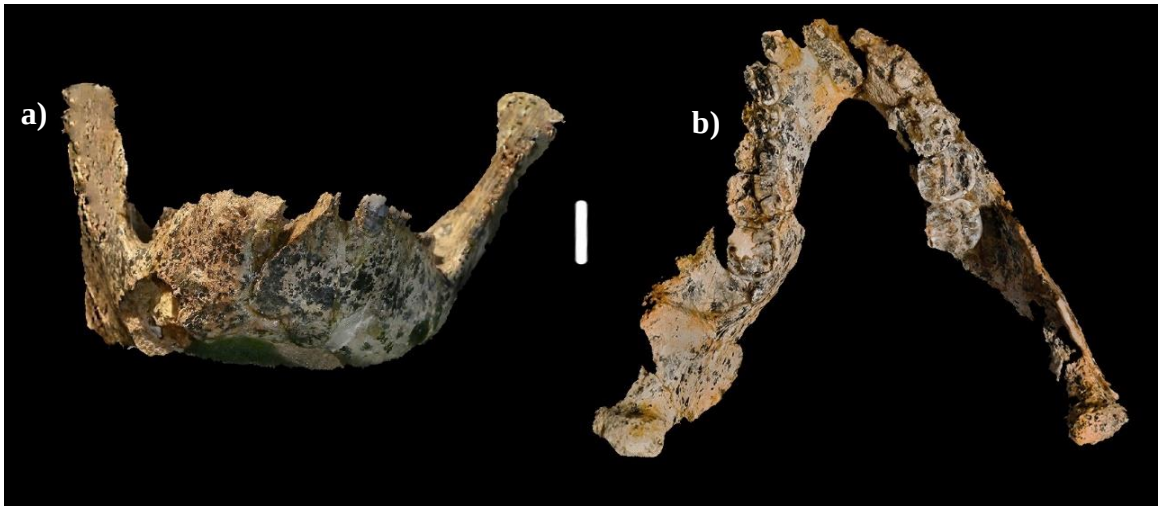

Figure 3.7. Sts 36 mandible: a) Anterior view; b) Occlusal view. Scale bar = 10 mm.

Sts 52 (Figure 3.8). A complete maxilla (Sts 52a) and mandible (Sts 52b) of a young adult *A. africanus* (Broom *et al*. 1950; Robinson 1956; Clarke 1990; Benazzi *et al*. 2013). The teeth exhibit moderate occlusal wear. Most of the left mandibular dentition is broken and measurements were unobtainable. The anterior maxilla is fairly narrow and rounded, presenting a convex mid-face. The palate is short and U-shaped. The mandibular corpus is thick and wide. Refer to Clarke (1990) for a complete physical reconstruction and description of this specimen, and see Benazzi *et al*. (2013) for a virtual reconstruction.



Figure 3.8. Sts 52 lower face: a) Sts 52a, anterior view of the maxilla; b) Sts 52b, occlusal view of the mandible; c) Sts 52a occlusal view of the maxilla. Scale bar = 10 mm.

Sts 71 (Figure 3.9). A partial cranium belonging to an adult female *A. prometheus* (Clarke 1990). The specimen preserves heavily worn right P^3 to M^3. Although incomplete, the palate appears to be shallow. The anterior region of the maxilla is extremely sloped, a classic feature of this species. See Clarke (1990) for a complete anatomical description of this specimen.

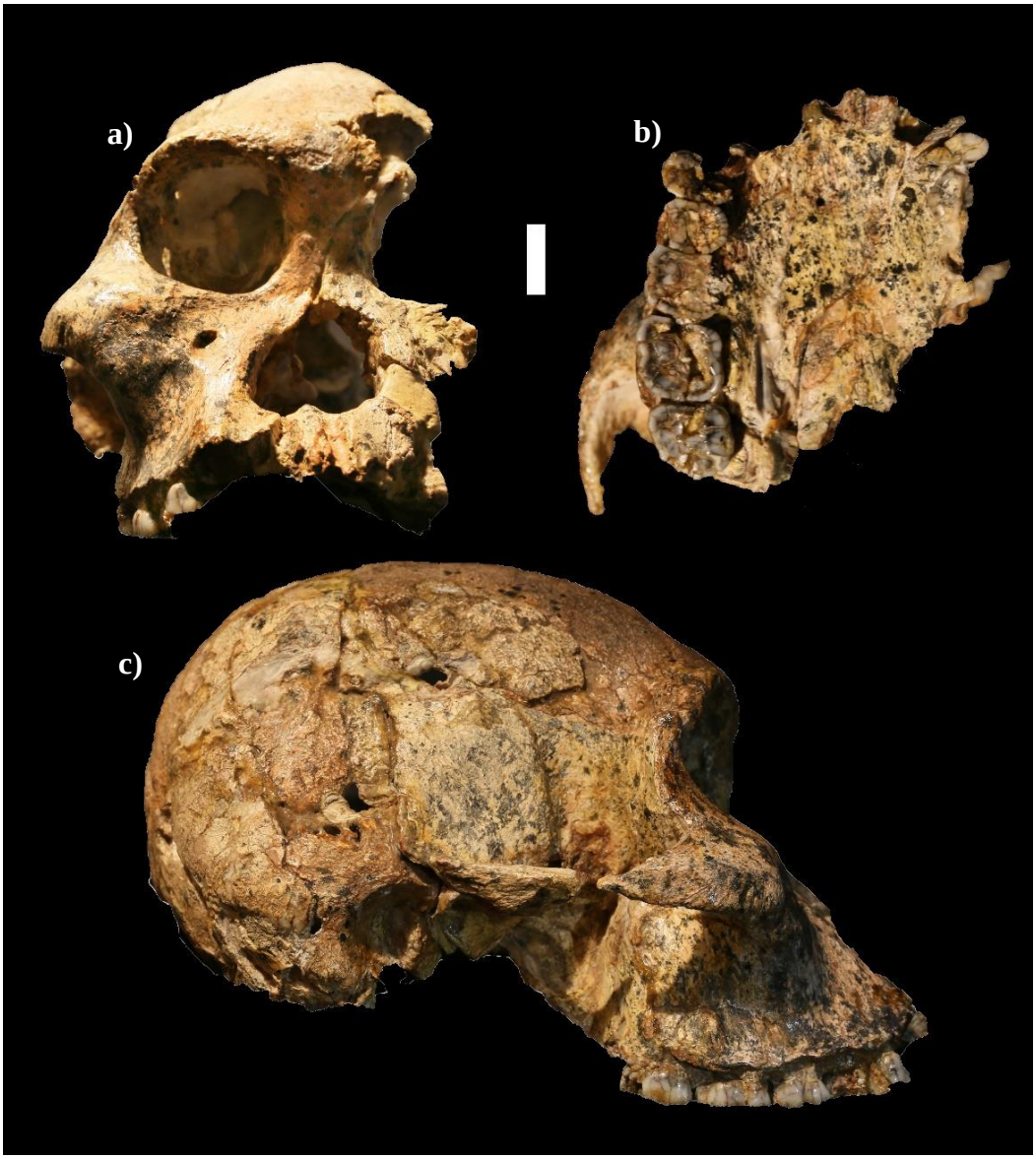

Figure 3.9. Sts 71 partial cranium: a) Anterior view; b) Occlusal view; c) Right lateral view. Scale bar = 10 mm.

StW 73 (Figure 3.10). A mostly complete maxilla belonging to *A. africanus* (Moggi-Cecchi *et al*. 2006; Clarke & Kuman 2018). The specimen preserves a fragmented right P^3, M^1, and M^2, and a complete, moderately worn left P^3 and P^4. Note the extremely narrow and rounded anterior maxilla. A full description of this specimen is provided by Moggi-Cecchi *et al*. (2006).

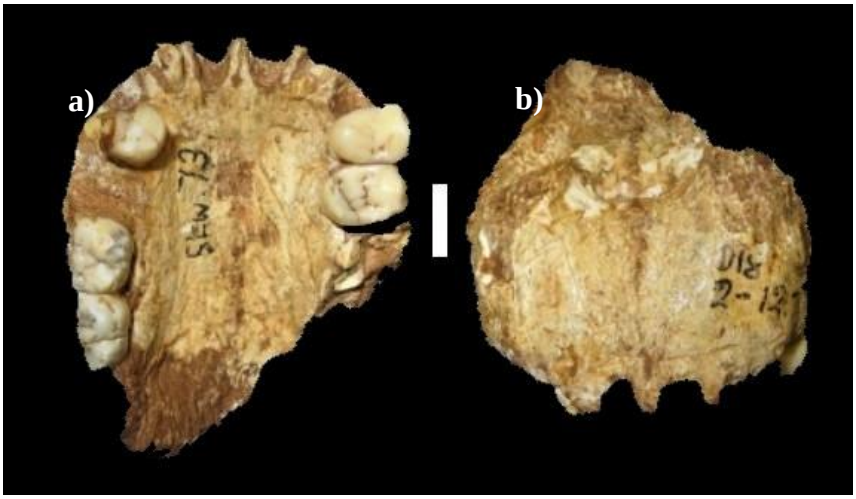

Figure 3.10. StW 73 maxilla: a) Occlusal view; b) Anterior view. Scale bar = 10 mm.

StW 183 (Figure 3.11). A left and right maxillary canine attributed to *A. prometheus* (Clarke 2008, *et seq*., Fornai 2009). Both crowns are minimally worn and both exhibit a prominent lingual median ridge.

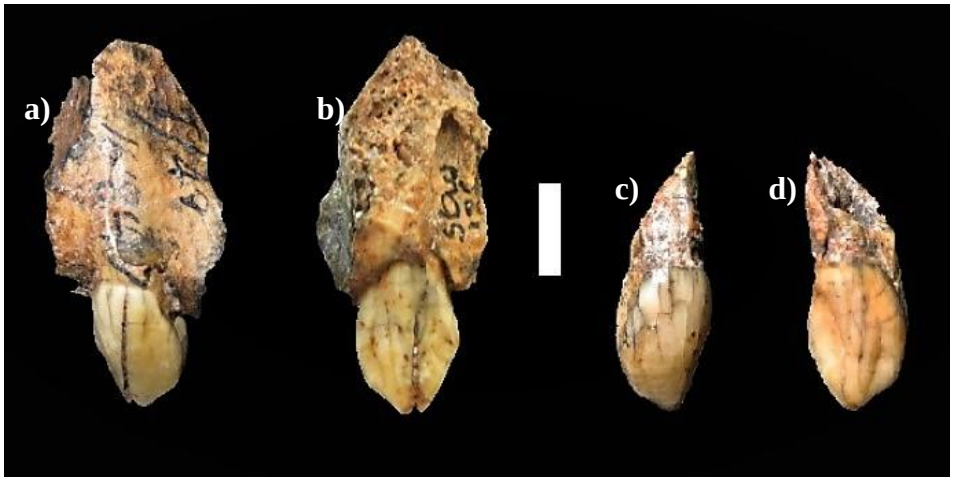

Figure 3.11. StW 183, right and left maxillary canines: a) Labial view of the RC^1; b) Lingual view of the RC^1; c) Labial view of the LC^1; d) Lingual view of the LC^1. RC^1 mesial to the right, and LC^1, mesial to the left. Scale bar = 10 mm.

StW 252 (Figure 3.12). A partial cranium with near complete maxillary dentition of a young adult *A. prometheus* (Clarke 1988; Clarke & Kuman 2018). The palate is relatively narrow, shallow anteriorly, and deep posteriorly. This specimen has been physically reconstructed and described in detail by Clarke (1988).



Figure 3.12. The Sterkfontein StW 252 maxilla: a) cast of the physical reconstruction done by Clarke (1988); b) original condition of StW 252 prior to reconstruction. Scale bar = 20 mm. Images courtesy of R.J. Clarke.

StW 287 (Figure 3.13). A left maxillary canine belonging to an adult *A. africanus*. The crown is virtually unworn. Refer to Moggi-Cecchi *et al*. (2006) for a complete description.

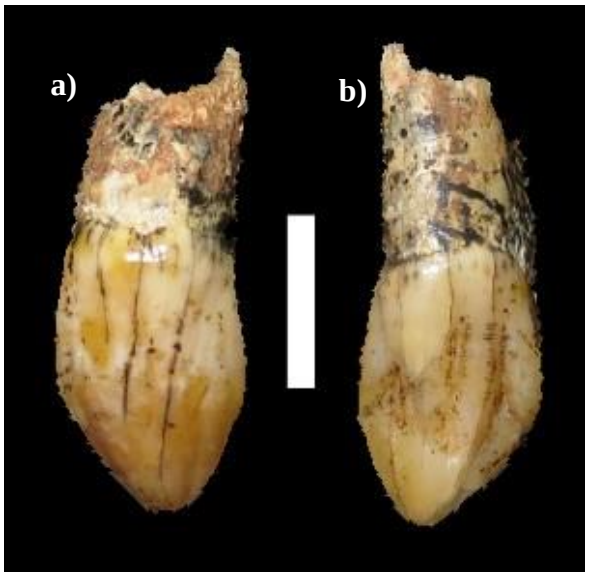

Figure 3.13. StW 287 LC^1. Left: labial view. Right: lingual view. Mesial to the left. Scale bar = 10 mm.

MLD 11/30 (Figure 3.14). Isolated maxillary teeth belonging to an associated maxillary fragment attributed to *A.* africanus. The right I^2 to P^3 are preserved. Teeth were isolated by Oakley *et al*. (1975). Only the RC^1 and P^3 were used in this study.

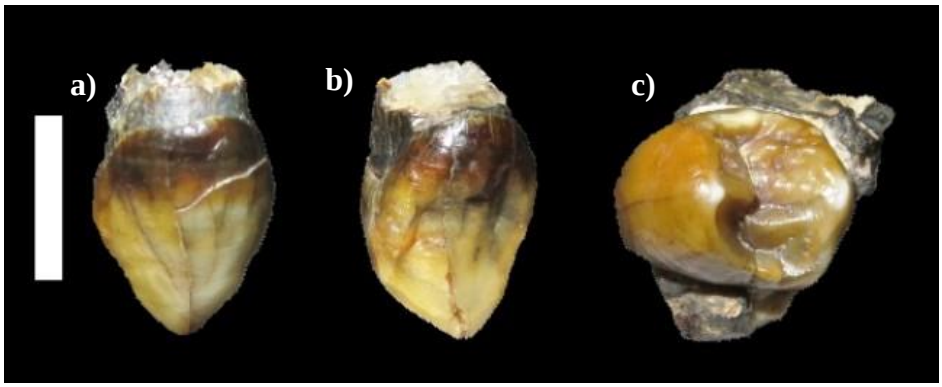

Figure 3.14. MLD 11/30 R^C and P^3: a) RC^1 labial view; b) RC^1 lingual view; c) Occlusal view of P^3 with adhering portions of maxilla surrounding its root. Mesial to right. Scale bar = 10 mm.

SK 843 (Figure 3.15). A partial right mandibular corpus from Swartkrans belonging to a young *P. robustus* (Skinner 2008). The M_1, M_2, and un-erupted M_3 crowns are preserved.

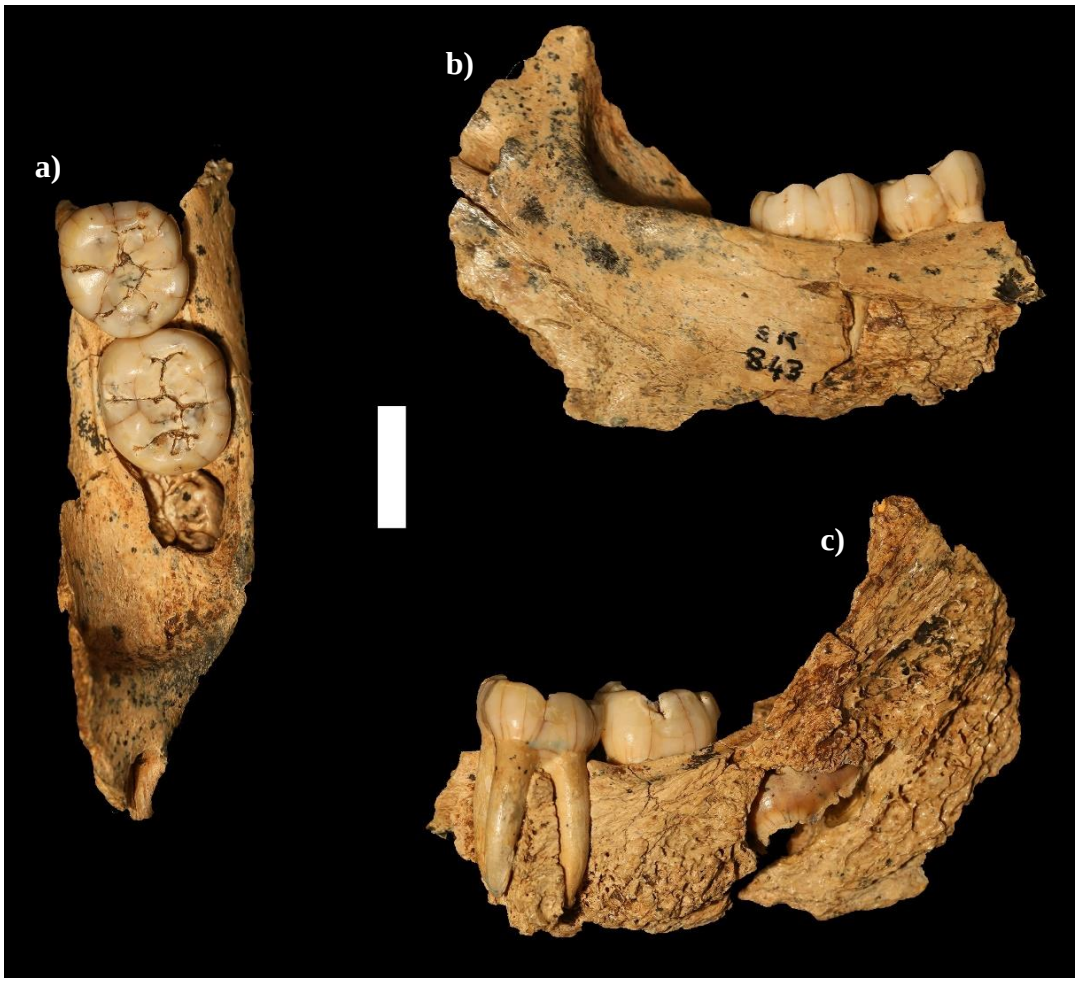

Figure 3.15. SK 843 right partial mandibular corpus. a) Occlusal view; b) Lateral view; c) Medial view. Scale bar = 10 mm.

TM 1517 (Figure 3.16). *P. robustus* type specimen from Kromdraai consisting of an adult partial cranium and right mandibular corpus (Broom 1938a). Only the palate and mandible (including dentition) were included in this study.

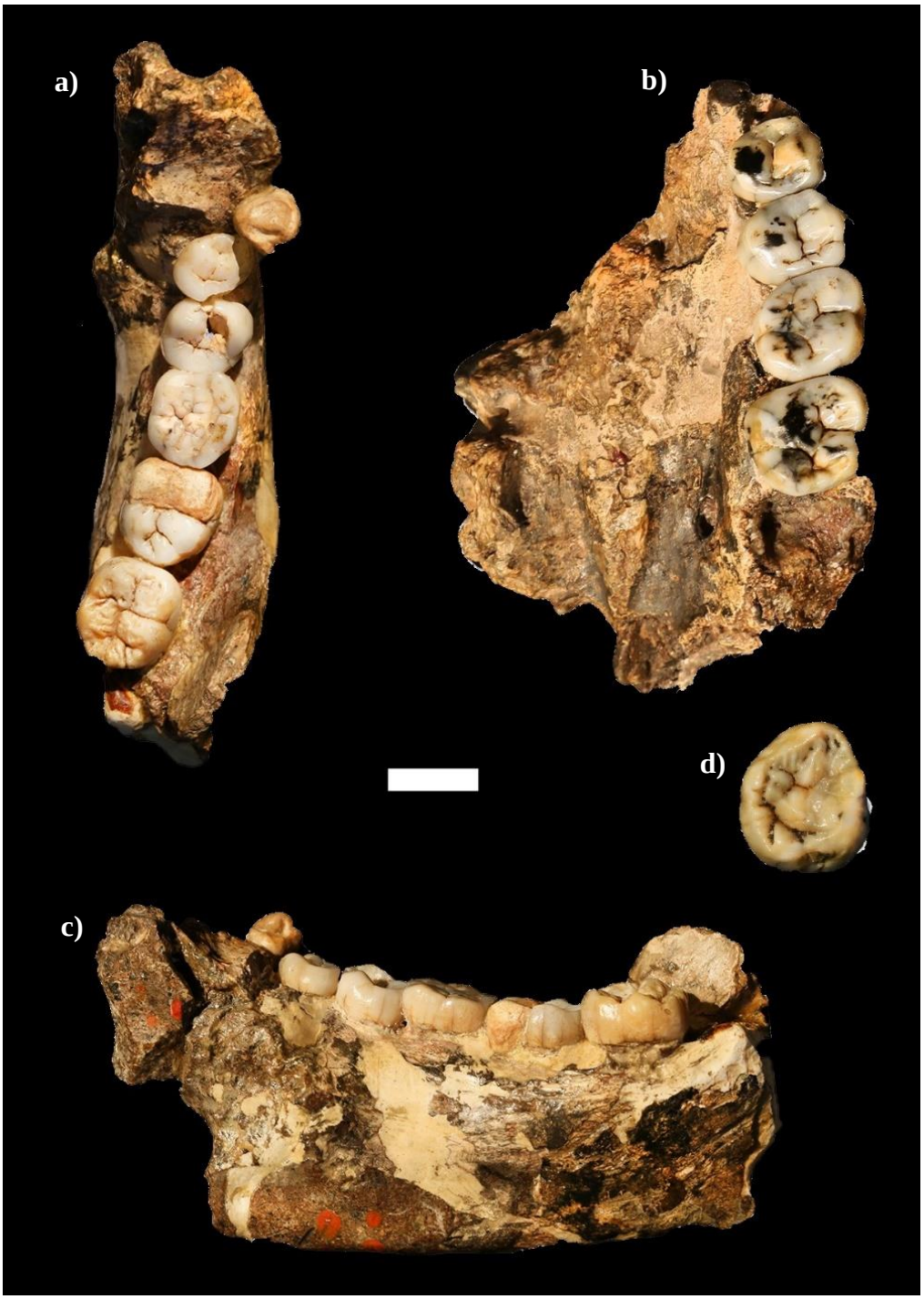

Figure 3.16. *P. robustus* type specimen from Kromdraai, TM 1517, right partial mandibular corpus and right partial maxilla: a) Partial mandible in occlusal view; b) Partial maxilla in occlusal view; c) Medial view of the mandible; d) Occlusal view of the isolated M^3. Scale bar = 10 mm.

3.2. Methods

3.2.1. Digitisation of StW 498 and comparative material

StW 498, Sts 36, Sts 71, StW 252, SK 843, and TM 1517 were microCT-scanned by Prof Kristian J. Carlson and Dr Kudakwashe Jakata using a Nikon Metrology XTH 225/320 LC dual source scanner at the Evolutionary Studies Institute of the University of the Witwatersrand (visit https://www.wits.ac.za/microct for a full description of the scanner facility). Sts 52 was microCT-scanned by Prof José Braga and Dr Jean Dumoncel at the Laboratoire d'Anthropologie Moléculaire et Imagerie de Synthèse of the University of Toulouse III, Paul Sabatier (visit http://amis.cnrs.fr for a full description of the scanner facility). Parameters needed for the image acquisition of StW 498 are provided in Table 3.2 and parameters required for the image acquisition of comparative specimens are reported in Table 3.3. Unfortunately, the isolated right maxillary central incisor and isolated mandibular left lateral incisor were not scanned due to an internal error; these fragments are, nonetheless, described in Chapter 4. Volume data for specimens were reconstructed from raw image data acquired using proprietary software (Inspect-X: X-ray and CT acquisition and processing software). Volumes were imported into and processed in Avizo 9.0.1 (Thermo Fisher Scientific Group, https://www.thermofisher.com). Detailed parameters used for image acquisition and image processing are detailed in Appendices A, B, and C.

Table 3.2. Parameters needed for image acquisition of StW 498.

Specimen	Voxel size (spatial resolution)	kV (kilo volts)	uA (microAmps)
StW 498a (1)	20µm	140	140
StW 498a(2)	20µm	140	140
StW 498a(3)	33µm	140	140
StW 498b(1)	25µm	140	140
StW 498b(2)	25µm	140	140
StW 498b(3)	25µm	140	140
StW 498c(1)	37µm	140	140
StW 498c(2)	37µm	140	140
StW 498c(3)	37µm	140	140
StW 498d(1.1)	38µm	140	140
StW 498d(1.2)	38µm	140	140
StW 498d(2)	37µm	140	140
StW 498e	30µm	140	140
StW 498f	44µm	80	85
StW 498g-p	28µm	80	85
StW 499	44µm	80	85

Table 3.3. Parameters needed for image acquisition of comparative material.

Specimen	Voxel size (spatial resolution)	kV (kilo volts)	uA (microAmps)
StW 252c	14µm	100	100
StW 252f	14µm	100	100
StW 252g	14 µm	100	100
StW 252i	14µm	100	100
StW 252j	14µm	100	100
StW 252l	14µm	100	100
Sts 36	83µm	120	100
Sts 52	41µm	40	100
Sts 71	58µm	190	100
SK 843	33µm	105	80
TM 1517	60µm	190	132

3.2.2 Quantitative measurements, qualitative observations, and descriptions

Direct study of selected comparative specimens and their high resolution image data served as the basis for comparisons of size and morphological features that differ among hominid taxon. These features included crown and cuspal morphology (e.g., see Fornai 2009), the enamel-dentine junction (EDJ) (e.g., see Smith 1986; 2008; Beynon & Dean 1987; Dean *et al*. 2001; Skinner *et al*. 2008), that was used to calculate the 3D average enamel thickness (AET) of second and third molars (e.g., see Kono 2004; Olejniczak *et al*. 2008), and the enamel distribution of maxillary and mandibular molars and premolars (e.g., see Kono 2004; Olejniczak *et al*. 2008; Zanolli 2015). In addition, several traditional measurements frequently incorporated in paleoanthropological dental analyses were collected following published methods (e.g., Robinson 1956; Tobias 1967; White 1977; Johanson, White & Coppens 1982):

1. Labiolingual diameter of maxillary and mandibular dentition. The greatest distance between the labial and lingual surfaces of the crown were taken for the anterior teeth (Tobias 1967; White 1977).
2. Buccolingual (BL) diameter of maxillary and mandibular dentition. The greatest distance between the buccal and lingual surfaces of the crown were taken for posterior teeth (Tobias 1967; White 1977; White, Black & Folkens 2012).
3. Mesiodistal (MD) diameter of maxillary and mandibular dentition. The maximum mesiodistal dimension with the two points of the callipers making contact with the tooth in a horizontal surface, i.e. parallel to the occlusal surface, was taken for each tooth (White 1977; White, Black & Folkens 2012).
4. Crown area of maxillary and mandibular premolars and molars (MD x BL) (Wood 1991).
5. Crown index shape of maxillary and mandibular premolars and molars (BL÷MD) x100 (Wood 1991).
6. Height of maxillary and mandibular canines, measured on the labiolingual surface from the cervix to the tip of the tooth (Robinson 1952; Wood 1991).
7. Root length. Each root was measured from the base of the cervical line to the tip of the root (Garn, van Astine & Cole 1978; Wood 1991).
8. Average enamel thickness (AET) calculated by dividing the volume (mm^3) of the enamel cap (Ve) by the surface area (mm^2) of the EDJ (SEDJ) (Ve÷SEDJ=AET) (Olejniczak *et al*. 2008; Zanolli 2015).
9. Enamel distribution of maxillary and mandibular premolars and molars using virtual, 3D colour-mapping (Zanolli *et al*. 2018).
10. Palate breadth (endomolare to endomolare) (Buikstra & Ubelaker 1994).
11. Palate length taken from orale (the central point of the palate behind the central incisor alveoli) to staphylion (the point where a line between the deepest part of the notches at the back of the palate crosses the midline) (Buikstra & Ubelaker 1994; Wood 1991).

12. Palate depth, measured from the staphylion at the midpoint of the maxillary third molars (Clarke & Kuman 2018).
13. Palate shape index: (breadth ÷ length) x100 (White, Black & Folkens 2012).
14. Greatest mandibular thickness between M_2 and M_3 (Clarke & Kuman 2018).
15. Mandibular height at M_1 (Wood 1991; Clarke & Kuman 2018).
16. Mandibular length (horizontal component of pogonion to gonion) (Buikstra & Ubelaker 1994).

A Principle Component Analysis (PCA) was used to assess morphological differences among fossils and the abovementioned cranio-dental features. Specifically, tooth-specific PCAs were performed on the sample of the upper canines, premolars and second and third molars of StW 498 and selected comparative specimens; each PCA was performed on the covariance matrix. A PCA was done for each tooth (i.e., one PCA for the third premolars, one for the fourth premolars, and so on) using four variables: buccolingual diameter, mesiodistal diameter, crown area, and crown shape index. A PCA was also done on a combined sample of maxillary and mandibular canines using three variables: buccolingual diameter, mesiodistal diameter, and crown height. The StW 498 specimens in the Principle Component space were projected for each tooth-specific PCA. A PCA was not done for the maxillary M^1s, mandibular premolars, and mandibular molars due to the small sample. Since molars exhibit a range of variation, I conducted another PCA by combining all the molars together, producing a PCA for all the maxillary molars (M^2 and M^3) (see Skinner, Gunz & Hublin 2009 for an example of a combined molar sample PCA).

Dental measurements were physically obtained from original fossils using a RACO Engineering Vernier callipers, accurate to 0.1 mm, when possible, or through published sources when not possible (see Tables 4.1 to 4.6 for a complete list of references). In some cases, e.g., for specimens that required digital reconstruction, buccolingual and mesiodistal diameters were taken from surface

renderings using the 3D measurement tool in Avizo 9.0.1. In order to ensure accuracy of this protocol, virtual measurements were taken for selected specimens and, where possible, compared to published physical measurements. Measurements obtained from published material were taken in the same way as those taken for this study. In all instances virtual measurements were consistently smaller than those taken physically:

Sts 36. Virtual measurements for this specimen were compared to the original measurements by Clarke (1988). A difference of less than 0.2 mm was documented. Thus, a 1.38% difference between the virtual and physical measurements was observed and is confidently inconsequential in the case of Sts 36.

Sts 71. Virtual measurements were compared to those taken by Clarke (1990). A difference of 0.2 mm was observed. Thus, an inconsequential difference of 1.36% was observed between the virtual and physical measurements of Sts 71.

StW 252. Virtual measurements of the dentition was compared to those taken by Clarke (1988). A difference of 0.02 mm was observed. A 1.26 % difference between the virtual and physical measurements was documented.

TM 1517. Virtual measurements were compared to physical measurements made by Robinson (1956). A difference of less than 0.2 mm was observed. Thus, a difference of 1.24% between the virtual and physical was observed and can confidently be called negligible.

Virtual measurements were also taken for SK 843. Physical measurements on the original specimens were taken for StW 73, StW 183, StW 287, and MLD 11/30. Physical measurements on the originals Sts 52 specimen were taken for the maxillary central and lateral incisors, the maxillary canines, and the right mandibular canine. Remaining measurements have been published by Clarke (1990).

Palatal dimensions for StW 498 and StW 73 were recorded, however, the missing staphylion of StW 498 made it impossible to obtain an accurate palate length on

the specimen. A gross estimated dimension, however, is provided in Table 4.3. This measurement was estimated by considering a typical position of the staphylion, e.g., at the midpoint of the maxillary third molars. Mandibular dimensions were recorded for StW 498, Sts 36, and Sts 52. Where possible, root measurements of the StW 498 dentition were recorded for descriptive purposes. All measurements were taken on three separate occasions and recorded to the nearest 0.1 mm. A difference of less than 1.22% was documented for the repeated intra-observer tests.

Anatomical descriptions on the maxilla and mandible, along with the associated dentition, report the palate shape, palatal and mandibular dimensions, bone surface modification, morphological features, occlusal attrition, enamel pathologies, crown size, and root length (where available). The descriptive terminology closely follows Robinson (1956) as modified by Tobias (1967), Johanson, White & Coppens (1982), and Moggi-Cecchi *et al*. (2006). Refer to the Glossary (page xviii) for a detailed list of terminology and associated definitions.

Degree of occlusal wear were categorised following Moggi- Cecchi *et al*. (2006):

1. Unworn: either incompletely or fully erupted crown, shows no evidence of wear. All of the morphological features are distinctly visible.
2. Light: there is no dentine exposed on the occlusal surface, but there are signs of enamel polish. There is no reduction of cuspal height and morphological features have not been obscured.
3. Moderate: there are small islands of exposed dentine. There is minimal reduction in cuspal height and the morphological features are fairly well-preserved and definable.
4. Heavy: there is extensive dentine exposure on the occlusal surface and significant reduction in cuspal height. Morphological features are lost or undefinable.

3.2.3. Virtual restoration and reconstruction of the lower face and dentition of StW 498

StW 498a (left maxilla), StW 498b (right maxilla), StW 498c (right mandible), and StW 498d (left mandible) were each scanned at high resolution in stages (see Table 3.2), thus producing three data volume (.vol) files for each specimen. This enabled optimal spatial resolution that facilitated the digital reconstruction process. Each .vol file representing a portion of one anatomical region was opened in Avizo 9.0.1 (Thermo Fisher Scientific Group, https://www.thermofisher.com) and aligned relative to the others comprising the same anatomical region (e.g., StW 498a) in order to digitally 'stitch' volumes and produce a single 16-bit TIFF composite image stack. A median 3 filter was applied to the combined image stacks representing StW 498a and StW 498d, and a median 2 filter was applied to the combined image stacks representing StW 498b and StW 498c. This procedure facilitated subsequent segmentation protocols by enabling smoother, more refined greyscale image slices. Segmentation involved manually or automatically tracing materials of interest in the image slices produced from CT scans.

Each filtered combined TIFF stack was opened in Avizo 9.0.1 (Thermo Fisher Scientific Group, https://www.thermofisher.com) and segmentation was performed using the following automatic tools: the magic wand tool, the watershed tool, the threshold tool, and the region-growing tool. Severely fragmented pieces were subjected to an additional step during manual segmentation (i.e., tracing material in a region of interest slice by slice) that required using the brush tool to produce individual materials (i.e., volumes) for each fragment. Ultimately, each tooth was segmented separately and was comprised of several individual label field modules (i.e., each fragment of bone, enamel and dentine was assigned to its own material using a unique label field). This permitted spatial manipulation and repositioning of each separate fragment in order to create the composite reconstruction of the specimen.

After a segmentation protocol was completed, each material (i.e., label field) was smoothed to remove any islands. Islands represent irregularities in the volume data (i.e., inclusions of higher or lower greyscale values than the material of

interest). Islands resulting from segmentation of the StW 498 image data were typically small ‘spikes’ or ‘peaks’, which resulted in a ‘bumpy’ surface appearance. Following the segmentation protocol, surface renderings of each fragment (e.g., Figure 3.17) were produced in order to facilitate reconstruction of individual teeth. The final step involved manually repositioning each fragment of bone, enamel and/or dentine in order to produce a complete, undistorted dental arcade.

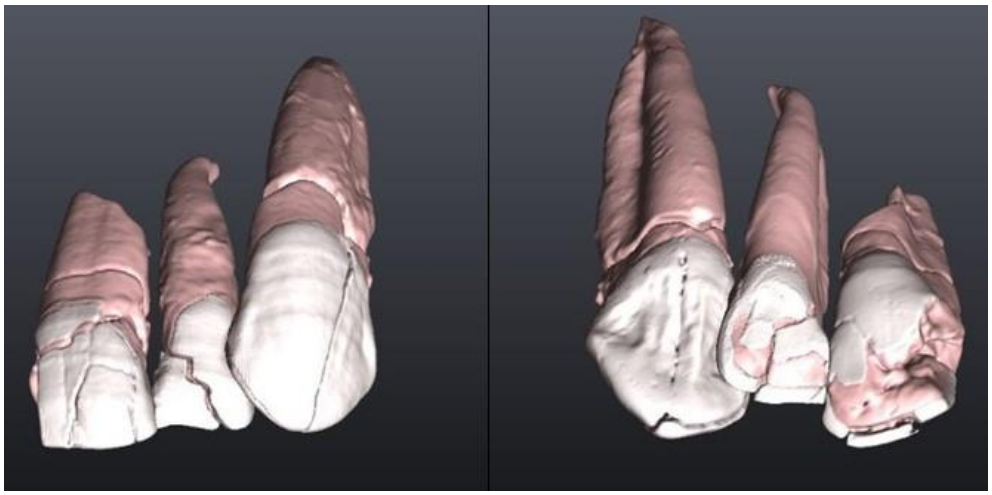

Figure 3.17. An example of the surface renderings resulting from segmentation of the StW 498a left maxillary I^1, I^2, and C^1 prior to final reconstruction. Each fragment is a separate material in the label field module. Left: labial view, mesial to left; Right: lingual view, mesial to right. See Figure 4.3 for the results of the re-alignment of the teeth. Not to scale.

The high resolution image data revealed features that were present in the right mandible, but absent in the left mandible. Specifically, the right mandible (StW 498c) preserved a partial mandibular symphysis, the left mandibular canine, and the left mandibular central incisor. Unfortunately, the right maxilla (StW 498b) and right mandible (StW 498c) were too fragmentary, and fragments too anatomically displaced, to generate a complete and reasonable reconstruction. However, I was able to digitally extract the right upper and lower teeth, along with some bone, by segmenting and reconstructing portions of the overall specimens. The description of the facial shape of StW 498 relied more heavily on

the better-preserved left maxilla and mandible, while descriptions of teeth were based on individual reconstructions.

The displaced posterior portion of the palate situated alongside the M^1 (StW 498a) was extracted and repositioned into anatomical position. Once the maxillary teeth and bone were reconstructed, the left I^1 to M^1 were repositioned into anatomical position using interproximal contact facets (IPCFs) and alveoli. The left M^2 and M^3 were aligned to the left partial maxilla using their IPCFs and the directionality of their roots.

Dentition from the left mandible was extracted in Avizo 9.0.1 (Thermo Fisher Scientific Group, https://www.thermofisher.com). Because of the crack on the corpus body between the right M_1 and M_2, the corpus was segmented in two parts. Subsequently, surface renderings for the two parts were positioned in anatomical position. The left P_4 and M_1 are fragmented and missing parts of their enamel caps on the buccal surface. The missing enamel for the P_4 occurred on a relatively flat surface which allowed me to fill-in the missing enamel using the shape of its occlusal outline (i.e., it was a 'predictable' contour to fill-in as there was very little interpolation to make because of the flat surface). This allowed for an estimate of the buccolingual diameter. Due to the unpredictable and variable shape of molars, and in the interest of being conservative, the missing enamel from the M_1 was not filled in.

The right mandible, StW 498c, was found to contain all of the right mandibular dentition, as well as the left canine and left broken central incisor that were found in the right mandible. Unfortunately, the left lateral incisor was not scanned as it only consisted of a partial lingual fragment (see Chapter 4, Figure 4.28). The right I_1 and I_2 are fragmented, but complete.

Following virtual reconstruction of the mandibular dentition, the isolated left P_3, P_4, and left canine were repositioned on the left mandibular corpus using their IPCFs. Because the left mandibular incisors are broken and missing parts of their enamel caps, the right I_1 and I_2 were mirrored and repositioned using their IPCFs to produce a complete left mandible.

In order to proceed with the final cranial reconstruction, the renderings (i.e., .surf files) of the left maxilla and mandible were mirrored in Avizo 9.0.1 (Thermo Fisher Scientific Group, https://www.thermofisher.com) Renderings of original and mirrored volumes were aligned to one another based on idealised (symmetrical) anatomical relationships in the maxilla, specifically the incisive canal, the intermaxillary suture, and the opening of the incisive fossa into the nasal cavity. It is recognized that this may ignore a small amount of natural asymmetry that could have been inherent in this individual within life. Once the mandible was reconstructed, the partial mandibular symphysis was restored using the position of the genial fossa as a guideline. The maxilla and mandible were aligned to one another using the dental occlusion.

Similar segmentation and reconstruction protocols, as those applied to StW 498, were followed for Sts 36, Sts 52, Sts 71, StW 252, SK 843, and TM 1517. Thus, these protocols are only briefly described in order to avoid redundancy. In each case, a 16-bit TIFF stack of each specimen was opened in Avizo 9.0.1 (Thermo Fisher Scientific Group, https://www.thermofisher.com). Tooth components for premolars and molars from each specimen were segmented separately using the magic wand tool, the watershed tool, and the region-growing tool to recreate individual materials in the label fields' module (Thermo Fisher Scientific Group, https://www.thermofisher.com). From each of these components, a surface rendering was produced that enabled repositioning fragments in order to reconstruct each individual tooth in a specimen.

3.2.4. Digital partitioning of the dentition for the analysis of dental form

In order to obtain dental measurements of the maxillary and mandibular dentition of StW 498 and the selected comparative material, 3D surface renderings (.surf files) of each reconstructed tooth were opened in Avizo 9.0.1 (Thermo Fisher Scientific Group, https://www.thermofisher.com). The 3D measurement tool was used to acquire buccolingual and mesiodistal linear dimensions for each tooth following measurement definitions for physical measurements of teeth.

Average enamel thickness (AET)

The average enamel thickness (AET) of premolars and molars are taxonomically unique (e.g., see Kono 2004; Olejniczak *et al*. 2008). In order to calculate the AET of maxillary and mandibular second and third molars, the enamel-dentine junction (EDJ) was isolated in each tooth crown using .surf files of a tooth opened in Avizo 9.0.1 (Thermo Fisher Scientific Group, https://www.thermofisher.com). In this protocol, the crown volume was separated from the EDJ and root and subsequently removed. Once the crown was isolated from the root, the cervical line became visible, thus allowing separation of the root from the dentine, leaving only the dentine surface of the EDJ (Figure 3.18). Each file (i.e., separate files for the enamel cap, dentine, and the pulp) was then saved as a separate surface. The *surface area volume* module was applied to each surface, which reported the dimensions for the volume (mm^3) of the enamel cap (Ve), dentine (Vd), and where available, the pulp (Vd). The surface area (mm^2) of the EDJ (sEDJ) was reported using the same module. The 3D average enamel thickness was then calculated by using the following formula:

$$AET = Ve \div sEDJ$$

For comparative specimens (i.e., Sts 52, StW 252, and TM 1517), AETs of the second and third molars were produced by extracting the EDJ using the same procedure as outlined for StW 498 and reporting volumes of the enamel cap, dentine, and pulp (where present). For some comparative specimens (i.e., StW 3, StW 179, StW 421, StW 529, StW 560, SK 31, and SK 41), AET dimensions reported by Olejniczak *et al*. (2008) were used rather than calculating them in the present study.

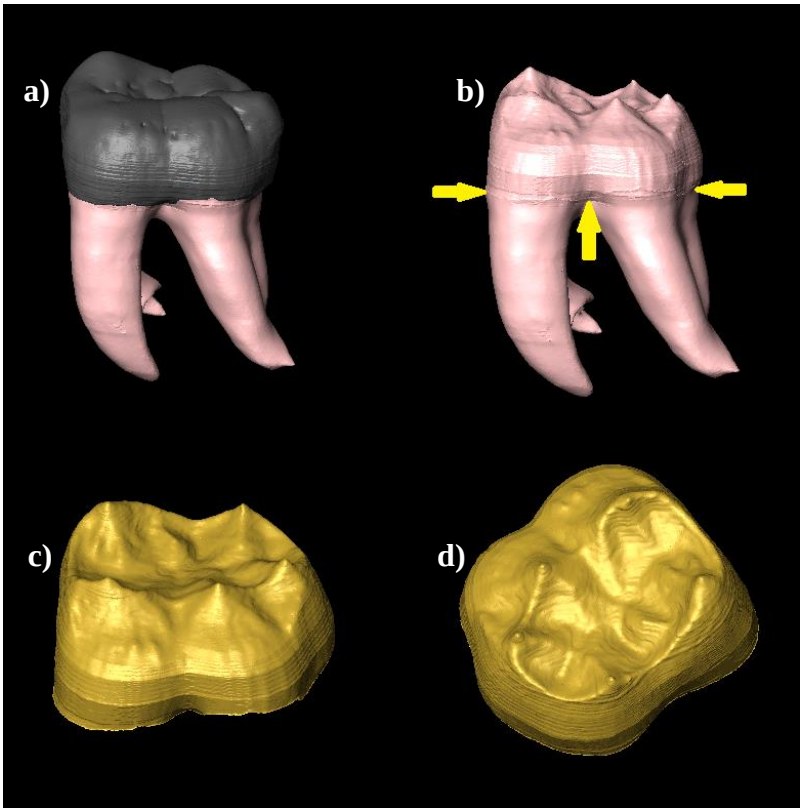

Figure 3.18. Reconstructed left M_2 (StW 498d): a) The enamel, dentine and root, mesial to left; b) the dentine and the root, the yellow arrows point to the cervical line, mesial to left; c) the EDJ after separating the enamel cap and the root, mesial to left; d) the EDJ in occlusal view, mesial to right. Not to scale.

Visualising enamel distribution

Colour mapping was used to visualise the distribution of enamel in selected premolars and molars. The distribution of enamel is calculated as the minimum orthogonal distance from a given point on the EDJ surface to the crown surface (i.e., the distance between the EDJ and the outer enamel surface). In order to calculate the enamel distribution, the enamel cap, root and dentine had to be separated (as was done for calculating the AET). Once the EDJ was separated from the enamel cap, the *surface distance* module was applied to 3D renderings of the EDJ and the enamel cap, effectively producing a topographic surface of the enamel cap where a colour scale represents local thicknesses as thinner (dark blue) to thicker (red) (e.g., Figure 3.19). Colour mapping was performed for the third and fourth premolars, and for the second and third molars of Sts 52, StW

252, and TM 1517 in order to assess their enamel distributions and compare them to those of StW 498.

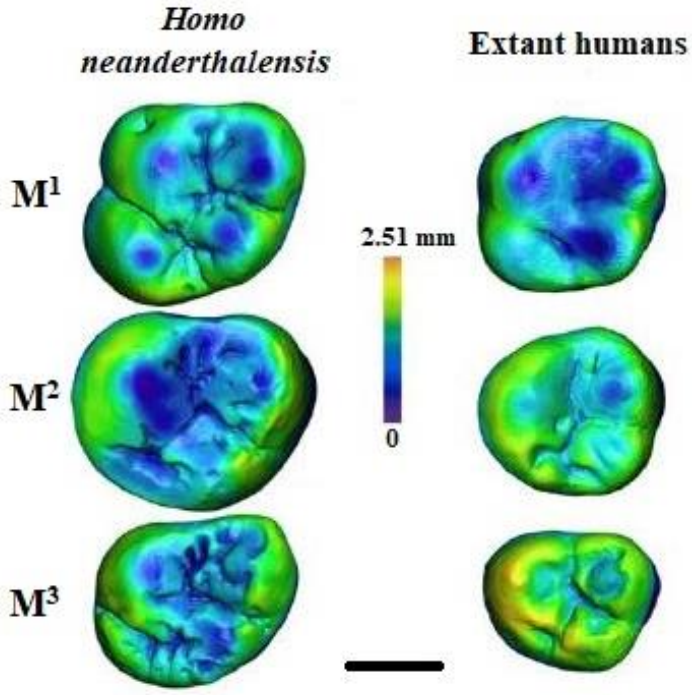

Figure 3.19. Enamel thickness distribution on the maxillary molars of *H. neanderthalensis* and extant humans. Mesial towards the top, buccal to the left. Scale bar = 5 mm (adapted from Zanolli 2015, Figure 2, p. 152).

Chapter 4

Results

This chapter presents the results of the *in silico* reconstruction and analysis of StW 498 and is divided into two sections. The first section provides the results of the segmentation, reconstruction, and description of the StW 498 maxilla and mandible. The second section reports the quantitative measurements and qualitative observations made throughout this study. All qualitative observations and quantitative measurements were made by the author unless stated otherwise.

4.1. Reconstruction and description of StW 498

This section presents the results of the digitisation and subsequent reconstruction of StW 498. For the purpose of this dissertation, the reconstruction and anatomical descriptions of the maxilla and associated dentition are presented first. This is followed by the reconstruction and anatomical descriptions of the mandible and associated dentition. Finally, the entire reconstructed lower face, along with associated pieces of the cranial vault, are presented.

The descriptive terminology closely follows that of Robinson (1956), as modified by Tobias (1967), Johanson, White & Coppens (1982), and Moggi-Cecchi *et al*. (2006). The dental measurements used throughout this study adhere to those described by White (1977), Wood (1991), and Buikstra & Ubelaker (1994).

The anatomy of this specimen has been briefly described by Schwartz and Tattersall (2005), and the broken, fragmented dentition has been briefly described by Moggi-Cecchi *et al*. (2006); these descriptions focused on tooth morphology. Unfortunately, due to the extreme fragmentation of StW 498 (especially on the right sides), these descriptions are incomplete and most of the right mandibular and maxillary dentition are not discussed. With a complete reconstruction. The descriptions of StW 498 discussed in this chapter provide a detailed account for all the preserved anatomical features of the maxilla and the mandible, including the associated dentition. The following observations made on the maxilla and

mandible are based on mirror images, unless stated otherwise, while dental observations are based on the reconstructions of individual teeth.

4.1.1. Reconstruction of the maxilla

The left maxilla is fairly well-preserved and there is minimal brittle deformation. It preserves fragmented, but in situ, I^1 to M^1 and the LM^2 and LM^3 are present as isolated and fragmentary teeth. The posterior portion of the palate situated alongside the M^1 has been displaced. The left maxilla and its associated dentition were segmented separately, allowing for manual realignment of individual pieces (Figure 4.1).

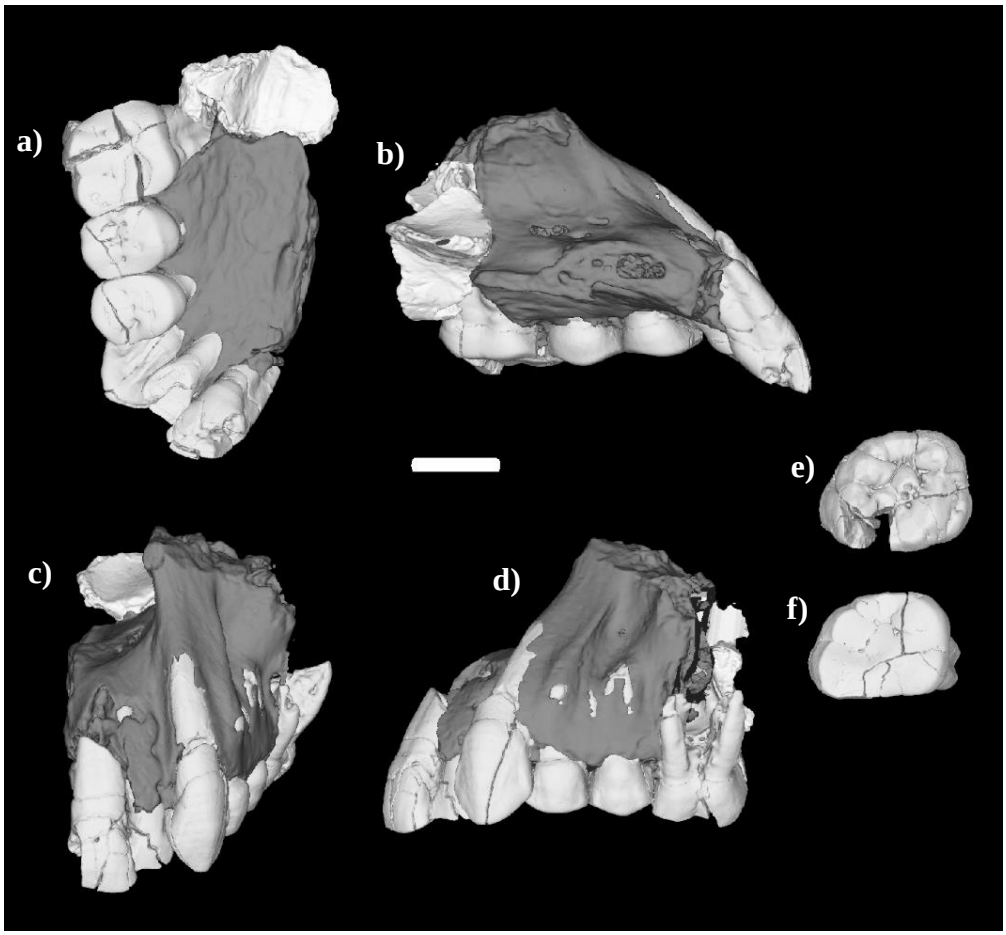

Figure 4.1. StW 498a left maxilla prior to digital reconstruction: a) Occlusal view; b) Medial view; c) Anterior view; d) Lateral view; e) Occlusal view of the LM^3; f) Occlusal view of the LM^2. Scale bar = 10 mm.

For the entire maxillary dentition, teeth were reconstructed according to crown morphology, interproximal contact facets, and the position of roots in the alveoli. Positions of the isolated LM^2 and LM^3 were established using interproximal contact facets (Figure 4.2).

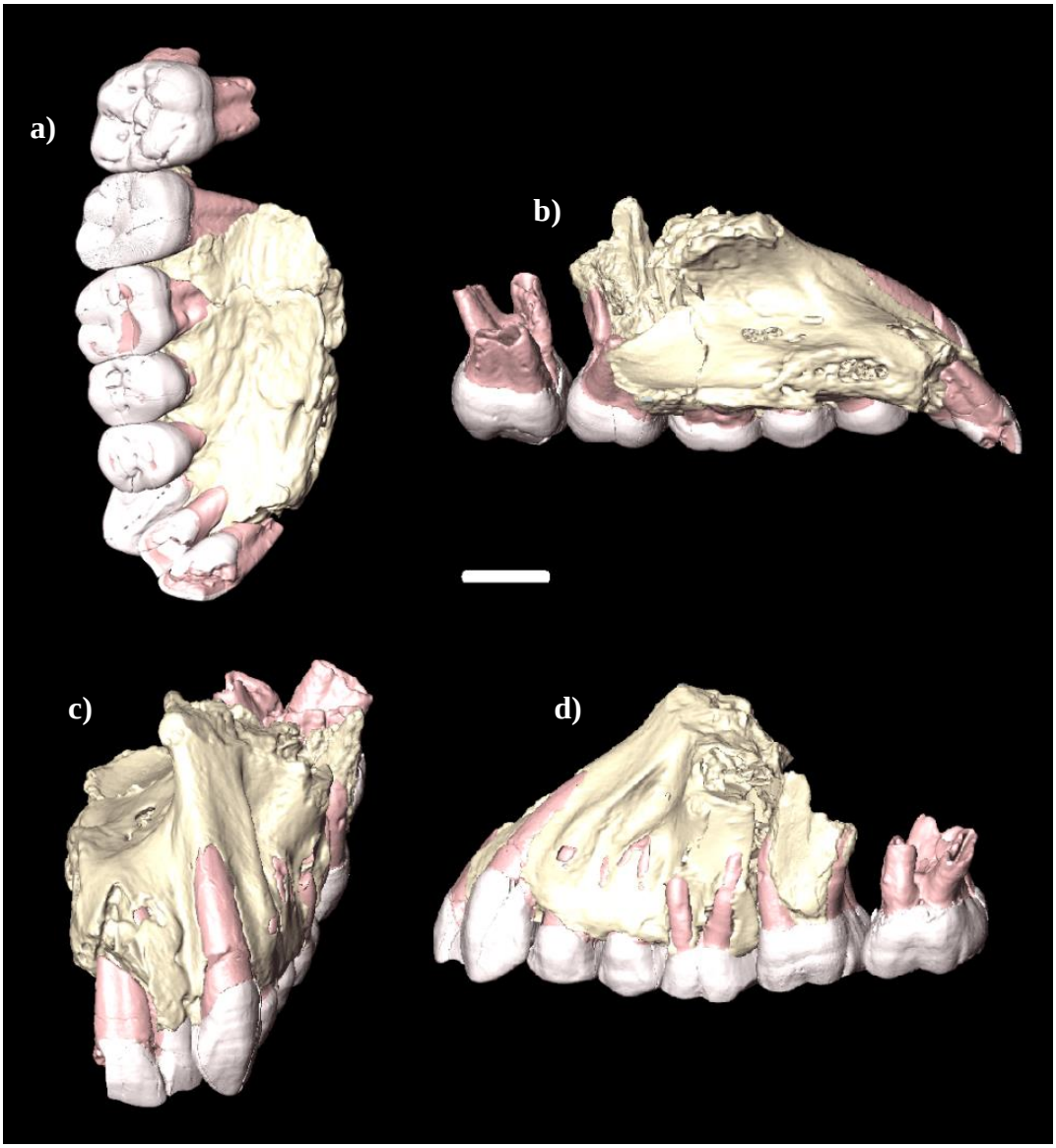

Figure 4.2. StW 498a left maxilla after virtual reconstruction. a) Occlusal view; b) Medial view; c) Anterior view; d) Lateral view. Scale bar = 10 mm.

The right maxilla, on the other hand, exhibits substantial distortion and crushing with variably crushed dentition (Figure 4.3). The dental observations are based on the reconstructions of individual teeth. Thus, each tooth was individually segmented and virtually reconstructed in order to provide an accurate description of the dentition of StW 498. Due to the severity of crushing exhibited by the right maxilla, StW 498b, it was not possible to reconstruct the bone or its alveolar margin.

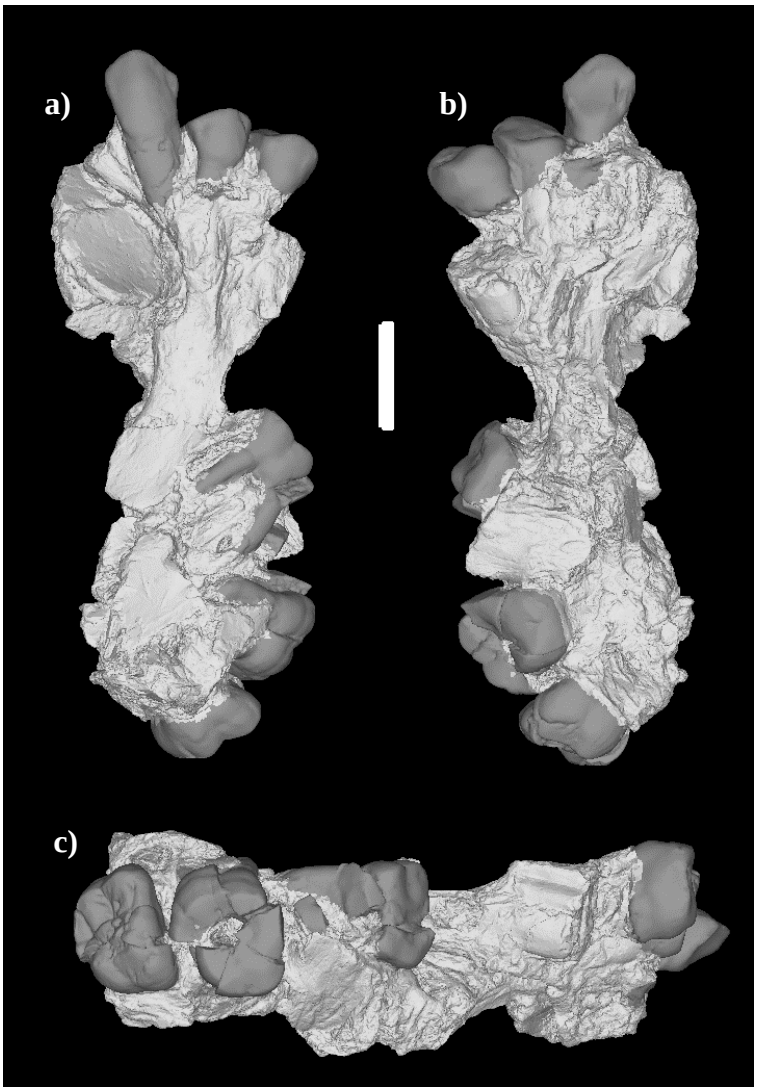

Figure 4.3. StW 498b crushed right maxilla: a) Basal view; b) Lingual view; c) Occlusal view. Scale bar = 10 mm.

Upon digital reconstruction of the teeth and realignment of bone fragments, the left maxilla was mirrored for comparison to the less well-preserved right maxilla. Fortunately, the left maxilla was preserved well enough in the sagittal plane

region that it enabled an estimated reconstruction of the entire maxilla. Specifically, the mirror image of the digitally reconstructed left maxilla was aligned in anatomical position with the rendering of the original left maxilla based on the structure of the incisive canal, the position of the intermaxillary suture, and the opening of the incisive fossa into the nasal cavity. Aligning both of these produced a complete reconstruction of the maxilla of StW 498 (Figure 4.4). It is important to note, however, that because of mirror imaging, the complete maxilla represents a close approximation of what the maxillary form originally looked like without any inherent bilateral asymmetry that may have existed when the individual was alive. The right central incisor has a mesial interproximal contact facet, thus the central incisors were in contact and the gap between the two central incisors is due to a missing mesial fragment of the left crown.

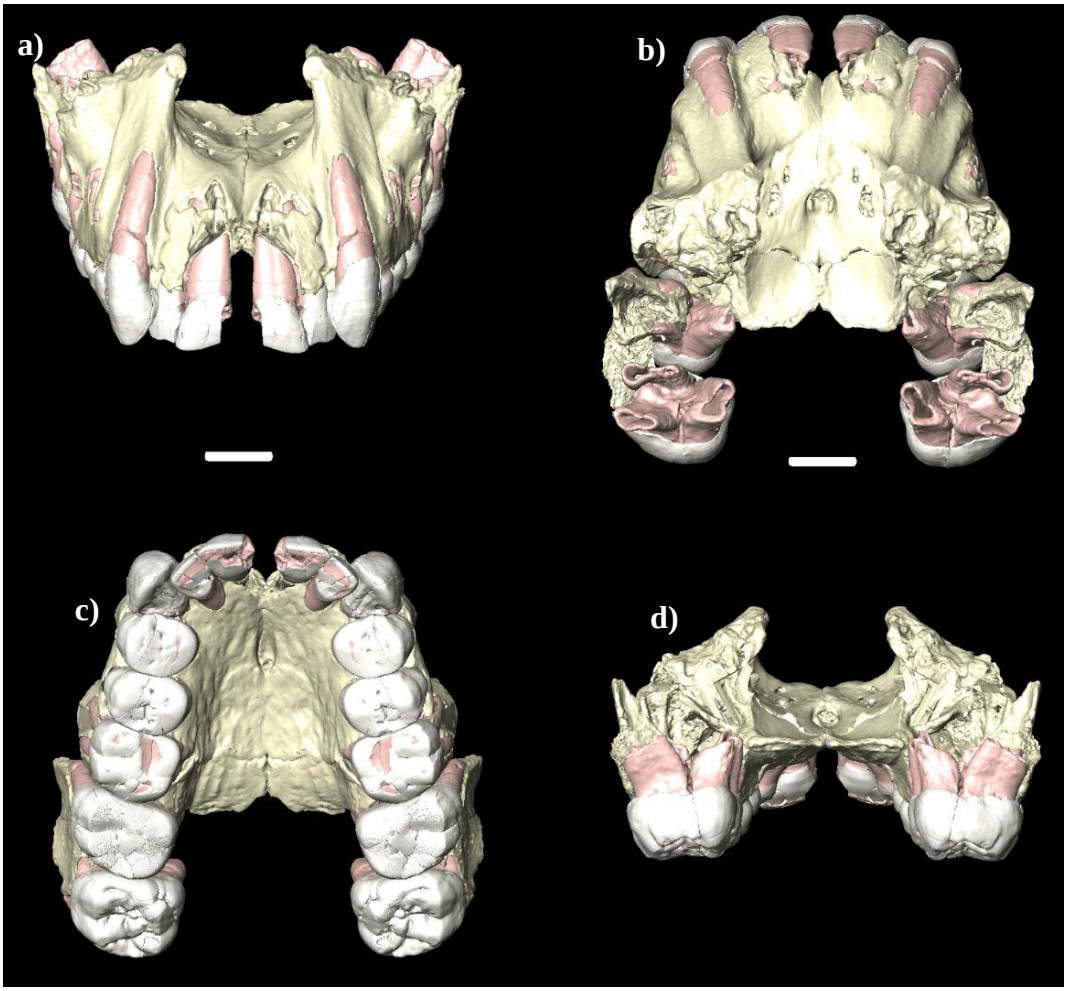

Figure 4.4. Complete virtual reconstruction of the StW 498 maxilla: a) Anterior view; b) Superior view; c) Palatal view; d) Posterior view. Scale bars = 10 mm.

4.1.2. Anatomical descriptions: the maxilla and associated dentition

A complete list of the maxillary dental measurements taken for StW 498 and comparative specimens is provided in Tables 4.1 and 4.2. Palate dimensions are listed in Table 4.3. Due to extreme crushing evident on the right maxilla, some teeth do not preserve roots.

StW 498a, b. Right and left maxillae with near complete dentition; the right lateral incisor was not recovered. The intermaxillary suture is preserved anteriorly on the left maxilla, extending from the prosthion back to the septum between the M^1 and M^2. Anterolaterally, the frontal processes of the maxillae are flat. In anterior view, the canine jugum is strong and prominent, continuing from the large canine root alongside the inferior portion of the nasal aperture, which has rounded margins. The nasoalveolar clivus gently curves from the midline to the canine jugum and slopes smoothly into the floor of the nasal cavity at its superior end. The well-preserved nasal spine is prominent and extends posteriorly far onto the floor of the nasal cavity. Posterior to the nasal spine is the incisive fossa, which appears to be small and rounded. The canine fossa is significantly larger and deeper than the incisive fossa, from which it is separated by the canine jugum. The canine fossa sits lateral to and behind the jugum, just above roots of the P^3. The posterior margin of the jugum curves sharply inferiorly into the fossa.

The palate is long and relatively narrow with inferolaterally sloping walls. Anteriorly, the palate is shallow, but it becomes relatively deep posteriorly. Palate depth at the M^1 to M^2 is 11.5 mm, while palate breadth (i.e., measured as endomolare to endomolare of the second molars) is approximately 30.6 mm. Staphylion is missing, making it impossible to obtain an accurate palate length, however, a gross estimate of palate length is approximately ~60.1 mm (details of how this was estimated are provided in the preceding chapter). The incisive canal is narrow and small and is situated directly opposite the third premolars. The dentition of the left maxilla is less worn than that of the right, but all teeth exhibit varying degrees of wear. Wear on the right and left I^1 to M^1 slopes medially; the anterior dentition is more worn than the posterior dentition. The anterior dentition is crowded and tooth rows are divergent (Figure 4.5). There appear to be

corrugations on the alveolar bone over the roots of the large central incisors, resulting in these roots protruding more than the others. I.e., the incisors are procumbent. There is no diastema between the LC^1 and the lateral incisor; the $LC^1$is displaced (most likely the result of dental crowding) and overlies the I^2 on the labial surface and the P^3 on the buccal surface.

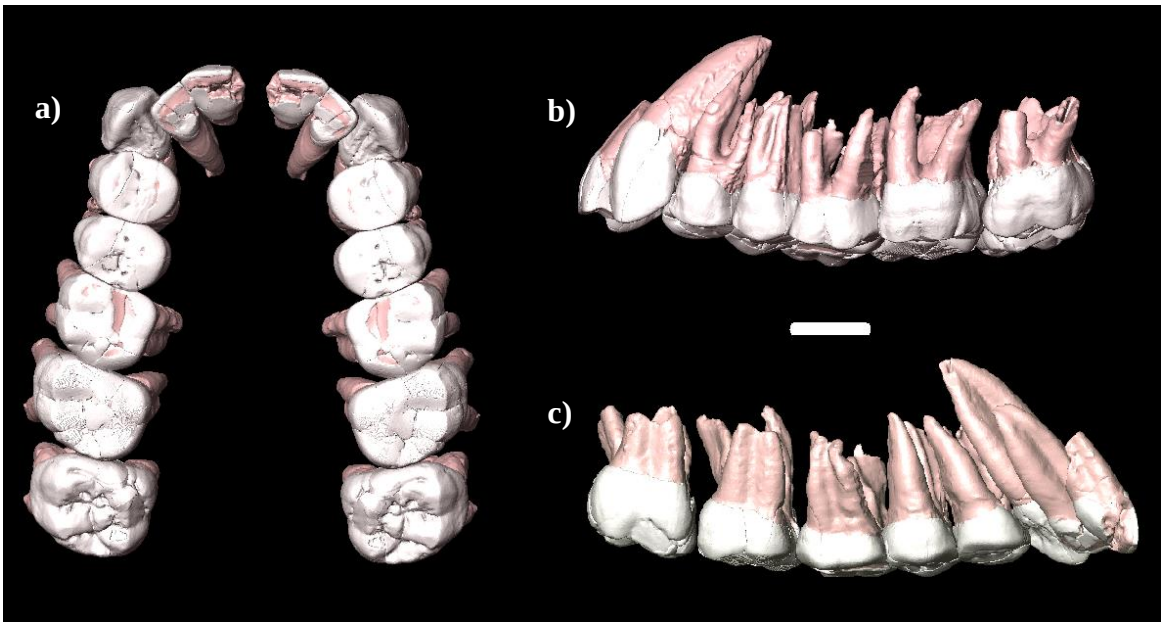

Figure 4.5. Complete virtual reconstruction of the StW 498 maxillary dental arcade: a) Occlusal view; b) Lateral view of the original (non-mirrored) dentition; c) Medial view of the original (non-mirrored) dentition. Scale bar = 10 mm.

LI^1 (Figure 4.6). The crown of the left central incisor is significantly larger than that of the left lateral incisor. The mesial edge of the left central incisor is missing. Wear is heavy and crown height is significantly reduced, as indicated by the large amount of dentine exposure on the incisal facet. The crown appears to distend more mesiodistally than buccolingually, such that on the labial surface the crown has a rectangular outline with a labiolingual breadth of 8.4 mm and a mesiodistal breadth of approximately 8.7 mm. On the labial surface, there is also a slight band of hypoplastic enamel, which extends across the cervical part of the central incisor. There is a moderate distal IPCF. There is no marginal or median ridge present and development of a median lingual ridge is unclear. The root

appears to be long, measuring approximately 19.2 mm, and mesiodistally broad, measuring 7.1 mm just above the cingulum. Anteroposteriorly, the root is 6.7 mm thick and has a shallow longitudinal groove on its mesial surface.

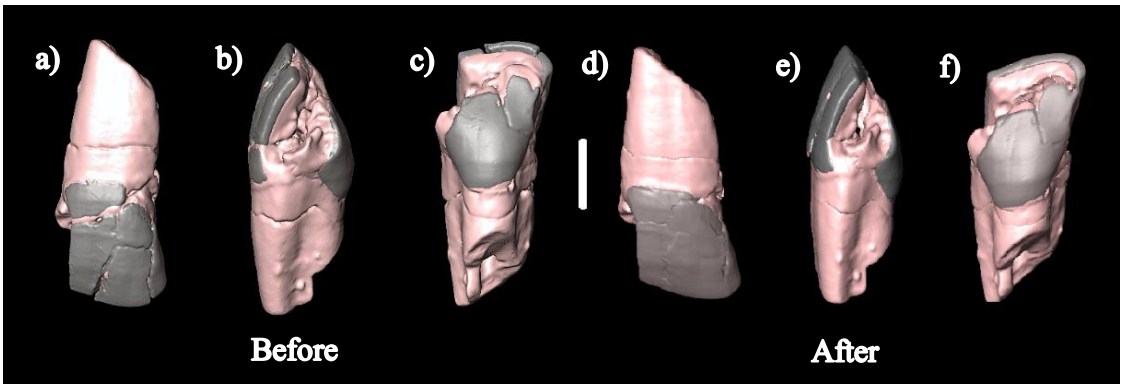

Figure 4.6. Renderings of the left maxillary central incisor (LI^1): a-c) Original condition of the tooth prior to reconstruction; d-f) reconstructed tooth; a, d) Labial view, mesial to left; b, e) Mesial view, labial to left; c, f) Lingual view, mesial to left. The enamel is seen in grey, while the dentine and root are seen in pink. Scale bar = 5 mm.

RI[1] (Figure 4.7). The crown is heavily worn and there is a large amount of dentine exposure on the incisal facet. Like the left central incisor, there is enamel missing on the mesial edge; the absent enamel is restricted to the labial surface. The crown appears to be rectangular in shape and measures 8.3 mm labiolingually, and approximately 8.8 mm mesiodistally. The labial surface presents a faint band of hypoplastic enamel near the incisal edge. In spite of the missing enamel on the label surface, there is evidence of a mesial IPCF. The distal IPCF is flat. There is a slight lingual median ridge, the origin of which cannot presently be determined due to the fragmentary condition of the specimen. Development of a MMR or DMR is unclear. The root is mesiodistally broad measuring 6.9 mm, and thick, measuring 6.6 mm anteroposteriorly. Length of the root cannot be determined due to breakage on the apical half.

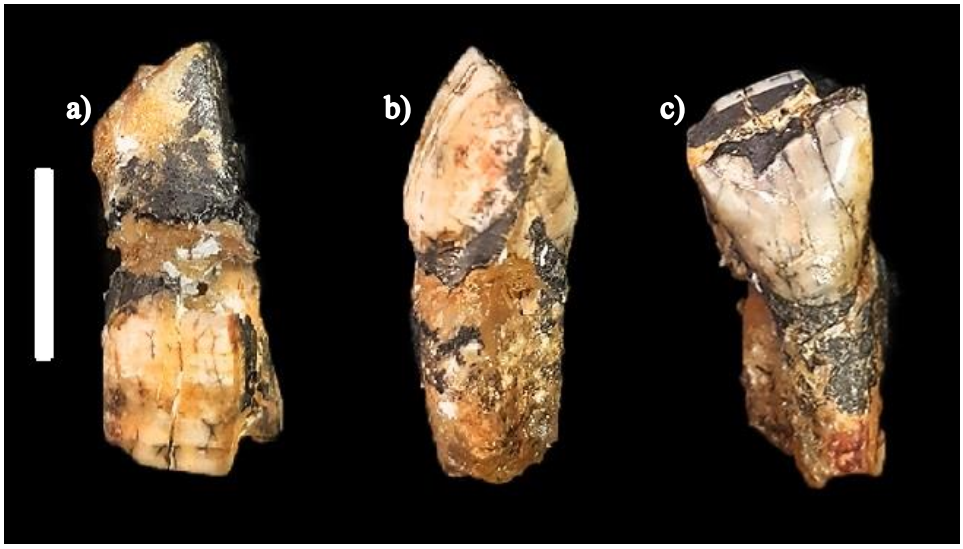

Figure 4.7. Right maxillary central incisor (RI^1): a) Labial view, distal to left; b) Distal view, labial to left; c) Lingual view, distal to left. This tooth was not scanned. Scale bar = 10 mm.

LI[2] (Figure 4.8). The crown of the lateral incisor is much smaller than the central incisor and is moderately worn. The incisal facet is broad and bevels lingually, resulting in exposed dentine that narrows distolingually. The mesial IPCF is considerably large and heavily worn. As a result of the atypical eruption of the L^C, the distal IPCF of the left lateral incisor sits on the labial surface, rather than on the distal surface, creating a small pit-like appearance. The incisal edge gently curves distally. There is no tubercle on the tooth, but rather the presence of

a slight enamel eminence on the cervical lingual surface. There is a slight DMR and MMR present, but no evidence of a lingual median ridge. The crown does not have a square outline, but rather appears rectangular in shape and gently curves distally, with a slight dip on the mesial surface of the incisal edge. The crown measures 7.1 mm labiolingually and 6.2 mm mesiodistally. There is no evidence of enamel hypoplasia. The root is moderately thick, measuring 6.9 mm anteroposteriorly and 18.7 mm long. There is a longitudinal groove on both the mesial and distal surfaces of the root. The root is narrow and markedly curves distally on its apical half.

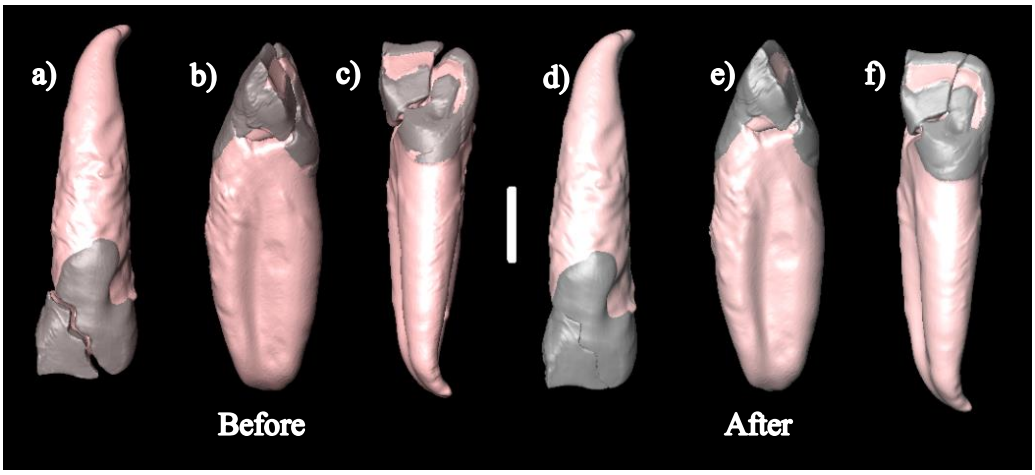

Figure 4.8. Renderings of the left maxillary lateral incisor (LI^2): a-c) Original condition of the tooth prior to reconstruction; d-f) Reconstructed tooth; a, d) Labial view, mesial to left; b, e) Mesial view; labial to left c, f) Lingual view, mesial to left. The enamel is seen in grey, while the dentine and root are seen in pink. Scale bar = 5 mm.

RI^2. Not preserved

LC^1 (Figure 4.9). The LC^1 is large and exhibits very little wear. There is minor enamel polishing on its lingual surface. The mesial and distal IPCFs are moderate, but clear, with the distal IPCF being slightly more blunted than the mesial IPCF. The crown has a somewhat rhomboidal occlusal outline. The canine is extremely large, measuring 11.8 mm labiolingually and 10.8 mm mesiodistally, with a crown height of 14.5 mm. The mesial occlusal edge is shorter and slightly more vertical than the distal occlusal edge, and curves labially toward the cervix. The MMR is slightly developed and longer than the more moderately developed

DMR. There is a strongly developed lingual median ridge that sits slightly mesial to the cingulum and extends from the cingulum until just before the apex. The mesial lingual fossa is elongated and moderately deep, most likely to accommodate its atypical position over the distal surface of the left lateral incisor. The distal lingual fossa is small and relatively deep. There is no evidence of enamel hypoplasia. The root curves distally and is very thick and long, measuring 11.8 mm anteroposteriorly, with a length of 22.9 mm. There are two distinct grooves: one on the mesial surface and one on the distal surface. The grooves run from the base of the cingulum to the distal tip of the root.

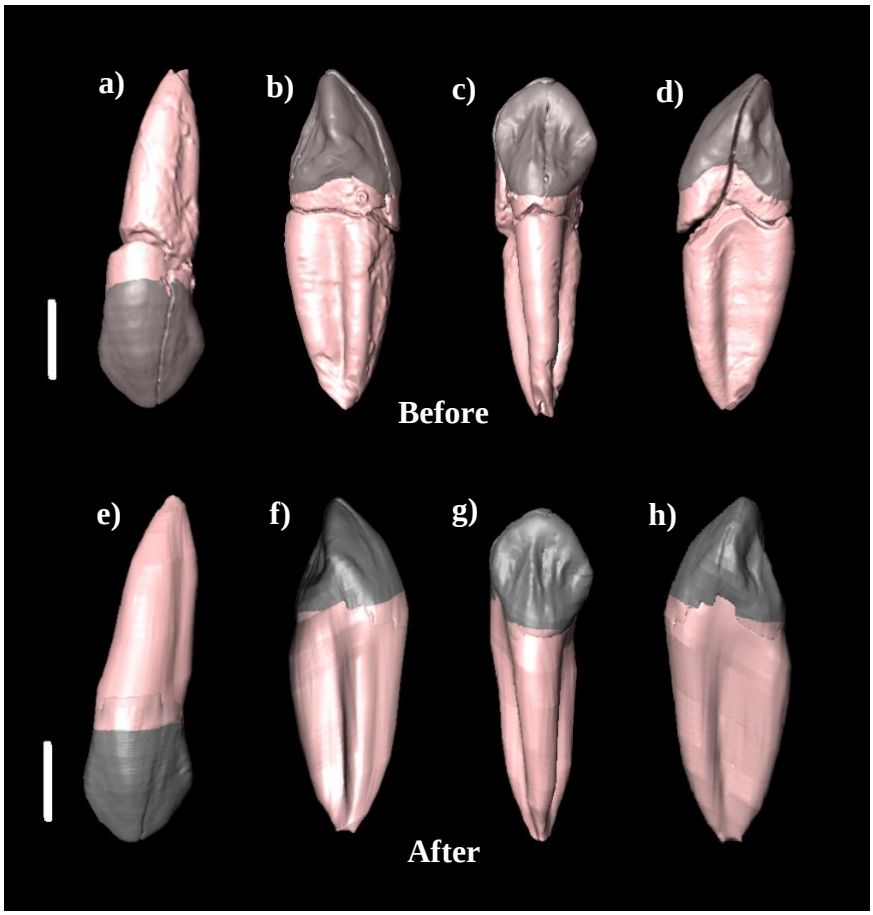

Figure 4.9. Renderings of the left maxillary canine (LC^1): a-d) Original condition of the tooth prior to reconstruction; e-h) Reconstructed tooth; a, e) Labial view, mesial to left; b, f) Distal view, labial to right; c, g) Lingual view, mesial to left; d, h) Mesial view, labial to left. The enamel is seen in grey, while the dentine and root are seen in pink. Scale bars = 10 mm.

RC^1 (Figure 4.10). The RC^1 has moderate wear on the apical half. As a result, there is a strip of dentine exposed on the distal occlusal edge. There is

enamel polish across the entire lingual surface. The mesial and distal IPCFs are distinct and flat. The crown has a broad rhomboidal-like occlusal outline. The canine is large, measuring 11.9 mm labiolingually and 10.5 mm mesiodistally, with a height of 13.3 mm. The distal occlusal edge is longer and more vertical than the mesial occlusal edge, which is slightly rounded. The MMR is short and moderately developed, while development of the DMR is slight. There is a strong lingual median ridge extending from the mesial aspect of the cingulum to just before the apex. There is a deep mesial lingual fossa separating the MMR and lingual median ridge. There appears to be evidence of enamel hypoplasia on the mesiolingual edge, in the proximity of the cingulum. The root is broken, most likely the result of taphonomic processes (e.g., crushing by falling rocks). Nonetheless, the root appears to curve distally and to have been thick and long, measuring 11.7 mm anteroposteriorly, with a length of approximately 22.7 mm. Like the LC^1, there are two distinct grooves present on root, one on the mesial surface, and the other on the distal surface.

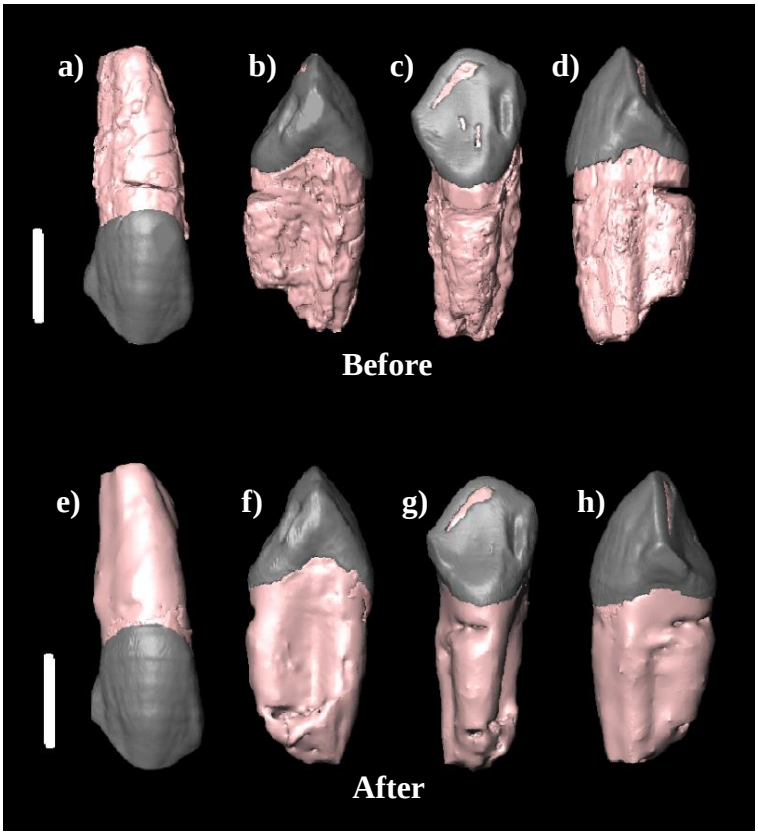

Figure 4.10. Renderings of the right maxillary canine (RC^1): a-d) Original condition of the tooth prior to reconstruction; e-h) Reconstructed tooth; a, e) Labial view, distal to left; b, f) Mesial view, labial to right; c, g) Lingual view, distal to left; d, h) Distal view, labial to left. The enamel is seen in grey, while the dentine and root are seen in pink. Scale bars = 10 mm.

LP^3 (Figure 4.11). Occlusal wear is moderate and lingually sloped. Wear has slightly reduced the size of the protocone and paracone, exposing a small amount of dentine on both cusps. The protocone is situated lingual to the paracone. It appears that the protocone may have been slightly larger than the paracone, although occlusal wear obfuscates a definitive comparison. There is a small mesial IPCF, but there is a large, flat distal IPCF. From occlusal view, the crown is oval shaped, measuring 13.4 mm buccolingually and 9.3 mm mesiodistally. The marginal ridges are thick, with the DMR being slightly sharper than the MMR. There is a shallow mesial depression and a small distal depression on the buccal surface. The anterior fovea is deep and is mesially directed below the paracone. The mesiobuccal edge is slightly shorter than the distobuccal edge, and the cervical enamel line is straight. The lingual surface has no significant attributes, aside from a gentle curve on the distal surface. There is no evidence of enamel hypoplasia. There are three roots present, each of which appears to be short and relatively thin in relation to the crown. The mesiobuccal root is 13.4 mm long, the distobuccal root is 10.6 mm long, and the lingual root measures 12.5 mm in length and is also the thickest with a width of 6.5 mm.

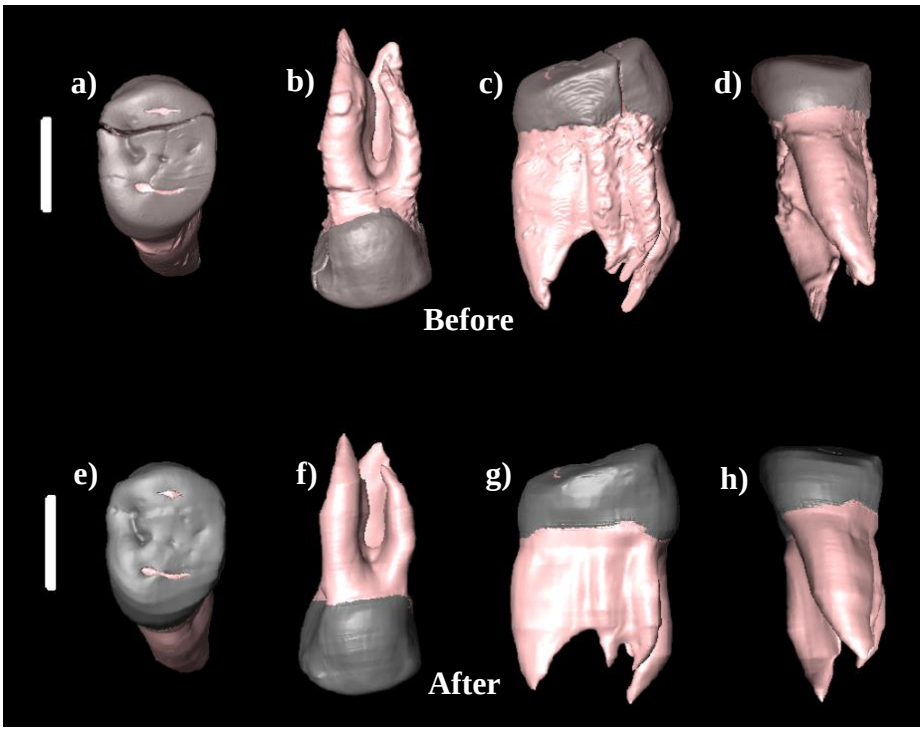

Figure 4.11. Renderings of the left maxillary third premolar (LP^3): a-d) Original condition of the tooth prior to reconstruction; e-h) Reconstructed tooth; a, e) Occlusal view, buccal to top, mesial to left; b, f) Buccal view, mesial to left ; c, g) Distal view, buccal to left; d, h) Lingual view, mesial to left. The enamel is seen in grey, while the dentine and roots are seen in pink. Scale bars = 10 mm.

RP^3 (Figure 4.12). Occlusal wear is lingually sloping and heavier than wear exhibited by the left maxillary P^3. Wear has significantly reduced occlusal details of the protocone and paracone to the point that there is a large amount of dentine exposure on the protocone and a small amount of dentine can be seen on the apex of the paracone. Mesial and distal IPCFs are large and flat. The crown has a similar shape as the left P^3, and is only slightly larger, measuring 13.8 mm buccolingually and 9.4 mm mesiodistally. Both the MMR and DMR are moderately thick. The distobuccal edge is more vertical and slightly shorter than the mesiobuccal edge; the cervical enamel line appears to be convex. There is a deep mesial depression near the bottom on the buccal surface. There is evidence of enamel hypoplasia presenting as several shallow pits on the occlusal surface. There is a shallow depression on the distolingual surface. The roots are completely broken, most likely the result of taphonomic processes.

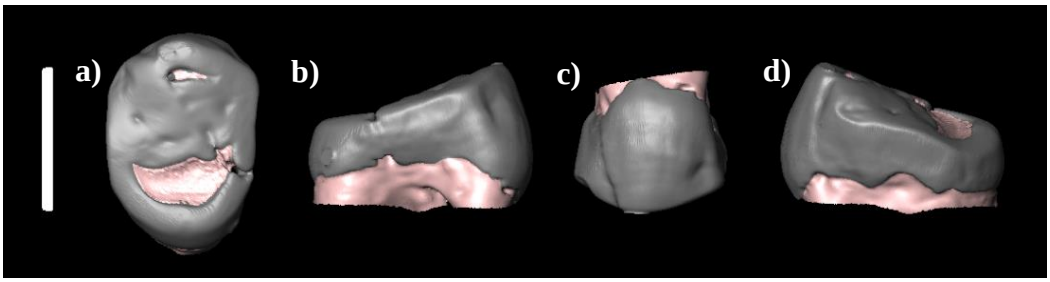

Figure 4.12. Renderings of the right maxillary third premolar (RP^3): a) Occlusal view, buccal to top, distal to left; b) Mesial view, lingual to left; c) Buccal view, distal to left; d) Distal view, buccal to left. Due to the breakage and loss of the apical part of the roots, the roots were smoothed to remove the rough edges for illustrative purposes. The enamel is seen in grey, while the dentine is seen in pink. Scale bar = 10 mm.

LP^4 (Figure 4.13). Occlusal wear is moderate and lingually sloped. Wear has reduced the protocone and paracone to a nearly flat surface, resulting in a very small amount of dentine exposed on the mesial side of the protocone. The protocone is centred lingual to the paracone. The protocone appears to have been slightly larger than the paracone, although it is difficult to determine with certainty due to wear. Both IPCFs are moderate, with the mesial IPCF being flat and the distal IPCF being slightly rounded. The crown has a rectangular occlusal outline, measuring 14.0 mm buccolingually and 9.5 mm mesiodistally. It appears to be rather bulky relative to the left M^1. The mesiobuccal edge is sharp and

vertical, while the distobuccal edge is rounded and vertical. Both edges appear sub-equal in size. The MMR is moderately thick, while the DMR is slightly thinner. The cervical enamel line is convex. The anterior fovea is represented by a small pit that is directed distally by a narrow transverse ridge between the two cusps. The posterior fovea is represented by a transverse fissure with buccal and lingual supplemental grooves that are joined by a deep and narrow median linear fissure. There is a faint enamel ridge running across the buccal surface near the cervix. There are no significant attributes on the lingual surface. There is no evidence of enamel hypoplasia. Two relatively short and thick are apparent. The buccal root measures 12.9 mm in length, and the lingual root 14.5 mm. The lingual root is the thickest and has a width of 7.7 mm. There is a deep, anterior longitudinal groove extending from the apex of the root to the cervix.

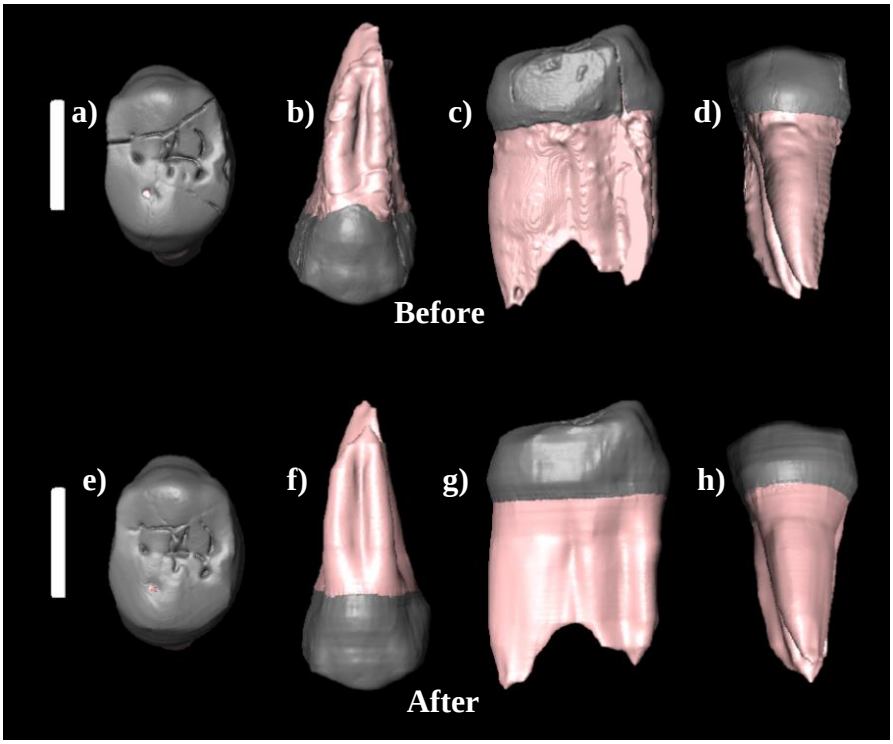

Figure 4.13. Renderings of the left maxillary fourth premolar (LP^4): a-d) Original condition of the tooth prior to reconstruction; e-f) Reconstructed tooth; a, e) Occlusal view, mesial to left, buccal to top; b, f) Buccal view, mesial to left; c, g) Distal view, lingual to left; d, h) Lingual view, mesial to left. The enamel is seen in grey, while the dentine and roots are seen in pink. Scale bars = 10 mm.

RP^4 (Figure 4.14). Occlusal wear is moderate and slopes lingually. Wear has reduced the cusps to a nearly flat surface, resulting in a very small island of

dentine exposure on the protocone. The protocone is situated lingual to the paracone and is more worn than the latter. Mesial and distal IPCFs are distinct and rectangular in shape. The occlusal aspect of the crown is ovo-rectangular, measuring 14.4 mm buccolingually and 10.1 mm mesiodistally; the tooth is relatively wide compared to the molars. Apical wear has somewhat blunted the distobuccal edge, which is slightly shorter than the mesiobuccal edge. Both marginal ridges are thick. The cervical enamel line is marginally convex. The anterior fovea is represented by a relatively broad, shallow fossa. The posterior fovea is distinct and represented by a transverse fissure with supplemental grooves on the buccal and lingual surfaces. There is a faint, longitudinal enamel ridge on the lingual surface. There is no evidence of enamel hypoplasia. The root of the tooth is not preserved, likely destroyed by post-depositional crushing in the deposit.

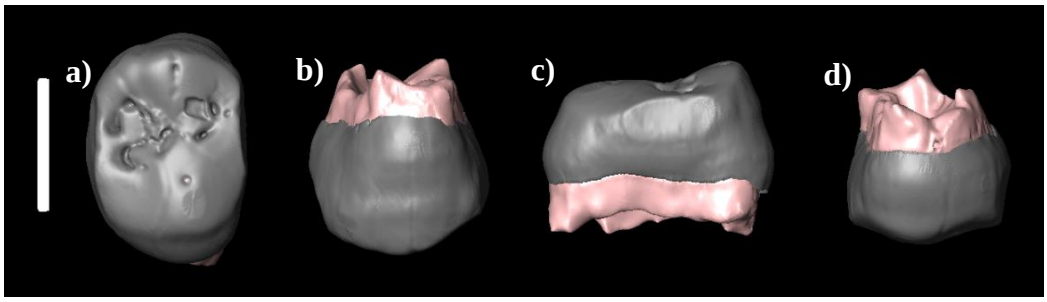

Figure 4.14. Renderings of the right maxillary fourth premolar (RP^4): a) Occlusal view, buccal to top, distal to left; b) Buccal view, distal to left; c) Mesial view, lingual to left; d) Lingual view, distal to left. The enamel is seen in grey, while the dentine is seen in pink. Scale bar = 10 mm.

LM^1 (Figure 4.15). The occlusal surface is heavily worn, which partially obscures differentiation of what seems to have been four, well-developed cusps. Wear has significantly reduced cuspal height, leaving little occlusal detail. There is a large amount of dentine exposure on the protocone and hypocone, while there is a small amount of exposure on the paracone and metacone. There is no evidence of the cusp of Carabelli. The mesial IPCF is marked and slightly concave, while the distal IPCF is moderate. In occlusal view, the crown is square, measuring 14.1 mm buccolingually and 12.4 mm mesiodistally. The size of the MMR is unclear, but the DMR is moderately thick. There are two shallow fossae present on the occlusal surface: the first is located distal to the paracone, and the

second is located distal to the metacone. There is a distinct and concave mesiobuccal groove. The lingual surface is unremarkable. There is no evidence of enamel hypoplasia. There are three relatively short and thick roots apparent and some post-depositional damage. Root lengths are as follows: the mesiobuccal root is 9.3 mm, the distobuccal root is 12.7 mm, and the lingual root is 12.6 mm. The lingual root is the thickest, measuring 9.6 mm wide and has a minor longitudinal groove. The roots appear to have a slight distal bend.

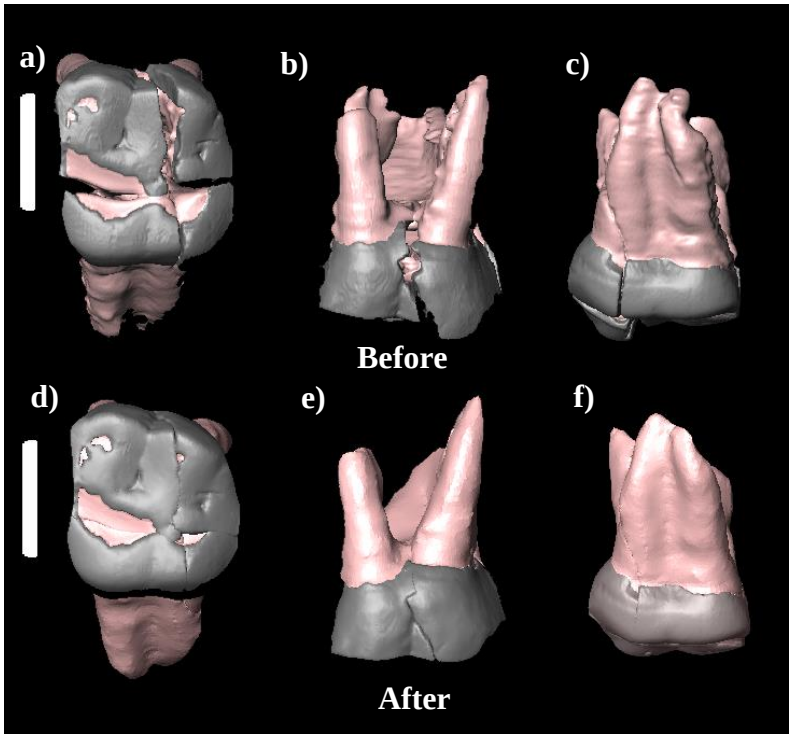

Figure 4.15. Renderings of the left maxillary first molar (LM^1): a-c) Original condition of tooth prior to reconstruction; d-f) Reconstructed tooth; a, d) Occlusal view, buccal to top, mesial to left; b, e) Buccal view, mesial to left; c, f) Lingual view, distal to left. The enamel is seen in grey, while the dentine and roots are seen in pink. Scale bar = 10 mm.

RM^1 (Figure 4.16). The tooth is very similar to the LM^1. Occlusal wear is heavy, with a significant amount of dentine exposure on the protocone and hypocone, a small amount is evident on the paracone, and a very small island of dentine is apparent on the metacone. Wear has destroyed almost all occlusal detail, including any potential evidence of a cusp of Carabelli. The mesial and distal IPCFs are flat. The occlusal surface is more rectangular, and also slightly narrower, than the LM^1. The crown measures 13.9 mm buccolingually and 10.6

mm mesiodistally. Development of a MMR and DMR is unclear. There is a longitudinal fissure with small, deep lingually-directed fissures between the metacone and paracone. A deep, narrow mesiobuccal groove is present. The lingual surface is unremarkable. There is no evidence of enamel hypoplasia. There are three roots present with a slight distal bend. The distobuccal root is relatively short, measuring 11.1 mm, while the mesiobuccal root is also relatively short, measuring 11.3 mm. The lingual root is short, measuring 11.7 mm, and the thickest of the roots with a width of 8.8 mm. The lingual root has a slight longitudinal groove extending from the cervix to its apex.

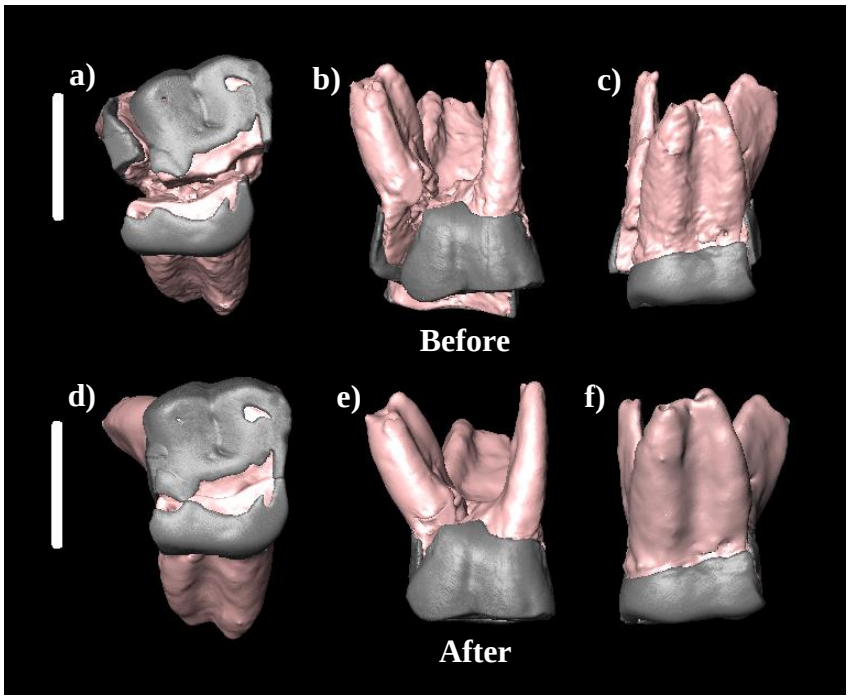

Figure 4.16. Renderings of the right maxillary first molar (RM^1): a-c) Original condition of the tooth prior to reconstruction; d-f) Reconstructed tooth; a, d) Occlusal view, buccal to top, distal to left; b, e) Buccal view, distal to left; c, f) Lingual view, mesial to left. The enamel is seen in grey, while the dentine and roots are seen in pink Scale bar = 10 mm.

LM^2 (Figure 4.17). Occlusal wear is moderate and flatter more than sloped. Wear has reduced the cusps to an almost curved, polished surface, and to the point that there is a small island of dentine exposed on the protocone. All four cusps are present: the protocone is the largest, the paracone and hypocone are sub-equal in size, and the metacone is reduced. A metaconule appears to have been present distobuccally between the metacone and the DMR. Wear has removed any

potential evidence of a cusp of Carabelli. The mesial IPCF is large and rectangular, extending to the edge of the occlusal outline. The distal IPCF, on the other hand, is smaller and more oval, terminating before the occlusal edge. The left M^2 measures 17.9 mm buccolingually and 13.4 mm mesiodistally, making it substantially larger than the left M^1. Marginal ridges are well-developed, with the DMR being moderately thicker than the MMR. The crown has a tapered rectangular occlusal outline. There is a narrow horizontal groove that runs distally below the metacone and metaconule, presenting an irregular enamel surface and resulting in enamel hypoplasia. The buccal surface presents two small pits, just above the buccal groove. The lingual surface has a small, somewhat deep depression near the occlusal edge on the mesial corner of the hypocone. There are three roots present all of which bend distally. The roots are short and relatively thick: the mesiobuccal root is 11.8 mm, the distobuccal root is 11.2 mm, and the lingual root is 11.3 mm, while the latter is also the thickest with a width of 9.4 mm.

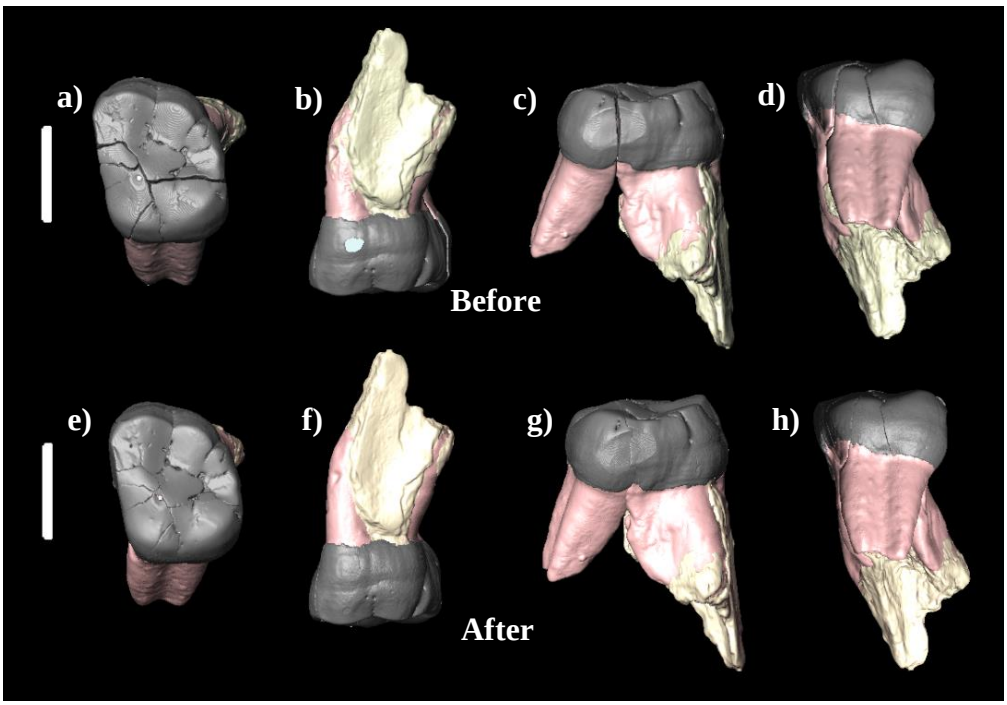

Figure 4.17. Renderings of the left maxillary second molar (LM^2): a-d) Original condition of the tooth prior to reconstruction; e-h) Reconstructed tooth; a, e) Occlusal view, buccal to top, mesial to left; b, f) Buccal view, mesial to left; c, g) Distal view, lingual to left; d, h) Lingual view, mesial to left. The enamel is seen in grey, while the dentine and roots are seen in pink. The yellow represents preserved bone. Scale bar = 10 mm.

RM^2 (Figure 4.18). Occlusal wear is moderate. Wear has significantly reduced the cusps. There appears to have been a small metaconule present, situated distobuccally between the metacone and the DMR. There is no evidence of a Carabelli cusp. The mesial IPCF is large and oval, while the distal IPCF is somewhat smaller. The DMR is well-developed and thicker than the MMR. In occlusal view, the crown is oval, measuring 17.2 mm buccolingually and 12.6 mm mesiodistally. There is a shallow anterior fovea with a buccally-directed longitudinal fissure between the paracone and protocone, and a slight posterior fovea located between the metacone and hypocone. The buccal surface exhibits a faint groove while the lingual surface is unremarkable. There is no evidence of enamel hypoplasia. There are three roots present. There appears to have been a deep, vertical groove on the lingual root, and a shallow groove along the distobuccal root. The roots appear to be short and thick: the mesiobuccal root length is 11.5 mm, the distobuccal root length is 13.0 mm, and the lingual root length is 12.9 mm, while the latter also is the thickest, measuring 9.1 mm.

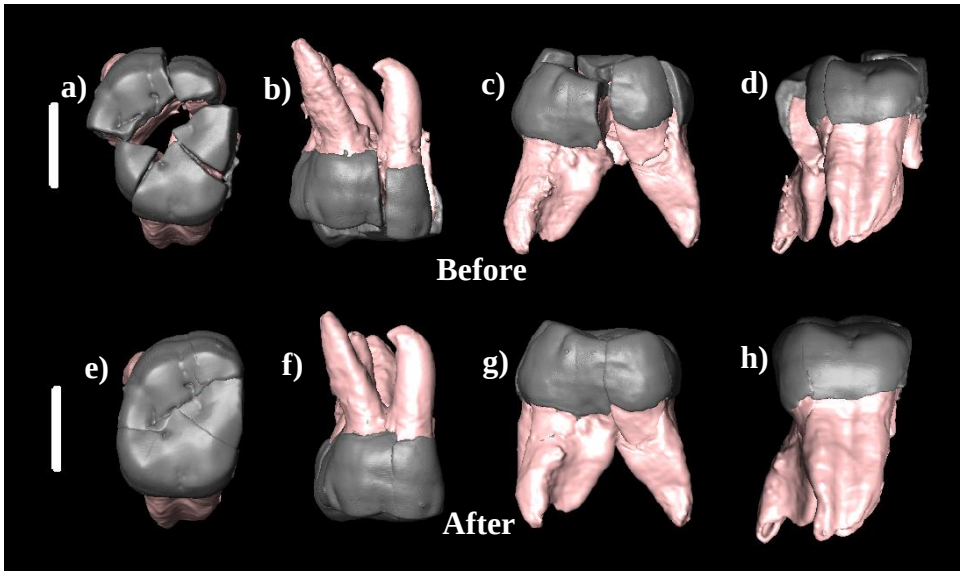

Figure 4.18. Renderings of the right maxillary second molar (RM^2): a-d) Original condition of the tooth prior to reconstruction; e-h) Final reconstruction; a, e) Occlusal view, buccal to top, distal to left; b, f) Buccal view, mesial to left; c, g) Mesial view, buccal to left; d, h) Lingual view, distal to left. The enamel is seen in grey, while the dentine and roots are seen in pink. Scale bar = 10 mm.

LM^3 (Figure 4.19). Wear is minimal and restricted to the tips of the protocone, paracone and metacone. There is no dentine exposure on any cusp. All

four primary cusps are present and well-developed. The cusps are differently sized, with the protocone being the largest, followed by the paracone, metacone, and the hypocone being the smallest. There is a relatively large metaconule located distobuccally between the metacone and hypocone. Supporting this metaconule is the DMR, which is relatively thick and notably low. The MMR is complete, moderately thin, and fairly low. The occlusal surface is ovo-rectangular, measuring 16.9 mm buccolingually and 14.1 mm mesiodistally, which makes it somewhat smaller than the left M^2. The anterior fovea is represented by a thin, buccally-directed fissure that extends distally with a relatively deep groove separating the protocone and paracone. The *crista obliqua* is relatively large and deeply incised. There are two occlusal fissures that distinguish the metaconule; these fissures, particularly the mesiobuccal one, continue onto the buccal surface of the crown. The buccal surface presents a small, shallow depression situated near the occlusal edge of the mesial corner of the paracone; the buccal groove is fairly shallow. The lingual surface presents a Carabelli cusp just below the protocone. The Carabelli cusp is demarcated by a large, horizontal fissure on the lingual surface. There is no evidence of enamel hypoplasia. There are three developmentally incomplete roots, each of which appear to have been short and thick. The mesiobuccal root is the shortest, measuring 9.5 mm in length; the distobuccal root is 9.8 mm in length; the lingual root is 9.9 mm long and is also the thickest of the roots, measuring 9.1 mm.

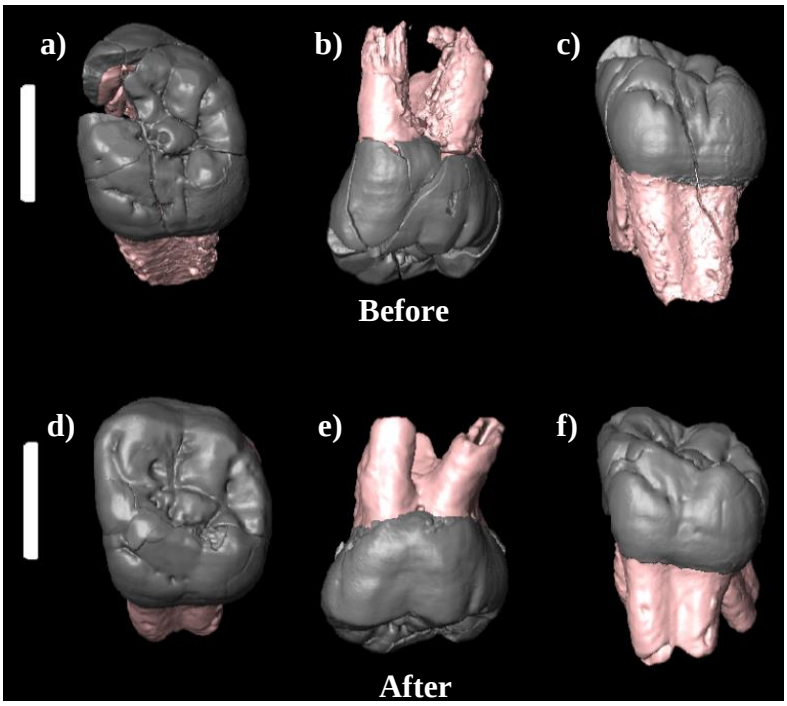

Figure 4.19. Renderings of the left maxillary third molar (LM^3): a-c) Original condition of the tooth prior to reconstruction; d-f) Final reconstruction; a, d) Occlusal view, buccal to top, mesial to left; b, e) Buccal view, mesial to left; c, f Lingual/occlusal view to emphasize important morphological features, mesial to left. The enamel is seen in grey, while the dentine and roots are seen in pink. Scale bars = 10 mm.

RM^3 (Figure 4.20). Wear is moderate and restricted to the tips of the cusps. There is no dentine exposure on any cusp. The protocone is the largest of the cusps, followed in size by the paracone, metacone, and hypocone. There appears to have been a metaconule present, although it has been extensively worn. The MMR is moderately thin and low, while the DMR is slightly thicker and very low. The occlusal surface appears to be more furrowed and has a sub-square occlusal outline. The tooth appears to be large relative to the left M^3, measuring 17.4 mm buccolingually and 15.3 mm mesiodistally. The anterior fovea is represented by a large, deep pit that is continuous with a fairly wide groove that is situated between the apex of the paracone and the MMR. There is a large fissure separating the paracone and metacone. Demarcating the metaconule are two occlusal fissures; the distolingual fissure is slight and ends just before the occlusal edge, while the distobuccal fissure continues onto the buccal surface of the crown, creating a shallow, groove-like depression. The *crista obliqua* is moderately incised. There

are several irregular pits situated toward the centre of the occlusal surface, which represents enamel hypoplasia. The buccal groove is shallow and notably sloped, resulting in a compressed appearance. There is a Carabelli cusp present on the lingual surface that is situated immediately below the protocone. This cusp is delineated by a small, but deep horizontal fissure on the lingual surface. The roots are developmentally incomplete, are short and stocky, and also slightly divergent. The mesiobuccal root is 8.4 mm long. The distobuccal root is the shortest, measuring 8.3 mm. The lingual root is 9.1 mm long and also is the thickest, measuring 9.3 mm.

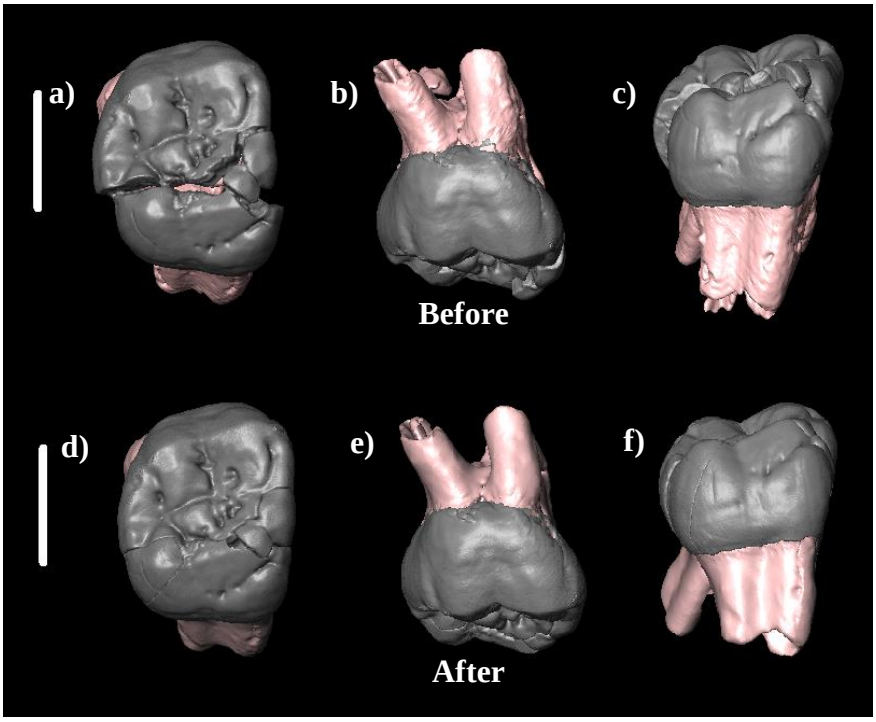

Figure 4.20. Renderings of the right maxillary third molar (RM^3): a-c) Original condition of the tooth prior to reconstruction; d-f) Final reconstruction; a, d) Occlusal view, buccal to top, distal to left; b, e) Buccal view; distal to left; c, f) Lingual/occlusal view to emphasize important morphological features, distal to left. The enamel is seen in grey, while the dentine and roots are seen in pink Scale bars = 10 mm.

4.1.3. Reconstruction of the mandible

The left mandibular corpus (StW 498d) is fairly well-preserved, with the exception of a broken M_1 and an inferiorly orientated crack along the corpus between the M_1 and M_2. The M_2 and M_3 are in situ and retain fairly well-preserved roots. The P_3 and P_4 are isolated (i.e., intact, but post-depositional processes separated from them from the mandible), but well-preserved. Each tooth, and where necessary, bone, was segmented separately in order to facilitate reconstruction (Figure 4.21). The P_4 was missing a fragment of enamel on its distobuccal occlusal surface. In order to compensate for this, the missing enamel was filled-in following the occlusal outline of the crown (see Figure 4.34) in order to allow for an estimated buccolingual measurement.

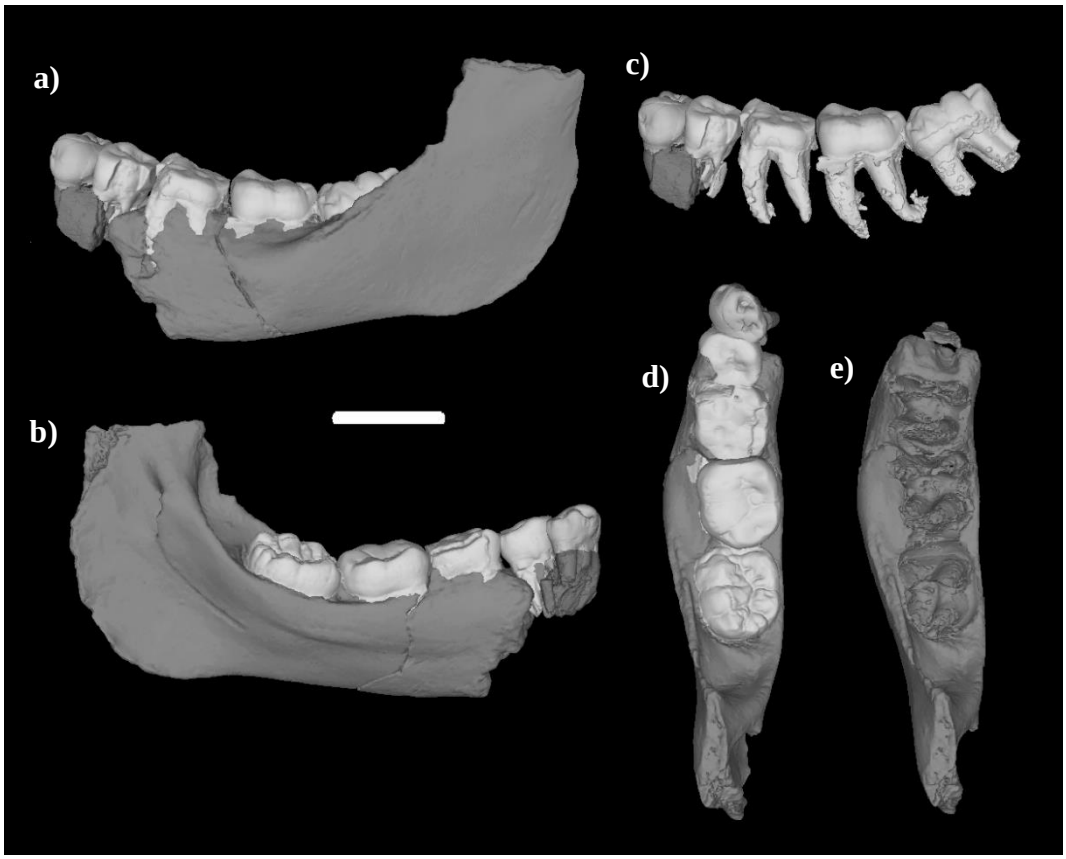

Figure 4.21. Renderings of the left mandible, StW 498d: a) Lateral view; b) Medial view; c) Extracted P_3 to M_3; d) Occlusal view; e) Occlusal view showing alveoli after tooth extractions. Scale bar = 20 mm.

The right mandible (StW 498c) is considerably more fragmented and anatomically displaced. The right incisors are broken and isolated. The right mandible preserves a left central incisor, which has been crushed into the right side, resulting in its displacement, and an isolated left lateral incisor fragment that broke off and separated from its alveolus during deposition. The P_3 and M_3 are virtually undamaged. The M_1 and M_2 are fragmented into several pieces and displaced, with no roots preserved. The left mandibular canine is embedded below the right canine. Upon further examination, the scans revealed a well-preserved mandibular symphysis retaining an exceptionally well-preserved genial fossa (Figure 4.22).

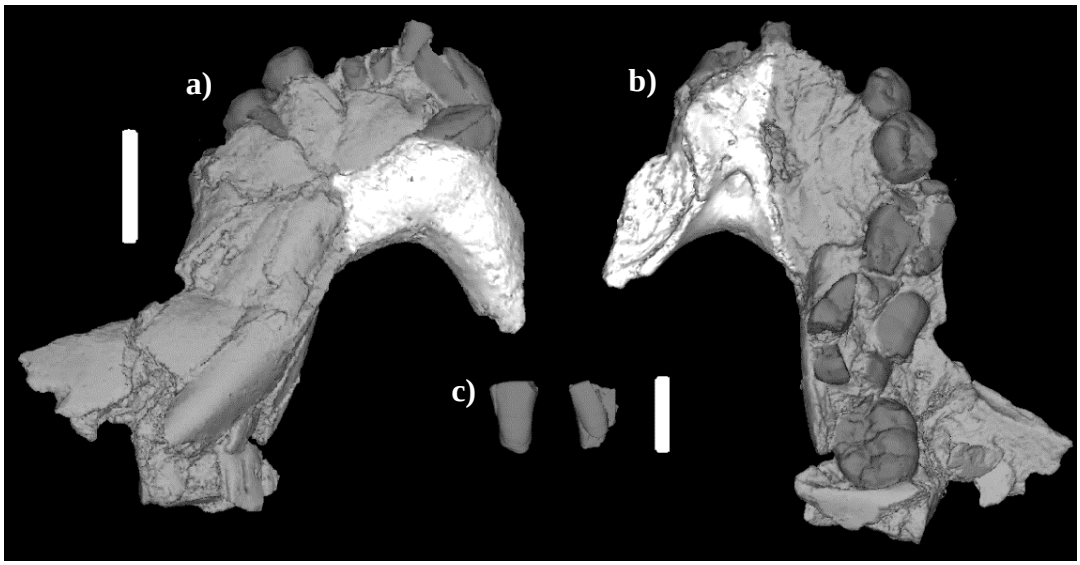

Figure 4.22. Renderings of the right mandible, StW 498c: a) Labial/buccal view; b) Occlusal view; c) Occlusal view of the isolated right I_1 and I_2. Scale bar next to the mandible = 20 mm, and the scale bar next to the isolated incisors = 10 mm.

According to Schwartz and Tattersall (2005: 311), eruption of the right lower canine is anomalous. However, the image data revealed that the position of the left canine was not pathological, but rather the result of taphonomic processes (i.e., post-depositional crushing). On the image data, it is visible that the right canine is badly broken and surrounded by sediment; the bone below the right canine (the symphysis), however, is intact. If the hypothetical malposition of the right canine was due to a pathological process, then it would be reasonably

expected that the bone near the present position of the fragmented tooth also would be severely crushed. It is not (Figure 4.23).

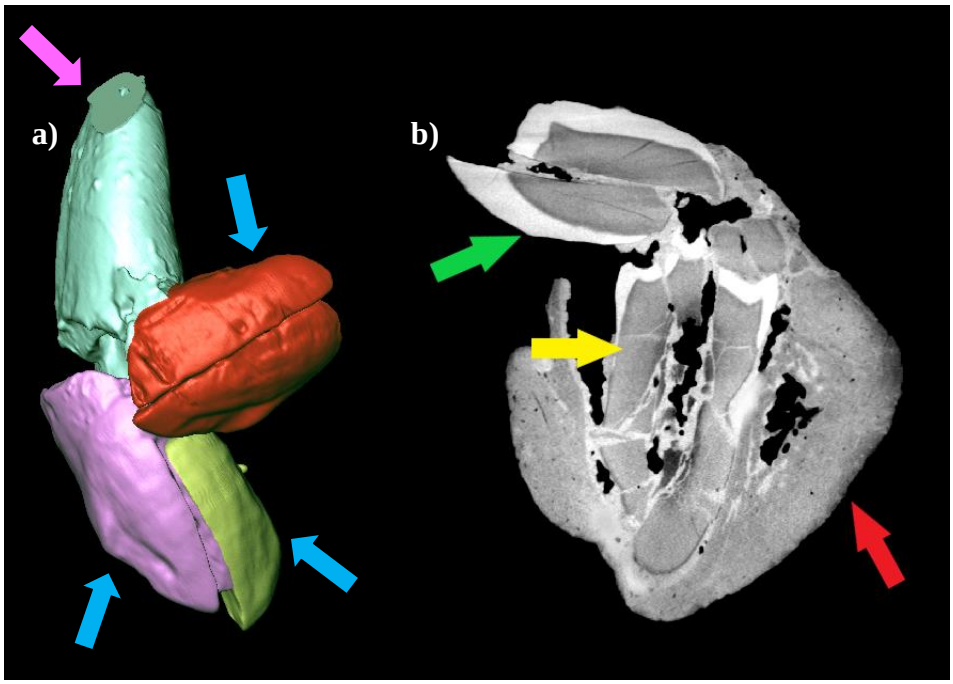

Figure 4.23. The 'problematic' position of the mandibular canines: a) Renderings demonstrating the position of the canines relative to one another. The overlap of the canines is the result of crushing. The blue arrows represent the enamel of the two canines mandibular canines and the pink arrow represents the root of the cracked canine; b) CT image 'slice'. The red arrow (symphysis), green arrow (left canine), and yellow arrow (right canine) indicate structures of interest. The greyscale in this image represents different material 'densities', where bone is darker grey, while the sediment

Knowing that the left canine was in fact originally in its correct position, by examining its interproximal contact facets in conjunction with the contact facets observed on the left mandibular third premolar (see Figure 4.32), allowed me to extract and reconstruct the canine in order to align it into correct anatomical position. Following this, the cracked corpus and the I_1 to M_1 were realigned and placed into anatomical position (Figure 4.24). Upon reconstruction of all the teeth, the left side was mirror imaged and aligned to the original left side. The mandibular corpus was then placed into anatomical position in order to produce a complete reconstruction of the mandible. In order visualise what the complete mandible as it most likely appeared in vivo, its anterior portion was filled by following the direction and shape of the symphysial outline (Figure 4.25).

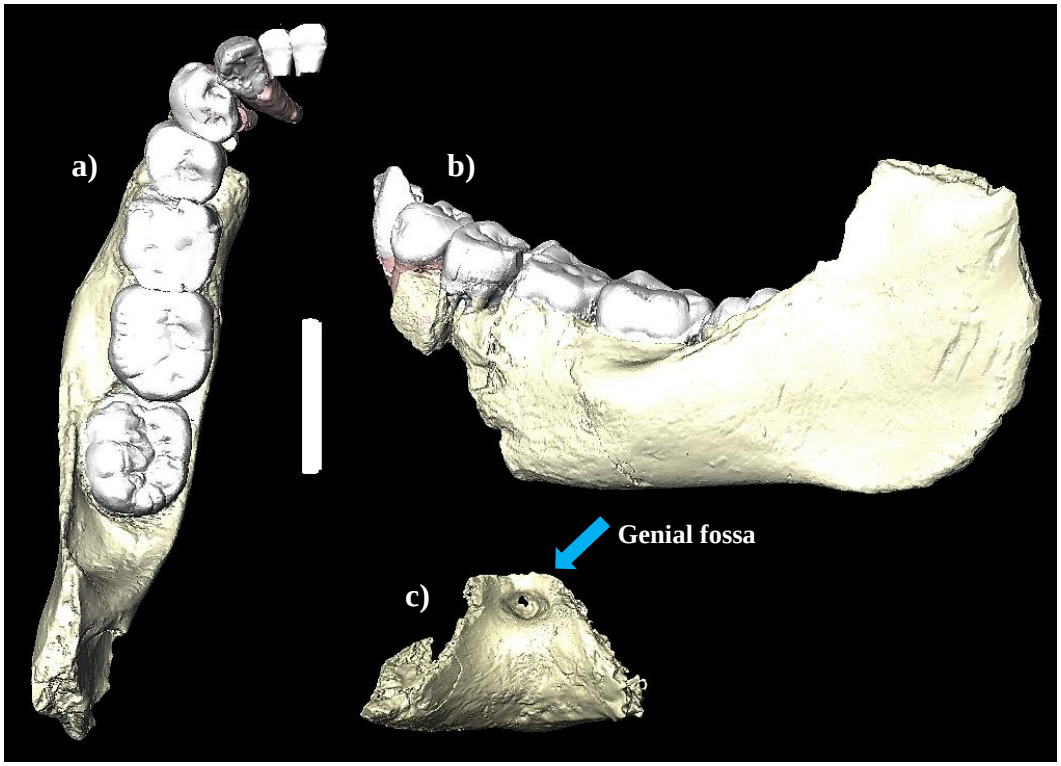

Figure 4.24. Renderings of the reconstructed left mandible, StW 498: a) Occlusal view; b) Lateral view; c) Fragment of the mandibular symphysis displaying the deep genial fossa. Scale bar = 20 mm.

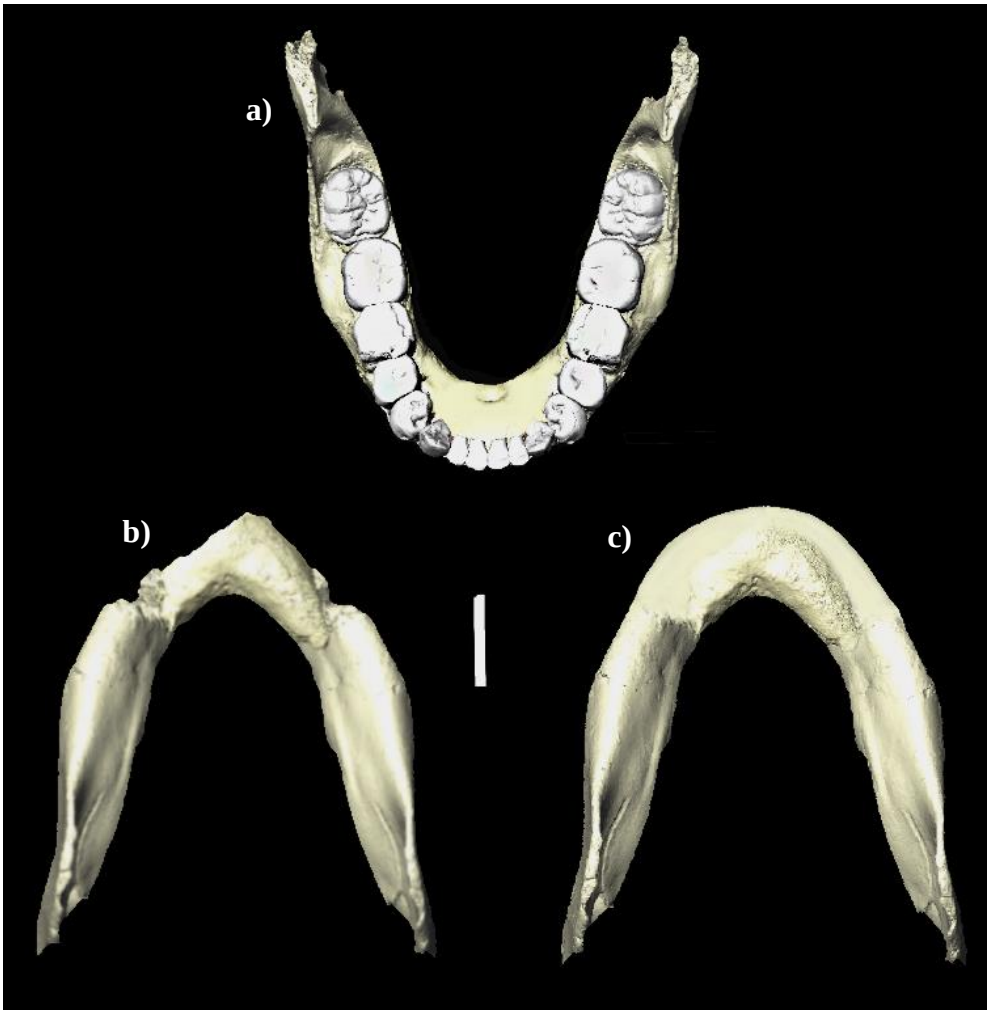

Figure 4.25. Renderings of the StW 498 reconstructed mandible: a) Occlusal view; b, c) inferior view prior to filling-in the symphysis; c) Inferior view of the mandible with the symphysis faintly filled-in to visualise the shape of the mandible. Scale bar = 20 mm.

4.1.4. Anatomical descriptions: the mandible and associated dentition

Mandibular dental measurements taken for StW 498 and comparative specimens are provided in Tables 4.4 and 4.5. Mandibular dimensions are provided in Table 4.6. Due to substantial crushing of the right mandibular corpus, most of the right mandibular dentition does not preserve roots.

StW 498c, d. These specimens include a mostly complete mandible with complete dentition, a mandibular corpus and ramus, which preserves a mandibular symphysis. The posterior teeth are large, and the mandible seems small in comparison. The condyles are missing, along with part of the ascending ramus. Nonetheless, the ramus appears to have been long along the anteroposterior axis and would have likely obscured the third molars in lateral view. The height of the corpus measures 26.4 mm at the left M_1 and the greatest corpus thickness (23.8 mm) occurs between the left M_2 and M_3. Mandibular length from pogonian to gonian is 103.8 mm. The gonial margin is rather thin, and in inferior view is curving slightly medially rather than being straight or everted; there is no evidence of muscle attachment scars on either of its lateral or medial surfaces. There are four parallel marks and other scratch marks on the lateral surface of the left ramus. These marks appear to have resulted from abrasion of sharp rocks within the talus and have been assessed by Pickering, Clarke and Moggi-Cecchi (2004), who conclude that the marks are the result of geological processes.

The left mandibular foramen and lingula are well-defined. The mylohyoid groove is shallow, beginning at the base of the lingula and ending below the M_3. The thick and long mylohyoid line obliquely crosses the medial surface of the body and is positioned relatively low, but slightly above the anterior end of the mylohyoid groove. There is a very large, deep genial fossa retained on the symphysial fragment. In inferior view, the corpus is somewhat V-shape, narrowing anteriorly and becoming progressively wider posteriorly. The corpus seems relatively small and shallow in comparison to the large, bulbous teeth (see Tables 4.4 and 4.6).

The tooth rows diverge posteriorly and there are varying degrees of wear on the occlusal surfaces. Wear is more prominent on the right side than on the left, and more prominent on the left and right I_1 to M_1 than on the left and right M_2 and M_3. Wear is sloped inferomedially. The incisors are small, with the central incisors being slightly larger than the lateral incisors. The canines are significantly larger than the incisors in all aspects. The third molars are not fully erupted, but cuspal morphology is clear and definable.

LI_1 (Figure 4.26). The tooth only preserves the mesiolabial aspect of the crown. The lingual surface is missing, such that it has been replaced by breccia. The tooth crown appears to have been relatively narrow and rectangular in shape. Labiolingual and mesiodistal dimensions cannot be determined due to its incompleteness. There is evidence of enamel hypoplasia on the labial surface, which presents as shallow horizontal bands near the apical and cervical halves of the crown. The root is not preserved; although it cannot be stated with certainty, its form would have likely been narrow near the neck based on the distal narrowing of the crown surface.

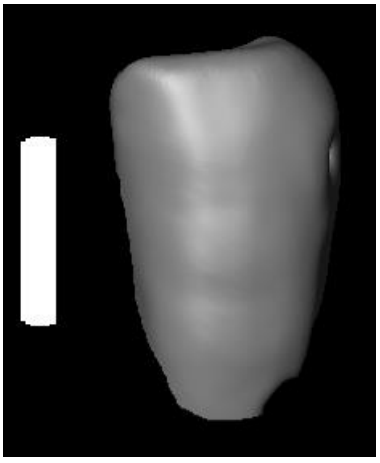

Figure 4.26. Rendering of the left mandibular central incisor (LI_1): Labial view, mesial to left. Scale bar = 5 mm.

RI_1 (Figure 4.27). The crown is moderately worn. There is a fragment of enamel missing near the mesial corner of the incisal edge, resulting in dentine exposure on the mesial surface. There is a large horizontal strip of exposed

dentine on the incisal surface of the crown. The tooth is relatively narrow, measuring approximately 6.4 mm mesiodistally, and relatively broad, measuring 7.8 mm labiolingually. It has a somewhat rectangular shape, with a crown that progressively narrows towards the cervix. There is enamel wear on the lingual surface and no indication of a mesial or distal lingual ridge. There is clear evidence of enamel hypoplasia on the labial surface, as bands near the cervical half and as horizontal grooves near the apex. The labial surface presents wear polish near the incisal edge. The lingual surface is unremarkable. There is no root preserved; although it cannot be stated with certainty, its form would have likely been narrow near the neck based on the distal narrowing of the crown surface, and thick based on its labiolingual breadth.

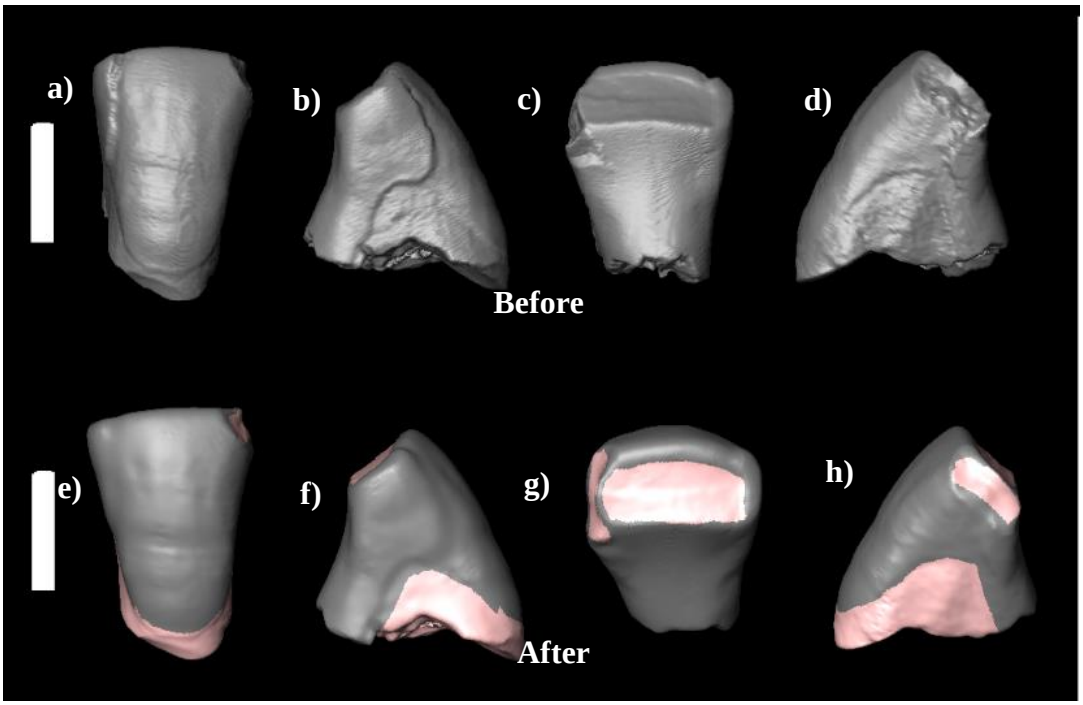

Figure 4.27. Renderings of the right mandibular central incisor (RI_1). Top row: Original condition of the tooth prior to reconstruction. Bottom row: Final reconstruction. a, e) Labial view, distal to left; b, f) Distal view; lingual to left c, g) Lingual view, mesial to left; d, h) Mesial view, labial to left. Enamel is seen in grey, while the dentine can be seen in pink. Scale bars = 5 mm.

LI_2 (Figure 4.28). The crown is moderately worn and damaged, preserving only an incomplete lingual surface. Labiolingual dimensions cannot be determined, however, the crown measures approximately 5.4 mm mesiodistally. There is no evidence of dentine exposure, but there is evidence of a distal marginal lingual ridge; presence of a mesial marginal lingual ridge is unclear. There is no root preserved.



Figure 4.28. Left mandibular lateral incisor (LI_2): Lingual view, distal to left. Scale bar = 5 mm.

RI_2 (Figure 4.29). The crown is moderately worn and damaged, with a large piece of enamel missing from the mesial corner of the labial surface. Wear has produced a broad, horizontal area of exposed dentine on the incisal surface. The outline of the crown appears to be ovo-rectangular in shape and relatively broad, measuring 6.5 mm labiolingually and approximately 5.6 mm mesiodistally. Enamel is polished along the entire lingual surface. The presence of distal or mesial lingual ridges cannot be determined. There is a slight horizontal groove on the labial surface, suggesting evidence of enamel hypoplasia. Enamel is also polished near the incisal edge of the labial surface. The lingual surface is unremarkable. The root is not preserved; although it cannot be stated with

certainty, its form would have likely been narrow near the neck based on the distal narrowing of the crown surface, and thick based on its labiolingual breadth.

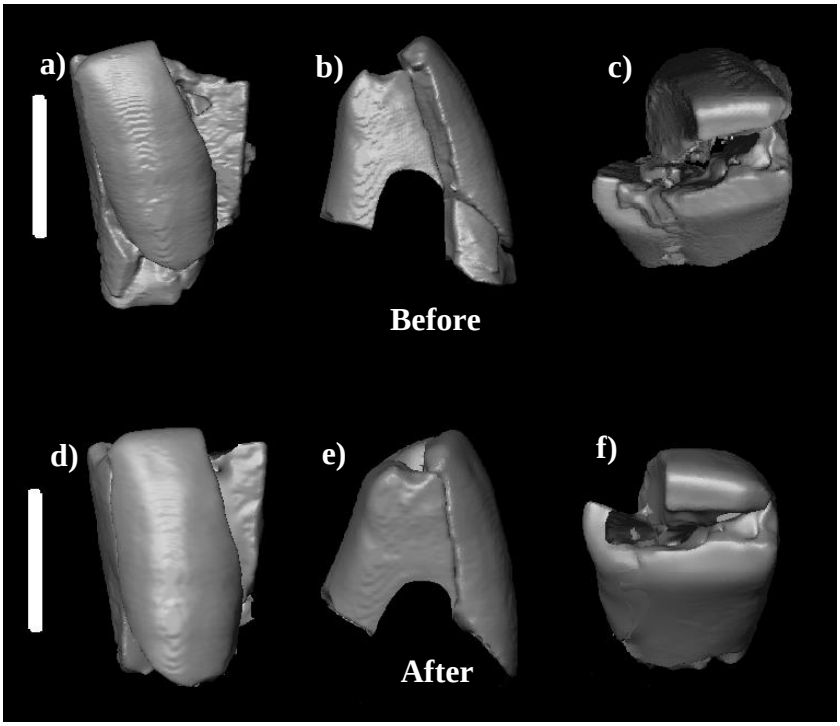

Figure 4.29. Renderings of the right mandibular lateral incisor (RI_2) which consists only of enamel: Top row: Original condition of the tooth prior to reconstruction. Bottom row: Final reconstruction. a, d) Labial view, distal to left; b, e) Mesial view, lingual to left; c, f) Lingual view, mesial to left. Scale bars = 5 mm.

LC_1 (Figure 4.30). The crown is moderately worn. The mesial occlusal edge is rounded and mesiodistally shorter than the sharply angled distal occlusal edge. The mesial and distal IPCFs are slight and somewhat rectangular in shape. The crown measures 10.6 mm mesiodistally and 11.2 mm labiolingually, with a crown height of 16.5 mm. Both the MMR and DMR are slightly developed. There is a short lingual median ridge that is distal to the cingulum. The distal lingual fossa is relatively large and deep, with one fissure that is positioned toward the mesiolabial aspect and one fissure directed toward the mesiolingual aspect. There is a deep, triangular depression on the base of the distal labial edge, which gives the appearance of a stylid; this is clear evidence of enamel hypoplasia (refer to figures ‘g’ and ‘h’ in Figure 4.30). The root is relatively thick, measuring 11.8

mm labiolingually and 7.7 mm mesiodistally, giving it a flattened cross-section; the root is considerably long, measuring 21.9 mm from its apex to the base of the cingulum. The root curves distally and there is a deep distinct groove running vertically along the length of the mesial surface of the root, and a shallower groove along the distal surface.

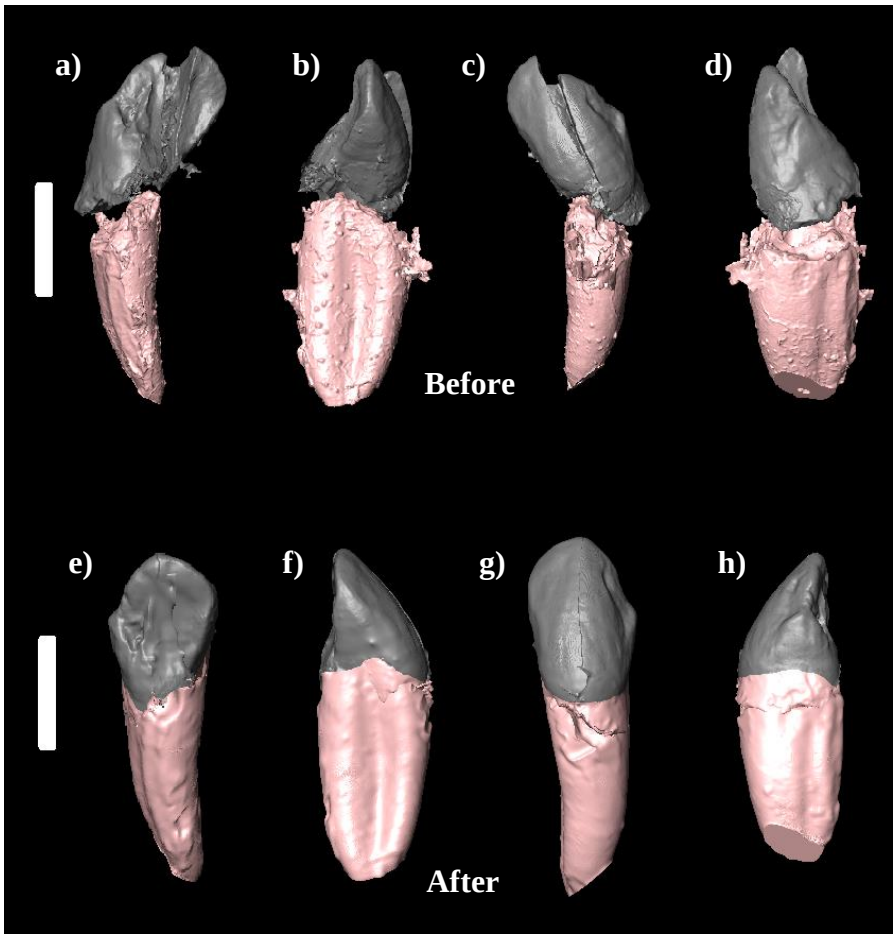

Figure 4.30. Renderings of the left mandibular canine (LC_1). Top row: Original condition of the tooth prior to reconstruction. Bottom row: Final reconstruction. a, e) Lingual view, distal to left; b, f) Mesial view, lingual to left; c, g) Labial view, mesial to left; d, h) Distal view, labial to left. Enamel is seen in grey, while the root can be seen in pink. Scale bars = 10 mm.

RC_1 (Figure 4.31). Lingual wear is moderate, but heavier than that exhibited on the LC_1. The mesial occlusal edge is shorter and mesiodistally rounder than the more angled distal occlusal edge. The mesial IPCF is small and positioned near the apex, while the position of the flat distal IPCF is distinct, positioned at the base of cervix. The crown measures 10.4 mm mesiodistally and 10.8 mm labiolingually, with a crown height of 15.5 mm. The DMR and MMR are slight. The entire crown, both labially and lingually, exhibits significant evidence of enamel hypoplasia. The distal lingual fossa exhibits a deep depression, with irregular, hypoplastic enamel fissures that continue onto the labial surface. Bordering this fossa is a significant median lingual ridge that runs distally from the centre of the surface, ending just before the cervix. The labial surface exhibits a deep, rectangular-shaped depression near the distal labial surface, resulting in a noticeably thin distal occlusal edge. There is a deeply incised groove on the labial surface near the mesial corner and a deep pit just beneath the tip of the mesial labial edge. Two other pits are centrally situated further down the labial surface. As previously stated, all of these irregularities represent a substantial amount of enamel hypoplasia. There is no root preserved, but based on the broad cervical base, it appears as if it would have been quite thick.

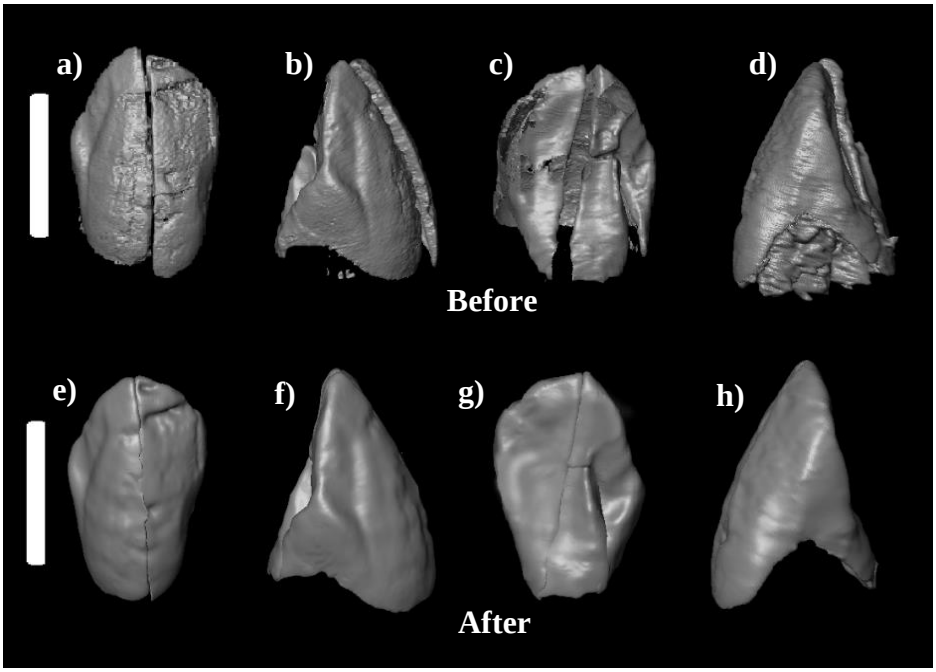

Figure 4.31. Renderings of the right mandibular canine (RC_1) which only consists of enamel. Top row: Original condition of the tooth prior to reconstruction. Bottom row: Final reconstruction. a, e) Lingual view, distal to left; b, f) Distal view, lingual to left; c, g) Lingual view, mesial to left; d, h) Mesial view, labial to left. Scale bars = 10 mm.

LP_3 (Figure 4.32). The crown is slightly worn. There is a small island of dentine exposed on the protoconid. The entire surface exhibits enamel polish and there is significant reduction in the height of the protoconid and metaconid, with the former being considerably bigger than the latter. The mesial IPCF is small, while the distal IPCF is broad and flat. The occlusal outline is somewhat trapezoidal in shape, with a round, swollen buccal surface and a moderately flat lingual face. The distolingual quadrant is sharply angled and oblique. The tooth appears 'chunky' in form, but is not significantly large, measuring 12.4 mm buccolingually and 10.4 mm mesiodistally. The MMR is low and thin, while the DMR is moderately thick and encircles the posterior fovea. The anterior fovea is located mesiolingually and presents as a deep depression. Distal to the anterior fovea is a thick, narrow crest that is situated between the two cusps. The posterior fovea is situated distolingually and is buccolingually deep. There is a Carabelli cusp located on the mesiolingual surface, with a deep triangular shaped depression. The lingual surface a small fissure near the apex of the occlusal margin. There is no evidence of enamel hypoplasia. Lingual and buccal roots are broken and missing inferiorly.

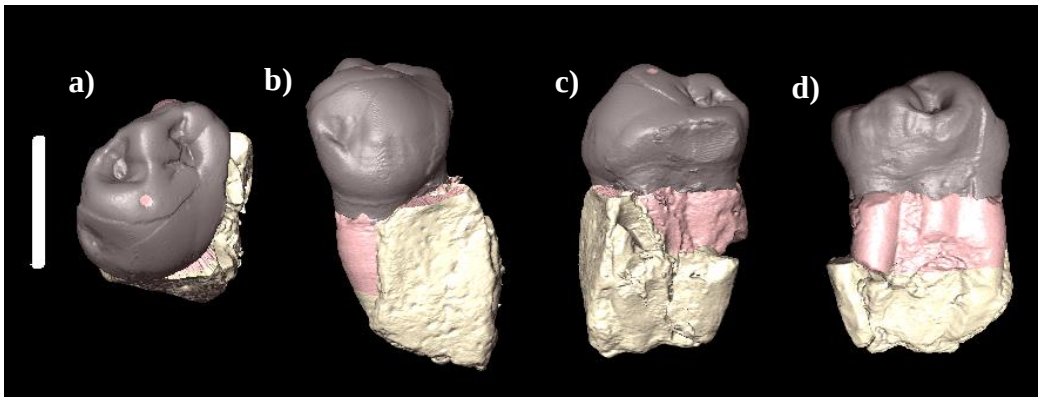

Figure 4.32. Renderings of the left mandibular third premolar (LP_3): a) Occlusal view, mesial to left; b) Buccal view, mesial to left; c) Distal view, labial to left; d) Lingual view, distal to left. The yellow material surrounding part of the root is bone. Enamel is seen in grey, while the root can be seen in pink. The yellow represents preserved bone. Scale bar = 10 mm.

RP$_3$ (Figure 4.33). The crown is moderately worn. There is a somewhat large island of dentine exposed on the protoconid. Enamel polish has significantly reduced cuspal height, but it appears that the protoconid was larger in size than the metaconid. The mesial IPCF is small and rectangular in shape, while the distal IPCF is broad and flat. The occlusal outline is trapezoidal in shape, with a round buccal face, and a moderately flat lingual face. The distolingual quadrant is obliquely sharply angled, although slightly less angled than the LP$_3$. The tooth is 'chunky' in form, measuring 11.4 mm buccolingually and 10.3 mm mesiodistally. The MMR and DMR are thin and low. The anterior and posterior foveae appear to be sub-equal in size, and both are relatively deep. There appears to have been a thick crest present between the two cusps. There is a Carabelli cusp present with a small pit located on the mesiolingual face. There is no evidence of enamel hypoplasia. There are no roots preserved, which were mostly likely broken away due to crushing within the deposit.

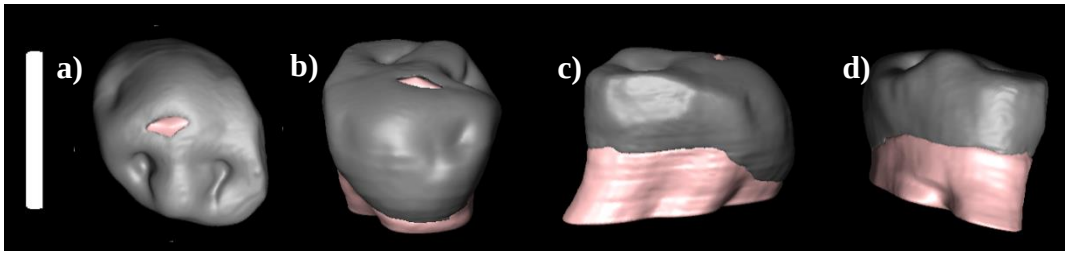

Figure 4.33. Renderings of the right mandibular third premolars (RP$_3$): a) Occlusal view, mesial to left; b) Buccal view, distal to left; c) Distal view, lingual to left; d) Lingual view, mesial to left. Due to the breakage and loss of the apical part of the roots, the roots were smoothed to remove the rough edges for illustrative purposes. Enamel is seen in grey, while the dentine can be seen in pink. Scale bar = 10 mm.

LP$_4$ (Figure 4.34). The crown is moderately worn. Enamel polish has significantly reduced cuspal height and there is a thin, narrow island of dentin exposed on the protoconid. The metaconid is smaller than the protoconid. Both IPCFs are large and flat. The occlusal outline is somewhat square in shape and measures approximately 13.1 mm buccolingually and 11.6 mm mesiodistally. The MMR is moderately thick and borders the anterior fovea. The DMR is low and significantly thicker than the MMR. The anterior fovea is represented by a longitudinal fissure between the two cusps. The posterior fovea is represented as a

shallow, basin-like depression. There is a short, but deep groove on the distobuccal surface originating from the occlusal margin. The lingual surface is unremarkable. The roots are not preserved and broke off from crushing within the deposit.

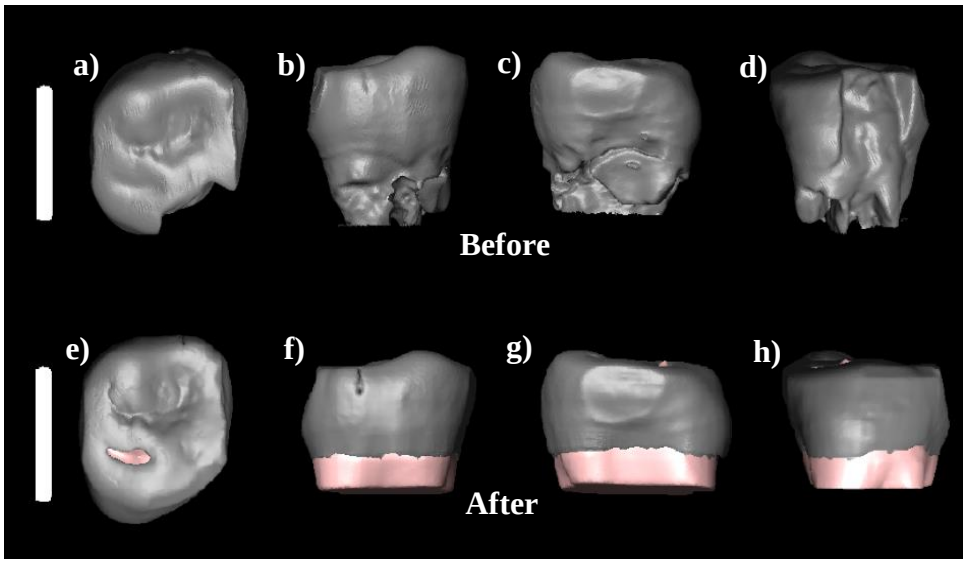

Figure 4.34. Renderings of the left mandibular fourth premolar (LP_4). Top row: Original condition of the tooth prior to reconstruction. Bottom row: Final reconstruction. a, e) Occlusal view, mesial to left; b, f) Lingual view, distal to left; c, g) Mesial view, buccal to left; d, h) Buccal view, mesial to left. Note the missing enamel on the buccal corner of the occlusal surface was filled-in. Due to the breakage and loss of the apical part of the roots, the roots were smoothed to remove the rough edges for illustrative purposes. Enamel is seen in grey, while the dentine can be seen in pink. Scale bars = 10 mm.

RP_4 (Figure 4.35). The crown is moderately worn, but more so than the left P_4. Wear has significantly reduced cuspal relief, especially on the protoconid, which appears to have been larger than the metaconid. There is a large island of dentine present on the protoconid and a small area of dentine exposure found distal to the cusp. The mesial IPCF is large and flat, while the distal IPCF is small. The crown has a square occlusal outline and measures 12.9 mm buccolingually and 12.4 mm mesiodistally. The MMR is slight and low. The DMR is significantly thicker than the MMR. The anterior fovea is represented by a mesiobuccally directed groove and a mesiolingually directed fissure. The posterior fovea is a basin-like depression with small, lingually-directed irregular

fissures, suggesting enamel hypoplasia. The buccal surface exhibits a distally-situated enamel ridge that is demarcated by a shallow depression and several small fissures toward the mesial end. The lingual surface is unremarkable. The root system was destroyed by heavy crushing within the deposit.

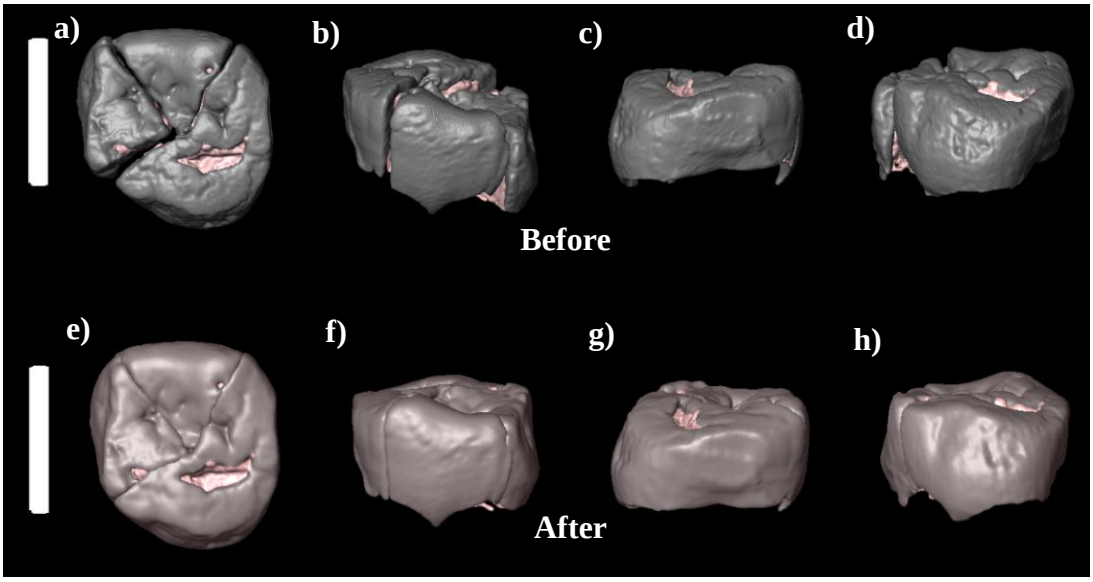

Figure 4.35. Renderings of the right mandibular fourth premolar (RP_4). Top row: Original condition of the tooth prior to reconstruction. Bottom row: Final reconstruction. a, e) Occlusal view, mesial to left; b, f) Lingual view, distal to left; c, g) Mesial view, lingual to left; d, h) Buccal view, distal to left. Enamel is seen in grey, while the dentine can be seen in pink. Scale bars = 10 mm.

LM_1 (Figure 4.36). The crown is heavily worn and there is a missing area of enamel on the mesiobuccal edge. Wear has reduced cuspal height to a nearly flat plane. There is a large area of dentine exposure on the protoconid and hypoconid, a slightly smaller exposure on the hypoconulid, and a transversely orientated area of dentine exposure across the entoconid and metaconid. The protoconid and metaconid appear to have been the largest of the cusps, while the hypoconulid the smallest. Wear has removed any potential evidence of the presence or absence of a protostylid, C6, or C7. The distal ICPF is broad and flat. The mesial IPCF cannot be assessed due to the missing enamel. The occlusal outline has a somewhat square shape, measuring 14.1 mm buccolingually and 15.9 mm mesiodistally. Development of both the MMR and DMR is unclear. The occlusal surface presents a typical Y-5 fissure pattern. The buccal surface exhibits a mesially-directed transverse groove and a short groove at the edge of the occlusal

margin. The lingual surface is unremarkable. There are four roots present, each exhibiting slight damage due to taphonomic processes. There is a slight longitudinal groove on the distobuccal root. The roots appear to be short and thick, with the mesiobuccal root measuring 14.7 mm, the distobuccal root 14.4 mm, and the distolingual root measuring 12.2 mm; the mesiolingual root is broken. Greatest root thickness is 6.3 mm on the distolingual root.

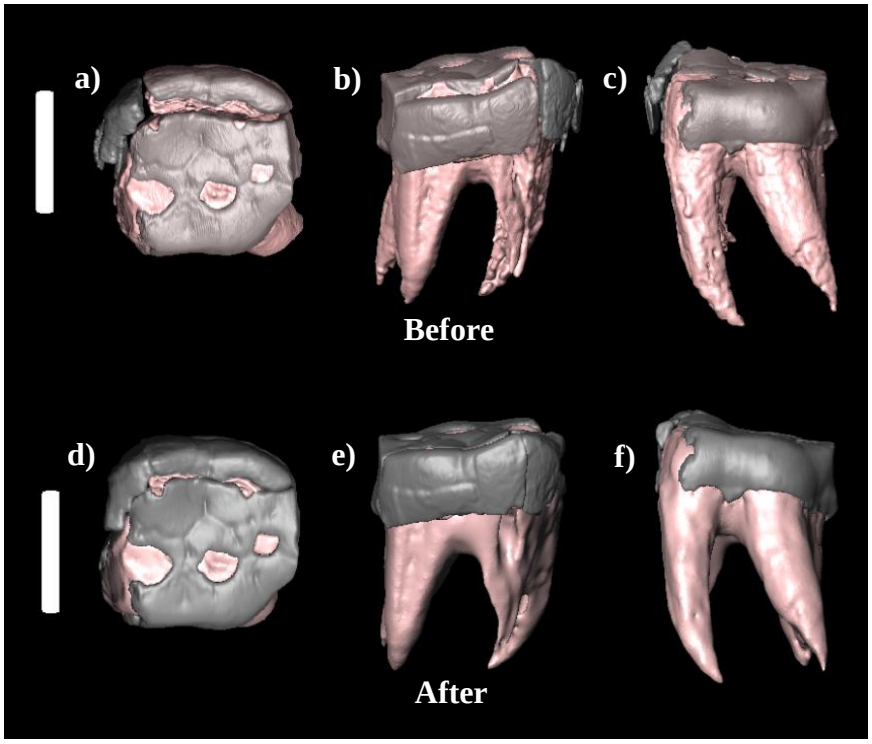

Figure 4.36. Renderings of the left mandibular first molar (LM_1): Top row: Original condition of the tooth prior to reconstruction. Bottom row: Final reconstruction. a, d) Occlusal view, mesial to left; b, e) Lingual view, distal to left; c, f) Buccal view, mesial to left. Enamel is seen in grey, while the dentine can be seen in pink. Scale bars = 10 mm.

RM_1 (Figure 4.37). The crown is heavily worn and damaged, with cervical areas of enamel missing on the distal and lingual faces. Wear has significantly reduced cuspal height to a nearly flat plane and resulted in islands of dentine exposure on the protoconid, hypoconid, and hypoconulid. Wear has obliterated evidence of the presence or absence of a C6 or C7. The mesial IPCF is broad and flat. The occlusal surface has a square shape and measures 14.5 mm buccolingually and 17.2 mm mesiodistally. Development of both the MMR and

DMR is unclear. The occlusal surface demonstrates a Y-fissure pattern. There appears to be evidence of enamel hypoplasia on the occlusal surface of the protoconid, hypoconulid, and metaconid. The root is not preserved.

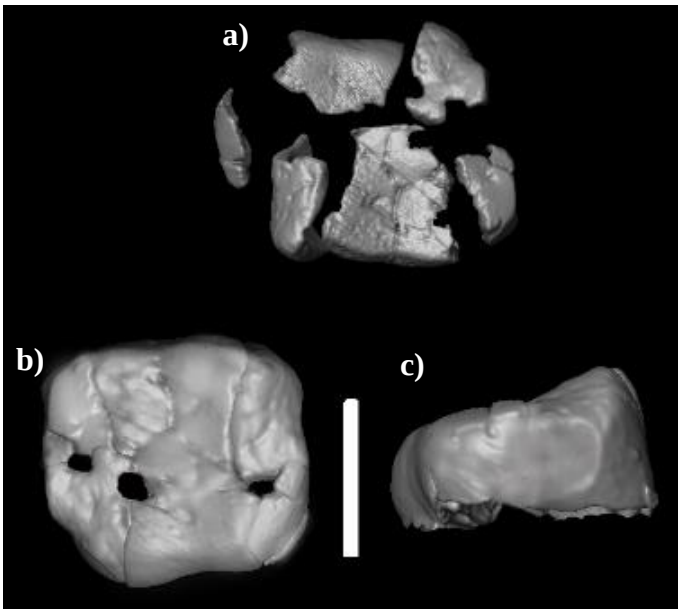

Figure 4.37. Renderings of the right mandibular first molar (RM_1): a) Original condition and position of the tooth prior to reconstruction; b) Occlusal view of the reconstructed RM_1, mesial to left; c) Mesial view of the reconstructed RM_1, lingual to left. Scale bar = 10 mm.

LM_2 (Figure 4.38). The crown is moderately worn. There is enamel polish across the entire surface and a very small island of dentine is present on the protoconid. All five primary cusps are present, with the protoconid being the largest in size, followed by the metaconid and hypoconid, while the hypoconulid and entoconid appear to be equal in size at the low end of the range. There is no development of either a C6, C7, or a protostylid. The mesial IPCF is large and flat, while the distal IPCF is small and slightly rounded. The crown has an ovo-rectangular occlusal outline and is considerably larger than the LM_1, measuring 15.7 mm buccolingually and 17.3 mm mesiodistally. There is a distinct, symmetrical Y-5 fissure pattern. The distobuccal and distolingual fissures are present as deep, narrow grooves. Although the MMR is worn, it appears to have been relatively thick. The DMR is well-developed and moderately thick. The

anterior fovea is small and connects with a vertical fissure between the protoconid and metaconid. Between the triangular-shaped hypoconulid and entoconid there is a large talonid basin that bears a small cusplet. Distal to this basin is the posterior fovea, which presents as a small depression. There is a small, distally-directed triangular depression near the occlusal edge of the hypoconulid. There are several small pits that extend across the buccal surface of the protoconid and hypoconid, representing enamel defects. The lingual surface is unremarkable. There are two fused roots, which curve distally. The mesiolingual root surface measures 14.7 mm in length, the distolingual root surface measures 13.8 mm, the mesiobuccal root surface measures 14.1 mm, and the distobuccal root surface measures 15.5 mm. The thickest of the roots is the mesiolingual root, measuring 8.4 mm.

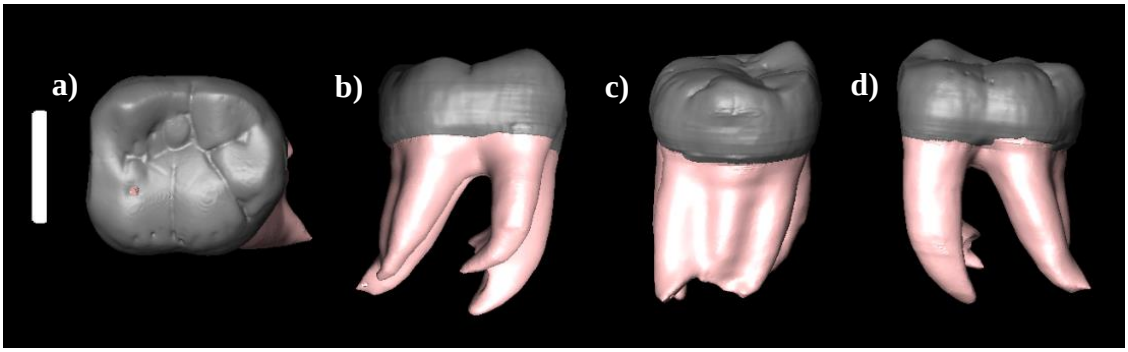

Figure 4.38. Renderings of the left mandibular second molar (LM_2): a) Occlusal view, mesial to left; b) Lingual view, distal to left; c) Distal view, lingual to left; d) Buccal view, mesial to left. Enamel is seen in grey, while the dentine and roots are seen in pink. Scale bar = 10 mm.

RM_2 (Figure 4.39). The crown is moderately worn and damaged. Cervical enamel is missing from the mesial surface. Wear has significantly reduced cuspal height, but there is no dentine exposure. All five primary cusps are present. The protoconid is the largest in size, followed by the metaconid, hypoconid, the hypoconulid, while the entoconid is the smallest. There is no evidence of a C6 or C7, but this is difficult to assess with certainty because of wear. The distal IPCF is somewhat round and flat; the mesial IPCF is high (and situated quite buccally) and somewhat square and flat. The occlusal surface has a somewhat square, distally round shape. The crown measures 15.7 mm buccolingually and 17.1 mm mesiodistally. The MMR is worn, but appears to have been thin; the DMR is

prominent. The occlusal surface presents a Y-5 fissure pattern and exhibits signs of enamel hypoplasia. The distobuccal fissure is a narrow groove which is split by a ridge of enamel that extends over on to the buccal surface. The anterior fovea is a narrow groove that separates the protoconid and entoconid, while the posterior fovea is a shallow pit. There is a small groove between the protoconid and hypoconid that extends over on to the lingual face, just below the apex, resulting in a slight triangular depression on the lingual surface.

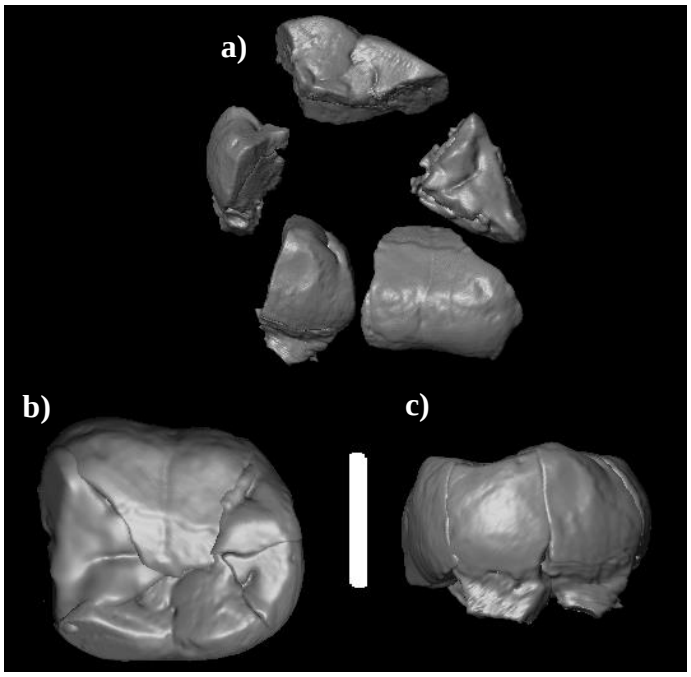

Figure 4.39. Renderings of the right mandibular second molar (RM_2): a) Original condition and position of the tooth prior to reconstruction; b) Occlusal view of the reconstructed RM_2, mesial to left; c) Distal view, lingual to left. Scale bar = 10 mm.

LM_3 (Figure 4.40). The occlusal surface exhibits very little wear, with the wear that is evident being restricted to the apices of all five principle cusps. All the cusps are well-developed and arranged in an asymmetrical Y-5 pattern. The metaconid is the largest, followed by the entoconid and hypoconid, while the protoconid and hypoconulid are sub-equal in size. There is a large C6 present, but no evidence of a C7. A protostylid appears on the mesiobuccal quadrant of the protoconid. The mesial IPCF is large and somewhat concave. The occlusal outline

is oval in shape and the tooth is only slightly larger than the LM_2, measuring 15.9 mm buccolingually and 18.5 mm mesiodistally. The mesiobuccal groove is shallow, while the distobuccal groove is relatively deep. The MMR is thin and positioned relatively low. There is no evidence of a DMR. The anterior fovea is a transverse fissure and the posterior fovea is absent. The apex of the metaconid is a thin, transverse enamel ridge, which extends to the mesial side on the apex of the protoconid. There are two small, distally-directed cusplets between the metaconid and entoconid. There is a small pit present near the occlusal edge on the entoconid. There is a relatively deep groove on the apex of the C6, resulting in a cleft-like appearance. There is deep groove on the apex of the hypoconulid. The buccal surface presents two triangular-shaped depressions, one on the protoconid and one on the hypoconulid. There are two fused roots that curve distally and are relatively short and thick. The mesiolingual root surface measures 9.1 mm in length, the distolingual root surface measures 8.8 mm, the mesiobuccal root surface measures 8.9 mm, and the distobuccal root surface measures 8.7 mm in length. The thickest root is the distobuccal root, measuring 7.7 mm.

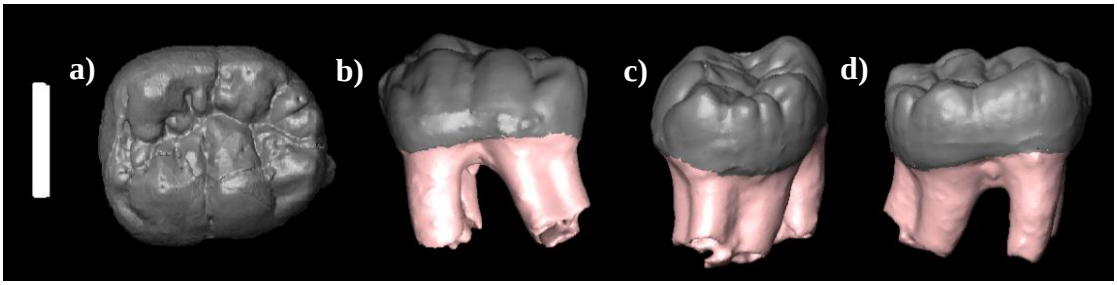

Figure 4.40. Renderings of the left mandibular third molar (LM_3): a) Occlusal view, mesial to left; b) Buccal view, mesial to left; c) Distal view, lingual to left; d) Lingual view, distal to left. Enamel is seen in grey, while the roots can be seen in pink. Scale bar = 10 mm.

RM_3 (Figure 4.41). The crown exhibits very little wear, with the wear that is evident being restricted to the apices of the five primary cusps. All the cusps are well developed and arranged in a classic, asymmetrical Y-5 pattern. The metaconid is the largest in size, followed by the entoconid and protoconid, while the hypoconid and hypoconulid are sub-equal in size. There is a small C6 present, but no C7. There is a relatively sharp, protruding protostylid present on the mesiobuccal aspect of the protoconid. The mesial IPCF is broad and concave and

is positioned relatively high, near the occlusal edge. The occlusal outline has an oval shape, and measures 15.6 mm buccolingually and 18.1 mm mesiodistally. The mesiobuccal and distobuccal grooves are narrow and deep and continue on the buccal surface of the crown. There is no evidence of either the MMR or DMR. The anterior fovea is represented by a relatively narrow, but deep vertical fissure, while there is no posterior fovea. The apex of the metaconid is a thin, transverse enamel ridge, which extends to the mesial side on the apex of the protoconid. There is an irregular depression with fissures on the entoconid that extends over onto the buccolingual face, suggesting enamel hypoplasia. There is small pit on the apex of the C6, and a large, wedge-shaped depression demarcating the hypoconulid. There is a deep, lingually-directed pit on the hypoconid. There are two small enamel ridges cutting across the mesiobuccal groove, connecting the hypoconid and protoconid. The buccal surface presents two deep triangular-shaped depressions situated on either side of the hypoconid. The lingual surface presents a distally-directed Y-shaped fissure. Most of the roots are missing, probably because it was destroyed by post-depositional crushing. Although it cannot be stated with certainty, it is reasonable to assume that the roots were short and relatively thick, like those of the left M_3.

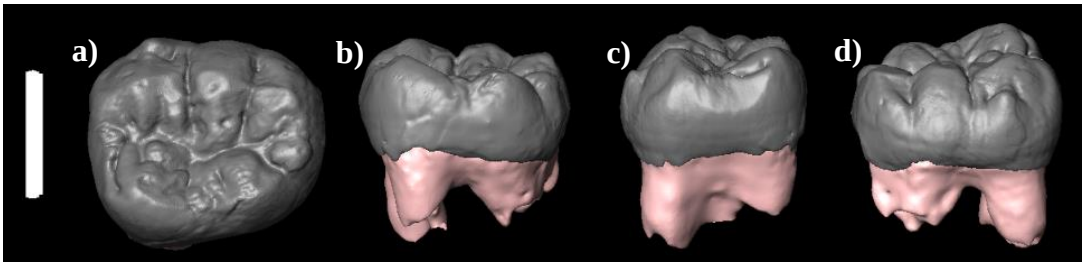

Figure 4.41. Renderings of the right mandibular third molar (RM_3): a) Occlusal view, distal to left; b) Lingual view, mesial to left; c) Mesial view, lingual to left; d) Buccal view, distal to left. Enamel is seen in grey, while the partial roots can be seen in pink. Scale bar = 10 mm.

4.1.5. The complete reconstruction of StW 498

Once the maxilla and mandible were fully reconstructed, they were aligned relative to one another. Correct alignment was determined by occluding the maxillary and mandibular dentition. In this manner, a complete reconstruction of the lower face of StW 498 was produced (Figure 4.42 and 4.43).

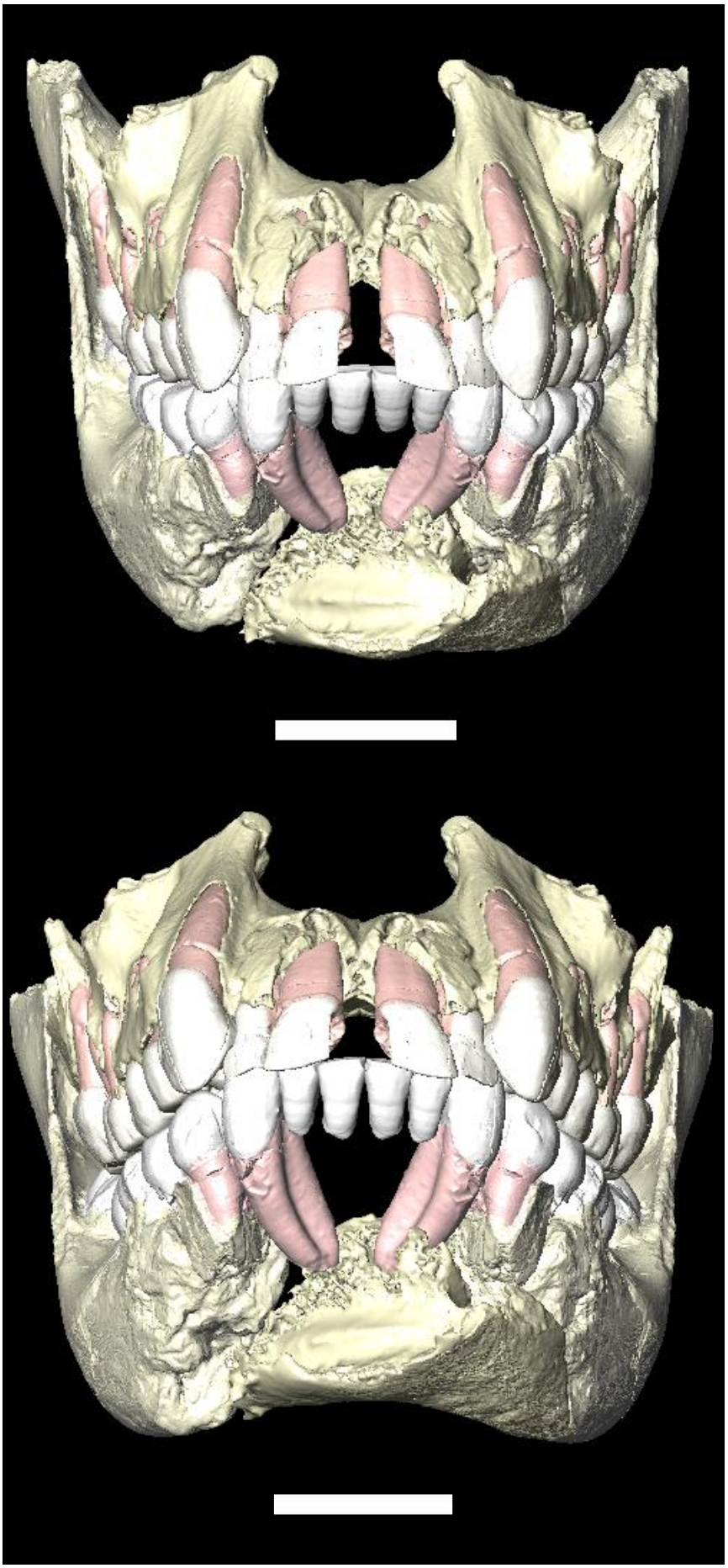

Figure 4.42. Renderings of the reconstructed lower face of StW 498. Top: Anterior view. Bottom: Anterior view with the maxilla tilted slightly backwards. Note the large, mesiodistally broad mandibular canine roots (in pink) and distinct mesial grooves; there are no incisor roots preserved. Scale bar = 20 mm.

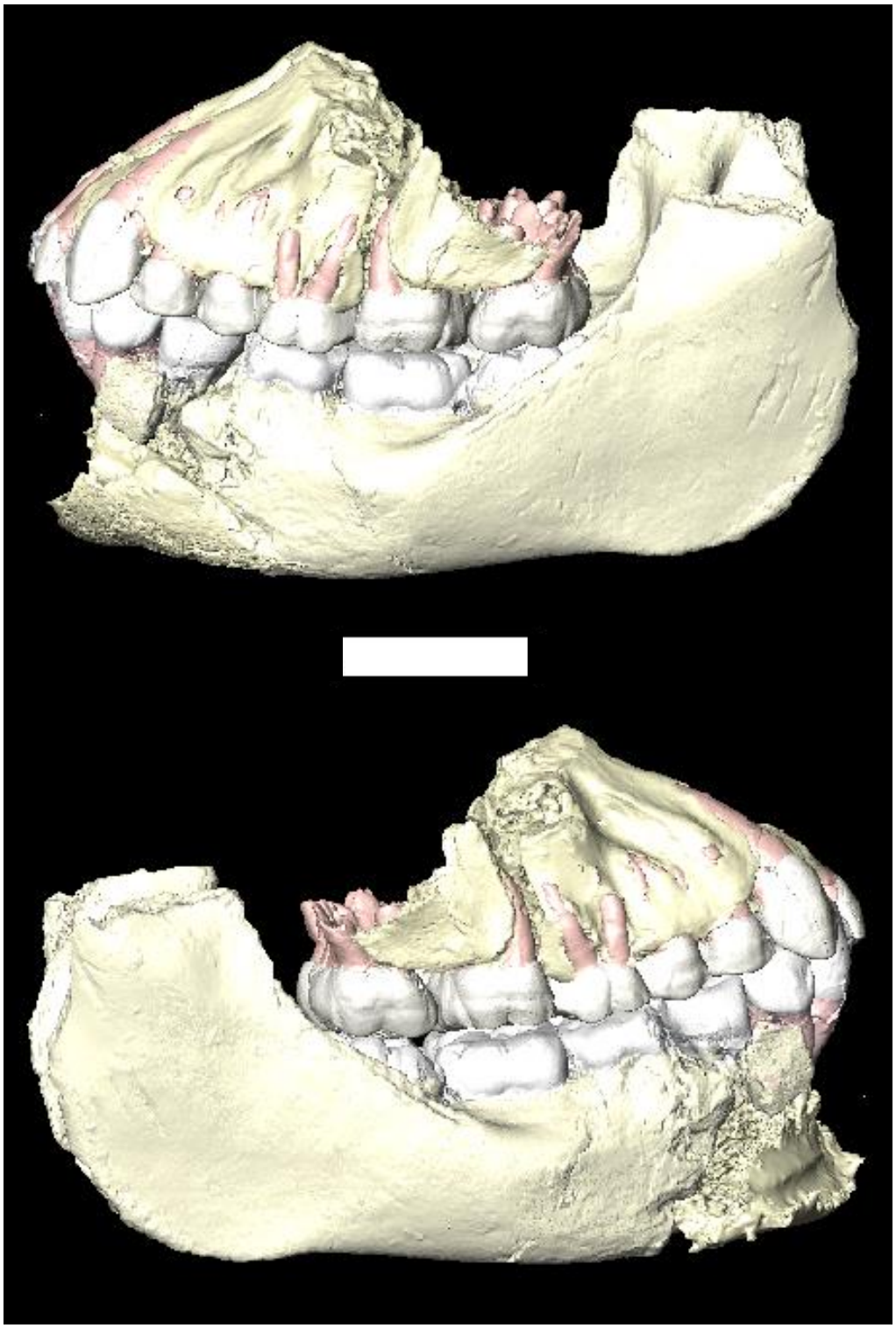

Figure 4.43. The reconstructed lower face of StW 498. Top: Left lateral view. Bottom: Right lateral view. Note the steeply sloped profile and procumbence of the anterior maxilla. Note that the degree of protrusion of the alveolar region and the steeply sloped profile is dependent on accurate positioning in the Frankfurt horizontal plane. Scale bar = 20 mm.

Although the cranial fragments were not reconstructed and analysed in the present study, I was able to restore some pieces of the cranial vault, namely StW 498f, StW 498q, and StW 499 (Figure 4.44). These fragments belong to the frontal and parietal bones. These fragments belong to the frontal and parietal bones. Description and analysis of the cranial fragments will be undertaken in a future project.

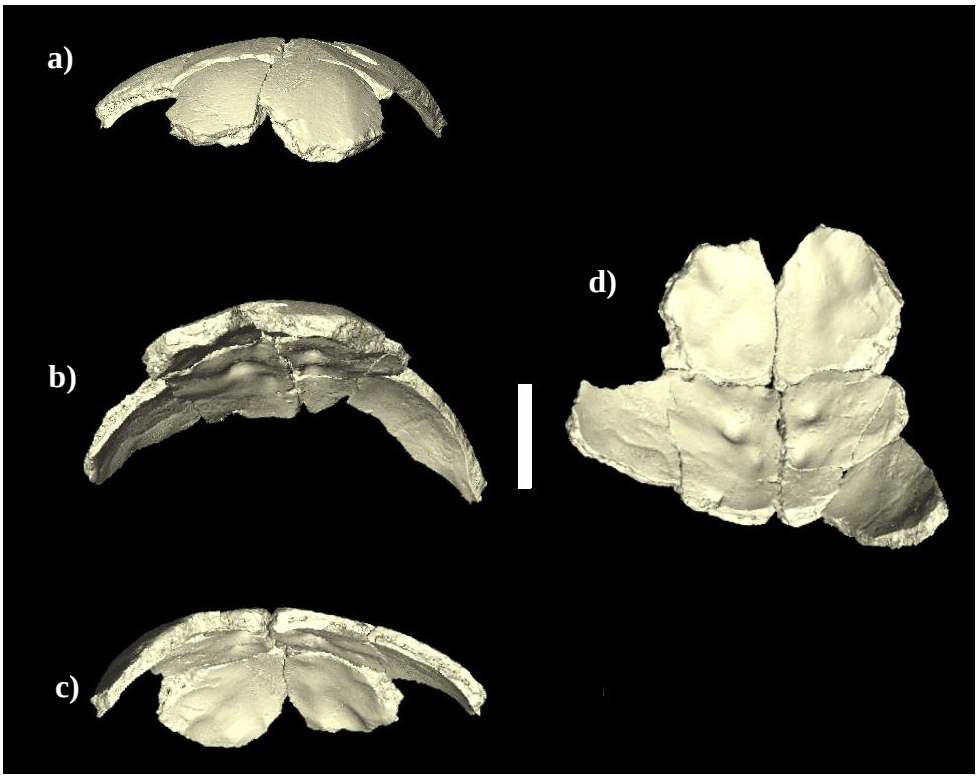

Figure 4.44. Renderings of the reconstructed cranial vault fragments of StW 498: a) Anterior view; b): Anterior view with the vault slightly tilted backwards; c) Posterior view; d) Endocranial view, anterior towards the top. Scale bar = 20 mm.

These fragments were aligned based on the position and direction of the temporal lines and added to the reconstruction of the lower face. Note that the aim of the image below (Figure 4.45) is to provide a general idea of what StW 498 may have looked like with portions of its calotte or partial braincase reassembled. Since there is no fragment that connects the partial calotte with the articulated maxillary and mandibular fragments, there is little basis for verifying their accurate placements relative to one another.

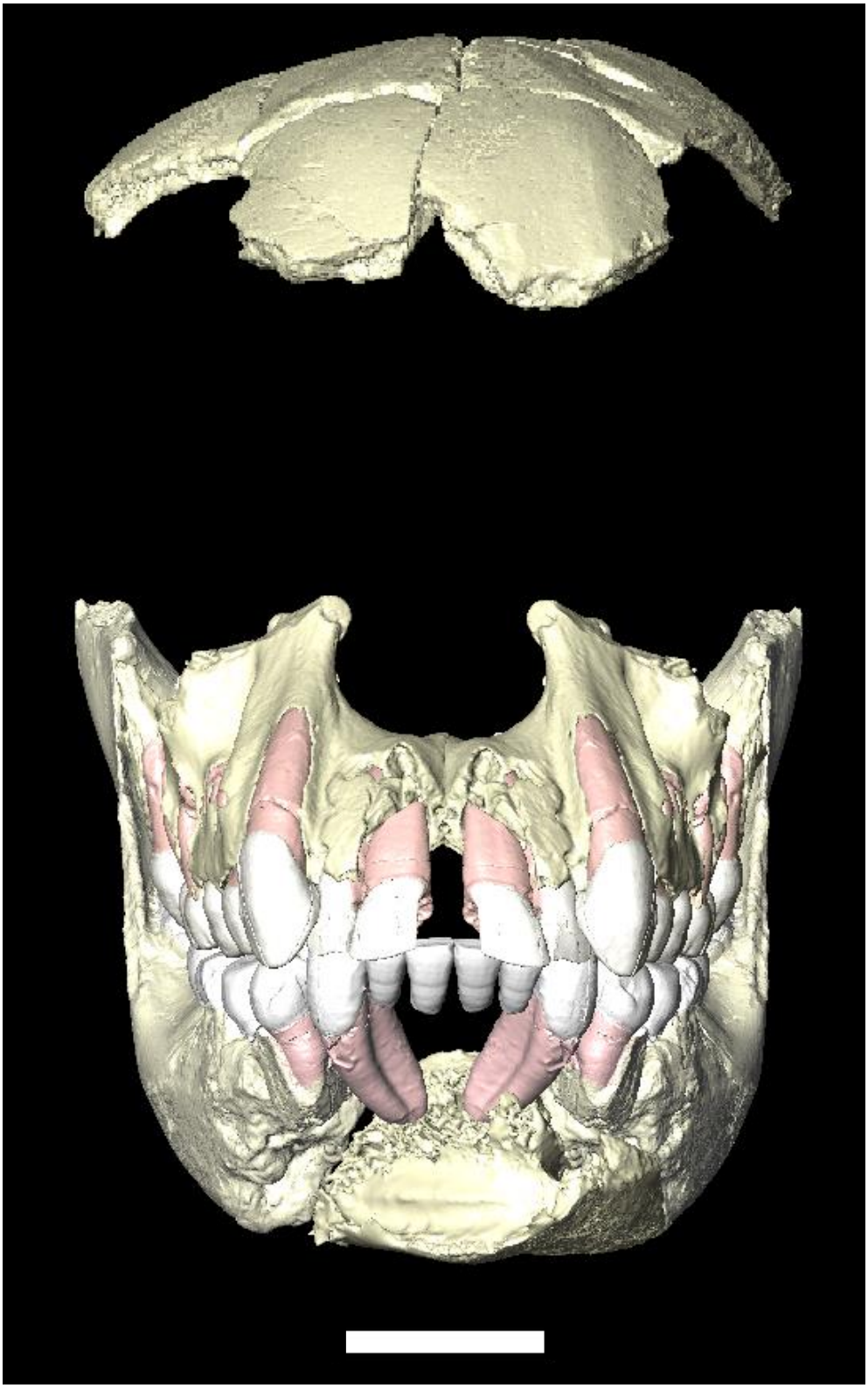

Figure 4.45. Renderings of the anterior view of the reconstructed partial skull of StW 498 combining fragments of the associated cranial vault and the lower face. Scale bar = 20 mm.

4.2. Quantitative measurements and qualitative observations

This section provides the results of the quantitative analysis and the comparative qualitative observations that were made throughout this study. Specifically, this section presents the comparative metric data of the maxilla, mandible, and dentition of StW 498 and of specimens attributed to *A. prometheus*, *A. africanus*, and *P. robustus*. In addition, I report the observed morphologies that distinguish these taxa and their relevance to StW 498. The results presented in the sections below are critically assessed and discussed in Chapter 5.

4.2.1. Comparative metric analysis

Maxillary dental dimensions taken for StW 498 and comparative material are provided in Table 4.1. Crown area and crown shape index of the maxillary premolars and molars are presented in Table 4.2, while palatal dimensions are provided in Table 4.3. Mandibular dental dimensions are provided in Table 4.4, and the crown area and crown shape index of the mandibular premolars and molars are presented in Table 4.5. Mandibular dimensions are provided in Table 4.6.

Results of the Principle Component Analyses (PCAs) are also presented in this section.

Table 4.1. Maxillary dental dimensions of StW 498 and comparative specimens. All measurements are in mm unless stated otherwise. BL = buccolingual. MD = mesiodistal. — = tooth not present. nd = measurements cannot be determined. Measurements listed in parentheses are estimates. Height refers to the crown height of the maxillary canines.

		I^1		I^2		C		Height	P^3		P^4		M^1		M^2		M^3		Reference
Specimen	**Side**	**BL**	**MD**	**BL**	**MD**	**BL**	**MD**		**BL**	**MD**	**BL**	**MD**	**BL**	**MD**	**BL**	**MD**	**BL**	**MD**	
StW 498	Right	8.3	8.8	—	—	11.9	10.5	13.3	13.8	9.4	14.4	10.1	13.9	10.6	17.2	12.6	17.4	15.3	This study
StW 498	Left	8.4	(8.7)	7.1	6.2	11.8	10.8	14.5	13.4	9.3	14.0	9.5	14.1	12.4	17.9	13.4	16.9	14.1	This study
A. prometheus																			
Sts 71	Right	—	—	—	—	—	—	—	13.1	9.3	nd	9.8	14.5	12.3	16.0	14.7	nd	(13.0)	This study
StW 183	Right	8.8	9.4	7.4	6.5	10.9	10.2	15.1	—	—	—	—	—	—	—	—	17.5	15.5	Moggi-Cecchi *et al*. (2006); C dimensions from this study
StW 183	Left	—	—	7.3	—	11	10.3	15.2	13.2	9.2	—	—	15.1	13.4	17.4	14.9	—	—	Moggi-Cecchi *et al*. (2006); C dimensions from this study
StW 189	Left	—	—	—	—	—	—	—	—	—	—	—	—	—	—	—	16.1	14.8	Moggi-Cecchi *et al*. (2006)
StW 252	Right	(7.5)	10.2)	7.6	8.0	11.3	11.2	13.8	14.2	9.9	15.4	10.9	nd	nd	17.0	15.8	17.7	15.9	I^1 dimensions and C height from this study. Remaining teeth from Clarke (1988)
StW 252	Left	8.0	11.0	7.7	7.9	11.4	10.9	14.4	13.9	9.6	15.2	10.9	15.2	14.6	17.0	15.9	18.2	15.9	C height from this study. Remaining teeth dimensions from Clarke (1988)
StW 280	Right	—	—	—	—	—	—	—	14.2	9.1	14.3	9.5	—	—	—	—	—	—	Moggi-Cecchi *et al*. (2006)
StW 280	Left	—	—	—	—	—	—	—	—	—	14.7	9.6	15.1	14.0	17.0	15.1	18.1	15.8	Moggi-Cecchi *et al*. (2006)
StW 450	Right	—	—	—	—	—	—	—	—	—	—	—	13.0	12.9	—	—	—	—	Moggi-Cecchi *et al*. (2006)
StW 578	Right	—	—	—	—	—	—	—	—	—	—	—	14.1	(12.5)	14.9	(12.7)	15.5	(12.4)	Partridge *et al*. (2003)
A. africanus																			
Sts 52	Right	8.3	9.3	6.1	6.8	9.7	9.9	11.9	12.5	8.7	(13.1)	(9.4)	(13.9)	12.1	15.2	13.3	14.3	(12.2)	I^1 to C dimensions from Robinson (1956). P^3 to M^3 dimensions from this study
Sts 52	Left	8.2	9.5	7.0	7.3	9.9	9.8	12.8	12.6	8.5	(12.9)	9.1	13.8	(12.5)	15.6	13.2	14.2	12.4	I^1 to C dimensions from Robinson (1956). P^3 to M^3 dimensions from this study
StW 73	Left	—	—	—	—	—	—	—	12.5	9.2	13.6	9.3	—	11.7	—	13.2	—	—	M^1 and M^2 dimensions from Moggi-Cecchi *et al*. (2006). P^3 and P^4 dimensions this study
StW 287	Left	—	—	—	—	10.4	11.6	15.1	—	—	—	—	—	—	—	—	—	—	This study
StW 524	Right	—	—	—	—	—	—	—	—	—	—	—	—	—	—	—	15.6	13.3	Moggi-Cecchi *et al*. (2006)
MLD 11/30	Right	—	—	—	—	8.2	9.5	14.2	11.2	8.9	—	—	—	—	—	—	—	—	This study

Table 4.1 *(continued)*.

		I^1		I^2		C		Height	P^3		P^4		M^1		M^2		M^3		Reference
Specimen	**Side**	**BL**	**MD**	**BL**	**MD**	**BL**	**MD**		**BL**	**MD**	**BL**	**MD**	**BL**	**MD**	**BL**	**MD**	**BL**	**MD**	
P. robustus																			
TM 1517	Right	—	—	—	—	—	—	—	—	—	—	—	—	—	—	—	15.7	13.9	This study
TM 1517	Left	—	—	—	—	—	—	—	13.6	10.1	15.1	10.3	14.8	12.6	15.9	13.6	14.8	11.6	This study; M^3 dimensions from Robinson (1956)
SK 13/14	Right	—	—	—	—	—	—	—	13.2	9.9	15.1	10.7	15.0	13.1	16.3	15.1	17.6	14.7	Clarke (1988)
SK 13/14	Left	—	—	—	—	—	—	—	13.2	9.6	15.2	10.5	15.1	14.0	16.6	16.0	17.6	14.5	Clarke (1988)
SK 46	Right	—	—	—	—	—	—	—	13.2	8.4	14.6	9.2	15.2	11.8	16.1	13.0	16.8	14.7	Clarke (1988)
SK 46	Left	—	—	—	—	—	—	—	—	—	14.6	9.0	14.5	11.3	16.3	13.0	16.3	14.8	Clarke (1988)
SK 48	Right	—	—	—	—	9.0	8.2	—	13.6	9.3	13.9	9.6	13.9	12.2	14.5	12.6	—	—	Clarke (1990)
SK 48	Left	—	—	—	—	—	—	—	—	—	—	—	14.0	12.7	14.8	13.0	17.3	13.2	Clarke (1990)

Table 4.2. Crown area and crown shape index of the maxillary premolars and molars of StW 498 and comparative specimens. All measurements are in mm unless stated otherwise. — = tooth not present. Measurements listed in parentheses are estimates.

Specimen	Side	P^3		P^4		M^1		M^2		M^3	
		Crown area (mm^2)	Crown shape index	Crown area (mm^2)	Crown shape index	Crown area (mm^2)	Crown shape index	Crown area (mm^2)	Crown shape index	Crown area (mm^2)	Crown shape index
StW 498	Right	127.7	146.8	145.4	142.6	147.3	131.1	216.7	136.5	266.2	113.7
StW 498	Left	124.6	144.1	133.0	147.4	174.8	113.7	239.9	133.6	238.3	119.8
A. prometheus											
Sts 71	Right	121.8	133.7	—	—	178.4	117.9	235.2	108.8	—	—
StW 183	Right	—	—	—	—	—	—	—	—	271.3	112.9
StW 183	Left	121.4	143.5	—	—	202.3	112.7	259.3	116.8		
StW 189	Left	—	—	—	—	—	—	—	—	238.3	108.8
StW 252	Right	140.6	143.4	167.9	141.3	—	—	268.6	107.6	281.4	111.3
StW 252	Left	133.4	144.8	165.7	139.4	221.9	104.1	270.3	106.9	289.4	114.5
StW 280	Right	129.2	156.0	135.8	150.5	—	—	—	—	—	—
StW 280	Left	—	—	141.1	153.1	211.4	107.8	256.7	112.6	286.0	114.6
StW 450	Right	—	—	—	—	167.7	100.8	—	—	—	—
StW 578	Right	—	—	—	—	176.3	112.8	189.3	117.3	192.2	125.0
A. africanus											
Sts 52	Right	108.6	143.7	123.1	139.4	(168.2)	(114.9)	202.2	114.3	(174.5)	(117.2)
Sts 52	Left	107.1	148.2	(117.4)	(141.8)	(172.5)	(110.4)	205.9	118.2	176.1	114.5
StW 73	Left	115.0	135.9	126.5	146.2	—	—	—	—	—	—
StW 524	Right	—	—	—	—	—	—	—	—	207.5	117.3
MLD 11/30	Right	99.7	125.8	—	—	—	—	—	—	—	—
P. robustus											
TM 1517	Right	—	—	—	—	—	—	—	—	218.2	112.9
TM 1517	Left	137.4	134.7	155.5	146.6	186.5	117.5	216.2	116.9	171.7	127.6
SK 13/14	Right	130.7	133.3	161.6	141.1	196.5	114.5	246.1	107.9	258.7	119.7
SK 13/14	Left	126.7	137.5	159.6	144.8	211.4	107.9	265.6	103.8	255.2	121.4
SK 46	Right	110.9	157.1	134.3	158.7	179.4	128.8	209.3	123.8	246.9	114.3
SK 46	Left	—	—	131.4	162.2	163.9	128.3	211.9	125.3	241.2	110.1
SK 48	Right	126.5	146.2	133.4	144.8	169.6	113.9	182.7	115.1	—	—
SK 48	Left	—	—	—	—	177.8	110.2	192.4	113.8	228.4	131.1

Table 4.3. Palatal dimensions for StW 498 and selected comparative material. nd = measurements cannot be determined. All measurements are in mm unless stated otherwise. Measurements listed in parenthesis are estimates.

Specimen	Palate Length	Palate Breadth	Palate Depth	Palate Shape Index	Reference
StW 498	(60.1)	(30.6)	11.5	(50.9)	This study
A. prometheus					
Sts 71	nd	38	nd	nd	Wood (1991)
StW 573	(69.0)	(35.0)	11.3	(50.7)	Clarke & Kuman (2018)
A. africanus					
Sts 5	65.3	35.7	18.0	54.7	Kimbel, Rak & Johanson (2004)
Sts 53	54.0	32.0	nd	59.3	Kimbel, Rak & Johanson (2004)
StW 13	67	24	12	35.8	Wood (1991); Palate shape index caluclated in this study
StW 73	58.0	30.0	14.5	51.7	Kimbel, Rak & Johanson (2004)
P. robustus					
SK 13/14	nd	26	8	nd	Wood (1991)
SK 47	59	25	8	42.4	Wood (1991); Palate shape index caluclated in this study
SK 48	63	27	14	42.9	Wood (1991); Palate shape index caluclated in this study
SK 847	nd	28	12	nd	Wood (1991)

*Palate length was measured from the orale to the staphylion. Palate length for StW 498 is a gross estimate staphylion is missing and was measured from the orale to the midpoint of the maxillary third molars.

*Palate breadth was measured from endomolare to endomolare at the centre of the second molars. The breadth for StW 498 is an estimate as it was measured on the mirrored reconstruction.

*Palate depth was measured at the M^1 to M^2.

*Palate shape index = (breadth/length) x100.

Table 4.4. Mandibular dental dimensions of StW 498 and comparative specimens. All measurements are in mm unless stated otherwise. BL = buccolingual. MD = mesiodistal. — = tooth not present. nd = measurements cannot be determined. Measurements listed in parentheses are estimates. Height refers to the crown height of the mandibular canines.

Specimen	Side	I_1		I_2		C		Height	P_3		P_4		M_1		M_2		M_3		Reference
		BL	MD	BL	MD	BL	MD		BL	MD	BL	MD	BL	MD	BL	MD	BL	MD	
StW 498	Right	7.8	(6.4)	(6.5)	5.6	10.8	10.4	15.5	11.4	10.3	12.9	12.4	(14.5)	(17.1)	(15.7)	(17.2)	15.6	18.1	This study
StW 498	Left	nd	nd	nd	(5.4)	11.2	10.6	16.5	12.4	10.4	(13.1)	11.6	14.1	15.9	15.7	17.3	15.9	18.5	This study
A. prometheus																			
Sts 36	Right		—	—	—	—	—	—	—	—	nd	nd	nd	nd	(16.2)	14.4	(16.6)	15.8	Clarke (1990)
Sts 36	Left	—	—	—	—	10.8	9.3	10.8	13.6	10.1	12.8	9.0	14.4	11.6	(16.5)	(15.5)	16.5	15.7	Clarke (1990). C dimemsions from this study
StW 14	Right	—	—	—	—	—	—	—	—	—	—	—	—	—	—	—	14.6	17.8	Moggi-Cecchi *et al* . (2006)
StW 280	Right	—	—	—	—	—	—	—	—	—	—	—	—	—	—	—	16.4	16.8	Moggi-Cecchi *et al* . (2006)
StW 384	Right	—	—	—	—	—	—	—	—	—	—	—	15.1	15.5	16.8	17.0	16.8	18.2	Moggi-Cecchi *et al* . (2006)
A. africanus																			
Sts 52	Right	8.0	5.8	8.0	7.2	10.4	9.1	11.4	12.1	9.6	11.7	10.5	13.00	13.9	13.4	14.3	12.6	13.8	Clarke (1990); C height from this study
Sts 52	Left	—	—	—	—	—	—	—	nd	nd	nd	nd	nd	nd	13.6	(15.1)	13.0	13.7	This study
StW 109	Right	—	—	—	—	—	—	—	—	—	—	—	—	—	15.6	16.7	15.6	17.4	Moggi-Cecchi *et al* . (2006)
StW 116	Right	—	—	9.1	7.4	11.4	10.0	—	—	—	—	—	—	—	—	—	—	—	Moggi-Cecchi *et al* . (2006)
StW 116	Left	7.6	6.3	9.2	7.5	—	—	—	—	—	—	—	—	—	—	—	—	—	Moggi-Cecchi *et al* . (2006)
StW 123	Right	—	—	—	—	—	—	—	—	—	—	—	11.8	13.3	—	—	—	—	Moggi-Cecchi *et al* . (2006)
StW 123	Left	—	—	—	—	—	—	—	—	—	—	—	12.1	13.4	—	—	—	—	Moggi-Cecchi *et al* . (2006)
StW 131	Right	—	—	—	—	—	—	—	—	—	11.7	10.1	12.6	14.4	—	—	—	—	Moggi-Cecchi *et al* . (2006)
StW 131	Left	—	—	—	—	—	—	—	—	—	11.9	10.7	—	—	—	—	—	—	Moggi-Cecchi *et al* . (2006)
StW 133	Left	—	—	—	—	—	—	—	—	—	—	—	—	—	—	—	15.0	16.5	Moggi-Cecchi *et al* . (2006)
StW 193	Right	—	—	—	—	—	—	—	—	—	11.8	10.4	—	—	—	—	—	—	Moggi-Cecchi *et al* . (2006)
StW 193	Left	—	—	—	—	—	—	—	—	—	12.4	9.5	—	—	—	—	—	—	Moggi-Cecchi *et al* . (2006)

Table 4.4 (*continued*).

Specimen	Side	I_1		I_2		C		Height	P_3		P_4		M_1		M_2		M_3		Reference
		BL	MD	BL	MD	BL	MD		BL	MD	BL	MD	BL	MD	BL	MD	BL	MD	
A. africanus																			
StW 213	Right	—	—	—	—	—	—	—	10.0	9.3	10.3	9.7	—	—	12.7	14.4	—	—	Moggi-Cecchi *et al*. (2006)
StW 213	Left	—	—	—	—	8.8	8.5	—	9.9	9.4	10.5	9.9	—	—	12.8	14.4	—	—	Moggi-Cecchi *et al*. (2006)
StW 288	Right	—	—	—	—	11.2	9.5	—	—	—	—	—	—	—	—	—	—	—	Moggi-Cecchi *et al*. (2006)
StW 412	Right	—	—	—	—	—	—	—	—	—	—	—	—	—	13.0	14.6	—	—	Moggi-Cecchi *et al*. (2006)
StW 412	Left	—	—	—	—	—	—	—	—	—	—	—	—	—	13.0	14.6	—	—	Moggi-Cecchi *et al*. (2006)
StW 421	Right	—	—	—	—	—	—	—	—	—	—	—	13.7	15.3	—	—	—	—	Moggi-Cecchi *et al*. (2006)
StW 421	Left	—	—	—	—	—	—	—	—	—	—	—	13.8	15.3	—	—	—	—	Moggi-Cecchi *et al*. (2006)
StW 446	Left	—	—	—	—	8.8	9.1	—	—	—	—	—	—	—	—	—	—	—	Moggi-Cecchi *et al*. (2006)
StW 491	Right	—	—	—	—	10.1	9.4	—	—	—	—	—	—	—	—	—	—	—	Moggi-Cecchi *et al*. (2006)
StW 491	Left	—	—	—	—	9.7	9.2	—	—	—	—	—	12.7	13.3	13.9	14.7	14.0	15.8	Moggi-Cecchi *et al*. (2006)
StW 529	Right	—	—	—	—	—	—	—	—	—	—	—	—	—	14.4	15.1	14.0	15.2	Moggi-Cecchi *et al*. (2006)
StW 529	Left	—	—	—	—	—	—	—	—	—	—	—	—	—	—	—	14.6	15.2	Moggi-Cecchi *et al*. (2006)
StW 537	Right	—	—	8.0	7.6	11.0	9.8	—	—	—	—	—	—	—	15.3	16.6	—	—	Moggi-Cecchi *et al*. (2006)
StW 537	Left	—	—	7.9	7.6	10.9	9.7	—	—	—	12.7	11.2	13.5	15.0	15.5	16.6	16.1	16.6	Moggi-Cecchi *et al*. (2006)
P. robustus																			
TM 1517	Right	—	—	—	—	—	—	—	—	—	—	—	—	—	—	—	15.2	16.7	This study
TM 1517	Left	—	—	—	—	—	—	—	12.6	10.3	13.5	11.8	—	—	—	—	—	—	This study
SK 843	Left	—	—	—	—	—	—	—	—	—	—	—	13.5	14.6	13.9	15.8	—	—	This study

Table 4.5. Crown area and crown shape index of the mandibular premolars and molars of StW 498 and selected comparative specimens. All measurements are in mm unless stated otherwise. — = tooth not present. Measurements listed in parentheses are estimates.

Specimen	Side	P_3		P_4		M_1		M_2		M_3	
		Crown area (mm^2)	Crown shape index	Crown area (mm^2)	Crown shape index	Crown area (mm^2)	Crown shape index	Crown area (mm^2)	Crown shape index	Crown area (mm^2)	Crown shape index
StW 498	Right	117.4	111.8	159.9	104.0	(249.4)	(84.3)	(268.5)	(91.8)	282.4	86.2
StW 498	Left	129.0	119.2	152.0	112.9	224.2	88.7	271.6	90.8	294.2	85.9
A. prometheus											
Sts 36	Right	—	—	—	—	—	—	233.3	112.5	262.3	105.1
Sts 36	Left	137.4	134.7	115.2	142.2	167.0	124.1	255.8	106.5	259.1	105.1
StW 14	Right	—	—	—	—	—	—	—	—	259.9	82.0
StW 280	Right	—	—	—	—	—	—	—	—	275.5	97.6
StW 384	Right	—	—	—	—	234.1	97.4	285.6	98.8	305.8	92.3
A. africanus											
Sts 52	Right	116.2	126.0	122.9	111.4	180.7	93.5	191.6	93.7	173.9	91.3
Sts 52	Left	—	—	—	—	—	—	(205.4)	(90.1)	178.1	94.9
StW 109	Right	—	—	—	—	—	—	260.5	93.4	271.4	89.7
StW 123	Right	—	—	—	—	156.9	88.7	—	—	—	—
StW 123	Left	—	—	—	—	162.4	90.3	—	—	—	—
StW 131	Right	—	—	118.2	115.8	181.4	87.5	—	—	—	—
StW 131	Left	—	—	127.3	111.2	—	—	—	—	—	—
StW 133	Left	—	—	—	—	—	—	—	—	247.5	90.9
StW 193	Right	—	—	122.7	113.5	—	—	—	—	—	—
StW 193	Left	—	—	117.8	130.5	—	—	—	—	—	—
StW 213	Right	93.0	107.5	99.9	106.2	—	—	182.9	88.2	—	—
StW 213	Left	93.1	105.3	104.0	106.1	—	—	184.3	88.9	—	—
StW 412	Right	—	—	—	—	—	—	189.8	89.0	—	—
StW 412	Left	—	—	—	—	—	—	189.8	89.0	—	—
StW 421	Right	—	—	—	—	209.6	89.5	—	—	—	—
StW 421	Left	—	—	—	—	211.1	90.2	—	—	—	—
StW 491	Left	—	—	—	—	168.9	95.5	204.3	94.6	221.2	88.6
StW 529	Right	—	—	—	—	—	—	217.4	95.4	212.8	92.1
StW 529	Left	—	—	—	—	—	—	—	—	221.9	96.1
StW 537	Right	—	—	—	—	—	—	253.9	92.2	—	—
StW 537	Left	—	—	142.2	113.4	202.5	90.0	257.3	93.4	267.3	96.9
P. robustus											
TM 1517	Right	—	—	—	—	—	—	—	—	253.8	91.0
TM 1517	Left	129.8	122.3	159.3	114.4	—	—	—	—	—	—
SK 843	Left	—	—	—	—	197.1	92.5	219.6	87.8	—	—

Table 4.6. Mandibular dimensions for StW 498 and selected comparative material. All measurements are in mm unless stated otherwise. nd = measurement cannot be determined. — = measurement was not taken. Measurements listed in parenthesis are estimates.

Specimen	Greatest corpus thickness	Mandibular height at M_1	Mandibular length	Reference
StW 498 (left)	23.8	26.4	103.8	This study
A. prometheus				
Sts 7 (left)	nd	41.5	nd	Wood (1991)
Sts 36	24.1	35.6	114.7	This study
StW 573 (left)	24.2	34.6	107.0	Clarke & Kuman (2018)
A. africanus				
Sts 52	27.5	28.2	(92.0)	This study
MLD 18 (right)	(34)	28	—	Wood (1991)
MLD 34 (right)	32	22	—	Wood (1991)
MLD 40 (left)	36	27	—	Wood (1991)
P. robustus				
SK 12 (right)	(40)	31	—	Wood (1991)
SK 12 (left)	37	27.5	—	Wood (1991)
SK 23 (right)	39	26	—	Wood (1991)
SK 23 (left)	40	25	—	Wood (1991)
SK 34 (right)	41	23	—	Wood (1991)
TM 1517 (right)	35	27.5	—	Wood (1991)

*Greatest corpus thickness was measured mediolaterally between the M_2 and M_3.

*Mandibular length was measured as the horizontal distance between pogonion and gonion.

Principle Component Analysis (PCA)

Individual PCAs were performed for the maxillary and mandibular canines, the maxillary premolars, M^2, and M^3 in order to assess and visualise variation in size and shape. Each PCA was performed on the covariance matrix and the StW 498 specimens in the Principle Component space were projected for each tooth-specific PCA.

A PCA was not performed on the M^1 since they are heavily worn. PCAs also were not conducted for the mandibular premolars or molars due to the small sample relative to the number of variables; PCAs in such situations are invalid.

PCA of maxillary canines

Three variables were included in the PCA on maxillary canines: crown height, mesiodistal diameter, and buccolingual diameter. Only the first two principle components were evaluated because they account for 88.6% of the variation in the sample. Principle Component (PC) 1 accounts for 62.6% of the overall variation in the sample and is driven by mesiodistal dimensions (Figure 4.46). PC 1 differentiates *A. africanus* from *A. prometheus*, where the latter tends to show larger dimensions in the variables driving PC 1. Note that there is a single *A. africanus* specimen that clusters with *A. prometheus* specimens on PC 1, but this needs to be investigated in a larger sample to confirm its status. PC 2 is driven predominantly by crown height and accounts for 26% of the overall variation (Figure 4.46). PC 2 does not differentiate *A. africanus* from *A. prometheus*. StW 498 appears to cluster with the *A. prometheus* samples. The PC loadings and scores are reported in Appendix D.

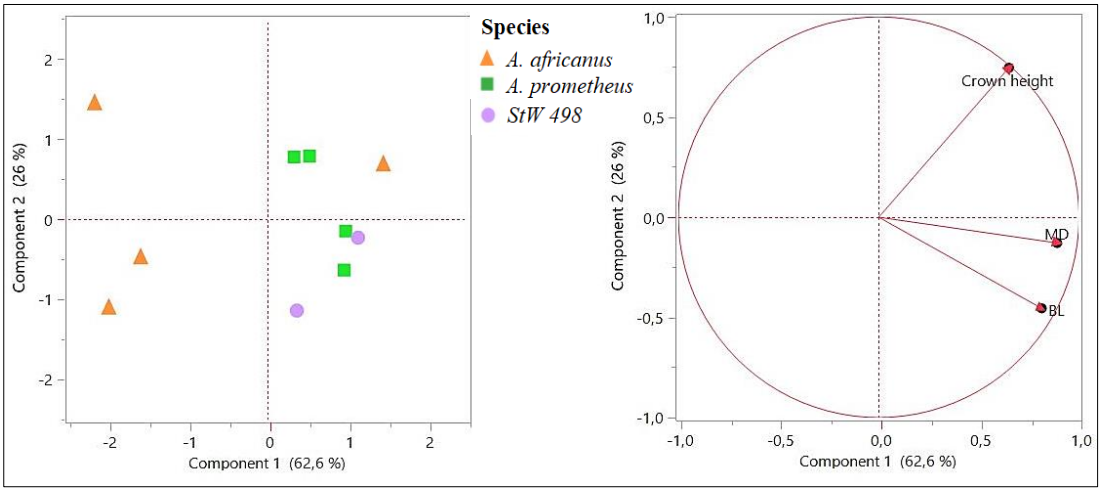

Figure 4.46. Principle Component Analysis of the maxillary canines of StW 498 and available comparative specimens. Left: Bivariate plot of PC 1 versus PC 2. Right: Magnitude and directions of variable loadings on PC 1 and PC 2.

PCA of maxillary and mandibular canines

Due to the small sample of mandibular canines, the maxillary canine PCA featuring the same three measurements (i.e., crown height, mesiodistal diameter,

and buccolingual diameter) was rerun after incorporating mandibular samples. PC 1 accounts for 70.7% of the overall variation within the sample and is driven primarily by the mesiodistal dimension (Figure 4.47). PC 1 differentiates *A. africanus* from *A. prometheus*, with the latter taxon typically showing larger dimensions. There is a single *A. africanus* specimen that clusters with *A. prometheus*, which requires further exploration. PC 2 is driven primarily by buccolingual dimensions and accounts for 22.1% of the overall variation and does not seem to differentiate any of the three taxa. StW 498 appears to cluster with the *A. prometheus* samples. The PC loadings and scores are reported in Appendix E.

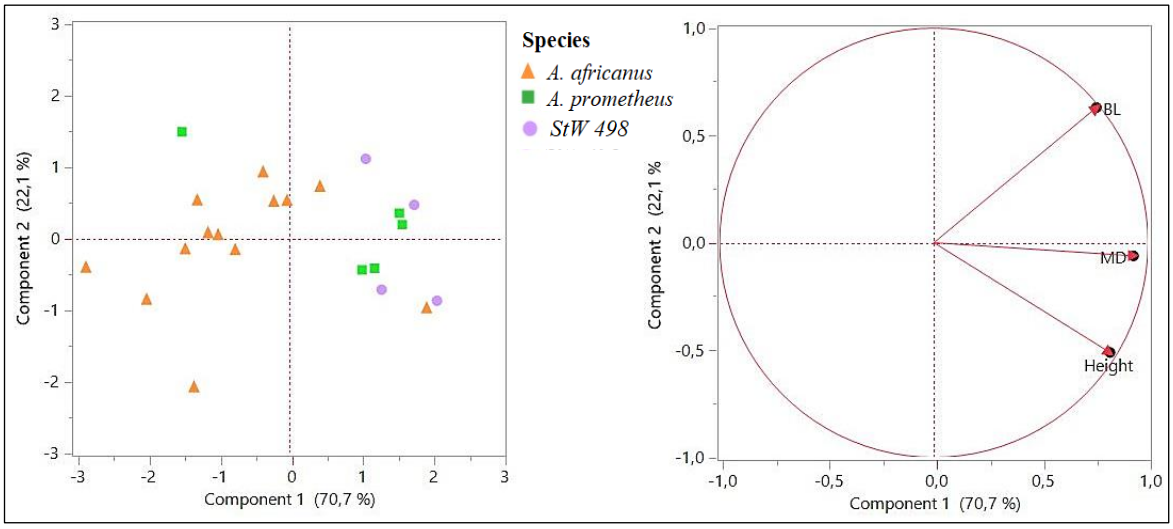

Figure 4.47. Principle Component Analysis of the maxillary and mandibular canines of StW 498 and available comparative specimens. Left: Bivariate plot of PC 1 versus PC 2. Right: Magnitude and directions of variable loadings on PC 1 and PC 2.

P^3 PCA

Four variables were used for the P^3 PCA: buccolingual dimensions, mesiodistal dimensions, crown area, and crown shape index (the same variables were also used for P^4, M^2, and M^3 PCAs). PC 1 accounts for 62.8% of the overall variation, and effectively differentiates *A. africanus* from either *A. prometheus* or *P. robustus*, but does not differentiate the latter two taxa (Figure 4.48). PC 1 seems to be driven mainly by crown area, with *A. prometheus* and *P. robustus* exhibiting larger areas than *A. africanus*. PC 2 accounts for 36.8% of the overall variation and is driven by crown shape index. PC 2 does not differentiate any of the taxa. StW 498 is clustered in between the *A. prometheus* and *P. robustus* samples. The PC loadings and scores are reported in Appendix F.

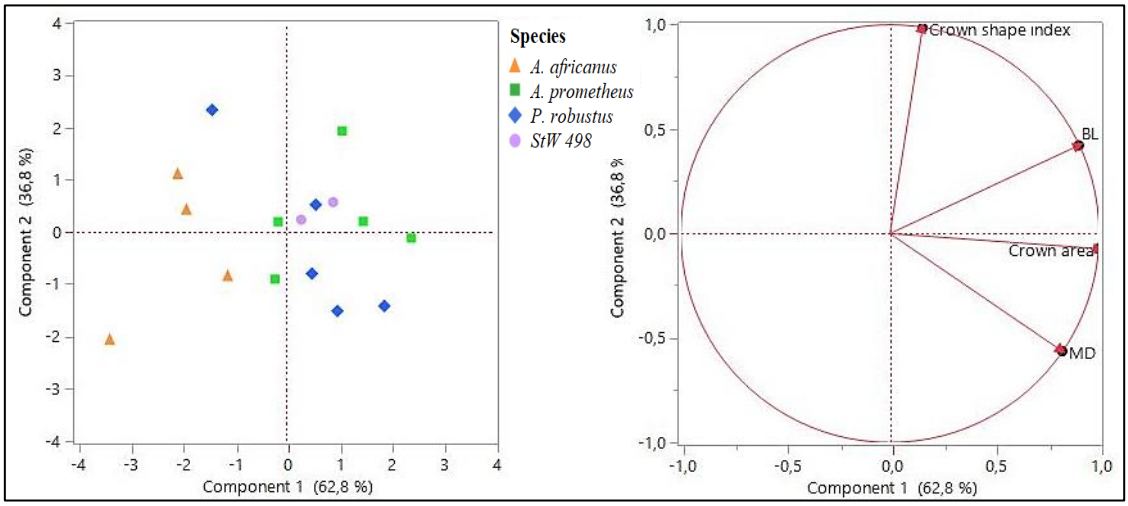

Figure 4.48. Principle Component Analysis of the maxillary P^3s of StW 498 and available comparative specimens. Left: Bivariate plot of PC 1 versus PC 2. Right: Magnitude and directions of variable loadings on PC 1 and PC 2.

P^4 PCA

PC 1 is driven primarily by crown area and mesiodistal dimensions and accounts for 67.5% of the overall variation, while PC 2 is driven by crown shape index and accounts for 28.3% of the variation (Figure 4.49). PC 1 distinguishes *A. africanus* from *A. prometheus*. Note that there is a single *P. robustus* specimen that clusters just beyond the periphery of the *A. africanus* cluster; further exploration is required to determine its status. PC 2 tends to separate *P. robustus* and *A. prometheus* from *A. africanus*, but like the P^3, PC 2 does not clearly differentiate *A. prometheus* from *P. robustus*. StW 498 clusters with all three taxa, however, StW 498 is more closely correlated with the *A prometheus* and *P. robustus* clusters. The PC loadings and scores are reported in Appendix G.

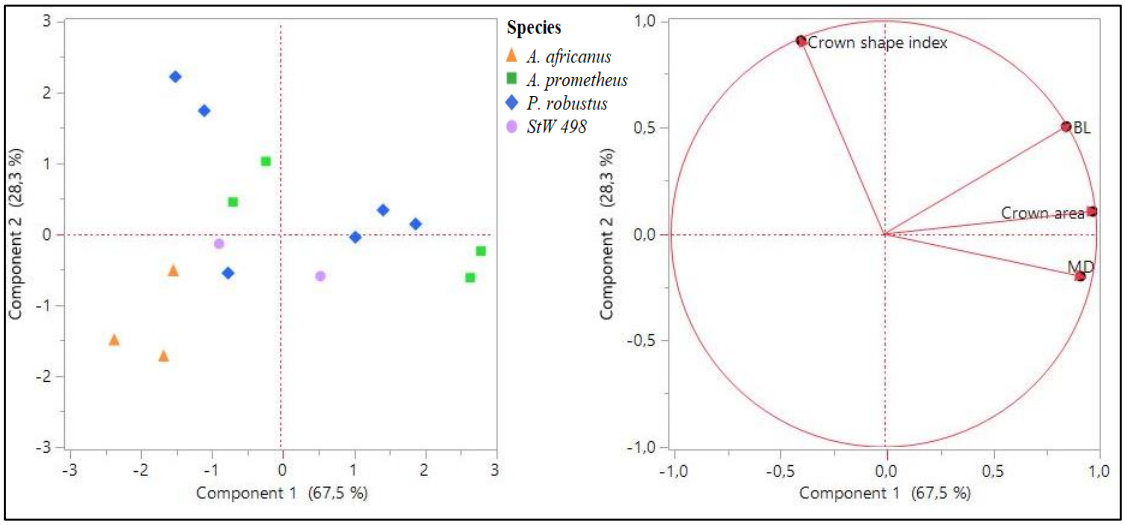

Figure 4.49. Principle Component Analysis of the maxillary P^4s of StW 498 and available comparative specimens. Left: Bivariate plot of PC 1 versus PC 2. Right: Magnitude and directions of variable loadings on PC 1 and PC 2.

M^2 PCA

PC 1 is driven by crown area and mesiodistal dimensions and accounts for 67.3% of the overall variation within the sample. PC 2 accounts for 32.6% of the variation and is driven primarily by crown shape index, and buccolingual dimensions to a lesser extent (Figure 4.50). PC 1 and PC 2 poorly differentiate *A. africanus* and *P. robustus*, but PC1 tends to differentiate *A. africanus* from *A.*

prometheus, with the exception of a single *A. prometheus* specimen that clusters near *A. africanus* in negative PC 1 space This specimen would benefit from further investigation to determine its most likely taxonomic status. StW 498 is separated from all three taxa. The PC loadings and scores are reported in Appendix H.

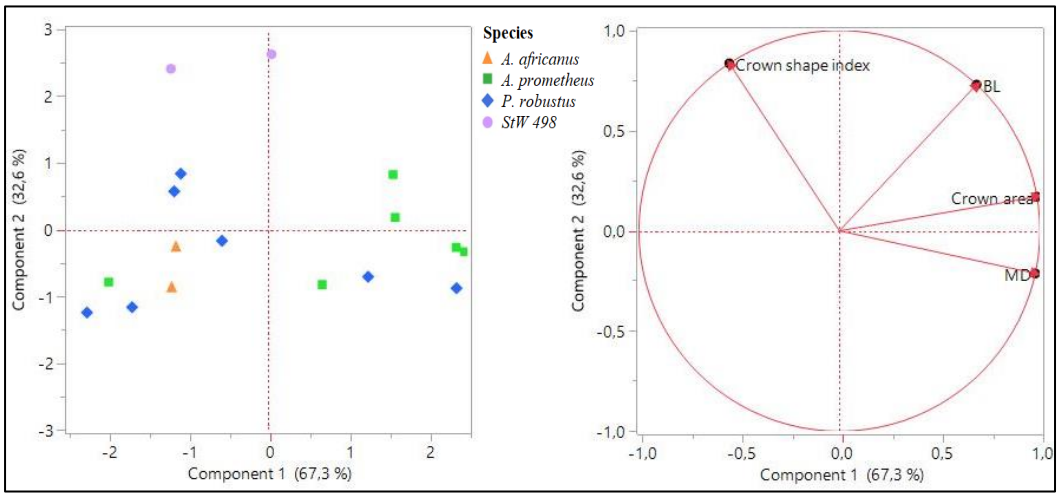

Figure 4.50. Principle Component Analysis of the maxillary M^2s of StW 498 and available comparative specimens. Left: Bivariate plot of PC 1 versus PC 2. Right: Magnitude and directions of variable loadings on PC 1 and PC 2.

M^3 PCA

Mesiodistal dimensions and crown area appear to drive PC 1, which accounts for 76.8% of the overall variation in the sample. Crown shape index drives PC 2, which accounts for 23.2% of the variation in the sample (Figure 4.51). *A. africanus* is distinguished from *A. prometheus* along PC 1, with the exception of one individual at the lowest extreme of the *A. prometheus* range. Further exploration is required of the single *P. robustus* specimen that is clustered with *A. africanus* along PC 1. *P. robustus* and *A. prometheus* are not clearly distinguished along PC 1 or PC 2. StW 498 plots within *P. robustus* and *A. prometheus* clusters on both PC 1 and PC 2. The PC loadings and scores are reported in Appendix I.

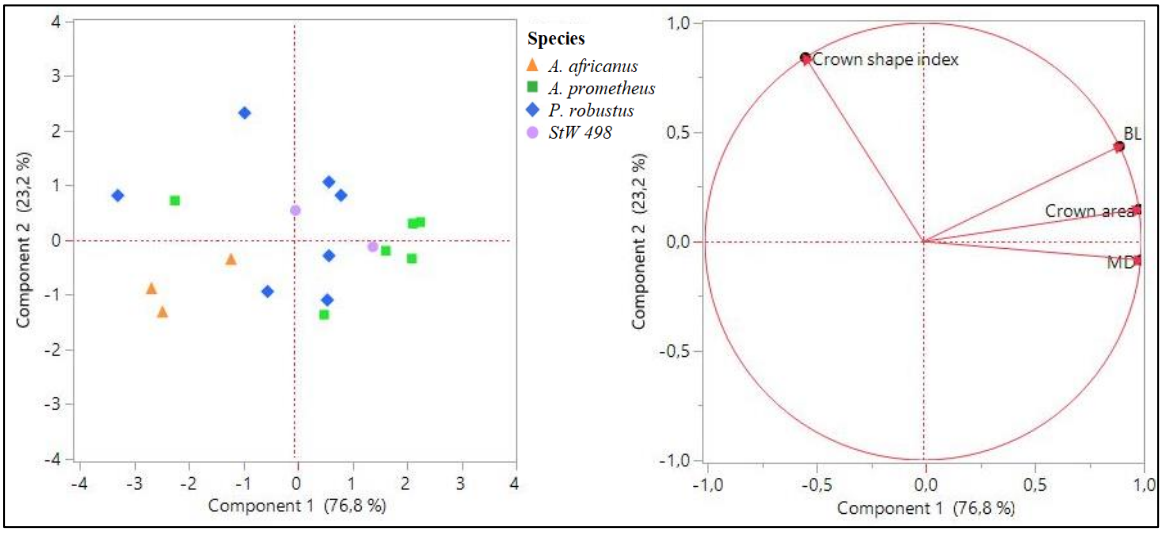

Figure 4.51. Principle Component Analysis of the maxillary M^3s of StW 498 and selected available specimens. Left: Bivariate plot of PC 1 versus PC 2. Right: Magnitude and directions of variable loadings on PC 1 and PC 2.

Combined M^2 and M^3 PCA

Quantitative results for the M^2 and M^3 were combined to further assess and visualise variation within maxillary molars. The same variables were used (i.e., buccolingual dimensions, mesiodistal dimensions, crown area, and crown shape index).

Mesiodistal dimensions and crown areas of both teeth drive PC 1, accounting for 70.8% of the overall variation. PC 2 is driven by crown shape index, which accounts for 29.1% of the variation (Figure 4.52). PC 1 and PC 2 poorly differentiate *A. africanus* from *P. robustus* from *A. africanus*. I.e., all three taxa are interspersed, which is likely due to intra-individual variation. StW 498 is separated from *A. africanus* on PC 1. The PC loadings and scores are reported in Appendix J.

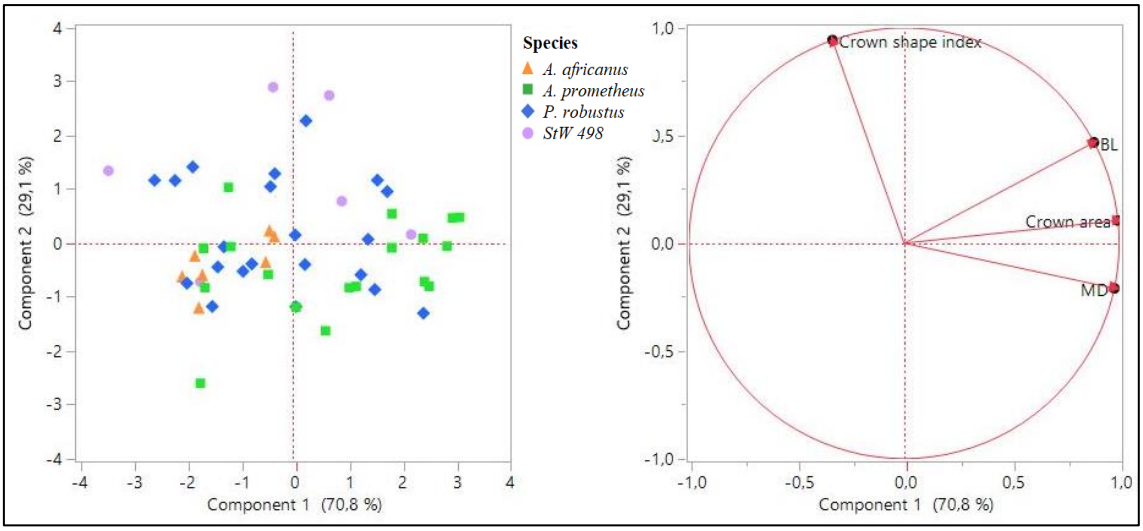

Figure 4.52. Principle Component Analysis of the maxillary M^2s and M^3s of StW 498 and available comparative specimens. Left: Bivariate plot of PC 1 versus PC 2. Right: Magnitude and directions of variable loadings on PC 1 and PC 2.

4.2.2. Virtual, three-dimensional analysis of dental form

Average enamel thickness (AET)

As outlined in Chapter 3, the average enamel thickness (AET; e.g., see by Olejniczak *et al.*; Zanolli 2015) and the enamel distribution analysis required separation of the enamel cap and dentine. Below are the results of the virtual partitioning of the maxillary and mandibular second and third molars of StW 498 (Figure 4.53), TM 1517 (Figure 4.54), and StW 252 (Figure 4.55).

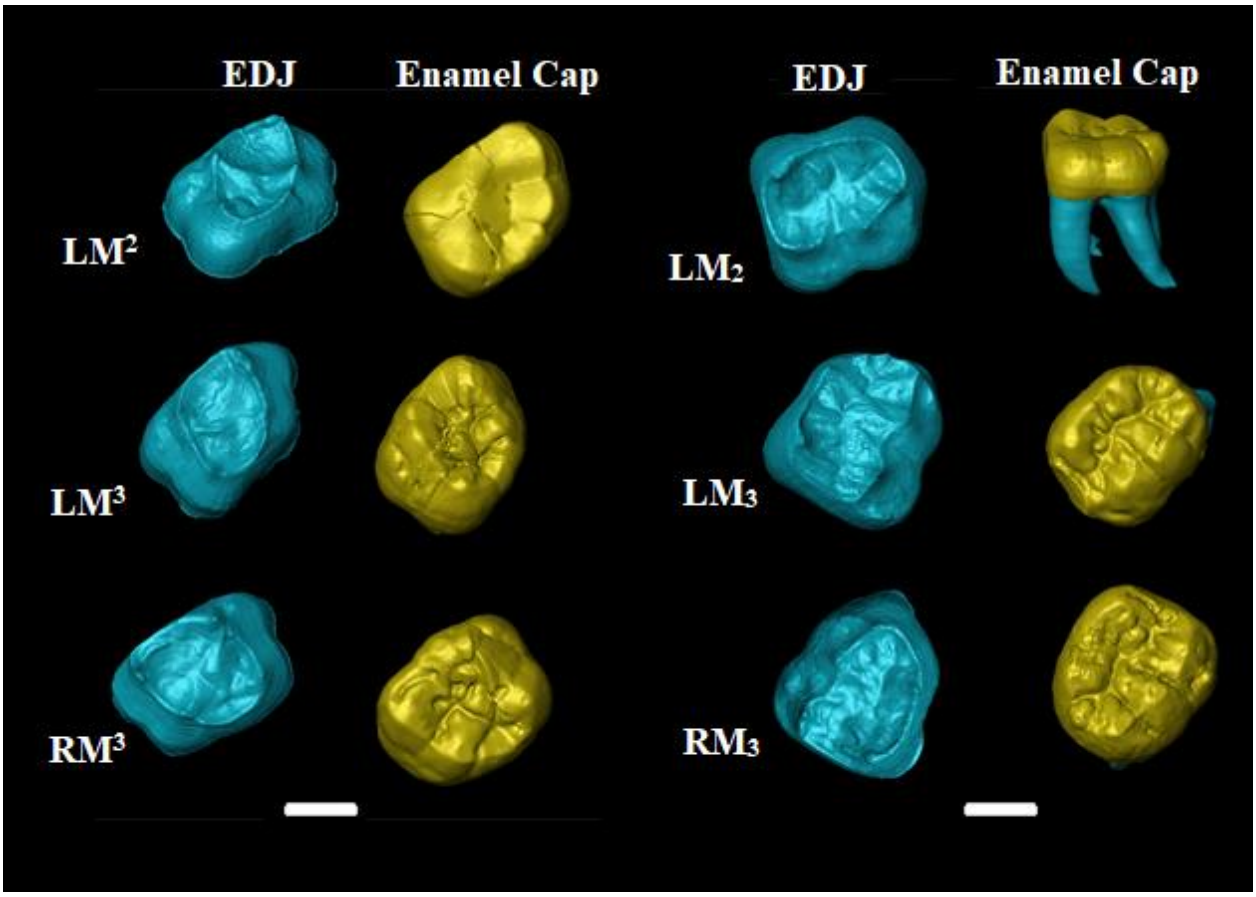

Figure 4.53. Virtually separated EDJ and enamel surfaces of selected teeth from StW 498. Maxillary molars, mesial towards the top; mandibular molars, mesial to the left. Scale bars = 10 mm.

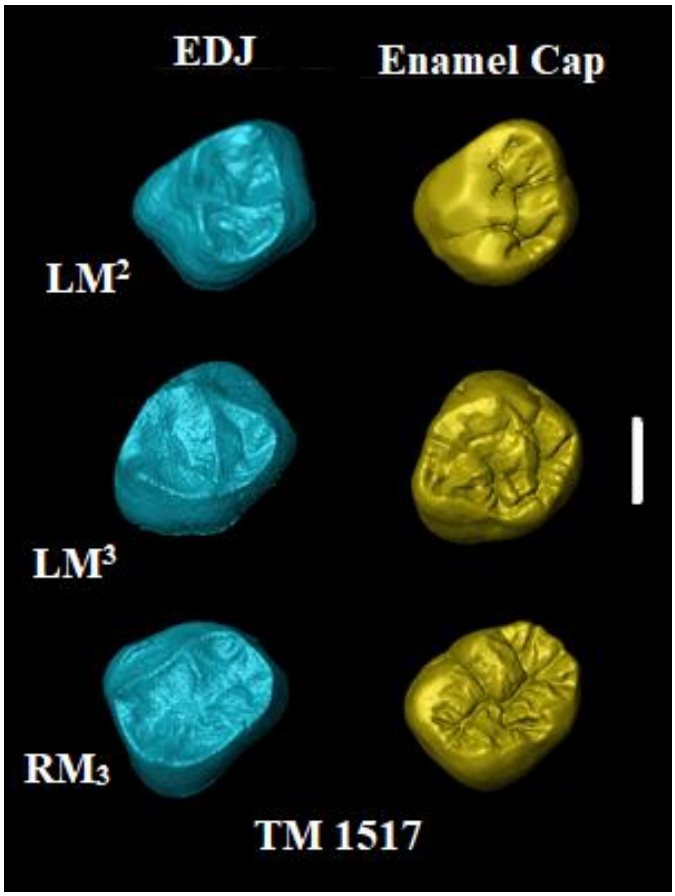

Figure 4.54. Virtually separated EDJ and enamel surfaces of selected teeth from TM 1517, a Sterkfontein fossil attributed to *P. robustus*. Maxillary molars, mesial towards the top; mandibular molars, mesial to the left. Scale bar = 10 mm.

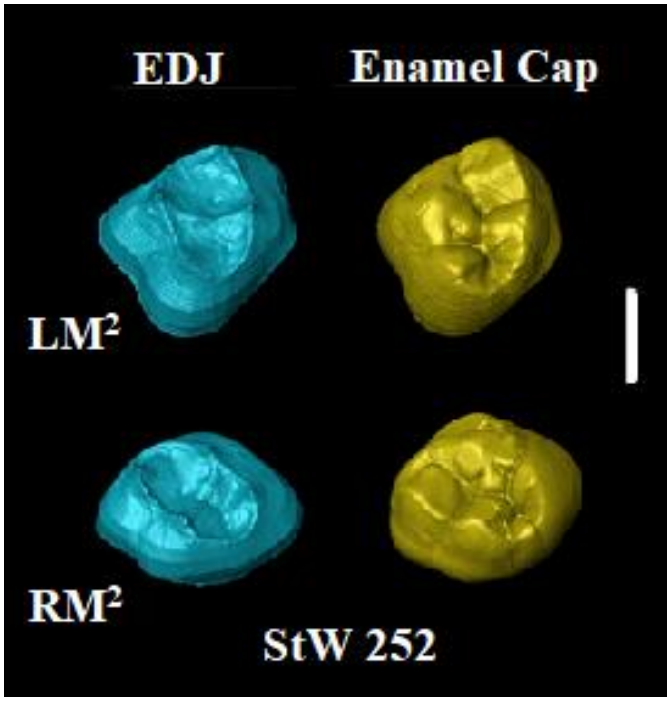

Figure 4.55. Virtually separated EDJ and enamel surfaces of selected teeth from StW 252, a Sterkfontein fossil attributed to *A. prometheus*. Mesial towards the top.Scale bar = 10 mm.

For some comparative specimens, AET dimensions reported by Olejniczak *et al*. (2008) were used. The results of the AET analysis are provided below in Tables 4.7 and 4.8.

Table 4.7. The average enamel thickness of the maxillary and mandibular second and third molars of StW 498 and selected comparative specimens.

Specimen	Tooth	Enamel volume (mm^3)	Dentine volume (mm^3)	Pulp volume (mm^3)	EDJ surface area (mm^2)	3D average enamel thickness (mm)	Reference
StW 498	LM^2	499	1074	—	528	0.95	This study
	LM^3	601	1049	—	530	1.13	This study
	RM^3	763	922	—	564	1.35	This study
	LM_2	610	1844	202	606	1.01	This study
	LM_3	810	1261	—	639	1.27	This study
	RM_3	773	1007	—	672	1.15	This study
A. prometheus							
StW 252	LM^2	474	576	21	428	1.11	This study
	RM^2	(594)	924	77	(530)	(1.12)	This study
A. africanus							
StW 3	LM_2	540.81	711.18	—	363.86	1.49	Olejniczak *et al* . (2008)
StW 421b	LM_2	503.57	589.82	—	409.39	1.23	Olejniczak *et al* . (2008)
	LM_3	345.47	531.32	—	353.52	0.98	Olejniczak *et al* . (2008)
StW 529	LM_3	554.49	561.71	—	347.45	1.60	Olejniczak *et al* . (2008)
StW 560	LM_3	551.06	777.22	—	394.43	1.40	Olejniczak *et al* . (2008)
StW 179	LM^3	480.39	573.15	—	288.14	1.67	Olejniczak *et al* . (2008)
P. robustus							
SK 31	RM^3	624.15	783.59	—	320.62	1.95	Olejniczak *et al* . (2008)
SK41	LM^3	574.60	620.92	—	419.66	1.37	Olejniczak *et al* . (2008)
TM 1517	LM^2	695	635	—	409	1.70	This study
	RM^3	690	414	—	399	1.73	This study
	RM_3	729	756	—	491	1.48	This study

Table 4.8. Average enamel thickness of the maxillary and mandibular molars of StW 498, along with samples of fossils attributed to *A. africanus*, *A. prometheus*, and *P. robustus*.

Specimen/Taxon	*n*	Mean AET (mm)
StW 498	6	1.14
A. africanus	6	1.40
A. prometheus	2	1.12
P. robustsus	5	1.65

Visualising enamel distribution

Colour mapping was used to visualise enamel distribution on selected premolars and molars. Colour mapping was performed for the third and fourth premolars, and the second and third molars of Sts 52, StW 252, and TM 1517 in order to assess their enamel distributions and compare them to those of StW 498. The enamel distribution is visualised as a topographic surface (Figure 4.56) where a colour scale represents local thicknesses from thinner (dark blue) to thicker values (red).

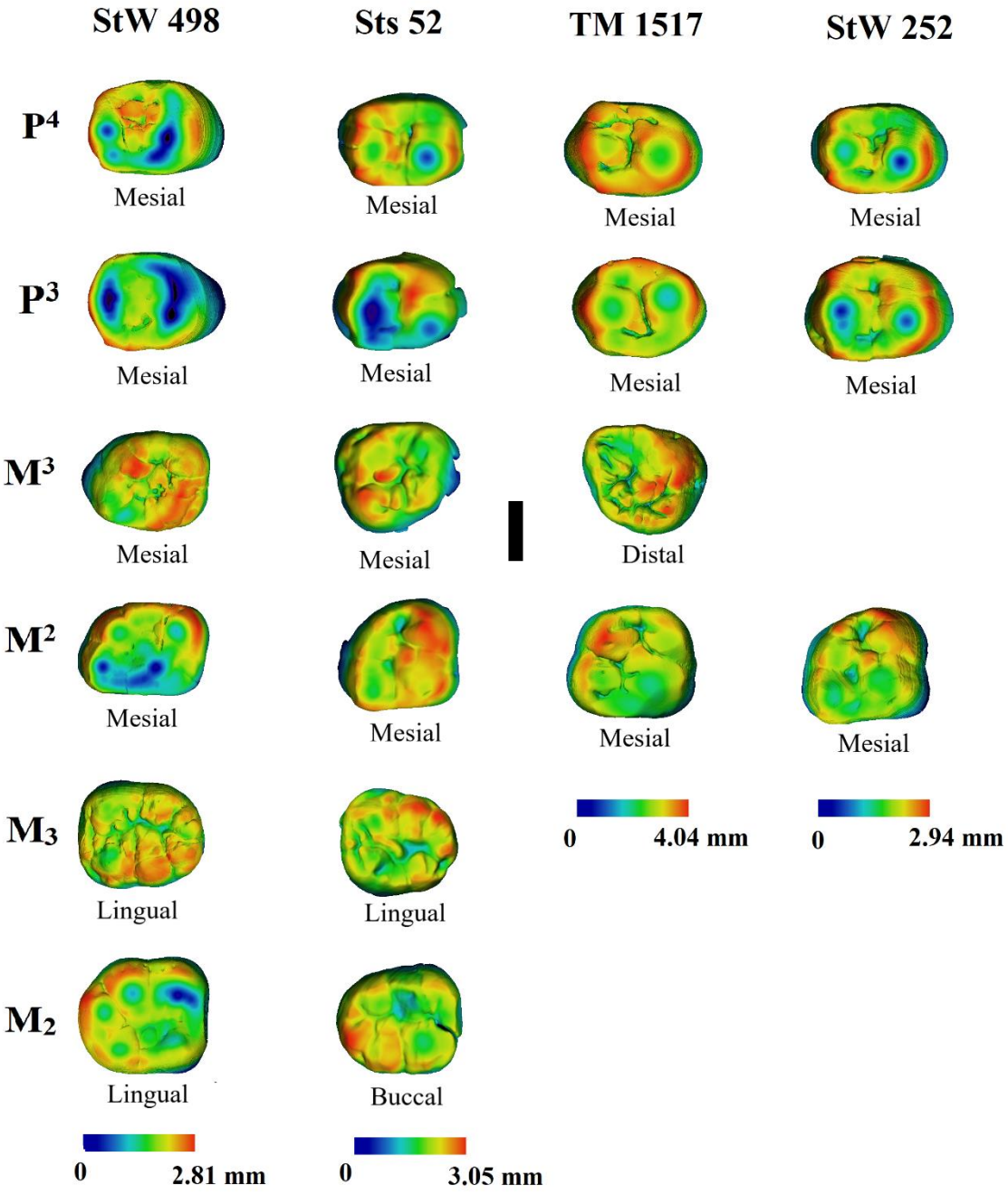

Figure 4.56. Topographic surface renderings representing enamel distribution on the minimally worn molars and premolars of StW 498, Sts 52 (*A. africanus*), TM 1517 (*P. robustus*), and StW 252 (*A. prometheus*). The colour scales indicate the maximum enamel thickness for each sample, where blue is thinner and red is thicker. I.e., the maximum enamel thickness for the premolars and molars of StW 498 is 2.81 mm, the greatest enamel thickness for Sts 52 is 3.05 mm, TM 1517 has a maximum thickness of 4.04 mm, and the greatest enamel thickness for StW 252 is 2.94 mm. Scale bar in the middle = 10 mm.

Maximum enamel thickness distributions in StW 498, StW 252, Sts 52 (*A. africanus*), and TM 1517 (*P. robustus*) are presented in Table 4.9.

Table 4.9. Maximum enamel thickness distribution for the P^3, P^4, M^2, M^3, M_2, and M_3 of StW 498 and selected belonging to StW 252 (*A. prometheus*), Sts 52 (*A. africanus*), and TM 1517 (*P. robustus*). All measurements are in mm unless stated otherwise.

	Maximum enamel thickness distribution					
Specimen	**P^3**	**P^4**	**M^2**	**M^3**	**M_2**	**M_3**
StW 498	1.87	1.85	2.49	2.75	2.45	2.81
StW 252	1.82	2.07	2.94	—	—	—
StS 52	2.38	2.39	2.91	3.05	2.79	2.86
TM 1517	2.72	3.12	4.04	3.72	—	—

4.2.3. Anatomical observations

The following section presents anatomical observations related to root morphology, maxillary shape, and mandibular shape and size, as seen in StW 498 and selected specimens representing *A. prometheus*, *A. africanus*, and *P. robustus*.

Root morphology

This study revealed that the roots of the incisors and canines of *A. prometheus* are morphologically different from those of *A. africanus* (Figures 4.57 and 4.58). The roots of the former exhibit distinct grooves on their mesial and/or distal surfaces. These grooves are absent from the analogous positions on the roots of *A. africanus*. Additionally, the canine and incisor roots of *A. prometheus* are mesiodistally broad and curve distally, while the roots of *A. africanus* are relatively narrow and straight. Note that in their paper, Moggi-Cecchi *et al*. (2006) attributed all the Sterkfontein Member 4 and Member 5 specimens to *A. africanus*, including StW 109. However, based on the above information on root morphology (and on the PCA of its mandibular molars), StW 109 is most aligned to other specimens attributed to *A. prometheus*.

Preserved roots of the StW 498 anterior dentition (i.e., the left maxillary lateral incisor, the left maxillary canine, and the right mandibular canine), each exhibit grooves on the mesial and distal surfaces accompanied by distal curving (Figures 4.57 and 4.58).

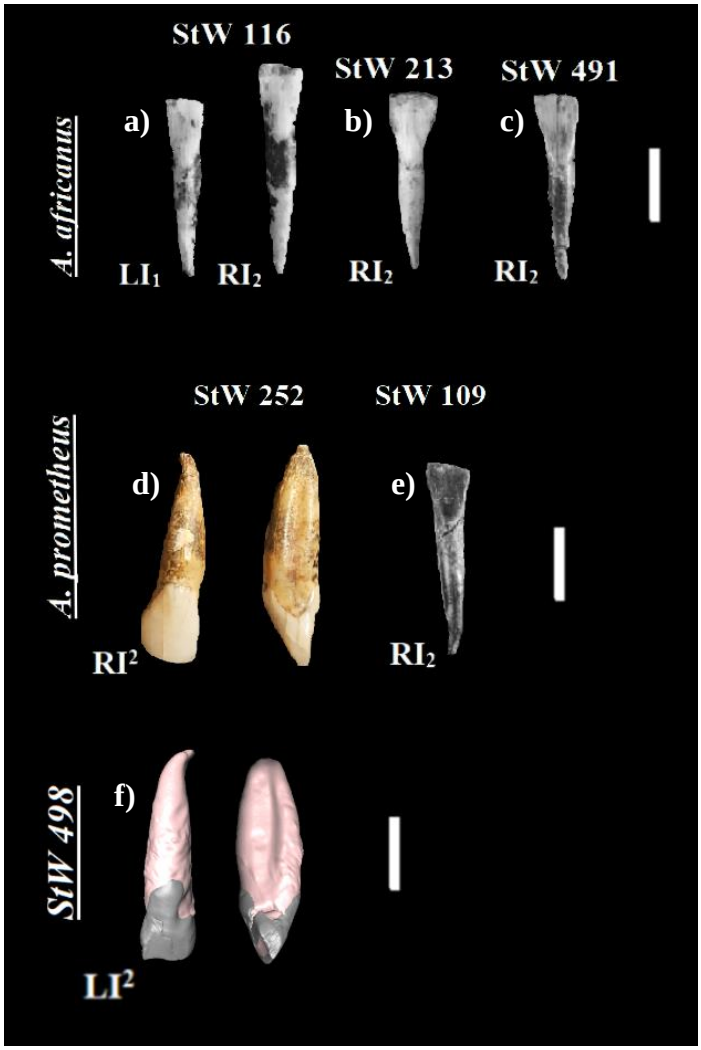

Figure 4.57. Incisor root morphology of specimens attributed to *A. africanus, A. prometheus*, and StW 498. All views are lingual unless stated otherwise: a) a) StW 116 left mandibular central incisor and right mandibular lateral incisor (adapted from Moggi-Cecchi *et al*. 2006, Figure 5, p. 274); b) StW 213 right mandibular lateral incisor (adapted from Moggi-Cecchi *et al*. 2006, Figure 7, p. 288); c) StW 491 right mandibular lateral incisor (adapted from Moggi-Cecchi *et al*. 2006, Figure 12, p. 311); d) StW 252 right maxillary lateral incisor, labial and distal views, respectively (taken by the author); e) StW 109 right mandibular lateral incisor, labial view (adapted from Moggi-Cecchi *et al*. 2006, Figure 4, p. 274).; f) StW 498 left lateral incisor, labial and mesial views, respectively. Scale bars = 10 mm.

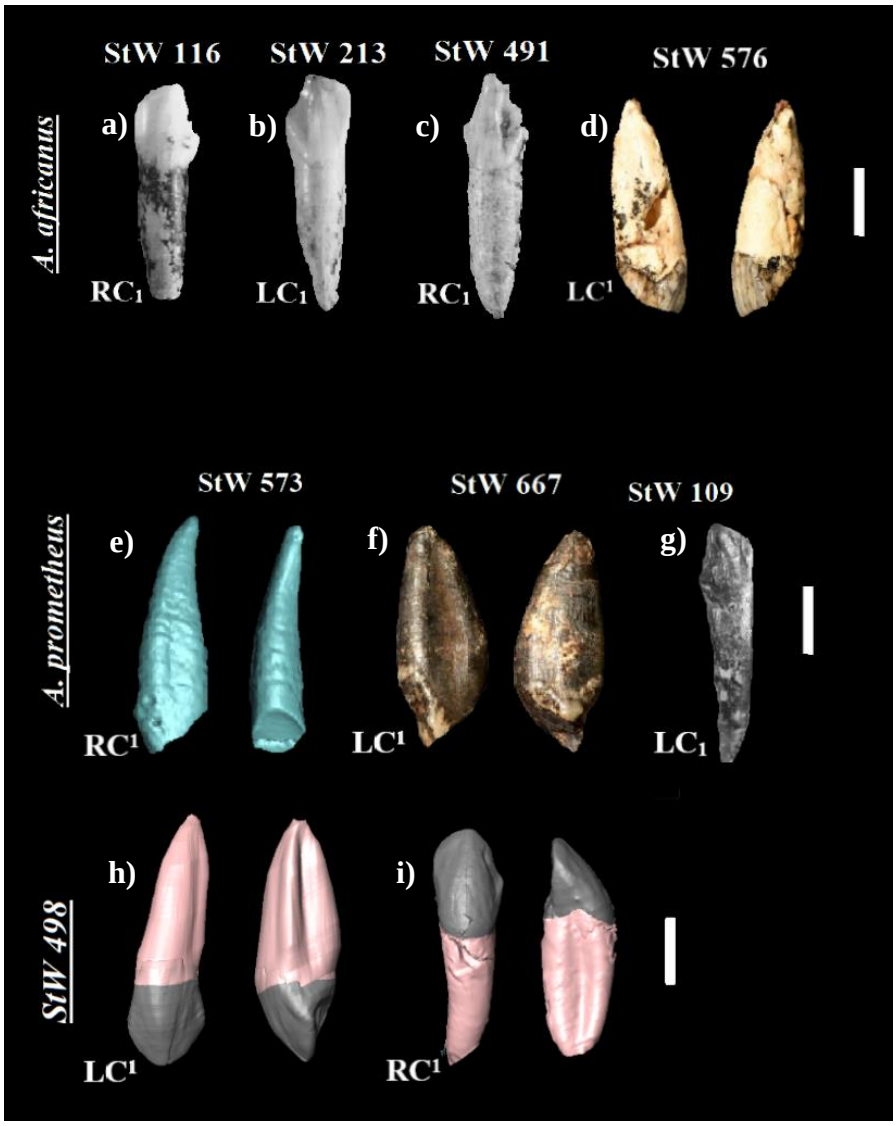

Figure 4.58. Canine root morphology of specimens attributed to *A. africanus*, *A. prometheus*, and StW 498: a) StW 116 right mandibular canine, lingual view (adapted from Moggi-Cecchi *et al*. 2006, Figure 5, p. 274); b) StW 213 left mandibular canine, lingual view (adapted from Moggi-Cecchi *et al*. 2006, Figure 7, p. 288); c) StW 491 right mandibular canine, lingual view (adapted from Moggi-Cecchi *et al*. 2006, Figure 12, p. 311); d) StW 576 left maxillary canine, mesial and distal views, respectively (adapted from Clarke & Kuman 2018); e) StW 573 right maxillary canine, mesial and lingual views of renderings, respectively (images courtesy of Tea Jashashvili); f) StW 667 left maxillary canine, mesial and distal views, respectively (adapted from Clarke & Kuman 2018, Figure 22, p. 61); g) StW 109 left mandibular canine, labial view (adapted from Moggi-Cecchi *et al*. 2006, Figure 4, p. 274); h) StW 498 left maxillary canine, labial and mesial views, respectively; i) StW 498 right maxillary canine, labial and mesial views, respectively. Scale bars = 10 mm.

Palate and maxillary shape

The shape of the palate differs significantly between *A. africanus*, *A. prometheus*, and *P. robustus*. The palate of *A. prometheus* is narrow, relatively long, shallow anteriorly and deep posteriorly, and somewhat rectangular in shape (e.g., StW 252, StW 573; Clarke & Kuman 2018). In contrast, in *A. africanus* the palate is short, relatively uniformly deep, and wider and more rounded, as can be seen in the palates of Sts 5, Sts 53, and StW 73 (Clarke & Kuman 2018). The palate of *P. robustus*, on the other hand, is broad, relatively long, shallow anteriorly and deep posteriorly, and rectangular in shape, as demonstrated by SK 48 (Figure 4.59).

In addition, *A. prometheus* exhibits corrugations on the alveolar bone over the incisor roots and a steeply sloped facial profile, as observed by Clarke and Kuman (2018). In *A. africanus*, however, there are no corrugations onthe alveolar bone over the incisor roots and the anterior maxilla is extremely rounded, presenting a convex mid-face (e.g., Sts 52; Clarke & Kuman 2018). The facial profile of *P. robustus* is sloped, but not to the same extent as observed in *A. prometheus*, and there are also corrugations on the alveolar bone over the incisor roots, as demonstrated by SK 12 (Figure 4.60) and SK 847 (Clarke 1977).

The palate of StW 498 is narrow, relatively long, shallow anteriorly and deep posteriorly, and has a somewhat rectangular shape. StW 498 has corrugations on the alveolar bone over the incisor roots. Refer to Table 4.3 for palatal dimensions of StW 498 and the above mentioned specimens.

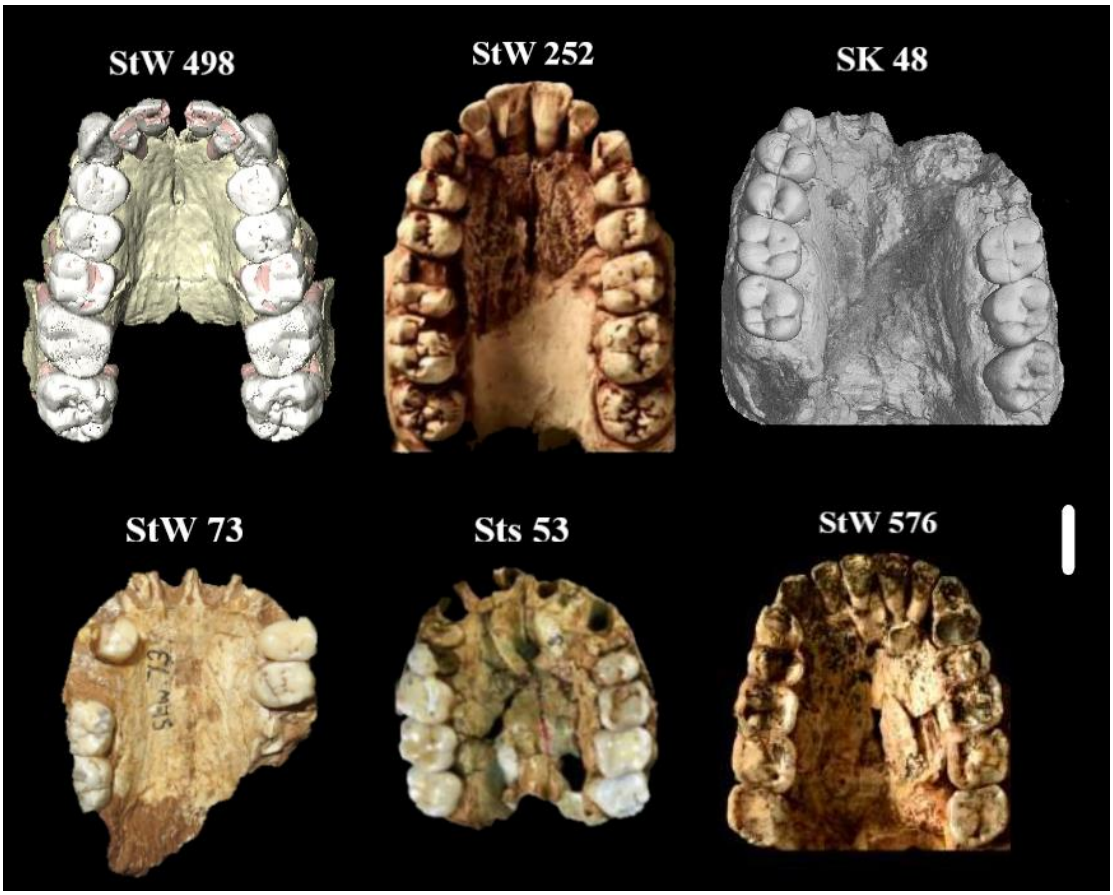

Figure 4.59. Comparisons of the palates of StW 498, SK 48 (*P. robustus*), StW 252 (*A. prometheus*), StW 73 (*A. africanus*), Sts 53 (*A. africanus*), and StW 576 (*A. africanus*). Images of StW 252, Sts 53, and StW 576 are adapted from Clarke & Kuman (2018, Figure 17, p. 56). Scale bar = 20 mm.

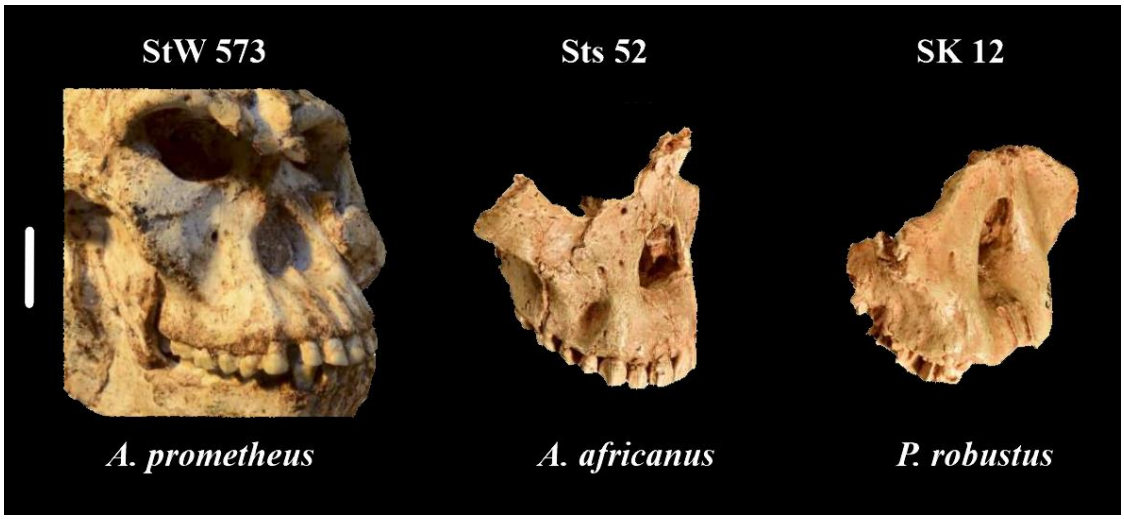

Figure 4.60. Comparisons of the anterior maxilla of StW 573 (*A. prometheus*), Sts 52 (*A. africanus*), and SK 12 (*P. robustus*). Note the corrugations on the alveolar bone over the incisor roots of StW 573. These are absent in Sts 52 (adapted from Clarke & Kuman 2018, Figure 14, p. 53). Scale bar =

As mentioned above, the roots in StW 498 exhibit distal curving that is not seen on the roots of *A. africanus* or *P. robustus*. The distal curving of the roots and anteriorly projecting incisor crowns in StW 498 closely resembles those seen in StW 252 (*A. prometheus*) and in the Sterkfontein Member 2 specimen StW 573 (*A. prometheus*), also known as 'Little Foot'. Moreover, there is a noticeable similarity in the shape and size of the maxillary dental arcade and in the sloping wear on the anterior dentition of SW 498 and StW 573 (Figure 4.61).

Note the difference of the incisor procumbence between StW 252 (*A. prometheus*) and Sts 52 (*A. africanus*) (Figure 4.62), and how the incisor crowns project anteriorly in StW 252; this compares favourably with the forms of the incisor crowns of StW 573 (*A. prometheus*) and StW 498. Clarke (1988, *et seq.*) suggests that the procumbent incisors and corrugations are diagnostic traits of *A. prometheus* and not seen in *A. africanus*.



Figure 4.61. Comparisons of the maxillary dental arcade and maxillary teeth belonging to StW 252 (*A. prometheus*), StW 573 (*A. prometheus*) and StW 498. Top row: Occlusal views. Bottom row: StW 252 medial view, and StW 573 and StW 498 lateral views. Note that the dentition of StW 573 is heavily worn. Images of StW 252 adapted from Clarke & Kuman (2018, Figure 17, p. 56, and Figure 21, p. 60). Images of StW 573 courtesy of Tea Jashashvili. Scale bar = 10 mm.

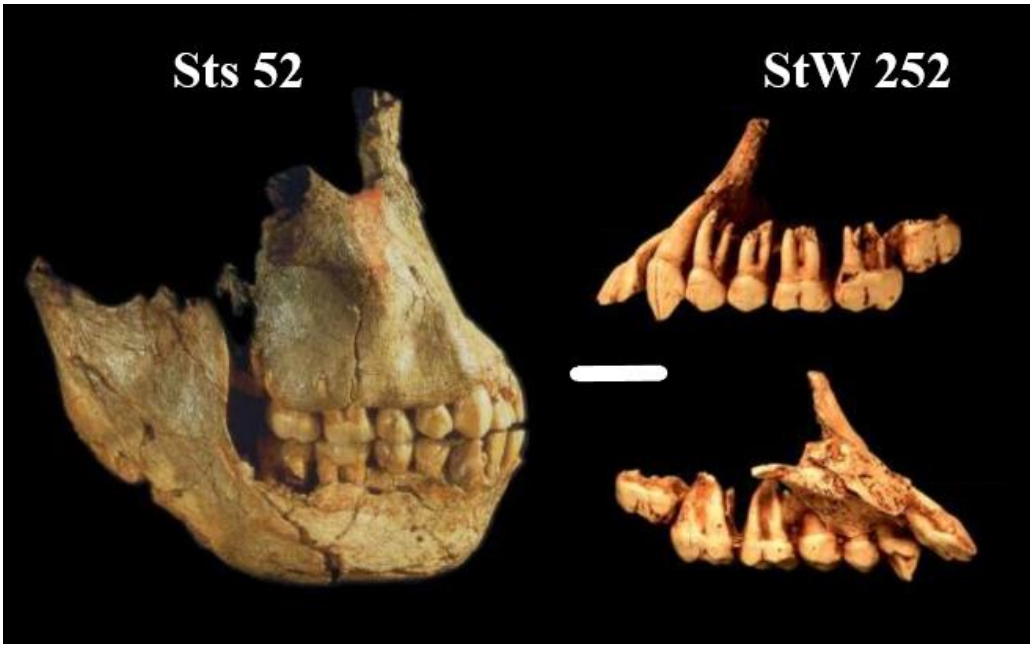

Figure 4.62. Comparisons of the incisor procumbence between Sts 52 (*A. africanus*) and StW 252 (*A. prometheus*). All views are lateral, except for the lower right view which is medial. Adapted from Clarke & Kuman (2018, Figure 21, p. 60). Scale bar = 20 mm.

In addition, the left maxilla of StW 498a joins together with the right maxilla of MLD 9, an *A. prometheus* from Makapansgat (Clarke, pers. comm., Figure 4.63).

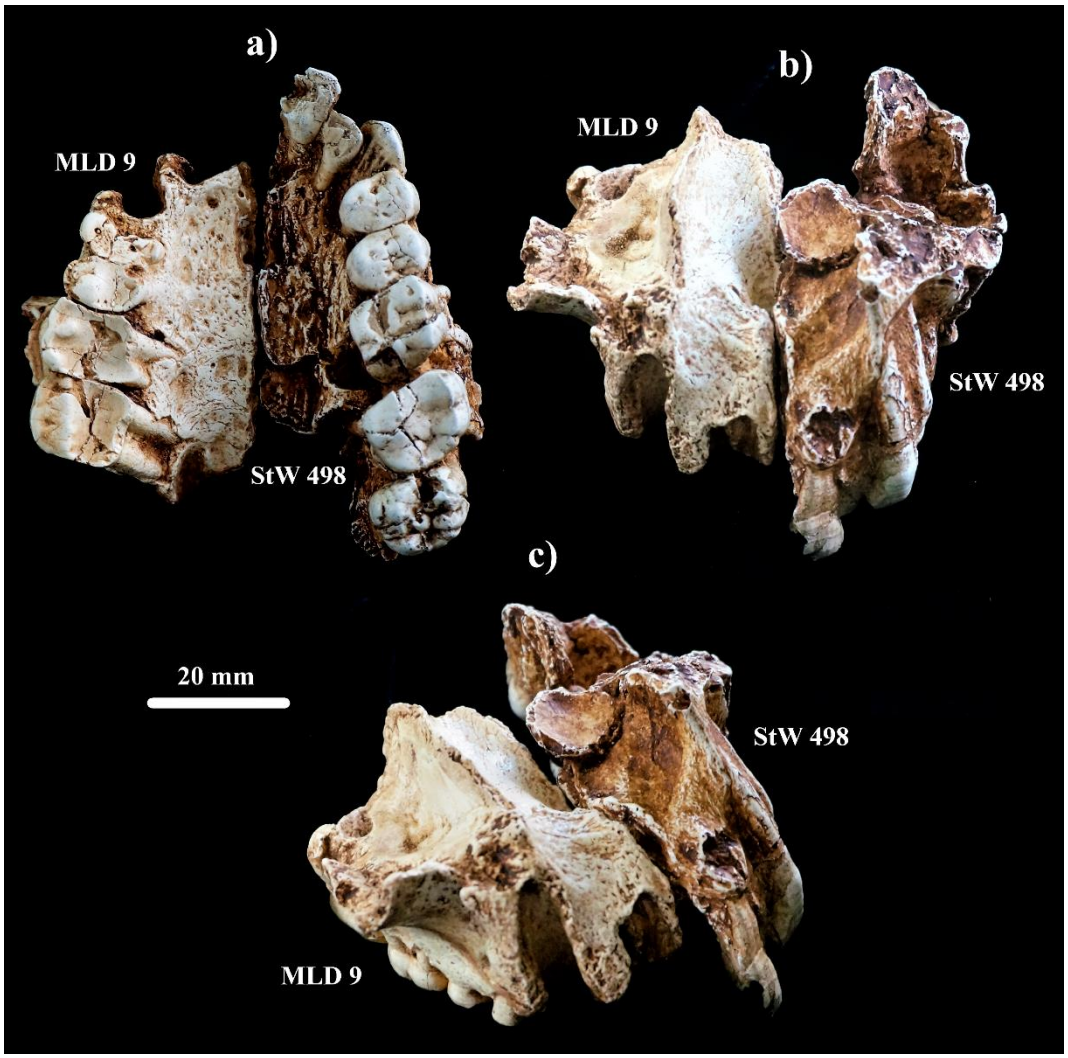

Figure 4.63. Left maxilla of StW 498a joined with the right maxilla of MLD 9 (*A. prometheus*): a) occlusal view; b) anterior view; c) three-quarter view. Images courtesy of R.J. Clarke.

Mandibular size and shape

As observed by Clarke and Kuman (2018), the mandible of *A. prometheus* is large, with a thick corpus body that becomes extremely thin on the inferodistal surface (by the gonion). Given the size and robusticity of the teeth in these mandibles, the corpus is relatively shallow (e.g., Sts 36 and StW 573). In contrast, the mandible of *A. africanus* is shallow, smaller, and has a consistently thick corpus (e.g., Sts 52). By comparison, *P. robustus* has a deep, robust, and thick mandibular body and ramus, which can be seen in the SK 843 mandibular fragment.

The shape and large size of the mandible of StW 498 is exemplified in an inferior view (Figure 4.64). StW 498 has a thick corpus body, which becomes thin on the inferodistal surface. Because the condyles are missing, it is not possible to assess the degree of flaring of the ramus. Refer to Table 4.6 for the mandibular dimensions of StW 498 and the above mentioned specimens.

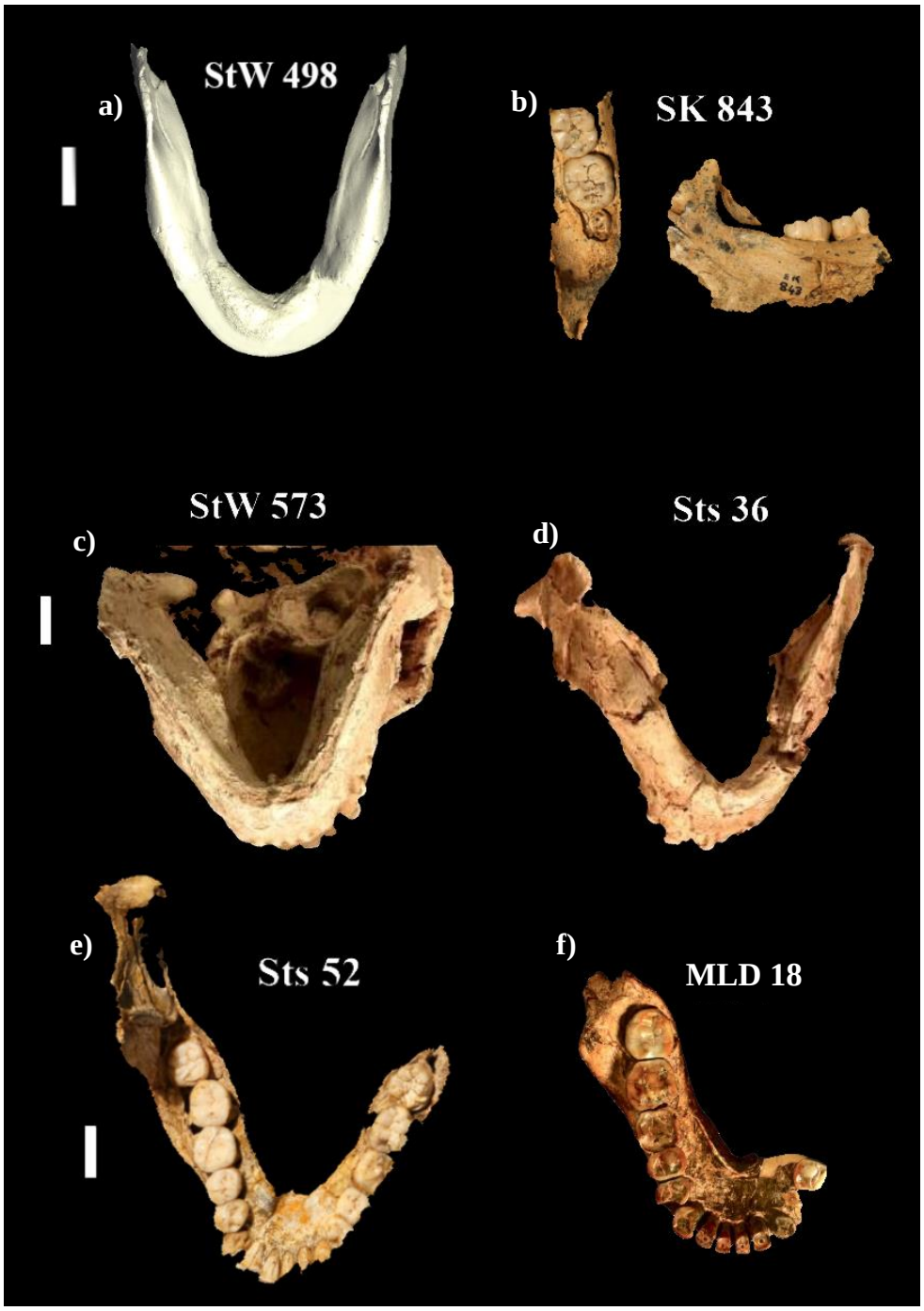

Figure 4.64. Comparison of mandibular shape and size, all views are inferior unless stated otherwise: a) StW 498; b) SK 843 (*P. robustus*), occlusal and lateral views, respectively; c) StW 573 (*A. prometheus*) (adapted from Clarke & Kuman 2018, Figure 19, p. 58); d) Sts 36 (*A. prometheus*) (adapted from Clarke & Kuman 2018, Figure 19, p. 58); e) Sts 52 (*A. africanus*), occlusal view; f) MLD 18 (*A. africanus*), occlusal view (adapted from Clarke & Kuman 2018, Figure 23, p. 62. Note the thick distal corpus of Sts 52 and MLD 18 even in occlusal views. Scale bars = 10 mm.

Moreover, the shape of the mandible of StW 498 compares favourably with that of Sts 36 (*A. prometheus*; Clarke & Kuman 2018) and contrasts with MLD 40 (*A. africanus*; Clarke & Kuman 2018) (Figure 4.65). The mandibular dentition of

StW 498 compares well with that of StW 109 (*A. prometheus*) and MLD 2 (Clarke pers. comm.). Although MLD 2 belongs to a juvenile *A. prometheus* (Dart 1948a-c), the unworn molars clearly demonstrate the low, bulbous cusps (Figure 4.66).



Figure 4.65. Casts comparing the mandibles of Sts 36 (*A. prometheus*), StW 498, and MLD 40 (*A. africanus*) in basal views. Images courtesy of R.J. Clarke.

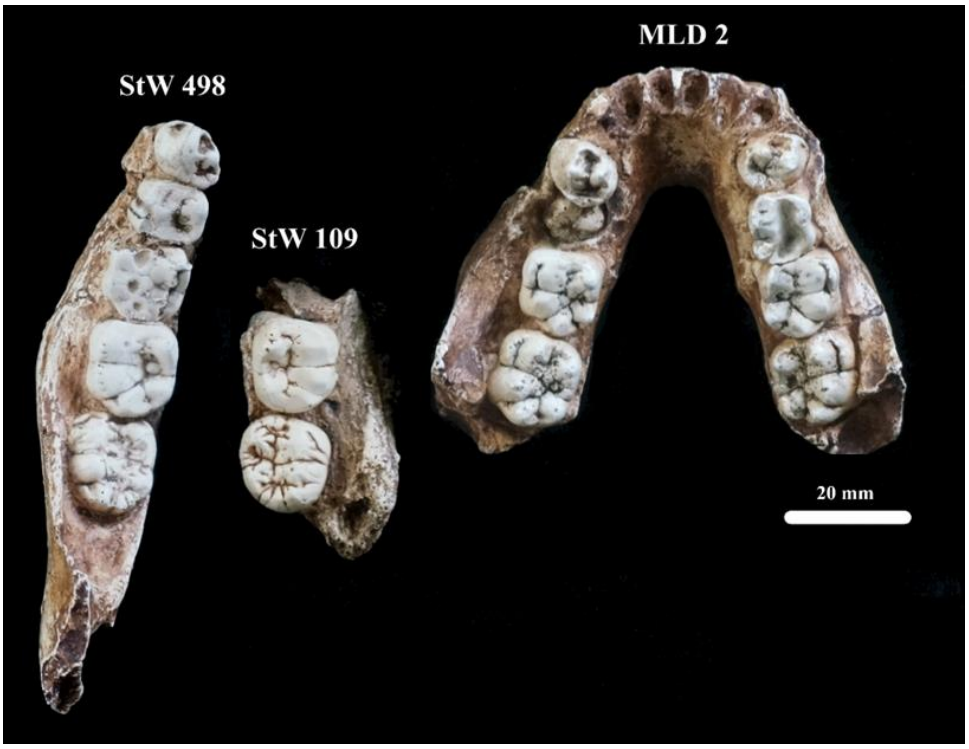

Figure 4.66. Comparisons of the mandibular second and third molars of StW 498, StW 109 (*A. prometheus*), and MLD 2 (*A. prometheus*). Images courtesy of R.J. Clarke.

Chapter 5

Discussion and Conclusions

This chapter, divided into two sections, provides a summary of the results and discusses the implications of the findings presented in the preceding chapters. The first section is divided into several sub-sections: first, the numerous materials and methods employed throughout this study are assessed and discussed. Second, the in silico reconstruction of StW 498 and anatomical observations are discussed and the taxonomic affinity of StW 498 is addressed. Finally, the limitations of this study and future directions are presented and discussed. A summary and conclusions, are provided in the last section.

5.1. Discussion

The following section assesses the reliability of virtual reconstruction methods, including its limitations, and of the quantitative-based morphological comparative methods utilised throughout the course of this research.

5.1.1. Materials and methods

High resolution microCT scanning and virtual reconstruction offers powerful and versatile non-destructive methods to correct plastic deformation and help restore broken specimens that may be too fragile or crushed to permit physical reconstruction. In the case of StW 498, physical reconstruction was not possible due to the extent of crushing and excessive fragmentation of bones, in addition to the presence of plastic deformation. Software programs, such as Avizo 9.0.1 (Thermo Fisher Scientific Group, https://www.thermofisher.com), enabled reconstruction of the left and right mandibles and the left and right maxillae of StW 498, which facilitated production of a complete three-dimensional (3D) rendering of the lower face and dentition. Virtual reconstruction allowed inspection of the internal anatomy of StW 498 that was crucial for determining whether the specimen exhibited any pathologies. The majority of the right side of

the partial skull was too fragmented to extract and could not be reconstructed, thus the reconstruction of the lower face of StW 498 relied mostly on mirror imaging the left maxilla and mandible as proxies for the right maxilla and mandible — a method that was highly valuable in this study.

Virtual methods, like any reconstruction process, have limitations. Virtual reconstruction can be extremely time consuming. In the case of StW 498, manual segmentation tools were necessary, which required slice-by-slice processing of thousands of image slices. It is important to note that high resolution image acquisition and processing can be extremely costly, since software programs such as Avizo and Amira (Thermo Fisher Scientific Group, https://www.thermofisher.com) can cost upwards of 10,000 USD for a license. Research-oriented high resolution scanning facilities are not readily available (especially in Africa) and are limited.

Through comparative metric multivariate analyses of the canines, maxillary premolars, and maxillary third molars, it was possible to differentiate morphotypes representing *A. africanus* from morphotypes of *A. prometheus* and *P. robustus*. However, it was not always possible to readily differentiate *A. prometheus* from *P. robustus*. By comparison, analysis of the maxillary M^2 was less effective for differentiating between these hominid taxa, most likely because of the small sample. Three-dimensional analysis of average enamel thickness and its distribution on unworn or minimally worn molars is an effective tool for differentiating *A. africanus* from *P. robustus* and *A. prometheus.* However, this type of analysis requires excellent preservation of both the enamel cap and the enamel-dentine junction (EDJ), as calculating average enamel thickness relies on the volume (mm^3) of both the enamel cap and the EDJ. Although a larger sample size is required for statistical analysis, such virtual analysis is still valuable in the interim since it enables us to visualise patterns in teeth, even in a small sample. It cannot, however, account for the range of variation that may exist.

5.1.2. StW 498: reconstruction and anatomical observations

Reconstruction

It is important to stress that reconstruction of StW 498 relied solely on the anatomy of the specimen, without any preconceptions. The left maxilla and mandible are, for the most part, well-preserved, and intact. Therefore, establishing anatomical positions of teeth on the left side of the dental arcade can be accomplished. Because the right side suffered extreme fragmentation and plastic deformation, it cannot be determined what the exact form of the right side was. However, it can be stated that the complete virtual reconstruction of StW 498 is close to the original form based on the following:

The high resolution CT scans enabled visualisation of internal anatomy of the specimen, which in turn enabled reconstruction of the broken, displaced dentition, which preserved interproximal contact facets. Thus, correct shape and morphology of the left and right maxillary and mandibular dentition (and most of the roots) are now known. Through segmentation of high resolution CT scans, the preserved alveoli, the incisive canal, the intermaxillary suture, and the mandibular symphysis (i.e., including its remarkably well-preserved genial fossa) could be visualised. These anatomical structures were crucial for determining shape of the anterior maxilla, the palate, and the mandible. The maxillary dentition (specifically, the left canine, premolars, and first and second molars) could be occluded with the mandibular dentition. Thus, it was possible to infer angle and positioning of the maxilla with the mandible placed in anatomical position. All of these features made it possible to create a virtual reconstruction of StW 498 that is close to the original form.

Anatomical observations

First, based on the internal morphology of the dental arcade and on the size and thickness of the molar enamel, StW 498 was likely a young adolescent male. The adolescent age of StW 498 is further supported by the incomplete development of the maxillary and mandibular third molar roots. The high resolution CT images

revealed that the specimen exhibited a dental pathology. Specifically, there is evidence of an atypical eruption and position of the left maxillary canine that appears to have resulted from dental crowding. However, it is unclear whether the right maxilla exhibited the same extent of dental crowding (if any) as the left. The current position of the right lower canine, however, was unlikely to be the result of a pathology exhibited in vivo (as suggested by Schwartz & Tattersall 2005), but rather due to post-depositional processes acting on the specimen during its fossilisation.

Maxillary occlusal wear is lingually sloped and is greater on the right side than on the left. There are two possible explanations. First, pathology of the maxillary dentition resulted in a mechanical issue — malocclusion can result in altered wear patterns because tooth rows do not precisely occlude. Second, it could be the results of a conscious behavioural adjustment related to pain. In other words, the right dental arcade may have been used more during life than the left side, possibly because of the problems evident on the left maxilla. The atypical position of the left canine (if the right side did not exhibit the same condition) could have made it uncomfortable to use the left side of the mouth, resulting in preferred usage of the right side and thus more occlusal wear. Another specimen that exhibits asymmetric wear patterns in the presence of evidence for dental pathology is SK 83, a Swartkrans partial cranium belonging to *P. robustus*. Clarke (1990) observed that the first and second right maxillary molars of SK 83 are much more worn than those on the left. SK 83 also exhibits a dental anomaly in the form of a retained central deciduous maxillary incisor that is positioned between the right central and lateral permanent incisors. Clarke (1990) noted that retention of the deciduous incisor after eruption of the permanent dentition resulted in the right lateral incisor being slightly rotated and thus displaced. However, further investigation with a larger sample size is required to determine the exact cause of the asymmetric wear patterns discussed here.

5.1.3. The taxonomic attribution of StW 498

According to Clarke and Kuman (2018: 20), "The appropriate way to identify a fossil species should be first to identify morphological characters that unite or separate individual specimens, and then to group those specimens according to similarities or differences between the clusters of morphological features, whilst allowing for expected variations due to gender, developmental status, or a reasonable amount of individual variation". The importance of this statement cannot be overstated.

The features discussed below are presented to differentiate *A. prometheus* from *A. africanus*. When referring to *A. prometheus*, the author accepts the definition put forth by Clarke (1988, *et seq*.).

Incisor and canine crown and root morphology

Root morphology was observed to differ substantially between *A. africanus* and *A. prometheus*. In all *A. prometheus* samples, (i.e., StW 667, StW 573, StW 252, and StW 109), the canine and incisor roots are mesiodistally thick (Clarke & Kuman 2018) and also have distinct grooves, as well as distal curvature.

In all *A. africanus* samples, the canines are smaller than those of *A, prometheus*. In addition, the incisor and canine roots lack analogous grooves that are exhibited in *A. prometheus* samples, plus the roots of the former taxon are straight rather than curved.

The large canines of StW 498 are unlike the smaller canines of *A. africanus*, such as those seen in specimens StW 213, StW 491, and StW 576 (see Tables 4.1 and 4.4). Rather, the SW 498 canines compare favourably with those of specimens such as TM 1516, StW 183, StW 252, StW 573, and StW 667 (see Figures 4.57 and 4.58); these specimens are attributed to *A. prometheus* (Fornai 2009; Clarke & Kuman 2018). In addition, the roots of the maxillary canines of StW 498 are flattened or oval in cross-section (i.e., much wider buccolingually than mesiodistally). This contrasts with the rounded cross-section of the canine root in

A. africanus specimens (e.g., StW 576; Clarke & Kuman 2018). Clarke and Kuman (2018) suggest that large, flattened maxillary canine roots, are a diagnostic trait of *A. prometheus*. In this feature, StW 498 is similar to the canine root belonging to StW 667, an *A. prometheus* identified by Clarke and Kuman (2018). Moreover, the canine and incisor roots of StW 498 exhibit grooves on their mesial and distal surfaces, are mesiodistally thick, and exhibit distal curvature. In all the aforementioned features, StW 498 contrasts with specimens such as StW 116, StW 213, StW 491, and StW 576, which exhibit straight, relatively narrow roots that lack grooves on the root surfaces. These specimens have been attributed to *A. africanus* (Moggi-Cecchi *et al*. 2006; Clarke & Kuman 2018).

Maxillary and mandibular shape and size

The shapes of the maxilla, palate, and mandible differ significantly between the species investigated in the present study. In *A. prometheus* samples the inferior nasal margin is smooth and concave, while the palates are long and rectangular, and shallow anteriorly (e.g., StW 252; StW 573; Clarke & Kuman 2018). The canine jugum is extremely large and the maxillary incisors of *A. prometheus* are procumbent, with corrugations on the alveolar bone over incisor roots on the nasoalveolar clivus (e.g., StW 252; StW 573; Clarke & Kuman 2018). This procumbence seems to be correlated with the anteriorly shallow palate and the steeply sloped facial profile (see Figures 4.59, 4.61, and 4.62).

All *A. africanus* maxillary samples exhibit a palate that is short and square, and anteriorly deeper (Dart 1925; Robinson 1956; Rak 1983). Moreover, there are no corrugations on the alveolar bone over the the incisor roots; the anterior maxilla is rounded, resulting in a convex mid-face (e.g., Sts 5, Sts 52, StW 53; Clarke & Kuman 2018). In *P. robustus*, the palate appears long and wide, the nasal aperture is concave, and there are corrugations (though not as prominent as those seen in *A. prometheus*) on the alveolar bone over the incisor roots on the nasoalveolar clivus (e.g., SK 12, SK 46; SK 48; Broom 1938a; Broom & Schepers 1946; Broom &

Robinson 1952; McCollum *et al*. 1993; Grine & Strait 1994; Clarke 1994) (see Figures 4.59 and 4.60).

The mandible of *A. prometheus* is large and shallow, but one feature particularly stands out: although the body of the corpus is thick, the base of the corpus is posteriorly thin, with large posterior teeth (e.g., MLD 2; Sts 36, StW 573; Dart 1948b; Clarke & Kuman, 2018). This pattern was not observed in *A. africanus* samples. Rather, the corpus and ramus are consistently very thick from the superior to inferior portions, and the posterior teeth are smaller (e.g., Sts 52) than those seen in specimens representing *A. prometheus*. *P. robustus*, on the other hand, exhibits a large mandible which is anomalously deep and transversely very thick, with large posterior teeth (e.g., SK 23, SK 52; Broom 1938a, Broom & Schepers 1946; Clarke, Howell & Brain 1970; Clarke 1996) (see Figure 4.64).

StW 498 exhibits a smooth, concave inferior nasal margin, corrugations on the alveolar bone over the incisor roots, procumbent incisors, a long, rectangular palate, and an anteriorly shallow palate that becomes posteriorly deeper. In these features, StW 498 contrasts with specimens attributed to *A. africanus* (e.g., Sts 5, Sts 52, StW 53, StW 576, TM 1512; Clarke & Kuman 2018), as well as contrasts with specimens attributed to *P. robustus* (e.g., SK 12, SK 46, SK 847; Clarke 1977). Rather, in these respects, StW 498 compares favourably with specimens attributed to *A. prometheus* (e.g., StW 183, StW 252, StW 573; Clarke & Kuman 2018). Moreover, the StW 498 left maxilla fits together with the MLD 9 right maxilla, (Clarke, pers. comm.; see Figure 4.63). The maxillary and dental arcade shape, procumbent incisors, large canine roots, and root curvature, of StW 498 closely resemble similar features exhibited by StW 252 and StW 573. This resemblance is exemplified in Figure 4.61.

The mandible of StW 498 is large with a thick mandibular body that becomes significantly thinner towards the distal end of the corpus; despite the slender corpus, the posterior teeth are large with low, bulbous cusps (see Figures 4.25, 4.40, 4.41 and 4.43). The features seen in the mandible of StW 498 contrast with those seen in specimens attributed to *A. africanus* (e.g., MLD 18, Sts 52; Clarke & Kuman 2018), and with those attributed to *P. robustus* (e.g., SK 15, SK 23;

Clarke, Howell & Brain 1970). The StW 498 mandible compares well with *A. prometheus* mandibles represented by Sts 7, StW 384, and StW 573 (Clarke & Kuman 2018). These specimens exhibit a large mandible, a noticeably slender corpus, and large posterior teeth with low, bulbous cusps. In addition, the shape of the mandible of StW 498 compares favourably with that of Sts 36 (*A. prometheus*; Clarke & Kuman 2018) and contrasts with MLD 40 (*A. africanus*; Clarke & Kuman 2018) (see Figure 4.65). Furthermore, the mandibular dentition of StW 498 compares well with that of StW 109 (*A. prometheus*) and MLD 2 (Clarke pers. comm.) Although MLD 2 belongs to a juvenile *A. prometheus* (Dart 1948a-c), the unworn molars clearly demonstrate the low, bulbous cusps (see Figure 4.66).

Crown shape, average enamel thickness, and enamel distribution

The following observations are based on the results of Principle Component Analyses (PCA), and on the results of enamel thickness and distributions presented in Chapter 4:

Based on the PCA of the maxillary canines, *A. africanus* is least likely a candidate group for StW 498. Rather, according to PC 1 and PC 2, StW 498 clusters most securely with *A. prometheus*, making it a likely candidate for attribution to that group.

The PCA results of the maxillary third premolars suggest that StW 498 is best matched with *A. prometheus* or *P. robustus*, and is largely based on the size profile (i.e., PC 1). According to the PCA results of the maxillary second molars, it is likely that StW 498 is grouped with either *P. robustus* or *A. prometheus*. However, the *A. africanus* sample is extremely small compared to representatives of the other taxon. Thus, for the purpose of being conservative, I consider the PCA results of the M^2s to be inconclusive until a larger sample is acquired and analysed. The PCA results of the maxillary third molars reveal that StW 498 plots within *P. robustus* and *A. prometheus* clusters on both PC 1 and PC 2. Thus, according to the size and shape profile of the maxillary M^3s, StW 498 is most

likely attributable to either *P. robustus* or *A. prometheus*. According to crown shape index of the PCA (PC 2) performed on the combined sample of the maxillary second and third molars, StW 498 closely fits within the *P. robustus* cluster, specifically at the periphery of its high end along PC 2, and StW 498 partially overlaps in the positive PC 2 region with *A. prometheus*.

Thus, the results of the Principle Component Analyses demonstrate that all the canine samples of *A. africanus* are noticeably smaller and shorter than those in the *A. prometheus* sample. As observed in this study (and by Clarke & Kuman 2018), both the maxillary and mandibular canines of *A. prometheus* are extremely large, even more so than those of *A. africanus* (see Tables 4.1 and 4.4). If we were to accept Kimbel and White's (1988) proposal that sexual dimorphism in the mandibular canines of *A. africanus* is less marked, then the hypothesis that the variation seen in the *Australopithecus* assemblages is the result of sexual dimorphism becomes highly unlikely (see Grine 2013 for review). The results of the Principle Component Analyses demonstrate that all the canine samples of *A. africanus* are noticeably smaller and shorter than those in the *A. prometheus* sample. Since sexual dimorphism in *A. africanus* canines is less marked (Kimbel & White 1988), the findings of the present study offer support to Clarke's (1988, *et seq*.) claim that variation seen in the *Australopithecus* assemblages cannot be explained by sexual dimorphism.

Principle Component Analysis of the shape and size profile of the maxillary premolars and third molars indicate that those of *A. africanus* are also smaller than those attributed to *P. robustus*. The *A. prometheus* maxillary premolars and third molars are, on average, smaller than those of *P. robustus*, but larger than those belonging to *A. africanus*. In StW 498, the size and shape of maxillary premolars and third molars falls within the overlapping region in the ranges of *A. prometheus* and *P. robustus* maxillary premolars and third molars. Thus, *A. africanus* can be considered as the least likely candidate to which StW 498 should be attributed.

The PCA results of the maxillary second and third molars are consistent with those of Fornai *et al.* (2010) who conducted detailed geometric morphometric

analyses (including PCAs) on maxillary molars from Cooper's Cave, Kromdraai, Makapansgat, Swartkrans, and Sterkfontein Member 4. The results of these studies indicated that maxillary molars attributed to *A. prometheus* were distinguishable from those attributed to *A. africanus*. Specifically, Fornai *et al*. (2010) found that the specimens *A. prometheus* specimens such as Sts 1, Sts 8, StW 183, StW 188, StW 189, StW 252, StW 280, and StW 450, are morphologically different from *A. africanus* specimens such as Sts 24, Sts 37, Sts 56, Sts 57, StW 179, StW 204, StW 402, StW 530, MLD 28, and TM 1511.

Fornai *et al*. (2010) found that some of the Sterkfontein maxillary molars exhibited a morphological similarity to those of *P. robustus*, while the maxillary molars of *A. africanus* were closely plotted to maxillary molars attributed to *Homo*. These findings, which correlate with those from the present study, support the hypothesis that *Australopithecus* specimens with relatively larger dentitions are ancestors of *Paranthropus* (e.g., Johanson & White 1979; White, Johanson & Kimbel 1981; Rak 1983).

As mentioned above, *A. prometheus* has large canines with extremely thick roots which exhibit mesial and/or distal grooves. It is possible that the grooves observed on the roots are a genetic evolutionary development associated with these large, mesiodistally thick roots being clustered and crowded together. This feature coincides with Clarke's (1988) proposal that a second species (now referred to as *A. prometheus*) is ancestral to *Paranthropus*, with the larger canines and incisors of *A. prometheus* becoming reduced over time to develop into *Paranthropus* morphology. Clarke's (1988) proposal is further supported by the findings made by Fornai *et* al. (2010) and the present study whereby the maxillary premolars and molars of *A. prometheus* share a close morphological affinity with those of *P. robustus*. Fornai *et al.* (2015) later stated that the maxillary second molars may be morphologically informative, though this may have been due to the extremely small sample used in their study. Nonetheless, the results of the present study, by extension, coincide with the hypothesis that *Australopithecus* specimens with relatively larger dentitions are ancestral to *Paranthropus* (e.g., Johanson & White 1979; White, Johanson & Kimbel 1981; Rak 1983). Some researchers (e.g.,

Kimbel & Rak 1993; Moggi-Cecchi, Tobias & Beynon 1998; Lockwood & Tobias 2002) agree that some specimens (e.g., StW 183; StW 252) exhibit *Paranthropus*-like features, and that it is possible that these specimens may belong to a second australopith species. However, they disagree with Clarke's (1988) diagnostic morphological traits and argue that the number of specimens Clarke has re-assigned to *A. prometheus* is overly exaggerated.

Enamel thickness of the molars of StW 498, measuring an average of 1.14 mm, is considerably thinner than that of *A. africanus*, which has an average of 1.40 mm, and also thinner than that of *P. robustus*, which has an average of 1.60 mm (see Table 4.8). It most closely resembles the average value of the small sample of *A. prometheus*.

In StW 498, enamel seems to be thicker on the lingual and distal surfaces than on the buccal and mesial surfaces. The maximum enamel thickness for all the minimally worn teeth of StW 498 is 2.81 mm. The same observation is seen in the minimally worn teeth of StW 252, which have a maximum thickness of 2.94 mm. The minimally worn teeth of Sts 52 (*A. africanus*) have a maximum of thickness of 3.05 mm, while the minimally worn teeth of TM 1517 (*P. robustus*) are considerably thicker with a maximum of 4.04 mm (see Figure 4.56).

The maximum enamel thickness of the StW 498 P^3s is 1.87 mm. This is similar to that of the StW 252 P^3 that measures 1.82 mm. Maximum thickness dimensions for Sts 52 and TM 1517 are 2.38 mm and 2.72 mm respectively; these measurements are considerably greater than those of either StW 498 or StW 252. The StW 498 P^4s have a maximum thickness of 1.85 mm and is comparable with that of StW 252. The StW 498 M^2s and M^3s have maximum thickness dimensions of 2.49 mm and 2.75 mm respectively (see Table 4.9). These measurements are smaller than those of StW 252, Sts 52, and especially TM 1517.

Dimensions for the M^3, M_2, and M_3 of StW 498 could only be compared to those of *A. africanus* and *P. robustus* in the present study. Neither the M^2, M^3, nor the M_2 of StW 498, fall within the range of those attributed to *A. africanus* or *P.*

robustus. However, the M_3 of StW 498, which measures 2.81 mm, is similar to the M_3 of Sts 52, which measures 2.86 mm.

Thus, based on the results of the AET and enamel distribution of hominid molars, two conclusions can be made: First, the average enamel thickness of *A. africanus* is greater than that of *A. prometheus*, but less than that of *P. robustus*. Second, the pattern of enamel thickness exhibited by StW 498 aligns most closely with the pattern exhibited by *A. prometheus* compared to the patterns exhibited by *A. africanus* or *P. robustus*. As with the results of the PCAs, we again see a close morphological similarity between *A. prometheus* and *P. robustus*, and a clear distinction between these taxa and *A. africanus*.

StW 498 is more similar to StW 252, an *A. prometheus*, than to other specimens. However, in the sample that was used to assess enamel thickness, *A. prometheus* is only represented by a single specimen. Thus, the comparisons between AET of StW 498 molars and those of the comparative groups must remain preliminary until larger samples are investigated.

In spite of the small sample, average enamel thickness and enamel distribution act as taxonomic discriminators (e.g., see Olejniczak *et al*. 2008; Zanolli 2015; Zanolli *et al*. 2017; Zanolli *et al*. 2018). If we were to accept *A. prometheus* as a valid species, it is plausible to assume that the enamel thickness and enamel distribution of this taxon is distinguishable from that of *A. africanus*. This assumption is supported by the results of the present study, albeit the limited sample.

5.1.4. Limitations and future directions

This research was limited by the small dataset and would benefit greatly from a larger comparative sample size. Future reconstruction and analysis of the cranial vault fragments associated with StW 498 will be conducted in order to further explore the variation that exists among the South African australopithecine assemblages. Such analysis will be conducted in collaboration with Dr. Amélie Beaudet, who has done exceptional work on various cranial specimens, such as

reconstructing the endocast of StW 573 (Beaudet *et al*. 2019a) and on the bony labyrinth of StW 573 (Beaudet *et al*. 2019a). Future analyses will include using geometric morphometrics and cross-sectional geometry to assess features such as mandibular strength properties (e.g., see Daegling & Grine 1991; Taylor 2006; Daegling 2007; Robinson 2012l Daegling *et al*. 2016), and mid-facial components such as the infraorbital region, zygomatic process, the nasoalveolar clivus, and the anterior pillar (e.g., see Rogers-Ackermann & Krovitz 2002; McCollum 2008; Grine *et al*. 2010).

Analysis of facial shape differences between specimens representing different hominid taxa will be conducted using geometric morphometric approaches, which may help to differentiate masticatory patterns, as well as species and phylogenetic relationships among fossil hominids. Such analysis can be conducted using computational, similarity-based methods of 3D surface registration and 3D inspection colour mapping (e.g., see Subsol *et al*. 2002; Subsol *et al*. 2008).

5.2. Summary and conclusions

This research was focused on reconstruction of the lower face and dentition of StW 498. The primary aims were to produce a complete virtual reconstruction of the specimen and to provide detailed anatomical descriptions complete with measurements. A secondary aim was to address the affinity of StW 498 by using quantitative metric analysis and qualitative, anatomical observations. Considering previous relevant published work and the comparative analysis conducted here (although this study would clearly benefit from a larger sample size), a number of conclusions can be made:

High resolution microCT scanning and virtual reconstruction offer powerful and versatile methods that can adjust for plastic deformation and help restore broken specimens that may be too fragile to survive a physical reconstruction. This was particularly relevant in the case of the fragmented partial skull, StW 498. Moreover, virtual reconstruction methods allow for the analysis of internal

structures without having to use destructive sampling. Again, this offered insights into StW 498 that would not have been achievable otherwise.

When attempting to differentiate cranio-dental remains of hominid taxa, traditional quantitative-based methods are not always sufficient, especially for a small sample. However, combining a traditional metric analysis with a virtual, three-dimensional analysis (i.e., 3D average enamel thickness and enamel thickness distribution), as well as with qualitative observations, offers the maximal opportunity for arriving at a stronger taxonomic discriminator.

In this study, I observed several features of *A. prometheus* specimens that substantially differ from features of *A. africanus*. Many of these features have been previously identified by Clarke (1988, *et seq*.), and are well-documented and summarised more recently by Clarke & Kuman 2018 (refer to Appendix N for a complete list of specimens attributed to *A. prometheus* and features that differentiate this taxon from *A. africanus*):

1. A long, narrow palate that is shallow anteriorly and becomes deeper posteriorly (Clarke 1988 *et seq*.)
2. A large, shallow mandible with a thick corpus body, and a posteriorly thin corpus base (Clarke & Kuman 2018).
3. Procumbent incisors resulting in a steeply sloped facial profile (Clarke & Kuman 2018).
4. Distally curving incisor and canine roots (as observed by the author).
5. Large canines with mesiodistally broad roots (Clarke & Kuman 2018), which also present with mesial and/or distal grooves (as observed by the author).
6. Large incisor roots that present with mesial and/or distal grooves (as observed by the author).
7. Lingually-sloped occlusal wear (Clarke & Kuman 2018).

During the course of this study, all of the abovementioned features characterising *A. prometheuns* were observed in StW 498. These features are consistently

observed together in specimens attributed to *A. prometheus* and absent in specimens assigned to *A. africanus* and *P. robustus*. Moreover, in every PCA that was conducted in this study, regardless of the small sample StW 498 specimens were more often clustering with *A. prometheus* and *P. robustus*, rather than with *A. africanus*.

Following the assessment of the relevant literature, the comparative analysis, and the abovementioned features, I conclude that the features that distinguish *A. prometheus* exceed what would reasonably be attributed to sexual dimorphism and individual variation (e.g., see Broom 1950; Broom & Robinson 1950; Robinson 1954; 1967; Johanson & White 1979; White, Johanson & Kimbel 1981; Rak 1983; 1985; Olson 1985; Grine 2013). We cannot disregard Clarke's (1988, *et seq*.) claim of a second australopith species simply because it is the general consensus to attribute variability in *Australopithecus* assemblages to either individual variation or sexual dimorphism.

Kimbel and White (1988: 186) argue that "it is unlikely that the total variation in the facial morphology in the Sterkfontein Type Site collection is attributed to sexual dimorphism", and suggest that that variability within the M4 assemblage cannot be explained by sexual dimorphism or individual variation. Rather, based on their observations, Kimbel & White (1988: 189) propose two alternative hypotheses. First, the samples taken from the M4 assemblage represent "temporally mixed populations of an evolving lineage". Or second, that there is more than one hominid species present in the Sterkfontein M4 hominid assemblage. This second hypothesis would corroborate Clarke's (1985a, b) proposal of a second australopith species at Sterkfontein.

Berger and Hawks (2019) question the validity of the species *A. prometheus*, and have go as far as to suggest that the species be considered as a *nomen dubium*. However, based on the results of the present study and assessment of the relevant literature, it becomes unintelligible not to at least consider the possibility of a second australopith species. The problem is the low-resolution fossil record and control over chronology as much as variables. Broom (1936; 1938a-b; 1940) often neglected post-cranial specimens and only focused on cranio-dental specimens. It

is essential to assess cranio-dental specimens in conjunction with post-cranial specimens; the StW 573 ('Little Foot') specimen is the most complete skeleton to date and will play a vital role in how we identify the various taxa. Although we are limited by the low-resolution fossil record, incorporating cranio-dental specimens with post-cranial specimens is key to understanding intra- and inter-specific variation. Finally, we need to recognise that the degree of individual variation may be unique to each taxon and requires further investigation by using new variables. We need to critically re-assess variability by continuously incorporating new variables (such as three-dimensional average enamel thickness and enamel distribution) with existing variables that act as taxonomic discriminators, such as canine size, root morphology, and maxillary and mandibular morphology.

StW 498 offers unique insight into hominid variation and taxonomy, especially that of *Australopithecus*. In spite of its dental pathology, the majority of the features in StW 498 can be clearly differentiated from those in specimens attributed to *A. africanus* (such as Sts 52, StW 73, Sts 53). Rather, the majority of the features in StW 498 align it with specimens (such as Sts 71, Sts 36, StW 252, and StW 573) that have been assigned to *A. prometheus* (Clarke 1988, *et seq.*). The only feature lacking in StW 498 that is present in other specimens attributed to *A. prometheus* (such as StW 252, and StW 573) is a large diastema between the lateral maxillary incisors and the maxillary canines. On the comparative specimens attributed to *A. prometheus*, the presence of a diastema is needed to accommodate the large canines. However, because the canines of *A. africanus* and *P. robustus* are smaller (e.g., Clarke 1985a; 1994; 1996; Kimbel & White 1988; this study), the need for a diastema is eliminated. The presence of a diastema was considered by Clarke (1988) to be a diagnostic trait of a second species, as represented by StW 252 (now classed as *A. prometheus*). However, it is concluded that the missing diastema in StW 498 is most likely the result of the pathological dental crowding exhibited by the specimen.

Although the sample size in this study was small, based on the data that were collected, StW 498 has numerous morphological features that align with the *A.*

prometheus phenotype as recognised by Clarke (1988, *et seq*.). Thus, based on the reconstruction, description, and multivariate metric analysis of StW 498, it is concluded that this specimen should be assigned to *A. prometheus*.

APPENDIX A

Parameters needed for image acquisition of StW 498.

Specimen	Voxel size (spatial resolution)	kV (kilo volts)	uA (microAmps)	fps (frames per second)	Pre-filtration (aluminium or copper in mm)	Number of projections
StW 498a (1)	20µm	140	140	1	1.2 Cu	3142
StW 498a(2)	20µm	140	140	1	1.2 Cu	3142
StW 498a(3)	33µm	140	140	1	1.2 Cu	3142
StW 498b(1)	25µm	140	140	1	1.2 Cu	3142
StW 498b(2)	25µm	140	140	1	1.2 Cu	3142
StW 498b(3)	25µm	140	140	1	1.2 Cu	3142
StW 498c(1)	37µm	140	140	1	1.2 Cu	3142
StW 498c(2)	37µm	140	140	1	1.2 Cu	3142
StW 498c(3)	37µm	140	140	1	1.2 Cu	3142
StW 498d(1.1)	38µm	140	140	1	1.2 Cu	3142
StW 498d(1.2)	38µm	140	140	1	1.2 Cu	3142
StW 498d(2)	37µm	140	140	1	1.2 Cu	3142
StW 498e	30µm	140	140	1	1.2 Cu	3142
StW 498f	44µm	80	85	1	—	3142
StW 498g-p	28µm	80	85	1	—	3142
StW 499	44µm	80	85	1	—	3142

APPENDIX B

Parameters needed for image acquisition of comparative material.

Specimen	Voxel size (spatial resolution)	kV (kilo volts)	uA (microAmps)	fps (frames per second)	Pre-filtration (aluminium or copper in mm)	Number of projections
StW 252c	14µm	100	100	2	Al & Cu	2400
StW 252f	14µm	100	100	2	Al & Cu	3600
StW 252g	14 µm	100	100	2	Al & Cu	3600
StW 252i	14µm	100	100	2	Al & Cu	3600
StW 252j	14µm	100	100	2	Al & Cu	3600
StW 252l	14µm	100	100	2	Al & Cu	3600
Sts 36	83µm	120	100	1	0.1 Al	1000
Sts 52	41µm	40	100	—	—	—
Sts 71	58µm	190	100	1	—	1000
SK 843	33µm	105	80	1	0.25 Al	1000
TM 1517	60µm	190	132	1	2 Cu	1000

APPENDIX C
Image processing.

Specimen	Program used	Thresholds used for visualisation	Tools used
StW 498a	Avizo 9.0.1	-60 to 90	Median filter 3, watershed tool, magic wand, threshold tool, brush tool, region growing, surface smoothing, mirror imaging
StW 498b	Avizo 9.0.1	-90 to 130	Median filter 2, watershed tool, magic wand, threshold tool, brush tool, region growing, surface smoothing
StW 498c	Avizo 9.0.1	-50 to 110	Median filter 2, watershed tool, magic wand, threshold tool, brush tool, region growing, surface smoothing
StW 498d	Avizo 9.0.1	-80 to 140	Median filter 3, watershed tool, magic wand, threshold tool, brush tool, region growing, surface smoothing, mirror imaging

APPENDIX D

Scores and loadings for the PCA of the maxillary canines.

	Scores		
Specimen	**PC 1**	**PC 2**	**PC 3**
StW 498(r)	0,366182486	-1,140090107	0,480682687
StW 498(l)	1,131530729	-0,230392672	0,360637707
StW 183(r)	0,330727498	0,775756375	0,685141108
StW 183(l)	0,525069211	0,785842464	0,649395598
StW 252(r)	0,958977457	-0,634442325	-0,523286411
StW 252(l)	0,977073949	-0,148415648	0,006941456
Sts 52(r)	-1,985662498	-1,09462001	-0,358747322
Sts 52(l)	-1,587707689	-0,465486649	0,068302489
StW 287(l)	1,447519073	0,693889705	-1,169351658
MLD 11/30(r)	-2,163710215	1,457958868	-0,199715654

	Loadings		
Variable	**PC 1**	**PC 2**	**PC 3**
BL	0,81424	-0,45482	0,36078
MD	0,891	-0,12858	-0,43542
Crown height	0,65002	0,74597	0,14491

	Summary		
Principle Component	**Eigenvalue**	**% of variance**	**Cumulative %**
PC 1	1,8794	62,646	62,646
PC 2	0,7799	25,995	88,642
PC 3	0,3408	11,358	100

APPENDIX E

Scores and loadings for the PCA of the maxillary and mandibular canines.

	Scores		
Specimen	**PC 1**	**PC 2**	**PC 3**
Maxillary canines			
StW 498(r)	1,29895331	-0,716253334	0,422008331
StW 498(l)	2,076220676	-0,870917094	0,747138819
StW 183(r)	-1,502813414	1,489572802	-0,265823553
StW 183(l)	-1,288247677	0,539756372	0,348000689
StW 252(r)	0,43291732	0,732732616	0,236273128
StW 252(l)	-2,850396533	-0,397991016	0,154734056
Sts 52(r)	-0,365302399	0,933750852	0,400344633
Sts 52(l)	-1,999171435	-0,8472663	-0,11100218
StW 287(l)	-0,995933332	0,055051979	0,129069533
MLD 11/30(r)	-1,457405971	-0,141945261	0,102897561
Mandibular canines			
StW 498(r)	-0,028555319	0,535735376	0,210101156
StW 498(l)	-0,214858904	0,523925673	0,225702849
Sts 36(l)	1,076660827	1,112239424	-0,114167413
Sts 52(r)	1,755592986	0,469343405	0,006154832
StW 116(r)	1,024149493	-0,440279822	0,505672268
StW 213(l)	1,200041536	-0,416876091	0,480214112
StW 288(r)	1,546708989	0,353529175	-0,839098082
StW 446(l)	1,589377094	0,192869439	-0,2762913
StW 491(r)	-1,137579073	0,083635582	-0,844502579
StW 491(l)	-0,755424003	-0,152691011	-0,330877447
StW 537(r)	1,93005896	-0,966454118	-1,070186544
StW 537(l)	-1,334993131	-2,07146865	-0,116362867

APPENDIX E (continued)

Scores and loadings for the PCA of the maxillary and mandibular canines.

	Loadings		
Variable	**PC 1**	**PC 2**	**PC 3**
BL	0,75863	0,62951	0,16789
MD	0,93232	-0,06109	-0,35643
Crown height	0,82237	-0,51146	0,24921

	Summary		
Principle Component	**Eigenvalue**	**% of variance**	**Cumulative %**
PC 1	2,121	70,702	70,702
PC 2	0,6616	22,054	92,755
PC 3	0,2173	7,245	100

APPENDIX F

Scores and loadings for the PCA of the maxillary third premolars.

	Scores			
Specimen	**PC 1**	**PC 2**	**PC 3**	**PC 4**
StW 498(r)	0,910724658	0,57750926	-0,007130318	0,121477413
StW 498(l)	0,30119714	0,240707416	0,011836393	-0,000255809
Sts 71(r)	-0,201028182	-0,897846714	-0,466353889	-0,003447695
StW 183(l)	-0,138112261	0,201539192	0,016910164	0,004718244
StW 252(r)	2,409641934	-0,111787563	0,003974309	-0,054803398
StW 252(l)	1,48697694	0,20889703	0,000534343	-0,021394172
StW 280(r)	1,083680342	1,937182146	-0,032649943	-0,010116558
Sts 52(r)	-1,895679967	0,439765258	0,023218175	-0,005776853
Sts 52(l)	-2,062012147	1,122878607	0,027126876	-0,025008629
StW 73(l)	-1,105685178	-0,829788241	0,051648056	0,015218792
MLD 11/30(r)	-3,361208726	-2,050518573	0,052933205	-0,00761017
TM 1517(l)	1,892346527	-1,411042499	0,10975692	-0,017431715
SK 13/14(r)	0,994970189	-1,507345	0,106247317	0,012387968
SK 13/14(l)	0,506556493	-0,791616879	0,056132545	0,009785664
SK 46(r)	-1,403073242	2,343430717	0,04887131	-0,009563477
SK 48(r)	0,580705481	0,528035844	-0,00305546	-0,008179606

	Loadings			
Variable	**PC 1**	**PC 2**	**PC 3**	**PC 4**
BL	0,90288	0,42242	-0,0782	0,01608
MD	0,82331	-0,5627	0,07248	0,01655
Crown area	0,99701	-0,07193	-0,00075	-0,02831
Crown shape index	0,15596	0,98492	0,07489	0,00049

	Summary		
Principle Component	**Eigenvalue**	**% of variance**	**Cumulative %**
PC 1	2,5114	62,784	62,784
PC 2	1,4703	36,758	99,542
PC 3	0,017	0,424	99,967
PC 4	0,0013	0,033	100

APPENDIX G

Score and loadings for the PCA of the maxillary fourth premolars.

	Scores			
Specimen	**PC 1**	**PC 2**	**PC 3**	**PC 4**
StW 498(r)	0,566799545	-0,593349283	0,151863546	-0,023979724
StW 498(l)	-0,860324226	-0,137538456	0,068383991	-0,01035496
StW 252(r)	2,825872526	-0,242059654	0,235854341	0,028001991
StW 252(l)	2,676434025	-0,615205036	0,253950169	0,025179899
StW 280(r)	-0,663213565	0,450322088	0,066631171	-0,016867726
StW 280(l)	-0,200313586	1,022733789	0,07327059	-0,023045791
Sts 52(r)	-1,641207626	-1,71844279	0,050715586	-0,000317807
Sts 52(l)	-2,336382506	-1,487463934	-0,003208992	0,027775866
StW 73(l)	-1,505207454	-0,512942429	0,036789274	0,003304889
TM 1517(l)	1,448604745	0,337373647	0,146362418	-0,022744738
SK 13/14(r)	1,059226445	-0,045706552	-1,44620462	0,00113688
SK 13/14(l)	1,907622883	0,139862195	0,175244563	-0,008652633
SK 46(r)	-1,068970764	1,737280284	0,054613211	0,007198447
SK 46(l)	-1,475572504	2,215626854	0,053864552	0,030379809
SK 48(r)	-0,733367939	-0,550490723	0,081870202	-0,017014402

	Loadings			
Variable	**PC 1**	**PC 2**	**PC 3**	**PC 4**
BL	0,85679	0,50522	-0,10237	-0,01321
MD	0,92374	-0,19791	0,32794	0,00006
Crown area	0,98114	0,10617	-0,16095	0,01376
Crown shape index	-0,38962	0,90914	0,14708	0,00574

	Summary		
Principle Component	**Eigenvalue**	**% of variance**	**Cumulative %**
PC 1	2,7018	67,545	67,545
PC 2	1,1322	28,306	95,851
PC 3	0,1656	4,139	99,99
PC 4	0,0004	0,01	100

APPENDIX H

Scores and loadings for the PCA of the maxillary second molars.

	Scores			
Specimen	**PC 1**	**PC 2**	**PC 3**	**PC 4**
TM 1517(l)	-0,570536055	-0,166248021	-0,026443647	0,01816757
SK 13/14(r)	1,25316886	-0,704324461	-0,002690478	0,02621851
SK 13/14(l)	2,356614364	-0,87571541	0,06845587	0,00469037
SK 46(r)	-1,166310598	0,573923301	0,002869615	0,0024176
SK 46(l)	-1,084045017	0,8376684	0,002276405	0,00340377
SK 48(r)	-2,254606693	-1,239882178	0,009325266	-0,0286014
SK 48(l)	-1,691837945	-1,160540076	-0,009517076	-0,0022185
Sts 52(r)	-1,198688032	-0,855921145	-0,013018015	0,01066867
Sts 52(l)	-1,145473464	-0,248607498	-0,009022619	0,00764834
Sts 71(r)	0,680781086	-0,821893688	-0,01267886	0,03440147
StW 183(l)	1,563845561	0,822922421	-0,065804447	-0,0204176
StW 252(r)	2,351532957	-0,265036086	0,014557931	-0,0173782
StW 252(l)	2,459546625	-0,327757556	0,022843933	-0,0190927
StW 280 (l)	1,591757705	0,182062304	-0,03694706	-0,0060865
StW 578(r)	-1,984466618	-0,784670233	0,009217167	-0,0197021
StW 498(r)	-1,208645652	2,407697882	0,073426956	0,00563485
StW 498(l)	0,047362916	2,626322043	-0,026850942	0,00024581

	Loadings			
Variable	**PC 1**	**PC 2**	**PC 3**	**PC 4**
BL	0,6836	0,72962	-0,01748	0,00683
MD	0,9769	-0,21249	0,02114	0,00824
Crown area	0,98534	0,17003	0,00239	-0,0135
Crown shape index	-0,54897	0,8356	0,02015	-0,0011

	Summary		
Principle Component	**Eigenvalue**	**% of variance**	**Cumulative %**
PC 1	2,6939	67,348	67,348
PC 2	1,3046	32,616	99,963
PC 3	0,0012	0,029	99,993
PC 4	0,0003	0,007	100

APPENDIX I

Scores and loadings for the PCA of the maxillary third molars.

	Scores			
Specimen	**PC 1**	**PC 2**	**PC 3**	**PC 4**
StW 498(r)	1,437803745	-0,124000421	0,003374854	0,00181377
StW 498(l)	0,018847942	0,542293203	-0,044108928	-0,0075274
StW 183(r)	1,676614014	-0,196162247	0,019069175	0,00463605
StW 189(l)	0,545960256	-1,369403223	-0,011207548	0,04372553
StW 252(r)	2,152769682	-0,340884521	0,048780503	0,01155452
StW 252(l)	2,309013827	0,328867372	0,046493839	-0,0255421
StW 280(l	2,172238007	0,300652192	0,038906052	-0,0217271
StW 578(r)	-2,191611512	0,719385414	0,009941155	0,01665395
Sts 52(r)	-2,62183616	-0,886491559	0,015332791	-0,0368556
Sts 52(l)	-2,41848924	-1,316980636	-0,000040458	-0,0426387
StW 524(r)	-1,162079287	-0,350032772	-0,033069555	-0,0003604
TM 1517(r)	-0,492156222	-0,943622387	-0,03985144	0,00911632
TM 1517(l)	-3,238663349	0,81489173	0,08474768	0,02579876
SK 13/14(r)	0,854410619	0,81900785	-0,031962116	-0,023611
SK 13/14(l)	0,633669309	1,062539349	-0,036812035	-0,0224186
SK 46(r)	0,633262397	-0,288906654	-0,023701411	0,01069085
SK 46(l)	0,603049466	-1,099819927	-0,016284792	0,03358816
SK 48(l)	-0,912803494	2,328667236	-0,029607766	0,02310288

	Loadings			
Variable	**PC 1**	**PC 2**	**PC 3**	**PC 4**
BL	0,89973	0,43566	-0,02573	-0,0048
MD	0,99623	-0,08427	0,00501	0,01984
Crown area	0,98865	0,14787	0,02365	-0,0121
Crown shape index	-0,53952	0,84189	0,00966	0,00657

	Summary		
Principle Component	**Eigenvalue**	**% of variance**	**Cumulative %**
PC 1	3,0705	76,763	76,763
PC 2	0,9275	23,189	99,951
PC 3	0,0013	0,033	99,985
PC 4	0,0006	0,015	100

APPENDIX J

Scores and loadings for the PCA of the maxillary second and third molars.

	Scores			
Specimen	**PC 1**	**PC 2**	**PC 3**	**PC 4**
Maxillary second molars				
TM 1517(l)	-0,692460902	-0,206577624	-0,031365028	0,019624488
SK 13/14(r)	1,011460603	-1,066676035	0,011605963	0,035443866
SK 13/14(l)	2,035384567	-1,407812117	0,097314004	0,035047587
SK 46(r)	-1,262279392	0,682710797	-0,005314745	0,013831751
SK 46(l)	-1,19078869	0,948695203	-0,0040171	0,016148024
SK 48(r)	-2,240968808	-1,060018425	-0,014885518	-0,024552511
SK 48(l)	-1,717219094	-1,073263109	-0,029750364	-0,003270099
Sts 52(r)	-1,263935562	-0,831876811	-0,027717765	0,010426782
Sts 52(l)	-1,226420924	-0,195695819	-0,020448639	0,011833954
Sts 71(r)	0,482890061	-1,101477532	-0,007027591	0,037871492
StW 183(l)	1,270907963	0,487598786	-0,033010144	-0,010403603
StW 252(r)	2,020045651	-0,772569502	0,05051786	0,007055916
StW 252(l)	2,12111596	-0,854333844	0,059960919	0,007420857
StW 280 (l)	1,308653539	-0,189389002	-0,009183181	0,005319762
StW 578(r)	-1,9981223	-0,621825499	-0,01122177	-0,013627515
StW 498(r)	-1,339412605	2,650985336	0,068998119	0,040864229
StW 498(l)	-0,172675436	2,653617383	-0,010834747	0,019777517
Maxillary third molars				
StW 498(r)	1,688590759	0,128444913	-0,013780946	-0,013647777
StW 498(l)	0,223453881	0,597754409	-0,04411714	0,01053595
StW 183(r)	1,93913352	0,083238525	-0,001214258	-0,02198199
StW 189(l)	0,623357413	-1,055270911	0,00052218	0,036736708
StW 252(r)	2,438517326	-0,007568064	0,023261041	-0,036401769
StW 252(l)	2,66421956	0,603734563	0,001174252	-0,068842146
StW 280(l	2,514747107	0,567176609	-0,001949377	-0,060142992
StW 578(r)	-2,126357099	0,541339538	0,036062227	-0,003268082
Sts 52(r)	-2,727519708	-0,907578859	0,005144489	-0,048764864
Sts 52(l)	-2,548183323	-1,265634394	-0,01511064	-0,042451252
StW 524(r)	-1,119252439	-0,299514186	-0,024464399	0,012810682
TM 1517(r)	-0,453649479	-0,763144545	-0,033225363	0,02637255
TM 1517(l)	-3,235448044	0,516850123	0,114462036	-0,045350112
SK 13/14(r)	1,143661483	0,917899502	-0,049282465	-0,013314504
SK 13/14(l)	0,928119306	1,113524691	-0,049625544	-0,009340449
SK 46(r)	0,81047494	-0,086570868	-0,02528388	0,013812032
SK 46(l)	0,707753164	-0,809765278	-0,00900669	0,030670182
SK 48(l)	-0,617792998	2,082992045	0,002814202	0,023755335

APPENDIX J (continued)

Scores and loadings for the PCA of the maxillary second and third molars.

	Loadings			
Variable	**PC 1**	**PC 2**	**PC 3**	**PC 4**
BL	0,8288	0,55895	-0,02438	0,00806
MD	0,9847	-0,17216	0,02133	0,01672
Crown area	0,98958	0,14195	0,00863	-0,0225
Crown shape index	-0,50225	0,86452	0,01859	0,00181

	Summary		
Principle Component	**Eigenvalue**	**% of variance**	**Cumulative %**
PC 1	2,8881	72,202	72,202
PC 2	1,1096	27,74	99,942
PC 3	0,0015	0,037	99,979
PC 4	0,0009	0,021	100

APPENDIX K

Morphological features which distinguish the two groups of Sterkfontein and Makapansgat Australopithecines according to Clarke (1988, *et seq*.). Adapted from Clarke & Kuman (2018, Table 5, p. 36). New diagnostic features, as observed by the author, are shown in bold.

	Group A (*A. prometheus*)		Group B (*A. africanus*)	
	Morphological Feautures	**Examples**	**Morphological Feautures**	**Examples**
1	Large face	StW 505	Smaller face	StW 53
2	Large braincase	StW 505, MLD 1	Smaller braincase	StW 53
3	Laterally expanded parietals	StW 252	Sides of braincase slope	StW 53
4	Low concave frontal squame	StW 252, StW 505	High convex frontal squame	StW 53
5	No metopic ridge	StW 252, StW 505	Metropic ridge	StW 53
6	Temporal lines converge medially behind brow ridge	StW 252, StW 505, Sts 71	Less convergence of temporal lines	StW 53, Taung skull
7	Small sagittal crest on adult parietals	StW 505	No sagittal crest on adult parietals	StW 53
8	Broad interorbital distance	StW 252, StW 505	Narrow interorbital distance	StW 53, Taung skull
9	Flat midface	StW 252, StW 505, Sts 71	Convex midface	StW 53, Taung skull
10	Deep malar	StW 505, Sts 71	Shallow malar	StW 53, Taung skull
11	Robust zygomatic arch	StW 505	More gracile zygomatic arch	StW 53, Taung skull
12	Large masseteric attachment	StW 505, Sts 71	Reduced masseteric attachment	StW 53
13	no supraporianic shelf	StW 505, StW 648, Sts 71	Supraporionic shelf	StW 53, Sts 5, Sts 19
14	Inferior nasal margin smoothly concave	MLD 9, StW 183, StW 498	Inferior nasal margin with transverse ridge	StW 53, StW 576, Sts 5, Sts 52
15	Procumbent upper incisors and roots	Sts 252, StW 498	Vertically oriented incisors and roots	Sts 52, StW 576, TM 1512
16	Clivus corrugated by incisor roots	StW 505	Relatively uncorrugated clivus	StW 576, StW 53
17	Inferior margin of zygomatic process runs superolaterally	StW 505	Inferior margin of zygomatic process runs more laterally	StW 53, StW 576, Sts 5
18	Large canines	TM 1516, StW 252, StW 183, StW 667	Smaller canines	StW 576
19	Large flattened upper canine roots	StW 252, StW 667	Smaller round-sectioned upper canine roots	StW 576
20	Shallow anterior palate	MLD 9, StW 252, StW 183	Deeper anterior palate	StW 53, Sts 5, MLD 6, Sts 52
21	Long rectangular palate	StW 252	Short square palate	StW 53, Sts 5
22	Upper incisor-canine diastema	StW 252, StW 183	No upper incisor-canine diastema	TM 1512, StW 576, Sts 52
23	Large posterior teeth	StW 252, StW 183, MLD 2	Smaller posterior teeth	Sts 52, StW 53, StW 576
24	Sides of posterior teeth slope towards occlusal surface	MLD 2, StW 252, StW 183	Vertical sides to posterior teeth	Sts 52, StW 53, StW 576
25	Low bulbous cheek teeth cusps	MLD 2, StW 252, StW 183	Higher pointed check teeth cusps	Sts 52
26	Excessive anterior tooth wear	MLD 9, Sts 36	More generalised tooth wear	StW 576
27	large mandible with big teeth but relatively slender corpus	Sts 7, Sts 36, StW 384, StW 498	Small mandible with smaller teeth but thicker corpus	MLD 40, MLD 18
28	Prominent occipitomastoid crest	StW 648	Low occipitomastoid crests	StW 53, Sts 5
29	**Distally curving incisor and canine roots**	**StW 109, StW 252, StW 498, StW 573, StW 667**	**Straight incisor and canine roots**	**StW 116, StW 213, StW 491, StW 576**
30	**Large incisor and canine roots which present with mesial and/or distal grooves**	**StW 109, StW 252, StW 498, StW 573, StW 667**	**Smaller incisor and canine roots without any grooves present**	**StW 116, StW 213, StW 491, StW 576**

REFERENCES

Ahern, J.C., 1998. Underestimating intraspecific variation: the problem with excluding Sts 19 from *Australopithecus africanus*. *American Journal of Physical Anthropology* 105: 461-480.

Bamford, M. 1999. Pliocene woods from an early hominid cave deposit, Sterkfontein, South Africa. *South African Journal of Science* 95: 231-237.

Beaudet, A., Clarke, R.J., de Jager, E.J., Bruxelles, L., Carlson, K.J., Crompton, R., de Beer, F., Dhaene, J., Heaton, J.L., Jakata, K. & Jashashvili, T. 2019a. The endocast of StW 573 ("Little Foot") and hominin brain evolution. *Journal of Human Evolution* 126: 112-123.

Beaudet, A., Clarke, R.J., Bruxelles, L., Carlson, K.J., Crompton, R., de Beer, F., Dhaene, J., Heaton, J.L., Jakata, K., Jashashvili, T. & Kuman, K. 2019b. The bony labyrinth of StW 573 ("Little Foot"): Implications for early hominin evolution and paleobiology. *Journal of Human Evolution* 127: 67-80.

Benazzi, S., Gruppioni, G., Strait, D.S. & Hublin, J.J. 2014. Virtual reconstruction of KNM-ER 1813 *Homo habilis* cranium. *American Journal of Physical Anthropology* 153: 154-160.

Berger, L.R. & Hawks, J. 2019. *Australopithecus prometheus* is a *nomen nudum*. *American Journal of Physical Anthropology* 168: 383-387.

Beynon, A.D. & Dean, M.C. 1987. Crown-formation time of a fossil hominid premolar tooth. *Archs Oral Biology* 32: 773-780.

Broom, R. 1936. A new fossil anthropoid skull from South Africa. *Nature* 138: 486-488.

Broom, R. 1938a. The Pleistocene anthropoid apes of South Africa. *Nature* 142: 377-379.

Broom, R. 1938b. Further evidence on the structure of the South African Pleistocene anthropoids. *Nature* 142: 897-899.

Broom, R. 1940. The South African Pleistocene cercopithecid apes. *Annals of the Transvaal Museum* 20: 89-100.

Broom, R. 1947. Discovery of a new skull of the South African ape-man, *Plesianthropus*. *Nature* 159: 672-672.

Broom, R. 1950. The genera and species of the South African fossil ape-men. *American Journal of Physical Anthropology* 8: 1-14.

Broom, R. & Robinson, J.T. 1947. Further remains of the Sterkfontein ape-man, *Plesianthropus*. *Nature* 160: 430-31.

Broom, R. & Robinson, J.T. 1949. A new type of fossil man. *Nature* 164: 322-323.

Broom, R. & Robinson, J.T. 1950. Further evidence of the structure of the South African ape-man *Plesianthropus*. *Transvaal Museum Memoir* 4: 7-83.

Broom, R. & Robinson, J.T. 1952. Swartkrans ape-man. *Transvaal Museum Memoir* 6: 4-9.

Broom, R., Robinson, J.T. & Schepers, G.W.H. 1950. Sterkfontein ape-man, *Plesianthropus*. *Transvaal Museum Memoir* No. 4: 14-33.

Broom, R. & Schepers, G.W.H. 1946. The South African fossil ape-men: the Australopithecinae. *Transvaal Museum Memoir* 2: 84-122.

Buikstra, J. E. & Ubelaker, D. H. 1994 Standards for data collection from human skeletal remains. *Arkansas Archaeological Survey* 44: 1-218.

Calcagno, J.M., Cope, D.A., Lacy, M.G. & Tobias, P.V. 1997. Is *A. africanus* the only hominid species in Sterkfontein Member 4? *American Journal of Physical Anthropology* 24: 86-87.

Chamberlain, A.T. & Wood, B.A. 1985. A reappraisal of variation in hominid mandibular corpus dimensions. *American Journal of Physical Anthropology* 66: 399-405.

Clarke, R.J., Howell, F.C. & Brain, C.K. 1970. More evidence of an advanced hominid at Swartkrans. *Nature* 225: 1219-1222.

Clarke, R.J. 1977. *The cranium of the Swartkrans hominid, SK 847 and its relevance to human origins*. PhD Thesis. Johannesburg: University of the Witwatersrand.

Clarke, R.J. 1985a. *Australopithecus* and early *Homo* in southern Africa. In: Delson, E. (ed.) *Ancestors: The hard evidence*: 171-177. New York: Alan R. Liss.

Clarke, R.J. 1985b. Early Acheulean with *Homo habilis* at Sterkfontein. In: Tobias, P. V. (ed.) *Hominid Evolution: Past, Present, and Future*: 287-298. New York: Alan R. Liss.

Clarke, R.J. 1988. A new *Australopithecus* cranium from Sterkfontein and its bearing on the ancestry of Paranthropus. In: Grine, F.E. (ed.) *Evolutionary History of the" robust" Australopithecines*: 285-292. New York: Aldine de Gruyter.

Clarke, R.J. 1990. Observations on some restored hominid specimens in the Transvaal Museum, Pretoria. In: Sperber, G.H. (ed.) *From Apes to Angels: Essays in Anthropology in Honor of Phillip V. Tobias*: 131-151. New York: Wiley-Liss.

Clarke, R.J. 1994. Advances in understanding the craniofacial anatomy of South African early hominids. In: Corruccini, R.S. & Ciochon, R.L. (eds.) *Integrative Paths to the Past: Advances in Human Evolution Series, Volume 2:* 205-222. New Jersey: Prentice Hall.

Clarke, R.J. 1996. The genus Paranthropus: what's in a name? In: Meikle, W.E., Howell F.C. & Jablonski N.G. (eds.) *Contemporary issues in human evolution (Memoir 21)*: 93-104. California: Academy of Sciences.

Clarke, R.J. 1998. First ever discovery of a well preserved skull and associated skeleton of *Australopithecus*. *South African Journal of Science* 94: 460-463.

Clarke, R. J. 2002. Newly revealed information on the Sterkfontein Member 2 *Australopithecus* skeleton. *South African Journal of Science* 98: 523-526.

Clarke, R. J. 2006. A deeper understanding of the stratigraphy of Sterkfontein fossil hominid site. *Transactions of the Royal Society of South Africa* 61: 111-120.

Clarke, R.J. 2008. Latest information on Sterkfontein's *Australopithecus* skeleton and a new look at *Australopithecus*. *South African Journal of Science* 104: 443-449.

Clarke, R.J. 2013. *Australopithecus* from Sterkfontein Caves, South Africa. In: Reed, K.E., Fleagle, J.G. & Leakey, R.E. (eds.) *The Paleobiology of Australopithecus, Vertebrate Paleobiology and Paleoanthropology*: 105-123. New York: Springer Science.

Clarke, R.J. & Kuman, K. 2018. The skull of StW 573, a 3.67 Ma *Australopithecus* skeleton from Sterkfontein Caves, South Africa. *bioRxiv*: 483495.

Daegling, D.J. 2007. Relationship of bone utilization and biomechanical competence in hominoid mandibles. *Archives of Oral Biology* 52: 51-63.

Daegling, D.J., Carlson, K.J., Tafforeau, P., de Ruiter, D.J. & Berger, L.R. 2016. Comparative biomechanics of *Australopithecus sediba* mandibles. *Journal of Human Evolution* 100: 73-86.

Daegling, D.J. & Grine, F.E. 1991. Compact bone distribution and biomechanics of early hominid mandibles. *American Journal of Physical Anthropology* 86: 321-339.

Dart, R. A. 1925. *Australopithecus africanus*, the man-ape of South Africa. *Nature* 115: 195-199.

Dart, R.A. 1948a. The Makapansgat proto-human *Australopithecus prometheus*. *American Journal of Physical Anthropology* 6: 259-284.

Dart, R.A. 1948b. The infancy of *Australopithecus*. In: Du Toit, A. (ed.) *Robert Broom Commemorative Volume*: 143-152. Cape Town: Royal Society of South Africa.

Dart, R.A. 1948c. The adolescent mandible of *Australopithecus prometheus. American Journal of Physical Anthropology* 6: 391-412.

Dean, M.C., Leakey, M.G., Reid, D., Schrenk, F., Schwartz, G.T., Stringer, C. & Walker, A. 2001. Growth processes in teeth distinguish modern humans from *Homo erectus* and earlier hominins. *Nature* 414: 628-631.

El-Zaatari, S., Grine, F.E., Teaford, M.F. & Smith, H.F. 2005. Molar microwear and dietary reconstructions of fossil Cercopithecoidea from the Plio-Pleistocene deposits of South Africa. *Journal of Human Evolution* 49: 180-205.

Fornai, C. 2009. *Testing the second Australopithecine species hypothesis for the South African site of Sterkfontein: geometric morphometric analysis of*

maxillary molar teeth. MSc Thesis. Johannesburg: University of the Witwatersrand.

Fornai, C., Bookstein, F.L. & Weber, G.W. 2015. Variability of *Australopithecus* second maxillary molars from Sterkfontein Member 4. *Journal of Human Evolution* 85: 181-192.

Fornai, C., Clarke, R.J., Moggi-Cecchi, J., Hemingway, J., De Beer, F.C. & Radebe, M.J. 2010. Testing the "second australopithecine species hypothesis" for Sterkfontein Member 4, South Africa. *American Journal of Physical Anthropology* 50:105-106.

Freedman, L. 1976. South African fossil Cercopithecoidea: a re-assessment including a description of new material from Makapansgat, Sterkfontein and Taung. *Journal of Human Evolution* 5: 297-315.

Garn, S.M., van Astine, W.L. & Cole, P.E. 1978. Relationship between root lengths and crown diameters of corresponding teeth. *Journal of Dental Research* 57: 636.

Granger, D.E., Gibbon, R.J., Kuman, K., Clarke, R.J., Bruxelles, L. & Caffee, M.W. 2015. New cosmogenic burial ages for Sterkfontein Member 2 *Australopithecus* and Member 5 Oldowan. *Nature* 522: 85.

Grine, F.E. 1987. The diet of South African australopithecines based on a study of dental microwear. *L'Anthropologie* 91: 467-482.

Grine, F.E. 1989. New hominid fossils from the Swartkrans Formation (1979-1986 excavations): cranio-dental specimens. *American Journal of Physical Anthropology* 79: 409-449.

Grine, F.E., 2013. The alpha taxonomy of *Australopithecus africanus*. Reed, K.E., Fleagle, J.G. & Leakey, R.E. (eds.) *The Paleobiology of Australopithecus, Vertebrate Paleobiology and Palaeoanthropology*: 73-104. New York: Springer Science.

Grine, F.E., Delanty, M.M. & Wood, B.A. 2013. Variation in mandibular postcanine dental morphology and hominin species representation in Member 4, Sterkfontein, South Africa. Reed, K.E., Fleagle, J.G. & Leakey, R.E. (eds.) *The Paleobiology of Australopithecus, Vertebrate Paleobiology and Paleoanthropology*: 125-146. New York: Springer Science.

Grine, F.E., Judex, S., Daegling, D.J., Ozcivici, E., Ungar, P.S., Teaford, M.F., Sponheimer, M., Scott, J., Scott, R.S. & Walker, A. 2010. Craniofacial biomechanics and functional and dietary inferences in hominin paleontology. *Journal of Human Evolution* 58: 293-308.

Grine, F.E. & Strait, D.S. 1994. New hominid fossils from Member 1 "Hanging Remnant", Swartkrans Formation, South Africa. *Journal of Human Evolution* 26: 57-75.

Grine, F.E., Weber, G.W., Plavcan, J.M. & Benazzi, S. 2012. Sex at Sterkfontein: 'Mrs. Ples' is still an adult female. *Journal of Human Evolution* 62: 593-604.

Gunz, P., Mitteroecker, P., Neubauer, S., Weber, G.W. & Bookstein, F.L. 2009. Principles for the virtual reconstruction of hominin crania. *Journal of Human Evolution* 57: 48-62.

Harmon, E. 2009. Size and shape variation in the proximal femur of *Australopithecus africanus*. *Journal of Human Evolution* 56: 551-559.

Herries, A.I. & Shaw, J. 2011. Palaeomagnetic analysis of the Sterkfontein palaeocave deposits: implications for the age of the hominin fossils and stone tool industries. *Journal of Human Evolution* 60: 523-539.

Hylander, W.L. 1979. The functional significance of primate mandibular form. *Journal of Morphology* 160: 223-239.

Johanson, D.C. & White, T.D. 1979. A systematic assessment of early African hominids. *Science* 202: 321-330.

Johanson, D.C., White, T.D. & Coppens, Y. 1982. Dental remains from the Hadar Formation, Ethiopia: 1974–1977 collections. *American Journal of Physical Anthropology* 57: 545-603.

Jones, T.R. 1937. A new fossil primate from Sterkfontein, Krugersdorp, Transvaal. *South African Journal of Science* 33: 709-728.

Kimbel, W. H. & Rak, Y. 1993. The importance of species taxa in palaeoanthropology and an argument for the phylogenetic concept of the species category. In: Kimbel, W.H. & Martin, L.B. (eds.) *Species, species concepts, and primate evolution*: 461–484. New York: Plenum.

Kimbel, W. H., & White, T. D. 1988. Variation, sexual dimorphism and the taxonomy of *Australopithecus*. In: Grine, F.E. (ed.) *Evolutionary History of the ''Robust" Australopithecines*: 175–192. New York: Aldine de Gruyter.

Kimbel, W.H., Rak, Y. & Johanson, D.C. 2004. *The Skull of Australopithecus afarensis*. New York: Oxford University Press.

Kono, R.T. 2004. Molar enamel thickness and distribution patterns in extant great apes and humans: new insights based on a 3-dimensional whole crown perspective. *Anthropological Science* 112: 121-146.

Kuman, K. & Clarke, R.J. 2000. Stratigraphy, artefact industries and hominid associations for Sterkfontein, Member 5. *Journal of Human Evolution* 38: 827-847.

Leakey, L.S.B., Tobias, P.V. & Napier, J.R. 1964. A new species of the genus *Homo* from Olduvai Gorge. *Nature* 202: 7-9.

Lockwood, C.A. & Moggi-Cecchi, J. 1998. The systematic position of Stw 183, an adolescent maxilla from Sterkfontein. *American Journal of Physical Anthropology* 26: 151-152.

Lockwood, C.A. & Tobias, P.V. 2002. Morphology and affinities of new hominin cranial remains from Member 4 of the Sterkfontein Formation, Gauteng Province, South Africa. *Journal of Human Evolution* 42: 389-450.

Loth, S.R., Henneberg, M. & Thackeray, J.F. 1995. Assessment of the sex of Sts 5 and Stw 53: a new consideration of sexual dimorphism in fossil hominids. *American Journal Physical Anthropology* 38:136-137.

McCollum, M.A. 2008. Nasomaxillary remodeling and facial form in robust *Australopithecus*: a reassessment. *Journal of Human Evolution* 54: 2-14.

McCollum, M.A., Grine, F.E., Ward, S.C. & Kimbel, W.H. 1993. Subnasal morphological variation in extant hominoids and fossil hominids. *Journal of Human Evolution* 24: 87-111.

Moggi-Cecchi, J., Grine, F.E. & Tobias, P.V. 2006. Early hominid dental remains from Members 4 and 5 of the Sterkfontein Formation (1966-1996 excavations): catalogue, individual associations, morphological descriptions and initial metrical analysis. *Journal of Human Evolution* 50: 239-328.

Moggi-Cecchi, J., Tobias, P.V. & Beynon, A.D. 1998. The mixed dentition and associated skull fragments of a juvenile fossil hominid from Sterkfontein, South Africa. *American Journal of Physical Anthropology* 106: 425-465.

Olejniczak, A.J., Smith, T.M., Skinner, M.M., Grine, F.E., Feeney, R.N., Thackeray, J.F. & Hublin, J.J. 2008. Three-dimensional molar enamel distribution and thickness in *Australopithecus* and *Paranthropus*. *Biology Letters* 4: 406-410.

Olson, T.R. 1985. Cranial morphology and systematic and the Hadar Formation hominids and "*Australopithecus africanus*". In: Delson, E. (ed.) *Ancestors: The Hard Evidence*: 102-119. New York: Alan R. Liss.

O'Regan, H.J. & Reynolds, S.C. 2009. An ecological reassessment of the southern African carnivore guild: a case study from Member 4, Sterkfontein, South Africa. *Journal of Human Evolution* 57: 212-222.

Partridge, T.C. 1978. Re-appraisal of lithostratigraphy of Sterkfontein hominid site. *Nature* 275: 282-287.

Partridge, T.C., Granger, D.E., Caffee, M.W. & Clarke, R.J. 2003. Lower Pliocene hominid remains from Sterkfontein. *Science* 300: 607-612.

Partridge, T.C. & Watt, I.B. 1991. The stratigraphy of the Sterkfontein hominid deposit and its relationship to the underground cave system. *Palaeontologica Africana* 28: 35-40.

Peterson, A., Abella, E.F., Grine, F.E., Teaford, M.F. & Ungar, P.S. 2018. Microwear textures of *Australopithecus africanus* and *Paranthropus robustus* molars in relation to paleoenvironment and diet. *Journal of Human Evolution* 119: 42-63.

Pickering, R., Kramers, J.D., Partridge, T., Kodolanyi, J. & Pettke, T. 2010. U–Pb dating of calcite–aragonite layers in speleothems from hominin sites in South Africa by MC-ICP-MS. *Quaternary Geochronology* 5: 544-558.

Pickering, T.R. 2000. *Taphonomic interpretations of the Sterkfontein early hominid site (Gauteng, South Africa) reconsidered in light of recent evidence*. PhD Dissertation. Madison: University of Wisconsin.

Pickering, T.R., Clarke, R.J. & Moggi-Cecchi, J. 2004. Role of carnivores in the accumulation of the Sterkfontein Member 4 hominid assemblage: a taphonomic reassessment of the complete hominid fossil sample (1936–1999). *American Journal of Physical Anthropology* 125: 1-15.

Potze, S. & Thackeray, J.F. 2010. Temporal lines and open sutures revealed on cranial bone adhering to matrix associated with Sts 5 ("Mrs Ples"), Sterkfontein, South Africa. *Journal of Human Evolution* 58: 533-535.

Rak, Y. 1983. *The Australopithecine Face*. New York: Academic Press.

Rak, Y. 1985. Sexual dimorphism, ontogeny and the beginning of the differentiation of the robust australopithecine clade. In: Tobias, P.V. (ed.) *Hominid Evolution: Past, Present, and Future*: 233–237. New York: Alan R. Liss.

Reddy, S. 2015. *A hominid juvenile partial maxilla (StW 629/631) from Sterkfontein and associated artefacts*. Honours Dissertation. Johannesburg: University of the Witwatersrand.

Robinson, C. 2012. Geometric morphometric analysis of mandibular shape diversity in Pan. *Journal of Human Evolution* 63: 191-204.

Robinson, J.T. 1953. *Telanthropus* and its phylogenetic significance. *American Journal of Physical Anthropology* 11: 445-502.

Robinson, J.T. 1954. The genera and species of the australopithecinae. *American Journal of Physical Anthropology* 12: 181-200.

Robinson, J.T. 1956. The dentition of the australopithecinae. *Transvaal Museum Memoir* No. 9: Pretoria.

Robinson, J.T. 1963. Adaptive radiation in the *Australopithecines* and the origin of man. In: Howell, F.C. & Bourlière, F. (eds.) *African Ecology and Human Evolution*: 385-416. Chicago: Aldine de Gruyter.

Robinson, J.T. 1967. Variation and taxonomy of the early hominids. In: Dobzhansky, T., Hecht, M.K. & Steere, W.C. (eds.) *Evolutionary Biology*: 69-100. New York: Appleton-Century-Crofts.

Robinson, J.T. 1972. *Early Hominid Posture and Locomotion.* Chicago: University of Chicago Press.

Rogers-Ackermann, R. & Krovitz, G.E. 2002. Common patterns of facial ontogeny in the hominid lineage. *The Anatomical Record* 269: 142-147.

Schwartz, J. H., & Tattersall, I. 2005. *The Human Fossil Record. Vol. 4: Craniodental Morphology of Early Hominids (Genera, Australopithecus, Paranthropus, Orrorin), an Overview*. New Jersey: John Wiley & Sons.

Schwartz, D., Vontobel, P., Lehmann, E. H., Meyer, C. A. & Bongartz, G. 2005. Neutron tomography of internal structures of vertebrate remains: A comparison with X-ray computed tomography. *Palaeontologia Electronica* 8: 1-11.

Scott, R.S., Ungar, P.S., Bergstrom, T.S., Brown, C.A., Grine, F.E., Teaford, M.F. & Walker, A. 2005. Dental microwear texture analysis shows within-species diet variability in fossil hominins. *Nature* 436: 693-695.

Skelton, R.R., McHenry, H.M., Drawhorn, G.M., Bilsborough, A., Chamberlain, A.T., Wood, B.A. & Vančata, V. 1986. Phylogenetic analysis of early hominids. *Current Anthropology* 27: 21-43.

Skinner, M.M. 2008. *Enamel-dentine junction morphology of extant hominoid and fossil hominin lower molars*. PhD Dissertation. Washington D.C: George Washington University.

Skinner, M.M., Gunz, P., Wood, B.A. & Hublin, J.J. 2008. Enamel-dentine junction (EDJ) morphology distinguishes the lower molars of *Australopithecus africanus* and *Paranthropus robustus*. *Journal of Human Evolution* 55: 979-988.

Skinner, M.M., Gunz, P., Wood, B.A., Boesch, C. & Hublin, J.J. 2009. Discrimination of extant *Pan* species and subspecies using the enamel–dentine junction morphology of lower molars. *American Journal of Physical Anthropology* 140: 234-243.

Smith, B.H. 1986. Dental development in *Australopithecus* and early *Homo*. *Nature* 323: 327-330.

Smith, T.M. 2008. Incremental dental development: methods and applications in hominoid evolutionary studies. *Journal of Human Evolution* 54: 205-224.

Sponheimer, M., Passey, B.H., De Ruiter, D.J., Guatelli-Steinberg, D., Cerling, T.E. & Lee-Thorp, J.A. 2006. Isotopic evidence for dietary variability in the early hominin *Paranthropus robustus*. *Science* 314: 980-982.

Spoor, F., Gunz, P., Neubauer, S., Stelzer, S., Scott, N., Kwekason, A. & Dean, M.C. 2015. Reconstructed *Homo habilis* type OH 7 suggests deep-rooted species diversity in early Homo. *Nature* 519: 83-90.

Strait, D.S. & Grine, F.E. 2004. Inferring hominoid and early hominid phylogeny using craniodental characters: the role of fossil taxa. *Journal of Human Evolution* 47: 399-452.

Stratford, D., Merlo, S. & Brown, S. 2016. The development of a new geospatial framework for the palaeoanthropological site of the Sterkfontein Caves, Cradle of Humankind, Gauteng, South Africa. *Journal of Field Archaeology* 41: 211-221.

Subsol, G., Braga, J., Thackeray, F., Dasgupta, G., Dedouit, F. & Telmon, N. 2008. Evolution of Late Pliocene Hominin Midfacial Morphology. An approach using Three-Dimensional Surface Registration. *Presented at the 77th Annual Meeting of the American Association of Physical Anthropologists* (pp. N-A).

Subsol, G., Mafart, B., Silvestre, A. & de Lumley, M.A. 2002. 3D image processing for the study of the evolution of the shape of the human skull: presentation of the tools and preliminary results. *Three-Dimensional Imaging in Palaeoanthropology and Prehistoric Archaeology* 1049: 37-45.

Suwa, G., Wood, B.A. & White, T.D. 1994. Further analysis of mandibular molar crown and cusp areas in Pliocene and early Pleistocene hominids. *American Journal of Physical Anthropology* 93: 407-426.

Taylor, A.B. 2006. Size and shape dimorphism in great ape mandibles and implications for fossil species recognition. *American Journal of Physical Anthropology* 129: 82-98.

Thackeray, J.F. 1997. Cranial bone of “Mrs Ples” (Sts 5): fragments adhering to matrix. *South African Journal of Science* 93: 169-170.

Thackeray, J.F. 2000. “Mrs Ples” from Sterkfontein: small male or large female? *The South African Archaeological Bulletin* 55: 155-158.

Thackeray, J.F. 2007. Approximation of a biological species constant? *South African Journal of Science* 103: 489.

Thackeray, J.F., Braga, J., Treil, J., Niksch, N. & Labuschagne, J.H. 2002. "Mrs Ples" (Sts 5) from Sterkfontein: an adolescent male? *South African Journal of Science* 98: 21-22.

Tobias, P.V. 1967. *Olduvai Gorge*, Vol. 2: *The Cranium and Maxillary Dentition of Australopithecus (Zinjanthropus) boisei*. Cambridge: Cambridge University Press.

Tobias, P. V. 1980. "*Australopithecus afarensis*" and *A. africanus*: critique and an alternative hypothesis. *Palaeontologia Africana* 23: 1-17.

Toussaint, M., Macho, G.A., Tobias, P.V., Partridge, T.C. & Hughes, A.R. 2003. The third partial skeleton of a late Pliocene hominin (StW 431) from Sterkfontein, South Africa. *South African Journal of Science* 99: 215-223.

Turner, A. & Wood, B. 1993. Comparative palaeontological context for the evolution of the early hominid masticatory system. *Journal of Human Evolution* 24: 301-318.

Wallace, J.A. 1972. *The dentition of the South African early hominids: a study of form and function*. PhD Dissertation. Johannesburg: University of the Witwatersrand.

White, T.D. 1977. New fossil hominids from Laetolil, Tanzania. *American Journal of Physical Anthropology* 46: 197-229.

White, T.D., Black, M.T. & Folkens, P.A. 2012. *Human Osteology Third Edition*. Burlington: Academic Press.

White, T. D., Johanson, D. C., & Kimbel, W. H. 1981. *Australopithecus africanus*: its phyletic position reconsidered. *South African Journal of Science* 77: 445-470.

Williams, F.L.E., Schroeder, L. & Ackermann, R.R. 2012. The mid-face of lower Pleistocene hominins and its bearing on the attribution of SK 847 and StW 53. *HOMO-Journal of Comparative Human Biology* 63:245-257.

Wolpoff, M.H. 1974. The evidence for two australopithecine lineages in South Africa. *Yearbook of Physical Anthropol*ogy 17: 113-139.

Wolpoff, M.H. 1975. Sexual dimorphism in the australopithecines. In: Tuttle, R. (ed.) *Paleoanthropology, Morphology and Paleoecology*: 245-284. Mouton: The Hague.

Wood, B.A. 1991. *Koobi Fora Research Project Volume 4: Hominid Cranial Remains*. New York: Oxford University Press.

Wood, B. A., Abbott, S. A., & Graham, S. H. 1983. Analysis of the dental morphology of Plio-Pleistocene hominids. II. Mandibular molars--study of cusp areas, fissure pattern and cross sectional shape of the crown. *Journal of Anatomy* 137: 287–314.

Zanolli, C. 2015. Brief communication: molar crown inner structural organization in Javanese *Homo erectus*. *American Journal of Physical Anthropology* 156: 148-157.

Zanolli, C., Bayle, P., Bondioli, L., Dean, M.C., Le Luyer, M., Mazurier, A., Morita, W. & Macchiarelli, R. 2017. Is the deciduous/permanent molar enamel thickness ratio a taxon-specific indicator in extant and extinct hominids? *Comptes Rendus Palevol* 16: 702-714.

Zanolli, C., Martinón-Torres, M., Bernardini, F., Boschian, G., Coppa, A., Dreossi, D., Mancini, L., de Pinillos, M.M., Martín-Francés, L., de Castro, J.M.B. &

Tozzi, C. 2018. The Middle Pleistocene (MIS 12) human dental remains from Fontana Ranuccio (Latium) and Visogliano (Friuli-Venezia Giulia), Italy. A comparative high resolution endostructural assessment. *PloS One* 13: 1-25.